



Oliver Linder

**Self-consistent modeling of electron
runaway in tokamak disruptions**



Technische Universität München
Fakultät für Informatik

Self-consistent modeling of electron runaway in tokamak disruptions

Oliver Linder

Vollständiger Abdruck der von der Fakultät für Informatik der Technischen Universität München zur Erlangung eines

Doktors der Naturwissenschaften (Dr. rer. nat.)

genehmigten Dissertation.

Vorsitzender: Prof. Dr. Hans-Joachim Bungartz

Prüfende der Dissertation:

1. Hon.-Prof. Dr. Frank Jenko
2. Prof. Dr. Hartmut Zohm

Die Dissertation wurde am 28.07.2021 bei der Technischen Universität München eingereicht und durch die Fakultät für Informatik am 01.02.2022 angenommen.

© Oliver Linder, 2021.



Distributed under the terms of the Creative Commons Attribution license CC BY 4.0 (<http://creativecommons.org/licenses/by/4.0/>), which permits unrestricted re-use, distribution, and reproduction in any medium, provided the original work is properly cited.

Cover: Schematic of the interior of the experimental fusion reactor ASDEX Upgrade.

Cover design by Jessica Linder

Für Dorothee

Kurzfassung

Energiegewinnung durch die Fusion leichter Atomkerne hat das Potenzial den Energiesektor zu revolutionieren. Die Realisierbarkeit soll in den kommenden Jahren durch den aktuell im Bau befindlichen Reaktor ITER demonstriert werden. Um den Erfolg dieses Projekts sicherzustellen, gilt es die Erzeugung relativistischer *Runaway-Elektronen* als Konsequenz makroskopischer Plasmainstabilitäten, *Disruptionen* genannt, zu verhindern und Materialschaden der Reaktorwand vorzubeugen. Hierzu könnten große Mengen zusätzlichen Gases in den Reaktor eingespeist werden. Ob dieses Konzept tatsächlich geeignet ist, wird derzeit in mehreren experimentellen Reaktoren untersucht, wozu ferner theoretische und rechnergestützte Studien durchgeführt werden.

In der vorgelegten Arbeit wird eine Software basierend auf den 1.5D Transport-Codes ASTRA und STRAHL vorgestellt, welche selbstkonsistente Simulationen von Hauptplasma, eingespeistem Material und Runaway-Elektronen in Fusionsreaktoren ermöglicht. Die fortwährende Beschleunigung thermischer Elektronen hin zu relativistischen Energien, *Runaway-Effekt* genannt, wird in diesem Zusammenhang durch simple analytische Modelle und modernste Fluidmodelle beschrieben. Letztere berücksichtigen dabei die Wechselwirkungen der Runaway-Elektronen mit der Elektronenhülle eingespeister Gasatome. Die Dichteverteilung einzelner Ionisationsstufen wird mittels Ratengleichungen atomarer Prozesse berechnet. Ferner transportieren neoklassische und magnetohydrodynamische Prozesse das eingespeiste Gas in das Kernplasma hinein.

Der beschriebene Ansatz konnte mittels selbstkonsistenter Simulationen des Tokamaks ASDEX Upgrade erfolgreich validiert werden. Die zeitliche Entwicklung relevanter Größen, wie Elektronendichte und Plasmastrom, wird durch die eingesetzte Software übereinstimmend mit experimentellen Beobachtungen berechnet. Insbesondere kann die Erzeugung des Runaway-Elektronen-Stroms nur unter Verwendung modernster Fluidmodelle akkurat beschrieben werden. Unter Vernachlässigung der Wechselwirkungen zwischen Runaway-Elektronen und Gasionen können einfachere analytische Modelle relevante Aspekte nur unzureichend wiedergeben. Folglich kommt jenen Wechselwirkungen besondere Relevanz bei der Erzeugung von Runaway-Elektronen zu, sodass diese Effekte im Rahmen selbstkonsistenter Simulationen nicht vernachlässigt werden dürfen.

Die Erzeugung eines signifikanten Runaway-Elektronen-Stroms zum Ende einer Disruption in Reaktoren mittlerer Größe ist hauptsächlich auf die lawinenartige Vervielfältigung einer geringen Initialpopulation zurückzuführen. Deren exakte Größe wirkt sich dabei lediglich geringfügig auf die Stärke des Runaway-Elektronen-Stroms am Ende der Disruption aus. Die durchgeführten Simulationen deuten ferner darauf hin, dass ein substanzieller Anteil der Initialpopulation in einem frühen Stadium der Disruption verloren geht. In zukünftigen Hochtemperaturfusionsreaktoren könnte dieser Effekt möglicherweise die von Runaway-Elektronen ausgehende Gefahr mindern.

Abstract

Nuclear fusion of light atomic nuclei has the potential of revolutionizing commercial energy production. The feasibility of this approach is to be demonstrated by the ITER reactor, currently under construction. However, to ensure its successful operation, generating a dangerously large population of relativistic *runaway electrons* during macroscopic plasma instabilities, referred to as *disruptions*, must be avoided and potential damage to plasma facing components mitigated. Through injection of massive amounts of material into the plasma vessel, this threat could be brought under control. The suitability of this scheme is being investigated across various experimental reactors, complemented by theoretical and computational studies.

In this work, a toolkit based on the coupled 1.5D transport codes `ASTRA` and `STRAHL` is presented, thus allowing self-consistent simulations of background plasma, material injected and runaway electron generation in fusion devices. The process of electron runaway due to rapid plasma cooling, momentum space diffusion and knock-on collisions is described by state-of-the-art reduced kinetic models under consideration of high- Z interactions, as well as by simple analytical models neglecting these effects. The impurity ionization stages of the material introduced are evolved following electron-impact atomic processes. Propagation into the core plasma can be attributed to neoclassical phenomena and magnetohydrodynamic effects.

Applying `ASTRA-STRAHL` in self-consistent simulations of the tokamak ASDEX Upgrade, the toolkit is demonstrated to reproduce the temporal evolution of key experimental observations successfully, such as the free electron density, the plasma current, as well as the runaway electron current. Importantly, characteristics of the evolution of the runaway electron current can only be reproduced under application of state-of-the-art reduced kinetic models describing electron runaway in the presence of partially ionized material. Simpler models neglecting these effects fail to capture the overall current evolution, thus highlighting the impact of interactions between non-fully ionized material and runaway electrons.

The formation of a postdisruption runaway electron current in midsize fusion devices is furthermore shown to be dominated by avalanche multiplication in simulations of ASDEX Upgrade. The exact strength of the runaway seed population is found to be only of secondary importance in determining the postdisruption runaway electron current. Simultaneously, these simulations suggest the presence of seed loss mechanisms, which could potentially alleviate the runaway electron threat in future high-temperature fusion devices.

Publications

Publications included in this dissertation

1. **O. Linder**, E. Fable, F. Jenko, G. Papp, G. Pautasso, the ASDEX Upgrade Team and the EUROfusion MST1 Team,
Self-consistent modeling of runaway electron generation in massive gas injection scenarios in ASDEX Upgrade,
Nuclear Fusion **60**, 096031 (2020).
<https://doi.org/10.1088/1741-4326/ab9dcf>
[arXiv:2003.00725](https://arxiv.org/abs/2003.00725) [physics.plasm-ph]
2. **O. Linder**, G. Papp, E. Fable, F. Jenko, G. Pautasso, the ASDEX Upgrade Team, and the EUROfusion MST1 Team,
Electron runaway in ASDEX Upgrade experiments of varying core temperature,
Journal of Plasma Physics **87**, 905870301 (2021).
<https://doi.org/10.1017/S0022377821000416>
[arXiv:2101.04471](https://arxiv.org/abs/2101.04471) [physics.plasm-ph]

Other publications

1. **O. Linder**, J. Citrin, G.M.D. Hogeweij, C. Angioni, C. Bourdelle, F.J. Casson, E. Fable, A. Ho, F. Koechl, M. Sertoli, the EUROfusion MST1 Team and the ASDEX Upgrade Team,
Flux-driven integrated modelling of main ion pressure and trace tungsten transport in ASDEX Upgrade,
Nuclear Fusion **59**, 016003 (2019).
<https://doi.org/10.1088/1741-4326/aae875>
[arXiv:2002.00680](https://arxiv.org/abs/2002.00680) [physics.plasm-ph]
2. H. Meyer for the ASDEX Upgrade Team including **O. Linder**,
Overview of physics studies on ASDEX Upgrade,
Nuclear Fusion **59**, 112014 (2019).
<https://doi.org/10.1088/1741-4326/ab18b8>
3. G. Pautasso, M. Dibon, M. Dunne, R. Dux, E. Fable, P. Lang, **O. Linder**, A. Mlynek, G. Papp, M. Bernert et al,
Generation and dissipation of runaway electrons in ASDEX Upgrade experiments,
Nuclear Fusion **60**, 086011 (2020).
<https://doi.org/10.1088/1741-4326/ab9563>

-
4. F. Sciortino, T. Odstrčil, A. Cavallaro, S. Smith, O. Meneghini, R. Reksoatmodjo, **O. Linder**, J.D. Lore, N.T. Howard, E.S. Marmor et al,
Modeling of particle transport, neutrals and radiation in magnetically-confined plasmas with Aurora,
Plasma Physics and Controlled Fusion **63**, 112001 (2021).
<https://doi.org/10.1088/1361-6587/ac2890>
arXiv:2106.04528 [physics.plasm-ph]

Conference and workshop contributions

1. **O. Linder**, G. Papp, E. Fable, F. Jenko, G. Pautasso, the ASDEX Upgrade Team and the EUROfusion MST1 Team,
The role of impurity transport and temperature in MGI induced runaway dynamics,
Invited talk at the IAEA/PPPL 2021 Virtual Theory and Simulation of Disruptions Workshop, 19.-23.07.2021.
<https://tsdw.pppl.gov/Talks/2021/Linder.pdf>
2. **O. Linder**, E. Fable, F. Jenko, G. Papp, G. Pautasso, the ASDEX Upgrade Team and the EUROfusion MST1 Team,
Validation of state-of-the-art runaway electron generation models in simulations of ASDEX Upgrade disruptions,
Contributed talk at the 47th EPS Conference on Plasma Physics, virtual, 21.-25.06.2021, O3.101.
<http://ocs.ciemat.es/EPS2021PAP/pdf/O3.101.pdf>
3. **O. Linder**, G. Papp, E. Fable, F. Jenko and G. Pautasso,
Runaway electron generation and model validation in self-consistent simulations of ASDEX Upgrade disruptions,
Contributed talk at the 37th ITPA MHD, Disruption and Control Topical Group Meeting, virtual, 22.-25.03.2021.
4. **O. Linder** and G. Papp,
Transport modeling of electron runaway with reduced kinetic tools for JT-60SA,
Contributed talk at the WPSA Project Planning Meeting, virtual, 15.-19.03.2021.
<https://indico.euro-fusion.org/event/870/contributions/2857/>
5. **O. Linder**, E. Fable, F. Jenko, G. Papp, G. Pautasso, the ASDEX Upgrade Team and the EUROfusion MST1 Team,
Electron runaway in massive material injection scenarios in ASDEX Upgrade using state-of-the-art generation models,
Invited talk at the 4th Asian Pacific Conference on Plasma Physics, virtual, 26.-31.10.2020, MF2-I21.
<http://aappsdp.org/DPP2020/pdf/MF2-I21.pdf>

6. **O. Linder**, E. Fable, F. Jenko, G. Papp and G. Pautasso,
Runaway electron modeling in massive material injection scenarios in ASDEX Upgrade,
Presentation at the HEPP Autumn Colloquium, Garching, Germany, 09.10.2020.
<https://www.ipp.mpg.de/events/26017/4986257>
7. **O. Linder**, E. Fable, F. Jenko, G. Papp and G. Pautasso,
Validation of state-of-the-art runaway electron generation models in simulations of ASDEX Upgrade disruptions,
Contributed talk at the IAEA (Virtual) Technical Meeting on Plasma Disruptions and their Mitigation, Saint-Paul-lez-Durance, France, 20.-23.07.2020.
<https://conferences.iaea.org/event/217/contributions/16690/>
8. **O. Linder**, E. Fable, F. Jenko, G. Papp and G. Pautasso,
Study of RE formation in MGI scenarios in ASDEX Upgrade with ASTRA,
Contributed talk at the 8th Meeting on Runaway Electron Modelling (REM), Gothenburg, Sweden, 13.-17.01.2020.
<https://ft.nephy.chalmers.se/?p=abstract&id=4>
9. G. Papp, G. Pautasso, J. Decker, L. Hesslow, M. Hoppe, M. Bernert, P. Blanchard, A. Bock, T. Bolzonella, **O. Linder** et al,
The effect of high-Z material injection on runaway electron dynamics,
Invited talk at the 46th EPS Conference on Plasma Physics, Milan, Italy, 08.-12.07.2019, I4.105.
<http://ocs.ciemat.es/EPS2019ABS/pdf/I4.105.pdf>
10. **O. Linder**, E. Fable, F. Jenko, G. Papp and G. Pautasso,
Impact of massive material injection on runaway electron generation,
Poster at the 46th EPS Conference on Plasma Physics, Milan, Italy, 08.-12.07.2019, P4.1034.
<http://ocs.ciemat.es/EPS2019PAP/pdf/P4.1034.pdf>
11. **O. Linder**, E. Fable, F. Jenko, G. Papp and G. Pautasso,
Impact of massive gas injection on runaway electron generation,
Presentation at the HEPP Seminar, Garching, Germany, 24.06.2019.
<https://www.ipp.mpg.de/events/18888/4050942>
12. **O. Linder**, E. Fable, F. Jenko, G. Papp and G. Pautasso,
Self-consistent modelling of runaway electron generation in massive material injection scenarios in current-carrying fusion devices,
Poster at the DPG-Frühjahrstagung der Sektion Materie und Kosmos (SMuk), München, Germany, 17.-22.03.2019, P 18.91.
<https://www.dpg-verhandlungen.de/year/2019/conference/muenchen/part/p/session/18/contribution/91>

-
13. **O. Linder**, E. Fable, F. Jenko, G. Papp and G. Pautasso,
Modelling the impact of MGI on RE generation with transport solvers,
Contributed talk at the 7th Meeting on Runaway Electron Modelling (REM),
Gothenburg, Sweden, 15.-18.01.2019.
 14. **O. Linder**, E. Fable, F. Jenko, G. Papp, G. Pautasso, the EUROfusion MST1 Team
and the ASDEX Upgrade Team,
*Towards self-consistent modelling of runaway electron generation in massive gas
injection scenarios*,
Poster at the ITER FuseNet PhD Event 2018, ITER Headquarters, France, 06.-
09.11.2018.
<https://www.iter.org/fusion-phd>
 15. G. Papp, G. Pautasso, J. Decker, D. Carnevale, P. Blanchard, D. Choi, S. Coda, B.
Duval, R. Dux, **O. Linder** et al,
*Parameter dependences of runaway electron dynamics on ASDEX Upgrade and
TCV*,
Contributed talk at the 60th Annual Meeting of the APS Division of Plasma Physics,
Portland, Oregon, USA, 05.-09.11.2018, YO5.13.
<http://meetings.aps.org/Meeting/DPP18/Session/YO5.13>
 16. G. Pautasso, M. Bernert, M. Dibon, M. Dunne, R. Dux, E. Fable, **O. Linder**, P.
McCarthy, A. Mlynek, G. Papp, the ASDEX Upgrade Team and the EUROfusion
MST1 Team,
Argon assimilation during thermal quench and runaway electron generation,
Poster at the 45th EPS Conference on Plasma Physics, Prague, Czech Republic, 02.-
06.07.2018, P4.1058.
<http://ocs.ciemat.es/EPS2018PAP/pdf/P4.1058.pdf>
 17. **O. Linder**, E. Fable, F. Jenko, G. Papp and G. Pautasso,
*Self-consistent modelling of runaway electron generation in massive gas injection
scenarios*,
Contributed talk at the 6th Runaway Electron Meeting, Prague, Czech Republic,
28.-30.06.2018.
 18. **O. Linder**, E. Fable, F. Jenko, G. Papp and G. Pautasso,
Modelling of runaway electron generation and benchmark against experiments,
Presentation at the HEPP Seminar, Garching, Germany, 23.04.2018.
<https://www.ipp.mpg.de/events/13783/4583121>

Nomenclature

The following quantities are used repeatedly throughout this work. Quantities are evaluated in SI units or SI derived units unless stated otherwise.

a	midplane minor radius
B	magnetic field
c	speed of light: $299\,792\,458\text{ m s}^{-1}$
D	diffusion coefficient
e	elementary charge: $1.602\,177 \times 10^{-19}\text{ C}$
E	electric field
f	particle distribution function
j	current density
I	current
K	adaptive upwinding parameter
k_B	Boltzmann constant: $1.380\,649 \times 10^{-23}\text{ J K}^{-1}$
m	particle mass
	poloidal mode number
n	particle density
	toroidal mode number
p	momentum
q	safety factor
r	radial coordinate
R	tokamak major radius
S	source
t	time
T	temperature (given in units of eV throughout this work)
U	voltage
v	velocity
V	volume
\mathbf{x}	position space vector
Z	electric charge in multiples of e
α	fine-structure constant: $1/137.035\,999$
γ	Lorentz factor
Γ	(particle) flux
	runaway electron generation rate
δ	triangularity of a flux surface
Δ	Shafranov shift of a flux surface
$\epsilon = r/R$	inverse aspect ratio
ϵ_0	vacuum permittivity: $8.854\,188 \times 10^{-12}\text{ F m}^{-1}$
θ	poloidal angle
κ	elongation of a flux surface
λ	length scale

$\ln \Lambda$	Coulomb logarithm
μ_0	vacuum permeability: $4\pi \times 10^{-7} \text{ H m}^{-1}$
ν	collision frequency
Ψ	poloidal magnetic flux
ρ	flux coordinate
σ	plasma electrical conductivity
τ	(normalized) time scale
ϕ	toroidal angle
Φ	toroidal magnetic flux
χ	heat diffusion coefficient

Acronyms

CQ	current quench
LCFS	last closed flux surface
MHD	magnetohydrodynamics
RE	runaway electron
TQ	thermal quench

Subscript abbreviations

add	additional
av	avalanche
bnd	bound
Br	Bremsstrahlung
c	critical
d	deflection
D	Dreicer
dec	decay
e	electron
eff	effective
ext	external
fin	final
hot	hot-tail
i	ion
inj	injection
p	plasma
rad	radiation
rel	relativistic
s	slowing-down
syn	synchrotron
th	thermal
tot	total

Contents

Preface	iii
Kurzfassung	iv
Abstract	v
Publications	vi
Nomenclature	x
Acronyms	xi
Subscript abbreviations	xi
Contents	xiii
1 Introduction	1
1.1 Nuclear fusion – a stellar idea	2
1.2 Magnetic confinement fusion	4
1.3 Plasma disruptions & their mitigation	6
1.4 Electron runaway	8
1.4.1 Generation mechanisms	10
1.4.2 Runaway modeling	11
1.5 Structure and scope of this thesis	13
2 Methodology	15
2.1 Generation of runaway electrons	16
2.1.1 The critical electric field	16
2.1.2 Impact of partially ionized impurities on runaway	18
2.1.3 Dreicer generation	20
2.1.4 Hot-tail generation	23
2.1.5 Avalanche generation	30
2.2 From magnetic flux surfaces to a radial coordinate	32
2.3 ASDEX Upgrade runaway electron experiments	34
2.4 The macroscopic transport equation	38
2.5 The transport code ASTRA	39
2.5.1 The ASTRA magnetic equilibrium	41
2.5.2 Simulating electron runaway	41
2.5.3 Simulating massive gas injection	42
2.5.4 Improvements to ASTRA	45
2.6 The impurity transport code STRAHL	48
2.6.1 Treatment of neutral impurities	49

2.6.2	The discretization scheme	51
2.6.3	Coupling to ASTRA	57
2.6.4	Simulating massive gas injection	58
2.7	Simulation specific details	60
3	Summary of included papers	63
3.1	Paper #1	64
3.2	Paper #2	66
4	Discussion	69
4.1	Material deposition	70
4.2	Breakup of magnetic surfaces	72
4.3	Agreement with experimental observations	73
4.4	Investigation of electron runaway	76
5	Summary & conclusion	83
	Bibliography	89
	Included papers	101
	Paper #1	103
	Paper #2	121



Introduction

1

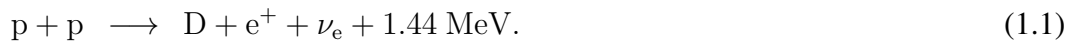
*Stand beneath the open sky
In due time, the Sun will rise
Longing for its stellar wisdom
We embrace the soothing light*

*Dearest Sun, She brings Us warmth
Dispels the void's bleak grip
Cradle, Earth, filled with breath
Her sons and daughters onward*

*But far from this just patron
The thirst cannot be quenched
Could We dig a well one day
And bring Our Sun to Earth?*

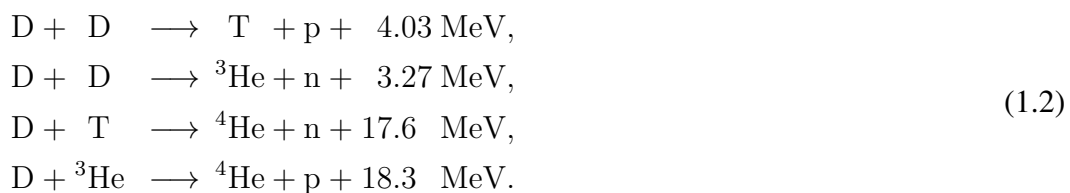
1.1 Nuclear fusion – a stellar idea

The mechanism powering the Sun, and all other stars, is nuclear fusion of light atomic nuclei into heavier elements [1]. In the process, energy is released as a result of competing attractive nuclear and repulsive Coulomb forces. An energetic minimum is eventually reached for iron and nickel isotopes [2]. Along the way, a myriad of nuclear reactions are possible. Similarly in the Sun, several chains of reactions are at play for creating heavier nuclei [3]. However, they all start, one way or another, with nuclear fusion of two protons (p) into deuterium (D),



The cross section σ for this process is minuscule and as such cannot be measured in the laboratory [4]. Yet, theoretical estimates put the reactivity $\langle\sigma v\rangle$ at temperatures of $1.55 \times 10^7 \text{ K}$ (1.34 keV) as prevailing in the Sun's center in the order of $10^{-49} \text{ m}^3 \text{ s}^{-1}$. The dependence of the fusion reactivity on temperature is shown in figure 1.1 for this process, $p(p, e^+\nu_e)D$, and other stellar fusion reactions involving hydrogen and helium (He) isotopes. A common feature of these processes is their small reactivity. However, given the high (number) density of these nuclei in the Sun's core [5], as well as its size, the Sun releases tremendous amounts of energy each second.

Contemplating the possibility of recreating the Sun's fusion processes on Earth for the production of energy, the high proton densities necessary seem to put a quick stop to this endeavor as these conditions are for practical purposes impossible to achieve artificially. However, by selecting a more suitable fusion reaction and increasing the temperature of the nuclei involved, artificial nuclear fusion can be achieved much easier. Promising alternatives to stellar fusion reactions involve heavier hydrogen isotopes, i.e. [6]



The reactivities of these fusion processes are several orders of magnitude larger than the ones of stellar reactions (see figure 1.1). Out of the processes introduced, fusion of deuterium and tritium (T) nuclei is the easiest to achieve. The corresponding reactivity reaches its maximum value for temperatures in the range of 70 keV ($8 \times 10^8 \text{ K}$), being around 50 times hotter than the center of the Sun. Given the largest reactivity of all nuclear fusion processes throughout a broad temperature range, nuclear fusion of deuterium and tritium is being considered as mechanism for energy production in first generation fusion reactors [7, 8]. For a discussion of the drawbacks of utilizing DT-fusion, see e.g. references 7, 8. In the majority of present-day experiments, however, only deuterium is used for the study of fundamental processes.

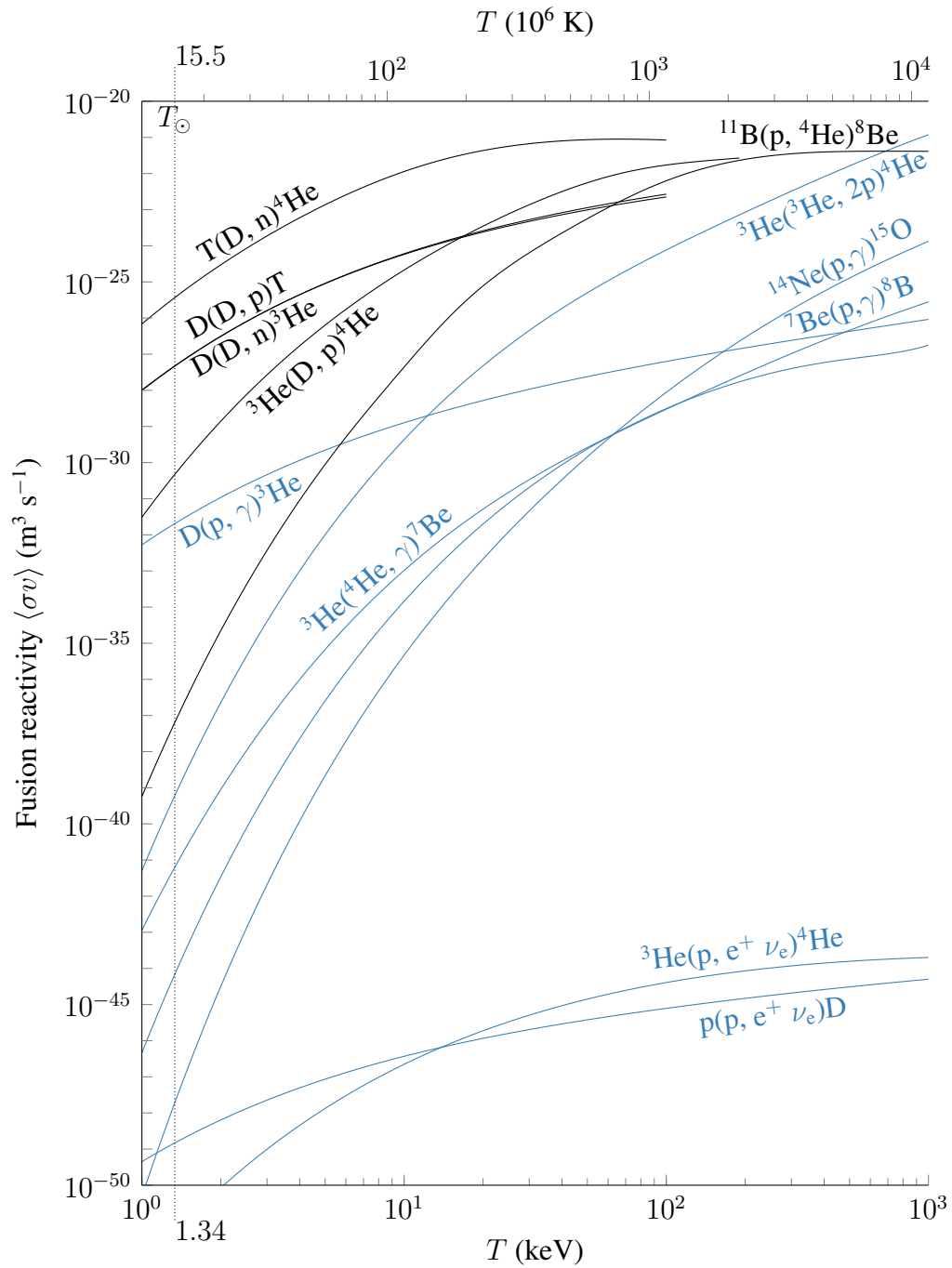


Figure 1.1: Reactivities of nuclear fusion processes involving hydrogen and helium isotopes as a function of temperature in a range relevant for stellar [4] and terrestrial [6, 9] fusion. Reactions occurring in the Sun’s core are illustrated in blue. For reference, the Sun’s core temperature T_{\odot} is marked with a vertical line. Nuclear fusion is easier to achieve for processes with a large reactivity at low temperatures (upper, left region of the figure). In the case of proton-proton fusion (see equation (1.1)), $\text{p}(\text{p}, \text{e}^+ \nu_e)\text{D}$, the reactivity is generally minuscule.

1.2 Magnetic confinement fusion

Following fundamental research on the nature of nuclear fusion in the 1920s to 1930s (see e.g. references 1–3) and early experiments during the 1940s [10], research on controlled nuclear fusion picked up pace in the 1950s with the emergence of different designs for fusion devices, most importantly in the US and the Soviet Union [10,11]. The central idea shared by these approaches consists of confining ionized material, referred to as a *plasma*, inside a magnetic field and heating it up to temperatures sufficient for nuclear fusion to take place.

One particularly promising design is the Russian conceived *tokamak*; a transliteration of the Russian acronym for *toroidal chamber with axial magnetic field*. As such, the term *tokamak* already provides a description of the fundamental design idea behind the device. An axial, i.e. *toroidal*, magnetic field required for plasma confinement is created by external planar coils [12] (see figure 1.2 for a schematic). To compensate the outward drift of the plasma in the resulting curved toroidal magnetic field, a helical magnetic field is necessary. The missing *poloidal* field component is created by driving a strong plasma current in the MA range along the toroidal direction. The current is generated by utilizing the plasma as secondary winding of a transformer circuit with an additional set of coils located in the torus center, the *central solenoid*, acting as primary winding. The operation of tokamak devices is thus by design restricted to a non-continuous, pulsed mode. It should be noted that since the tokamak's conception in the 1950s, methods for

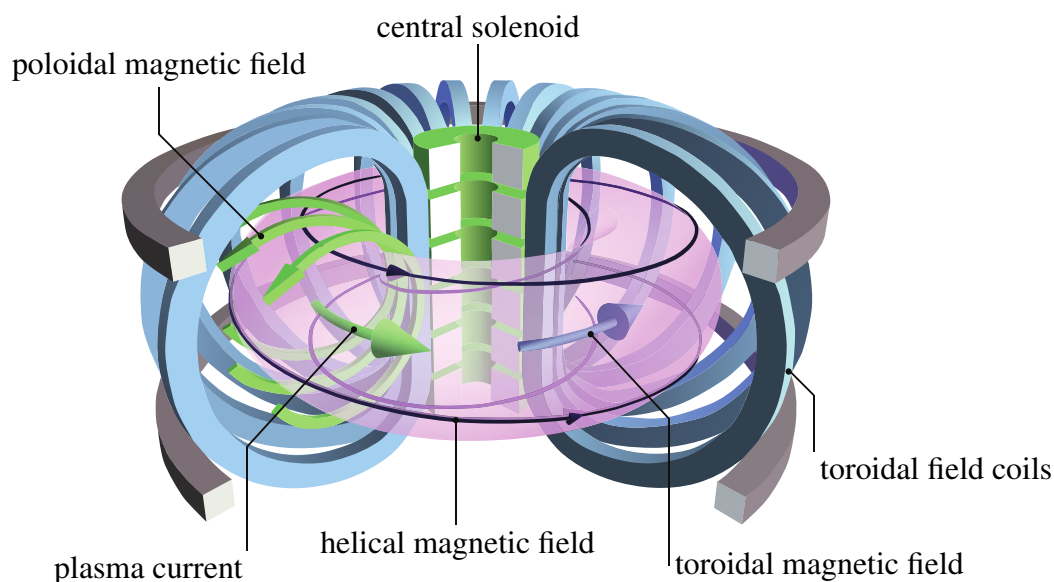


Figure 1.2: Schematic of a tokamak type fusion device. The hot plasma is confined inside a helical magnetic field, the toroidal component of which is created by toroidal field coils. The poloidal magnetic field component is generated by a plasma current, which in turn is induced by the changing magnetic flux of the central solenoid. CC Image courtesy of EUROfusion.

non-inductive current drive have been developed to overcome the tokamak's limitations (see e.g. reference 13).

By now, the tokamak type fusion reactor constitutes the most advanced approach to magnetic confinement fusion, given decades of research and development. Major contributions to this line of devices have been made by the German tokamak *ASDEX Upgrade* [15, 16] at the Max Planck Institute for Plasma Physics in Garching near Munich. Still, despite decades of research, the ultimate goal of net power production has yet to be achieved. To path the way to commercial fusion energy, the world's largest tokamak is currently being built in the south of France, named appropriately *ITER* (latin: the way) [17]. Expected to go into first operation in December 2025, the demonstration of net power generation, with tenfold amplification of the power input, is envisioned for 2035.

A challenger approach in the field of magnetic confinement fusion is the *stellarator* concept, proposed in the 1950s in the US [10, 18]. The plasma confining helical field is generated completely by external coils, thus intrinsically allowing steady-state operation in contrast to tokamak devices. However, confinement properties of stellarators historically fell behind the tokamak's capabilities [10, 19]. With the advancement of computing resources since the 1980s, optimization of the 3D magnetic geometry for plasma confinement has significantly improved stellarator performance [14, 19]. The most advanced stellarator Wendelstein 7-X (see figure 1.3 for a schematic), operated by the Max Planck Institute for Plasma Physics in Greifswald, is even expected to surpass tokamak devices in certain confinement properties [14]. Although in the current European roadmap to commercial fusion power, a tokamak *DEMONstration* power plant is envisioned, following first commercial plants could be of the stellarator line [20–22].

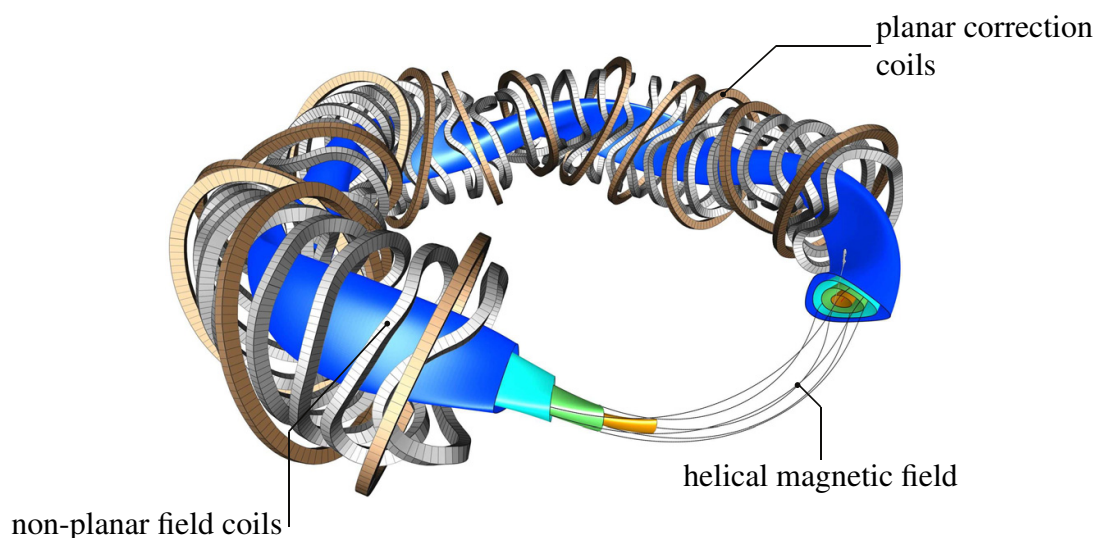


Figure 1.3: Schematic of Wendelstein 7-X, a stellarator type fusion device. The plasma confining helical magnetic field is created completely by non-planar field coils. Additional planar coils are used for magnetic field correction and plasma position control. CC Image from reference 14.

Besides by means of magnetic confinement, another approach to controlled nuclear fusion is inertial confinement fusion, where compression of the nuclear fuel creates fusion relevant conditions [23]. However, as the path to commercial fusion power following this approach is nebulous, it is mentioned only for completeness.

In the work presented in this thesis, questions relevant for the successful operation of tokamak-type fusion devices within the field of magnetic confinement fusion are addressed by simulations using experimental results from the ASDEX Upgrade tokamak. The material discussed in the following is thus applicable predominantly to tokamaks.

1.3 Plasma disruptions & their mitigation

A key challenge on the way to commercial tokamak type nuclear fusion devices is ensuring magnetohydrodynamic (MHD) stability of the fusion plasma while achieving a large fusion power output. To assist with generating reactor relevant amounts of fusion power, a high plasma pressure is necessary. By increasing the plasma temperature, individual nuclei are more likely to undergo a fusion reaction as the DT fusion reactivity increases up to temperatures of around 100 keV (see figure 1.1). With higher plasma density and as such more available nuclei, the overall fusion reaction rate increases quadratically. Additionally, confinement of the fusion plasma inside its magnetic cage is improved by driving a larger plasma current [24]. As such, applying a larger plasma pressure and current seems to path the way towards commercial nuclear fusion. However, above a critical level, pressure and current can drive the plasma MHD unstable, potentially leading to the abrupt loss of the plasma confinement [7, 12]. Such events are referred to as *disruptions*.

In a commercial fusion reactor, the occurrence of plasma terminating disruptions has to be avoided. Not only would disruptions halt power generation, they would also, and more importantly, subject the plasma vessel to large heat loads and mechanical stress, potentially damaging the reactor [12]. Even in the upcoming experimental reactor ITER with plasma currents up to 15 MA [25], major disruptive events must occur less than once every 1000 pulses for ITER to achieve its mission [26, 27]. In the case of present-day tokamaks, which are typically (much) smaller than ITER, the threat of disruptions is less severe, as these devices are operated at a much lower plasma current of hundreds of kA to a few MA. Additionally, their ratio of plasma stored thermal energy to vessel surface area is much more favorable. As opposed to tokamaks, the absence of a plasma current in stellarators significantly reduces the chance of triggering a disruption in these devices [7].

The physical mechanisms causing plasma disruptions are numerous [28]. However, typically these events are preceded by the occurrence of MHD modes with poloidal mode number = 2. Expressing the displacement of the plasma by such a perturbation in Fourier components $e^{i(m\theta - n\phi)}$ [29], a mode is characterized by poloidal and toroidal mode numbers m and n , respectively. The quantities θ and ϕ denote the poloidal and toroidal angle. An MHD unstable current density profile can drive such modes. As a result, the magnetic equilibrium may suddenly undergo relaxation, flattening the current density profile and drastically degrading confinement in the process. Under these conditions, the plasma

stored energy is rapidly lost on time scales between 100 μs and 1 ms [29], and deposited onto the reactor wall. The subsequent decay of the residual plasma current at rates exceeding 100 MA s^{-1} [12] induces currents in the plasma vessel, which can exert large mechanical forces on the vessel. At the same time, beams of relativistic *runaway electrons* (REs) can be generated in the plasma [28], as the strong electric fields induced during the decay of the plasma current accelerate parts of the electron population to energies in the range of tens of MeV. Upon impact on the reactor wall, severe localized melting of wall material may occur [30]. Further details on runaway electrons are discussed in section 1.4. As the reactor may be damaged in the process by the three mechanisms described, disruptions in tokamaks must be avoided or at least mitigated.

The guiding principle for the operation of fusion devices is to keep the plasma state at safe distance from known operational limits [29, 32]. In the case of off-normal events moving the plasma state towards these limits, the device's control system would steer the plasma state back to a safe operational point. If recovery towards a safe plasma state is not possible, the plasma would be shut down in a controlled manner. Under certain conditions, such as e.g. fast transient events, a controlled shut-down may not be possible to achieve. The unavoidable disruption must be mitigated. This operational philosophy can be thought of as driving a car down a road. On seeing an obstacle in front, one can use the steering wheel to drive around it. But if the obstacle is too close, one will have to quickly use the brake. And if this is not enough, the airbag will weaken the impact.

Despite this clear principle of fusion device operation, disruption mitigation and avoidance remains an open issue for future devices, as e.g. identified by the ITER Organiza-

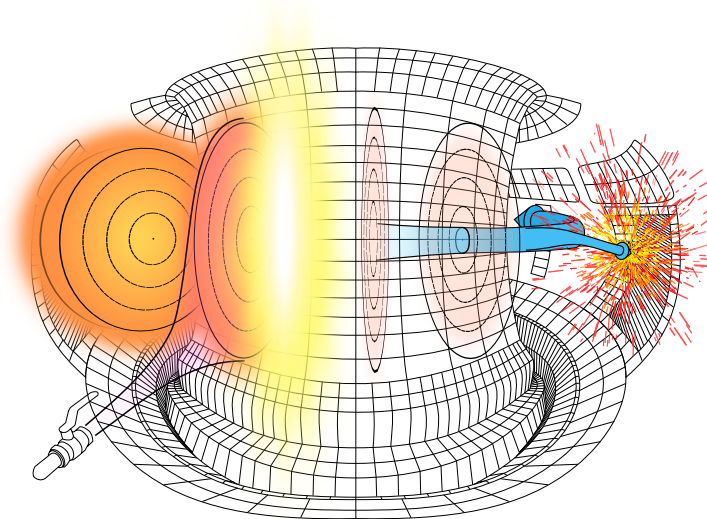


Figure 1.4: Application of massive gas injection in present-day devices for the study of runaway electron generation. Large amounts of impurities are injected from a gas valve into the healthy plasma and cool it down through impurity radiation, thus artificially inducing a disruption. In the cold plasma, the strong electric fields arising facilitate electron runaway. Beams of deconfined runaway electrons can damage plasma facing components (see e.g. figure 2 of reference 31).

tion [17, 28, 29] or described by the Office of Fusion Energy Sciences of the U.S. Department of Energy [33]. In particular, the design of an effective disruption mitigation system proves to be challenging. Any mitigation scheme for the dissipation of heat and electromagnetic loads must act sufficiently fast to dissipate a large fraction of the heat prior to the disruption while ensuring a decay of the plasma current within a predefined time range, being 50 to 150 ms in ITER [32]. Simultaneously, the generation of runaway electrons has to be suppressed. The method considered for future devices is massive material injection, far in excess of the plasma's particle content, into the plasma vessel to radiatively dissipate the plasma stored energy. Hydrogen or inert gases, such as neon (Ne) or argon (Ar), could be used for this purpose [29].

The material is envisioned to be delivered into the confined plasma by means of shattered pellet injection [17, 34]. A cryogenic pellet of material, roughly the size of a wine cork [26], is accelerated outside the reactor vessel to velocities of up to 800 m s^{-1} [26] and shattered into submillimeter fragments by a guiding tube. The spray of pellet shards is then fed into the vessel, where individual shards quickly ablate, offering sufficient heat dissipation and suppression of runaway electron formation. This scheme is currently investigated across several major tokamaks, such as DIII-D [35, 36], JET [37] and ASDEX Upgrade from 2021 [38] onward. Historically, injection of single "killer" pellets has also been investigated [39–42]. However, this scheme was rejected because it leads to strong runaway electron generation in the vicinity of the ablating pellet [29, 32].

A far simpler method of material delivery is massive gas injection through a valve in the vicinity of the plasma boundary [29] (see figure 1.4 for a schematic). From a high-pressure gas reservoir, particles propagate with room temperature sound speed (ranging from $\sim 300 \text{ m s}^{-1}$ for Ar up to $\sim 1000 \text{ m s}^{-1}$ for D_2) into the vacuum vessel. This approach has been studied across several devices, such as e.g. at ASDEX Upgrade [43–47], DIII-D [48, 49], JT-60U [50], TCV [51] or TEXTOR [52]. Applying this method, the entire plasma stored energy can be dissipated radiatively in small machines [48]. However, it is questionable if this method of delivery is sufficiently fast for application in larger, future fusion devices [29, 53]. In present-day devices, massive gas injection is often used for the study of runaway electron generation and dissipation in artificially induced disruptions.

1.4 Electron runaway

The application of massive material injection for the mitigation of tokamak disruptions is expected to fulfill the ITER requirements for heat and electromagnetic load dissipation [17]. The efficacy of this scheme regarding runaway electron suppression, however, still has to be assessed and suitable material injection parameters identified. The importance of this effort becomes apparent extrapolating runaway electron damage observed in present-day devices to ITER conditions. At JET, a runaway current of 0.9 MA caused melting of 12 mm^2 of the inner wall beryllium limiter [30]. Damage due to deconfined runaway electrons has also been reported on Alcator C-Mod [31]. Importantly, the kinetic energy carried by runaway electrons increases with the runaway electron current. Consequently,

potential damage in ITER disruptions with up to 10 MA of runaway current [32] could be significantly worse, especially in the case of substantial conversion of magnetic to kinetic runaway energy [56]. As such, runaway electrons might cause severe damage to the ITER plasma vessel, necessitating extensive repair in such cases [32]. Suppression of runaway electron generation is therefore imperative to ensure the success of ITER. For the design of an effective disruption mitigation system, it is vital to understand runaway electron generation during the injection of massive amounts of material.

The process of electron runaway generally occurs in plasmas in the presence of a sufficiently strong electric field E [57]. For electrons with momenta p above a critical momentum p_c , the acceleration by the electric field outweighs the collisional drag, which decreases for larger momenta (see figure 1.5). As a result, these electrons experience net acceleration and *run away* to relativistic energies. Therefore, these electrons are referred to as *runaway electrons*. This phenomenon appears not only in fusion plasmas [54], but also in atmospheric discharges [58] (lightning) and astrophysical discharges [59] (solar flares). At relativistic energies, the acceleration by the electric field is eventually balanced by synchrotron radiation and Bremsstrahlung in the presence of atomic nuclei, resulting in the formation of a bump on the tail of the electron momentum distribution function [60]. In the presence of particularly large electric fields countering the collisional drag at thermal momenta, the entire electron population experiences runaway. This phenomenon is referred to as *slide-away* [61].

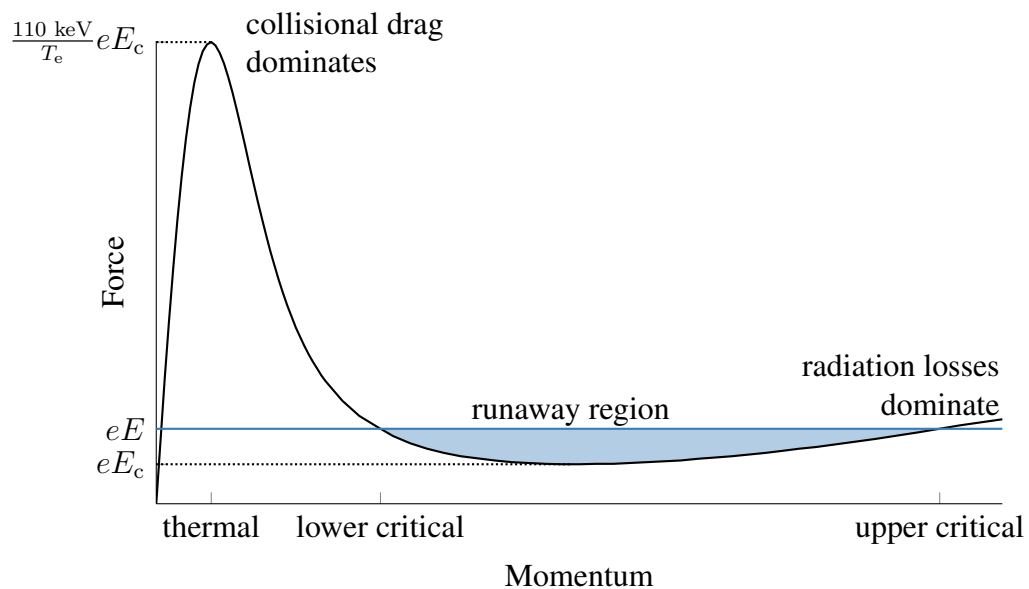


Figure 1.5: Schematic of decelerating collisional and radiative forces (black) acting on plasma electrons compared to the force of an applied electric field E (blue) as a function of the electrons' momenta. For a sufficiently strong electric field E above the critical field E_c (lower dotted line), the electric force exceeds the slowing-down in the region bounded by lower and upper critical momentum. At electric fields exceeding E_c $110 \text{ keV}/T_e$ (upper dotted line), the entire population slides away to relativistic energies. Figure adapted from references 54 and 55.

From the balance between electric field acceleration and slowing-down by collisional drag and radiative effects, the critical (or minimum) electric field E_c required for runaway to occur can be determined. Neglecting radiative effects, the electric field necessary to balance the collisional drag experienced by electrons traveling at the speed of light c is obtained in a fully ionized plasma as [62]

$$E_c = \frac{m_e c \nu_e(c)}{e} = \frac{n_e e^3 \ln \Lambda}{4\pi \varepsilon_0^2 m_e c^2}. \quad (1.3)$$

The quantities ν_e , m_e and n_e describe the electron collision frequency, electron mass and electron density. The elementary charge and vacuum permittivity are denoted by e and ε_0 , respectively. The Coulomb logarithm $\ln \Lambda$ describes the logarithmic ratio of the plasma shielding length scale to the impact parameter for a collisional process scattering by an angle of 90° [12]. For electron-electron collisions of thermal particles, the Coulomb logarithm is $\ln \Lambda = 14.9 - 0.5 \ln (n_e/10^{20} \text{ m}^{-3}) + \ln (T_e/\text{keV})$ [12], with T_e being the electron temperature. In fusion plasmas, the Coulomb logarithm amounts to $\ln \Lambda \approx 17$. The process of slide-away occurs for electric fields above $0.215 E_c m_e c^2 / T_e$ [63].

Importantly, as follows from the description of the critical electric field, a large electron density hinders runaway. This observation motivates the approach of injecting massive amounts of additional material to suppress runaway generation [32]. For ITER relevant densities of $n_e = 10^{20} \text{ m}^{-3}$ and temperatures of $T_e = 20 \text{ keV}$ during flat-top operation [25], the critical field corresponds to around 0.1 V m^{-1} . Simultaneously, the electric field induced to drive the Ohmic current is more than 100 times smaller [64]. As such, electron runaway in ITER is not expected to occur during flat-top operation, but during disruptions. However, in devices smaller than ITER, dedicated experiments are performed with low electron densities in the order of a few 10^{19} m^{-3} to facilitate and study electron runaway during flat-top, e.g. at TEXTOR [65], DIII-D [66], FTU [67] or TCV [68].

1.4.1 Generation mechanisms

Individual runaway electrons can be generated by various processes [54], each transferring electrons into the runaway region of momentum space for subsequent acceleration to relativistic energies. In analogy of the critical electric field of equation (1.3), the critical momentum for runaway to occur in the presence of an applied electric field E is obtained from the electron force balance. In the non-relativistic, pitch-angle independent case, the critical momentum in a fully ionized plasma can be expressed as

$$p_c^2 = \frac{n_e m_e e^3 \ln \Lambda}{4\pi \varepsilon_0^2 E}. \quad (1.4)$$

The flux of electrons across this separatrix p_c into the runaway region then defines the *runaway generation rate*. The earliest theoretical works on this subject describe the process of momentum space diffusion across the separatrix by long-range Coulomb colli-

sions [69, 70], being referred to as *Dreicer generation*. However, in future devices, this mechanism is assumed to contribute only marginally to runaway generation [71].

A generation mechanism of more relevance for tokamak disruptions is *hot-tail generation* [72, 73], initially referred to as *burst generation*. Under conditions of rapidly decaying plasma temperature on time scales faster than the collision frequency at the critical velocity [74], high-momentum electrons equilibrate slower than the thermal bulk, retaining higher momenta for a prolonged period. Simultaneously, the critical momentum (see equation (1.4)) shifts to lower momenta, due to a rise of the electric field in tokamak plasmas and a decrease of the Coulomb logarithm with electron temperature. As such, parts of the high-energy tail of the electron distribution can be transferred into the runaway region through a momentum space shift of the separatrix. In disruptions of high-temperature fusion plasmas, hot-tail generation is expected to provide a substantial population of runaway electrons [71, 74].

In (future) fusion devices studying DT-fusion, such as ITER, runaway electrons can also be created in processes following the decay of atomic nuclei. One such source is Compton scattering of electrons by gamma rays originating from wall material activated due to neutron irradiation [71]. Furthermore, as tritium nuclei undergo β^- -decay with a half-life of 12.3 years, electrons with energies of up to 18.6 keV are generated at a rate of around $10^{11} \text{ m}^{-3} \text{ s}^{-1}$ in ITER [71]. Depending on the disruption parameters, these electrons may reside in parts within the runaway region. However, as this work focuses on runaway generation in deuterium plasmas of ASDEX Upgrade, these nuclear runaway generation mechanisms are not considered in the studies presented.

Existing high-energy runaway electrons can themselves generate secondary runaway electrons through short-range, knock-on collisions with thermal electrons [75, 76]. In this *avalanche*-like process, the number of runaway electrons increases exponentially. During disruptions in future, high current devices, this mechanism is calculated to be capable of generating dangerous amounts of up to several MA of runaway electrons, even from a minuscule seed population [27, 77]. Consequently, the process of avalanche multiplication is considered a major issue for electron runaway in future, high current devices.

Importantly, runaway electrons generated following above definition of the runaway generation rate do not necessarily have relativistic energies to begin with, as is most obviously the case for runaway electrons generated in the process of tritium decay. Instead, newly generated runaway electrons require a finite amount of time for acceleration by the applied electric field up to relativistic energies.

1.4.2 Runaway modeling

Owing to the complexity of the problem of electron runaway during tokamak disruptions, the most complete tools available for the study of electron runaway are experimental devices. But unfortunately, these are challenging to diagnose, revealing their mysteries only hesitantly. Modeling efforts can additionally and complementarily provide valuable insights into the process of electron runaway.

In a theoretical framework, the temporal evolution of a distribution $f_e(t, \mathbf{x}, \mathbf{p})$ of electrons in position space \mathbf{x} and momentum space \mathbf{p} can be described by the Boltzmann equation $df_e(t, \mathbf{x}, \mathbf{p})/dt = C$, where C denotes the collision operator. The most sophisticated tools for runaway electron modeling available, such as CODE [78] or NORSE [63], describe the dynamics of the electron population in this framework, albeit being restricted to phase space evolution under the assumption of a homogeneous plasma. The process of electron runaway during disruptions is, however, a more complex phenomenon, not only limited to the electron momentum space evolution, but requiring the simultaneous evaluation of the particle distributions of multiple species, such as main plasma ions and impurities injected, as well as electromagnetic fields inside a 3D geometry. Evaluating these additional quantities is challenging inside kinetic tools [79].

The self-consistent evolution of a tokamak plasma species' densities and temperatures inside an evolving magnetic geometry can be treated in the framework of one-dimensional transport modeling, using tools such as ASTRA [47, 80] or GO [81, 82]. The spatio-temporal evolution of the conserved quantities is obtained through evaluation of coupled continuity equations. As the tokamak magnetic geometry consists of nested magnetic surfaces of constant flux [12], the dimensionality of the problem can be reduced to one radial coordinate. The computational requirements are thus greatly reduced. In these frameworks, runaway electron generation is calculated using a fluid treatment*, as a fully kinetic description of electron runaway is impractical due to the associated computational costs of additionally resolving two momentum space dimensions of the electron population [83]. Suitable fluid models, also referred to as *reduced kinetic* models, are available for all runaway generation mechanisms discussed in section 1.4.1. Their applicability has been benchmarked extensively against kinetic simulations [77, 84]. As such, transport codes allow for efficient calculation of the self-consistent evolution of background plasma, material injected and runaway electron dynamics.

An improved description of the spatio-temporal evolution of the magnetic field, but also of the background plasma and impurity fluid quantities in a fully 3D geometry is achieved in the framework of non-linear MHD. Tools, such as JOREK [85–87], have been shown capable of modeling material injection [88, 89], runaway electron generation [90] and beam termination [91] (in the absence of impurity species). These tools generally require supercomputing resources to perform simulations. Therefore, the description of electron runaway in an MHD framework is restricted to a fluid treatment.

The three approaches to modeling electron runaway all have strengths and weaknesses. Each framework focuses on different aspects of the runaway electron problem and requires different computational resources. Consequently, simulations in each framework are complementary rather than competing, offering valuable insights to the runaway electron problem. In this work, runaway electron generation during artificially induced disruptions is studied using the coupled transport codes ASTRA–STRAHL [47, 80, 92, 93].

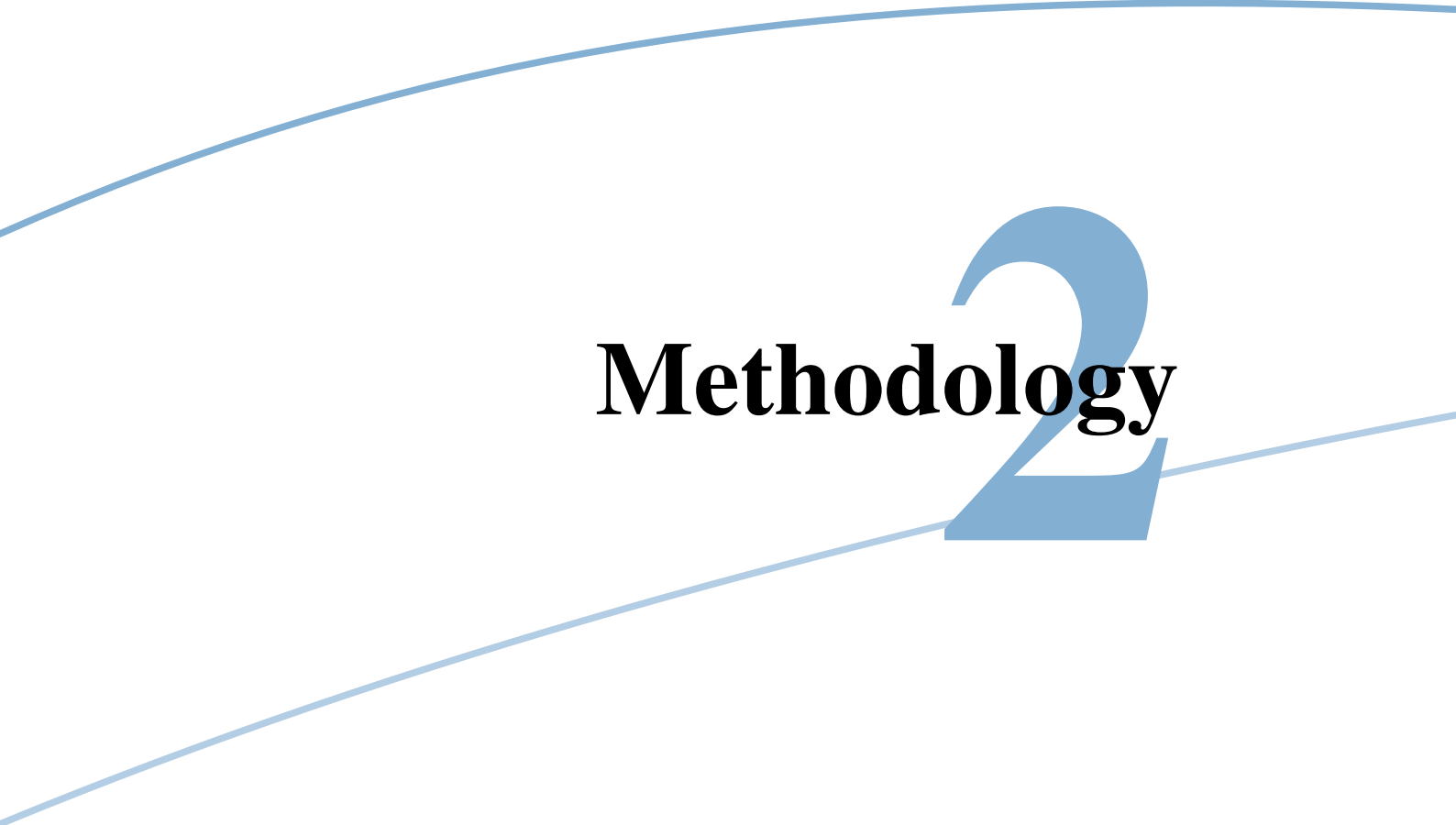
* In this context, *fluid* treatment refers to the evolution of quantities integrated over momentum space, e.g. $n_e(t, \mathbf{x}) = \int f_e(t, \mathbf{x}, \mathbf{p}) d\mathbf{p}$.

1.5 Structure and scope of this thesis

In this work, a 1.5D transport framework is presented for self-consistent simulations of the spatio-temporal evolution of background plasma, impurities injected and electron runaway population in tokamak disruptions induced by massive gas injection. The toolkit's capabilities are demonstrated in simulations of argon massive gas injection in an ASDEX Upgrade discharge representative of runaway electron experiments performed at ASDEX Upgrade. In this context, state-of-the-art reduced kinetic models for electron runaway are validated against experimental observations and dominating mechanisms for impurity transport are identified. In subsequent simulations of runaway electron experiments, the relevant contributions of runaway generation mechanisms to the postdisruption current are assessed. Consequences for future high temperature discharges are investigated through simulations of discharges with varying temperature in comparison with a database of ASDEX Upgrade discharges. These findings have been reported in two peer-reviewed publications, authored in charge by the author of this work, O. Linder. Both publications are appended at the end of this thesis. Paper #1 on *Self-consistent modeling of runaway electron generation in massive gas injection scenarios in ASDEX Upgrade* [47] is found on page 103, whereas paper #2 on *Electron runaway in ASDEX Upgrade experiments of varying core temperature* [93] is found on page 121.

The remainder of this work is organized as follows. In chapter 2, the methods applied are presented. A description of runaway electron generation by the three mechanisms discussed is provided in section 2.1. A radial coordinate to describe the tokamak magnetic geometry is introduced in section 2.2. Furthermore, the ASDEX Upgrade discharge investigated in this work is described in section 2.3. The macroscopic transport equation, as well as the toolkit ASTRA-STRAHL solving it are introduced in sections 2.4 to 2.6. Technical details of the simulations performed are discussed in section 2.7. In the chapter 3 following, a one-page summary for each of the two publications [47,93] is provided. The findings of this work and its contributions to the understanding of electron runaway in tokamak disruptions are discussed in chapter 4. For this purpose, relevant studies in this field are reviewed in the same chapter. Finally, a summary and conclusion of the work presented in this dissertation is provided in chapter 5.

Contributions by the author, O. Linder, to the work presented in this thesis are emphasized by describing these achievements in first person.



Methodology

2

Understanding runaway electron generation during tokamak disruptions is a key requirement for designing an effective disruption mitigation system for ITER and beyond. To complement experimental studies of runaway electron mitigation in present-day devices, computational tools of varying complexity are used. In this work, a toolkit based on the coupled transport codes ASTRA–STRAHL is presented to self-consistently model background tokamak plasma, material injected and electron runaway. Details on runaway electron generation models, the experimental scenario investigated and the tool ASTRA–STRAHL are described in this chapter.

2.1 Generation of runaway electrons

The process of electron runaway can be described in a fluid framework. Models describing relevant generation mechanisms in the presence of sufficiently strong electric fields are presented in this section. I implemented the models introduced in a standalone Fortran module `runawayelectrongeneration`, which is publicly available at <https://github.com/o-linder/runawayelectrongeneration>. The module allows application of the included models, e.g. in transport codes such as ASTRA–STRAHL.

2.1.1 The critical electric field

In the presence of a sufficiently strong electric field, parts of a plasma’s electron population can experience net acceleration up to relativistic energies. The critical electric field required is obtained from the force balance of an electron traveling with the speed of light c under consideration of only collisions with thermal electrons as

$$E_c = \frac{n_e e^3 \ln \Lambda}{4\pi \epsilon_0^2 m_e c^2}. \quad (2.5)$$

Importantly, this expression is valid only in fully ionized plasmas and when neglecting radiative effects. However, following the injection of massive amounts of material, impurities may not necessarily be fully ionized, particularly when injecting material with a high atomic charge, such as argon, or during the runaway beam phase. To take the increased collisional drag under these conditions into account, half the bound electron density may be added to the free electron density [76], i.e. $n_e \rightarrow n_e^{\text{free}} + \frac{1}{2}n_e^{\text{bnd}}$. However, recent work suggests, that the net effect of non-fully ionized impurities can be described more adequately by including bound electrons using a weighing factor of 1 – 2 instead [94]. Using the lower bound, the critical electric field including the total density of electrons is

$$E_c^{\text{tot}} = \frac{n_e^{\text{free}} + n_e^{\text{bnd}}}{n_e^{\text{free}}} E_c. \quad (2.6)$$

Consequently, the minimum electric field necessary for electron runaway to occur is increased in the presence of additional, bound electrons.

The critical electric field is further increased by Bremsstrahlung and synchrotron losses [94]. Considering collisions with partially ionized impurities, the effective critical electric field E_c^{eff} can be obtained from the momentum-dependent force balance [94]. In the limit of high critical momenta, $p_c(E_c^{\text{eff}}) \gg 1$, an analytical solution is found from [94]

$$\begin{aligned} \frac{E_c^{\text{eff}}}{E_c} \approx & \bar{\nu}_{s0} + \bar{\nu}_{s1} \left[1 + \frac{\bar{\nu}_{d1}}{\bar{\nu}_{d0}} \right] \ln \frac{\bar{\nu}_{d0}}{\bar{\nu}_{s1}} + \\ & + \sqrt{2\bar{\nu}_{d0} \left[\frac{\bar{\nu}_{D0}\tau_{\text{syn}}^{-1}}{E_c^{\text{eff}}/E_c} + \phi_{\text{Br}0} + \phi_{\text{Br}1} \ln \frac{\bar{\nu}_{d0}}{2\bar{\nu}_{s1}} \right] + \bar{\nu}_{s1}^2}. \end{aligned} \quad (2.7)$$

The quantities $\bar{\nu}_{si}$ and $\bar{\nu}_{di}$ denote, respectively, expansion coefficients of the generalized slowing-down and deflection frequencies, which are discussed further below in section 2.1.2 and in detail in references 94 and 95. The Bremsstrahlung contributions $\phi_{\text{Br}i}$ can be expressed as $\phi_{\text{Br}0} = 0.35 \alpha \bar{\nu}_{d1}$ and $\phi_{\text{Br}1} = 0.20 \alpha \bar{\nu}_{d1}$, with α being the fine-structure constant. The inverse synchrotron radiation-damping time scale τ_{syn}^{-1} normalized to the relativistic collision time $\tau_{\text{rel}} = 4\pi\epsilon_0^2 m_e^2 c^3 / n_e e^4 \ln \Lambda_{\text{rel}}$ is expressed as $\tau_{\text{syn}}^{-1} = 2\epsilon_0 B^2 / 3m_e n_e \ln \Lambda_{\text{rel}}$, where B denotes the magnetic field. The relativistic Coulomb logarithm $\ln \Lambda_{\text{rel}} = \ln \Lambda + \frac{1}{2} \ln(m_e c^2 / T_e)$ treats collisions between relativistic and thermal electrons [95].

Importantly, the effective critical electric field in the presence of weakly ionized impurities is larger than the critical electric field considering the total density of electrons, i.e. $E_c^{\text{eff}} \gtrsim E_c^{\text{tot}} \gg E_c$, as shown in figure 2.6. In the presence of a magnetic field, synchrotron radiation further increases the effective critical electric field. As such, electron runaway under these conditions is hindered.

The description of the effective critical electric field E_c^{eff} of equation (2.7) is implemented in the module `runawayelectrongeneration`, where it is used in calcula-

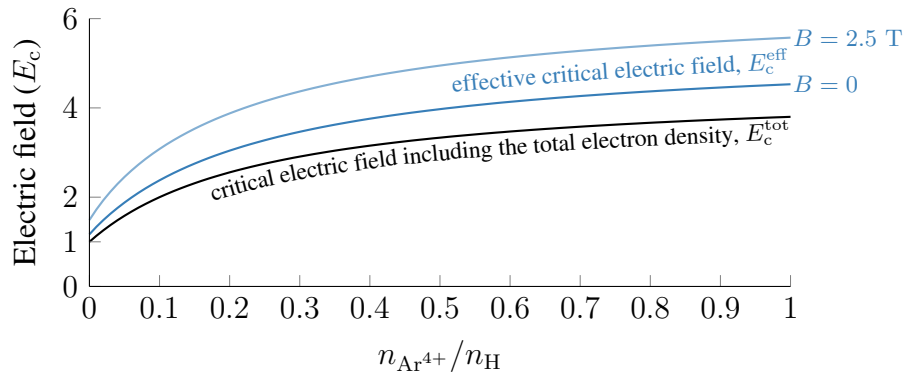


Figure 2.6: Effective critical electric field E_c^{eff} (blue; see equation (2.7)) and critical electric field including the total electron density E_c^{tot} (black; see equation (2.6)) normalized to the critical electric field E_c (see equation (2.5)) in a plasma consisting of H and Ar^{4+} ions of varying ratio. The electron density and temperature are chosen as $n_e = 10^{20} \text{ m}^{-3}$ and $T_e = 10 \text{ eV}$, respectively. The effective critical electric field is shown in the absence of a magnetic field and for $B = 2.5 \text{ T}$.

tions of runaway electron generation rates. Noticeably, expression (2.7) has to be evaluated iteratively, starting with $E_c^{\text{eff}} = E_c^{\text{tot}}$ [94]. Alternatively, in this work, equation (2.7) is rewritten as a cubic equation, $\sum_{i=0}^3 \mathcal{A}_i (E_c^{\text{eff}}/E_c)^i = 0$, where the coefficients \mathcal{A}_i are given by, with $\mathcal{A}_3 = 1$,

$$\mathcal{A}_2 = -2 \left[\bar{\nu}_{s0} + \bar{\nu}_{s1} \left\{ 1 + \frac{\bar{\nu}_{d1}}{\bar{\nu}_{d0}} \right\} \ln \left(\frac{\bar{\nu}_{d0}}{2\bar{\nu}_{s1}} \right) \right], \quad (2.8a)$$

$$\mathcal{A}_1 = \left(\frac{\mathcal{A}_2}{2} \right)^2 - \left[\bar{\nu}_{s1}^2 + 2\bar{\nu}_{d0} \left\{ \phi_{\text{Br}0} + \phi_{\text{Br}1} \ln \left(\frac{\bar{\nu}_{d0}}{2\bar{\nu}_{s1}} \right) \right\} \right], \quad (2.8b)$$

$$\mathcal{A}_0 = -2\bar{\nu}_{d0}^2 \tau_{\text{syn}}^{-1}. \quad (2.8c)$$

Writing the general cubic equation as a depressed cubic equation, i.e. $\mathcal{Y}^3 + 3\mathcal{P}\mathcal{Y} + 2\mathcal{Q} = 0$ with $\mathcal{P} = [3\mathcal{A}_1 - \mathcal{A}_2^2]/9$ and $\mathcal{Q} = [2\mathcal{A}_2^3 - 9\mathcal{A}_2\mathcal{A}_1 + 27\mathcal{A}_0]/54$, the effective critical electric field is obtained in the module `runawayelectrongeneration` through Cardano's formula (see e.g. reference 96) from

$$\frac{E_c^{\text{eff}}}{E_c} = \sqrt[3]{-Q + \sqrt{Q^2 + P^3}} + \sqrt[3]{-Q - \sqrt{Q^2 + P^3}} - \frac{\mathcal{A}_2}{3}. \quad (2.9)$$

A real solution exists for all values of the discriminant $Q^2 + P^3$. Importantly, evaluation of Cardano's formula in Fortran requires complex variables.

The Fortran implementation was verified against a Matlab implementation by Hesslow et al [94]*. The verification was carried out calculating the effective critical electric field iteratively with two iteration steps, as is done in the Matlab version, across all input parameters. The Fortran implementation was later changed to obtain the effective critical electric field as the solution of a cubic equation through Cardano's formula.

2.1.2 Impact of partially ionized impurities on runaway

As discussed in the previous section, the critical electric field is increased in the presence of non-fully ionized impurities when taking the impact of partial screening into account. Correspondingly, the deflection frequency ν_d and the slowing-down frequency ν_s are increased under these conditions, resulting in enhanced collisional drag. As both frequencies are required for the calculation of the effective critical electric field (see equation (2.7)), they are introduced in this section. The expressions presented are implemented in the module `runawayelectrongeneration`.

For application in the calculation of the effective critical electric field, both the deflection and slowing-down frequency for an electron with momentum p are normalized to the relativistic collision time τ_{rel} and generalized as $\bar{\nu}_d = \nu_d p^3 / \gamma$ and $\bar{\nu}_s = \nu_s p^3 / \gamma^2$, where $\gamma = \sqrt{1 + p^2}$ is the Lorentz factor. To calculate these quantities, expressions for the Coulomb logarithms $\ln \Lambda^{\text{ee}}$ and $\ln \Lambda^{\text{ei}}$ for electron collisions with electrons and ions,

* The Matlab implementation of expression (2.7) is provided by Hesslow et al [94] at <https://github.com/hesslow/Eceff>.

respectively, are needed, which are given over the thermal and suprathermal momentum range through [95]

$$\ln \Lambda^{ee} = \ln \Lambda + \frac{1}{\zeta} \ln \left(1 + \left(\frac{m_e c^2}{T_e} (\gamma - 1) \right)^{\zeta/2} \right), \quad (2.10a)$$

$$\ln \Lambda^{ei} = \ln \Lambda + \frac{1}{\zeta} \ln \left(1 + \left(2 \frac{m_e c^2}{T_e} p^2 \right)^{\zeta/2} \right). \quad (2.10b)$$

In the thermal limit of low momenta, $p \ll 1$, the thermal Coulomb logarithm $\ln \Lambda$ is obtained. A smooth transition to the suprathermal expression for large momenta is achieved using a parameter $\zeta = 5$.

As such, the generalized deflection frequency $\bar{\nu}_d$ in the presence of species k with density n_k , atomic number $Z_{0,k}$ and net electric charge Z_k (in multiples of the elementary charge e) is calculated from [94, 95]

$$\begin{aligned} \bar{\nu}_d = & \frac{\ln \Lambda^{ee}}{\ln \Lambda_{\text{rel}}} + Z_{\text{eff}} \frac{\ln \Lambda^{ei}}{\ln \Lambda_{\text{rel}}} + \frac{2}{3} \sum_k \frac{n_k}{n_e} \frac{N_{e,k}}{\ln \Lambda_{\text{rel}}} \\ & \times \left[\{Z_{0,k} + Z_k\} \ln \left(1 + (p\bar{\lambda}_k)^{3/2} \right) - \frac{N_{e,k} (p\bar{\lambda}_k)^{3/2}}{1 + (p\bar{\lambda}_k)^{3/2}} \right]. \end{aligned} \quad (2.11)$$

Here, the quantity Z_{eff} denotes the effective ion charge through $Z_{\text{eff}} = \sum_k Z_k^2 n_k / n_e$. The number of electrons bound to a nucleus is denoted by $N_{e,k} = Z_{0,k} - Z_k$. In above expression, the first term describes contributions by free electrons to the deflection frequency, whereas the second term considers ion contributions in the completely screened limit. The remaining terms describe the effect of partial screening on the deflection frequency. The quantity $\bar{\lambda} = 2\lambda/\alpha a_0$ is the effective ion length scale λ normalized to the fine-structure constant α and the Bohr radius $a_0 = e^2/4\pi\epsilon_0\alpha^2 c^2 m_e$ of a ground state hydrogen atom. Values for $\bar{\lambda}$ obtained from quantum mechanical modeling are provided by Hesslow et al [94, 95], being typically in the order of 10 to 100 for almost fully ionized and non-ionized atoms respectively.

The generalized slowing-down frequency is calculated similarly from [94, 95]

$$\bar{\nu}_s = \frac{\ln \Lambda^{ee}}{\ln \Lambda_{\text{rel}}} + \sum_k \frac{n_k}{n_e} \frac{N_{e,k}}{\ln \Lambda_{\text{rel}}} \left[\frac{1}{\zeta} \ln \left(1 + \left(\frac{p\sqrt{\gamma-1}}{W_k} \right)^{\zeta} \right) - \frac{p^2}{1+p^2} \right], \quad (2.12)$$

where W_k denotes the mean excitation energy of species k normalized to the electron rest mass energy $m_e c^2$. Values for W are again given by Hesslow et al [94, 95]. However, Linnea Hesslow kindly provided higher precision values for both the mean excitation energy W and for the effective length scale $\bar{\lambda}$ for commonly used elements, which are used in this work.

For the calculation of the effective critical electric field according to expression (2.7), both the generalized deflection frequency and slowing-down frequency of equations (2.11)

and (2.12) can be evaluated in the relativistic limit through an expansion in $\ln p$, writing $\bar{\nu}_d \approx \bar{\nu}_{d0} + \bar{\nu}_{d1} \ln p$ and $\bar{\nu}_s \approx \bar{\nu}_{s0} + \bar{\nu}_{s1} \ln p$. Recalling the momentum dependence of the Coulomb logarithms $\ln \Lambda^{\text{ee}}$ and $\ln \Lambda^{\text{ei}}$ (see equation (2.10)), the series coefficients for the generalized deflection frequency are obtained as [94]

$$\bar{\nu}_{d0} = 1 + Z_{\text{eff}} + \frac{1}{\ln \Lambda_{\text{rel}}} \sum_k \frac{n_k}{n_e} N_{e,k} \left[\{Z_{0,k} + Z_k\} \ln \bar{\lambda}_k - \frac{2}{3} N_{e,k} \right], \quad (2.13a)$$

$$\bar{\nu}_{d1} = \frac{1}{\ln \Lambda_{\text{rel}}} \sum_k \frac{n_k}{n_e} Z_{0,k}^2. \quad (2.13b)$$

Correspondingly, the coefficients for the generalized slowing-down frequency are [94]

$$\bar{\nu}_{s0} = 1 - \frac{1}{\ln \Lambda_{\text{rel}}} \sum_k \frac{n_k}{n_e} N_{e,k} [\ln W_k + 1], \quad (2.14a)$$

$$\bar{\nu}_{s1} = \frac{1}{2} \frac{1}{\ln \Lambda_{\text{rel}}} \left[1 + 3 \sum_k \frac{n_k}{n_e} N_{e,k} \right]. \quad (2.14b)$$

Using these expressions for the factors $\bar{\nu}_{di}$ and $\bar{\nu}_{si}$ of the expansion of generalized deflection and slowing-down frequencies, the effective critical electric field E_c^{eff} can be calculated according to equation (2.7). The implementation of these factors in the module `runawayelectrongeneration` was verified indirectly against the Matlab version by Hesslow et al [94] during verification of the implementation of the effective critical electric field.

2.1.3 Dreicer generation

In the presence of a sufficiently strong electric field above the critical electric field, thermal electrons can cross the separatrix of the runaway region through momentum space diffusion by long-range Coulomb collisions with the collective thermal electron population. As a result, a continuous flux of electrons into the runaway region is obtained. This process has first been described by Dreicer [69, 70] as depletion of a Maxwellian, thermal electron distribution into an empty runaway region. As such, generation of runaway electrons due to momentum space diffusion is commonly referred to as *Dreicer generation*. A characteristic electric field in this context is the Dreicer electric field [69],

$$E_D = \frac{n_e e^3 \ln \Lambda}{4\pi \varepsilon_0^2 T_e}, \quad (2.15)$$

which formally describes electron runaway at thermal velocities [97] and is as such related to the critical electric field through $E_D = E_c m_e c^2 / T_e$ (cf. equation (2.5)).

The treatment of momentum space diffusion has been improved in subsequent work by Gurevich [98], Lebedev [99] and Kruskal & Bernstein [100] in the 1960s by considering a non-Maxwellian distribution in the vicinity of the separatrix, dividing momentum space

into five separate regions and matching the solutions between these regions. By additionally considering relativistic effects for high critical momenta, Connor & Hastie [62] derived the most complete analytical description of Dreicer generation to date. As such, the Dreicer runaway growth rate is obtained as

$$\Gamma_D = C_D n_e \nu_e \left(\frac{E_{\parallel}}{E_D} \right)^{-\mathcal{F}_1} \exp \left(-\mathcal{F}_2 \frac{E_D}{E_{\parallel}} - \mathcal{F}_3 \sqrt{\frac{E_D}{E_{\parallel}}} \right). \quad (2.16)$$

The unknown constant C_D is of order unity and set to $C_D = 0.35$ by Connor & Hastie [62]. In recent work [84], $C_D = 1$ was identified and is as such applied throughout this work and in the module `runawayelectrongeneration`. The frequency ν_e of collisions between thermal electrons is given by

$$\nu_e = \frac{n_e e^4 \ln \Lambda}{4\pi \varepsilon_0^2 \sqrt{m_e T_e^3}}. \quad (2.17)$$

The remaining numerical factors of equation (2.16) are obtained as, setting $\varepsilon \equiv E_{\parallel}/E_c$,

$$\mathcal{F}_1 = \frac{Z_{\text{eff}} + 1}{16} \left[1 + 2 \frac{\varepsilon - 2}{\varepsilon - 1} \sqrt{\frac{\varepsilon}{\varepsilon - 1}} \right] + \frac{1}{2} \frac{1}{\varepsilon - 1}, \quad (2.18a)$$

$$\mathcal{F}_2 = 2\varepsilon \left[\varepsilon - \frac{1}{2} - \sqrt{\varepsilon} \{\varepsilon - 1\} \right], \quad (2.18b)$$

$$\mathcal{F}_3 = \frac{\varepsilon}{2} \sqrt{\frac{Z_{\text{eff}} + 1}{\varepsilon - 1}} \left[\frac{\pi}{2} - \arcsin \left(1 - \frac{2}{\varepsilon} \right) \right]. \quad (2.18c)$$

As the processes responsible for Dreicer generation involve momentum space diffusion of plasma electrons, the presence of impurity-bound electrons does not increase the density of target electrons. As such, the free plasma electron density n_e^{free} is to be used in above expressions. For electric fields approaching the critical field, i.e. $E_{\parallel}/E_c \rightarrow 1^+$, the Dreicer growth rate vanishes, expressed by $\mathcal{F}_1 \rightarrow -\infty$ and $\mathcal{F}_3 \rightarrow \infty$ under these conditions. For electric fields below the critical field, expression (2.16) becomes complex, requiring setting $\Gamma_D = 0$ in this case.

In tokamak disruptions, the Dreicer mechanism generates a significant population of runaway electrons only in the presence of applied electric fields exceeding around 3% of the Dreicer electric field (see figure 2.7). For typical tokamak parameters, the Dreicer runaway current generation rate exceeds $1 \text{ MA m}^{-2} \text{ ms}^{-1}$ under these conditions (assuming runaway propagation with the speed of light), which is required to replace Ohmic current density in the order of MA m^{-2} on sub-ms time scales.

The expression introduced by Connor & Hastie [62] is valid only in the presence of fully ionized plasma species. As such, this model cannot be applied easily in tokamak disruptions following the injection of massive amounts of material. As has been shown using the full- f Fokker-Planck solver CODE [78], the steady-state flux of electrons into the runaway region is noticeably reduced under these conditions for $E_{\parallel}/E_D \leq 0.1$ [95].

However, generalization of the model by Connor & Hastie [62] to conditions with large densities of partially ionized impurities is not straightforward, due to the complicated energy dependence of collision frequencies at near-thermal energies [84]. To still take the impact of non-fully ionized impurities on Dreicer runaway generation into account in the framework of fluid modeling, a neural network of CODE has been trained by Hesslow et al [84] for this purpose.

The training of the CODE neural network has been carried out with argon and neon impurities, but using eight generalized input parameters \mathbf{x} to allow for application of the neural network to other impurities as well [84]. As this work studies the injection of argon in ASDEX Upgrade discharges, the CODE neural network is applied to calculate the Dreicer runaway generation rate in the presence of partially ionized impurities. The growth rate is obtained through evaluation of

$$\Gamma_D^{\text{nn}} = n_e \nu_e \exp(b_5 + \mathbf{W}_5 \tanh(\mathbf{b}_4 + \mathbf{W}_4 \tanh(\mathbf{b}_3 + \mathbf{W}_3 \tanh(\mathbf{b}_2 + \mathbf{W}_2 \tanh(\mathbf{b}_1 + \mathbf{W}_1 \mathbf{x}))))). \quad (2.19)$$

Details on the biases \mathbf{b}_i , weights \mathbf{W}_i and input parameters \mathbf{x} are described by Hesslow et al [84]. I implemented the neural network version of CODE in the Fortran module `runawayelectrongeneration`, based on the implementation by Hesslow et al for Matlab*, which includes the numerical values of the weights and biases. The Fortran implementation was verified against the Matlab version and against figures of reference 84.

The presence of partially ionized impurities impacts Dreicer runaway electron generation already at low densities. For example, in an almost pure hydrogen plasma with a

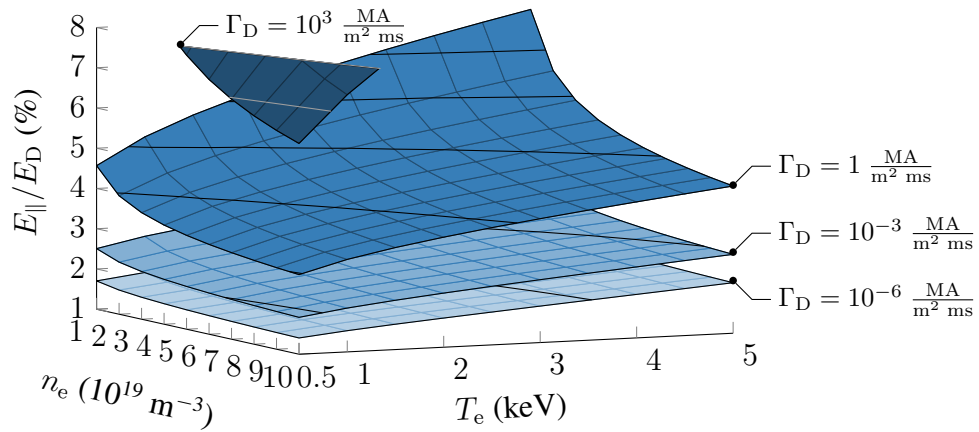


Figure 2.7: Surfaces of constant Dreicer runaway current generation rate Γ_D according to equation (2.16) in a hydrogen plasma with a small admixture of argon, $n_{\text{Ar}^{4+}} = 0.01 n_{\text{H}}$, inside the parameter region (n_e, T_e) relevant for tokamak disruptions. Runaway electrons are assumed to propagate with the speed of light. Significant Dreicer generation at rates of around $1 \text{ MA m}^{-2} \text{ ms}^{-1}$ requires electric fields E_{\parallel} in the range of 3% to 5% of the Dreicer field E_D .

* An implementation of the CODE neural network for Matlab is provided by Hesslow et al [84] at <https://github.com/unnerfelt/dreicer-nn>.

low content of additional Ar^{4+} , being e.g. $n_{\text{Ar}^{4+}} = 0.01 n_{\text{H}}$, the parallel electric field required for significant Dreicer generation of $1 \text{ MA m}^{-2} \text{ ms}^{-1}$ is increased to around 6% E_{D} (see figure 2.8). Correspondingly, the Dreicer growth rate is already reduced by a few orders of magnitude in this example when taking the impact of partially ionized impurities into account. In applications of massive material injection where the amount of impurities introduced (far) exceeds the tokamak vessel's deuterium content, the Dreicer mechanism is thus expected to provide a negligible contribution to the total runaway electron population [101]. However, during the initial phase of a tokamak disruption, favorable conditions for Dreicer runaway cannot be ruled out. As such, both models introduced to describe Dreicer runaway electron generation are included in the module `runawayelectrongeneration` and considered in this work.

2.1.4 Hot-tail generation

In rapidly cooling plasmas during a tokamak disruption, the high-momentum tail of the electron distribution equilibrates slower than the thermal bulk and may as such be suddenly located inside the runaway region of momentum space, as an increasing electric field shifts the separatrix to lower momenta [72, 73]. This process, commonly referred to as *hot-tail generation*, occurs when the time scale of plasma cooling is faster than the collision time of high-energy electrons.

Suitable fluid models describing electron runaway in rapidly cooling plasmas were introduced by Smith & Verwichte [74] and Féher et al [64]. However, the effect of the electric field on the electron distribution is not taken into account by these models [54, 102]. Although these models were thus found to underestimate hot-tail runaway electron generation by up to an order of magnitude in studies with the kinetic solver CODE [78], recent work with the Fokker-Planck solver CQL3D suggests that the model by Smith &

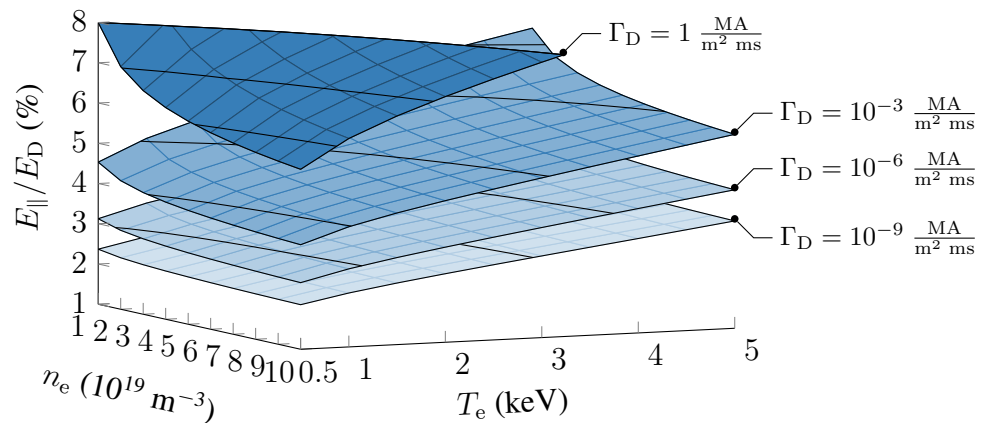


Figure 2.8: Surfaces of constant Dreicer runaway current generation rate for the same values of Γ_{D} as in figure 2.7, but calculated by the CODE neural network of expression (2.19). Considering the impact of even small amounts of non-fully ionized impurities, $n_{\text{Ar}^{4+}} = 0.01 n_{\text{H}}$, significant Dreicer generation at rates of around $1 \text{ MA m}^{-2} \text{ ms}^{-1}$ requires larger electric fields E_{\parallel} exceeding 6% of the Dreicer field E_{D} .

Verwichte [74] can be improved to better agree with kinetic calculations by introducing a Z_{eff} dependent factor of order unity in the definition of the critical momentum [103]. Simultaneously, improved fluid models are currently being developed [104] and validated against CODE simulations. However, even though promising models have been identified and shown to agree with kinetic calculations in cases of either low or high effective plasma charge, a single model suitable over a large range of Z_{eff} is not available yet for practical applications. As such, the original model by Smith & Verwichte [74] is applied in this work.

Contrary to the models introduced for Dreicer generation, the model by Smith & Verwichte [74] yields the density of hot-tail runaway electrons $n_{\text{RE}}^{\text{hot}}$ at time t , instead of the instantaneous generation rate of runaway electrons. The hot-tail population is as such obtained as velocity space integral of an initially Maxwellian electron distribution function across the runaway region [74]

$$n_{\text{RE}}^{\text{hot}}(t) = \frac{4n_{e,0}}{\sqrt{\pi}v_{\text{th},0}^3} \int_{v_c}^{\infty} [v^2 - v_c^2] \exp\left(-\left(\left(\frac{v}{v_{\text{th},0}}\right)^3 + 3\tau\right)^{2/3}\right) dv. \quad (2.20)$$

The quantities v_{th} and v_c denote respectively the thermal velocity, $v_{\text{th}}^2 = 2T_e/m_e$, and the critical velocity for runaway, $v_c^2 = n_e e^3 \ln \Lambda / 4\pi \varepsilon_0^2 m_e E_{\parallel}$ (cf. equation (1.4)). A subscript of "0" denotes quantities at the onset of the disruption. The delayed equilibration of the high-energy tail is described through the evolution of the parameter τ , being a normalized time according to

$$\tau(t) = \nu_{e,0} \int_{t_0}^t \frac{n_e(\tilde{t})}{n_{e,0}} d\tilde{t}. \quad (2.21)$$

In their work, Smith & Verwichte [74] assumed an instantaneous drop of the initial electron temperature $T_{e,0}$ down to a final temperature $T_{e,\text{fin}}$. However, in the presence of radiative cooling, the electron temperature measured experimentally decays in good approximation exponentially on time scales τ_{dec} ,

$$T_e(t) = [T_{e,0} - T_{e,\text{fin}}] \exp\left(-\frac{t - t_0}{\tau_{\text{dec}}}\right) + T_{e,\text{fin}}. \quad (2.22)$$

In this case, an improved description of the hot-tail runaway density can be obtained by modifying the parameter τ . For this purpose, Smith & Verwichte [74] performed numerical calculations of $\tau(t)$ through integration of a high velocity moment of a two-component electron distribution function. Considering also an exponential increase of the electron density on identical time scales τ_{dec} , the parameter τ at times $t - t_0 > 3 \tau_{\text{dec}}$ is well described by

$$\tau(t) = \nu_{e,0} \frac{n_{e,\text{fin}}}{n_{e,0}} [t - t_0 - \tau_{\text{dec}}] \Theta(t - t_0 - \tau_{\text{dec}}). \quad (2.23)$$

However, based on the numerical calculations presented by Smith & Verwichte [74], the parameter τ can be described more accurately in the early phase of the disruption. As such, the following, alternative expression is applied throughout this work instead of expression (2.24) [105]:

$$\tau(t) = \nu_{e,0} \frac{n_{e,\text{fin}}}{n_{e,0}} \begin{cases} \frac{(t-t_0)^2}{4 \tau_{\text{dec}}}, & t - t_0 < 2 \tau_{\text{dec}} \\ [t - t_0 - \tau_{\text{dec}}], & t - t_0 \geq 2 \tau_{\text{dec}} \end{cases}. \quad (2.24)$$

Using this expression inside equation (2.20), the hot-tail density is obtained. Following this approach, a closed form cannot be provided, requiring numerical integration across the runaway region of velocity space. In the module `runawayelectrongeneration`, numerical integration is achieved using Kepler's rule. As the integrand of equation (2.20) falls off sufficiently fast for $v \rightarrow \infty$, the upper integration boundary is set to the value of v , where the exponential function falls below a threshold value of 10^{-100} .

During tokamak disruptions, the hot-tail mechanism can provide a substantial population of seed runaway electrons. Hot-tail formation is facilitated in low density plasmas with high temperature. The deposition of additional material throughout the disruption impedes hot-tail runaway. In cases where the plasma cools down from predisruption temperatures of several keV down to a few eV on sub-ms time scales, a significant current density in the order of 1 MA m^{-2} can be generated (see figure 2.9). As such, this mechanism is expected to contribute noticeably to electron runaway in simulations of ASDEX Upgrade discharges.

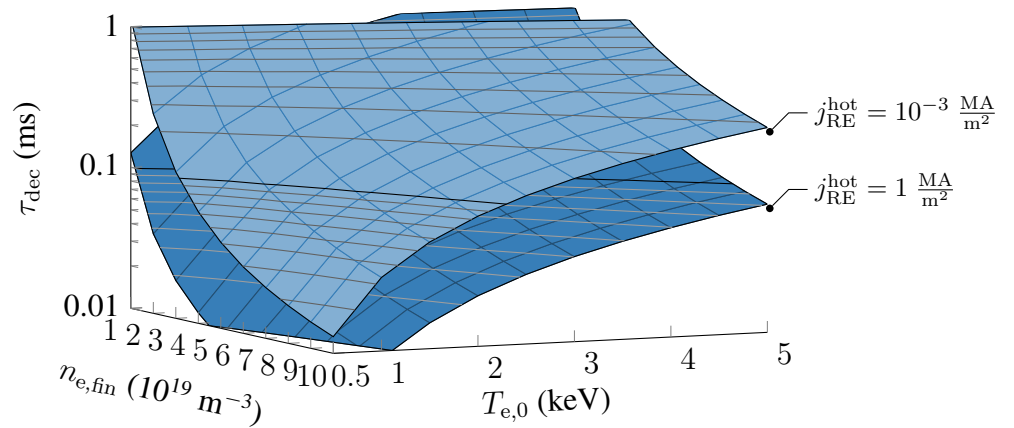


Figure 2.9: Surfaces of constant hot-tail current density $j_{\text{RE}}^{\text{hot}}$ calculated with the model by Smith & Verwichte [74] for an exponentially changing electron density and temperature on time scales τ_{dec} inside the parameter region $(n_{e,\text{fin}}, T_{e,0})$ relevant for tokamak disruptions. Initial electron density and final temperature are taken as $n_{e,0} = 10^{19} \text{ m}^{-3}$ and $T_{e,\text{fin}} = 10 \text{ eV}$, respectively. The electric field is assumed to evolve as $E_{\parallel}(t) = j_0/\sigma(t)$, with an initial current density of $j_0 = 1 \text{ MA m}^{-2}$ and σ being the thermal conductivity. Significant hot-tail generation with current densities of around 1 MA m^{-2} requires a change of plasma parameters on sub-ms time scales.

Importantly for the evaluation of the hot-tail runaway electron population during the loss of plasma stored energy, the hot-tail density $n_{\text{RE}}^{\text{hot}}$ has to be assumed to increase monotonically with time, demanding $\frac{d}{dt}n_{\text{RE}}^{\text{hot}}(t) \geq 0$. As argued above, the effect of the electric field on the electron distribution is not taken into account in the model by Smith & Verwichte [74]. As such, acceleration of electrons located inside the runaway region is not considered. Instead, high-energy electrons eventually equilibrate, as described by the parameter $\tau(t)$. Consequently, the density of hot-tail runaway electrons at the end of the disruption would vanish, i.e. $n_{\text{RE}}^{\text{hot}}(t_{\text{fin}}) = 0$, thus being in contrast to expectations. As such, inside the module `runawayelectrongeneration`, the hot-tail density at time t_j is evaluated as the maximum value of current j and previous time step $j - 1$, i.e. $n_{\text{RE}}^{\text{hot}}(t_j) = \max(n_{\text{RE}}^{\text{hot}}(t_j), n_{\text{RE}}^{\text{hot}}(t_{j-1}))$.

The postdisruption hot-tail density

The non-monotonic evolution of the hot-tail density requires evaluation of the density throughout the entire disruption. Calculating $n_{\text{RE}}^{\text{hot}}$ only at an arbitrary time is not possible. However, an estimate of the hot-tail density at the end of the disruption can be obtained, as I will derive in the following. For this purpose, expression (2.20) has to be simplified first to allow for analytical integration over velocity space. This can be achieved by noting, that velocities near the critical velocity contribute most to the integral. As such, the exponent can be expanded around $v/v_c(t) \approx 1$, yielding

$$-\left(\left(\frac{v}{v_{\text{th},0}}\right)^3 + 3\tau(t)\right)^{2/3} \approx \frac{\left(\frac{v}{v_c(t)}\right)^2 \left(\frac{v_c(t)}{v_{\text{th},0}}\right)^3 + 3\tau(t)}{\sqrt[3]{\left(\frac{v}{v_{\text{th},0}}\right)^3 + 3\tau(t)}}. \quad (2.25)$$

Integration of equation (2.20) using this exponent gives, introducing for clarity the quantity $\tilde{\gamma}^3 \equiv (v_c/v_{\text{th},0})^3 + 3\tau$,

$$\frac{n_{\text{RE}}^{\text{hot}}(t)}{n_{e,0}} = \frac{2}{\sqrt{\pi}}\tilde{\gamma}e^{-\tilde{\gamma}^2} + \sqrt{\tilde{\gamma}}\frac{v_c^{3/2}}{v_{\text{th},0}^{3/2}}e^{-\frac{3\tau}{\tilde{\gamma}}}\left[\tilde{\gamma}\frac{v_{\text{th},0}^3}{v_c^3} - 2\right]\left[1 - \text{erf}\left(\frac{1}{\sqrt{\tilde{\gamma}}}\frac{v_c^{3/2}}{v_{\text{th},0}^{3/2}}\right)\right]. \quad (2.26)$$

The second term in this expression approaches zero in the limiting cases of $t \rightarrow t_0$ or $t \rightarrow \infty$, where either the factor $[1 - \text{erf}(\dots)]$ or $\exp(-3\tau/\tilde{\gamma})$ vanishes. While at the onset of the disruption $v_c/v_{\text{th},0} \gg 1$ and $\tau = 0$, at a later stage $\tau \gg 1$ and $v_c/v_{\text{th},0} \rightarrow 1$. As such, the hot-tail density can be approximated as

$$n_{\text{RE}}^{\text{hot}}(t) = \frac{2}{\sqrt{\pi}}n_{e,0}\sqrt[3]{\left(\frac{v_c(t)}{v_{\text{th},0}}\right)^3 + 3\tau(t)}\exp\left(-\left(\left(\frac{v_c(t)}{v_{\text{th},0}}\right)^3 + 3\tau(t)\right)^{2/3}\right). \quad (2.27)$$

The same expression is obtained by Smith & Verwichte [74] by neglecting the direction of the electric field. The hot-tail runaway electron density at the end of the disruption can then be derived from above expression by finding its global maximum, occurring at the minimum value of the exponent. To evaluate the evolution of the critical velocity $v_c(t)$, the evolution of the electric field has to be assessed. Under the assumption of negligible feedback of the hot-tail runaway population on electric field diffusion and a negligible postdisruption electron temperature $T_{e,\text{fin}} \ll T_{e,0}$, such that $T_e(t) \approx T_{e,0} \exp(-t/\tau_{\text{dec}})$, the electric field evolves as (used also in figure 2.9 for the calculation of the hot-tail density)

$$E_{\parallel}(t) = \frac{j_0}{\sigma(t)} = \frac{e^2 \sqrt{m_e} \ln \Lambda}{8\sqrt{2}\pi\epsilon_0^2 T_e^{3/2}} j_0 = E_{\parallel,0} \exp\left(\frac{3}{2} \frac{t}{\tau_{\text{dec}}}\right). \quad (2.28)$$

The quantity σ denotes the plasma conductivity. As expected, the electric field increases strongly as the plasma is cooled down. With this relation, the ratio of critical to initial thermal velocity is found as

$$\frac{v_c(t)}{v_{\text{th},0}} = \sqrt{\frac{en_{e,0}}{j_0}} \sqrt{\frac{2T_{e,0}}{m_e}} \exp\left(-\frac{3}{4} \frac{t}{\tau_{\text{dec}}}\right) = \frac{v_{c,0}}{v_{\text{th},0}} \exp\left(-\frac{3}{4} \frac{t}{\tau_{\text{dec}}}\right). \quad (2.29)$$

Using the approximation $\tau(t) = \nu_{e,0}[t - \tau_{\text{dec}}]n_{e,\text{fin}}/n_{e,0}$ introduced by Smith & Verwichte [74] (see equation (2.23)), the minimum of the exponent (and as such the maximum of the hot-tail density) is found at time

$$t_{\text{max}} = \frac{4}{9}\tau_{\text{dec}} \ln\left(\frac{3}{4} \frac{n_{e,0}}{n_{e,\text{fin}}} \frac{\nu_{e,0}^{-1}}{\tau_{\text{dec}}} \left(\frac{v_{c,0}}{v_{\text{th},0}}\right)^3\right). \quad (2.30)$$

Reintroducing the quantity $\tilde{\gamma}^3 \equiv (v_c/v_{\text{th},0})^3 + 3\tau$, as well as using $\tilde{\nu}$ and \tilde{v} to collect all physical constants in the expressions $\nu_{e,0}n_{e,\text{fin}}/n_{e,0} \equiv \tilde{\nu}n_{e,\text{fin}}/T_{e,0}^{3/2}$ and $v_{c,0}/v_{\text{th},0} \equiv \tilde{v}\sqrt{4T_{e,0}}\sqrt{n_{e,0}/j_0}$, the value of $\tilde{\gamma}$ at time t_{max} is found as

$$\tilde{\gamma}(t_{\text{max}}) = \frac{\sqrt[3]{n_{e,\text{fin}}\tau_{\text{dec}}}}{\sqrt{T_{e,0}}} \underbrace{\sqrt[3]{\frac{4}{3}\tilde{\nu} \left[\ln\left(\frac{3}{4} \frac{\tilde{v}^3}{\tilde{\nu}\tau_{\text{dec}}} \frac{n_{e,0}^{3/2}}{n_{e,\text{fin}}} \frac{T_{e,0}^{9/4}}{j_0^{3/2}}\right) - \frac{5}{4}\right]}}_{\equiv \mathcal{F}} \quad (2.31)$$

Importantly, a variation of $\tilde{\gamma}$ stems predominantly from the factors in front of \mathcal{F} due to the logarithmic dependence of these factors inside \mathcal{F} . As such, the factor \mathcal{F} can be set constant when studying the variation of the hot-tail density for changing disruption parameters, e.g. the radial variation of a specific experiment. A simplified expression for

the hot-tail density at the end of the disruption is thus found as

$$n_{\text{RE}}^{\text{hot}}(\tau_{\text{fin}}) = \frac{2}{\sqrt{\pi}} n_{e,0} \frac{\sqrt[3]{n_{e,\text{fin}} t_{\text{dec}}}}{\sqrt{T_{e,0}}} \mathcal{F} \exp \left(- \left(\frac{\sqrt[3]{n_{e,\text{fin}} \tau_{\text{dec}}}}{\sqrt{T_{e,0}}} \mathcal{F} \right)^2 \right). \quad (2.32)$$

From this relation, the most important physical quantities determining the hot-tail runaway density in the model by Smith & Verwichte [74] are identified as the predisruption temperature $T_{e,0}$, the time scale of exponential change τ_{dec} and the postdisruption electron density $n_{e,\text{fin}}$. Correspondingly, the strong variation of the hot-tail density with these quantities is shown in figure 2.9, already discussed above. Importantly, the variation of $n_{\text{RE}}^{\text{hot}}$ in figure 2.9 follows the exponential dependence of the relevant quantities. As such, the prime dependencies can be described by

$$n_{\text{RE}}^{\text{hot}}(t_{\text{fin}}) = \frac{2}{\sqrt{\pi}} n_{e,0} \mathcal{G} \exp \left(- \frac{n_{e,\text{fin}}^{2/3} \tau_{\text{dec}}^{2/3}}{T_{e,0}} \right), \quad (2.33)$$

where non-exponential factors are collected in the quantity \mathcal{G} . Using this relation, the radial variation of the hot-tail density inside ASDEX Upgrade disruptions is described sufficiently accurate.

Generalization of the parameter τ

In the work by Smith & Verwichte [74], the parameter $\tau(t)$ is given as the temporal integral over the density evolution (see equation (2.21)) in the case of an instantaneous loss of the plasma stored thermal energy. However, describing the realistic evolution of the plasma temperature requires numerical calculation of the parameter $\tau(t)$. Assuming an exponential change of electron density and temperature on identical time scales τ_{dec} , the numerical solution for τ converges for $t > 3 \tau_{\text{dec}}$ to $\tau(t) = \nu_{e,0} [t - \tau_{\text{dec}}] n_{e,\text{fin}} / n_{e,0}$ (see equation (2.23)). Yet, the full numerical solution presented by Smith & Verwichte [74] can conveniently be described by

$$\tau(t) = \nu_{e,0} \frac{n_{e,\text{fin}}}{n_{e,0}} \left[t - \tau_{\text{dec}} \left\{ 1 - \exp \left(- \frac{t}{\tau_{\text{dec}}} \right) \right\} \right]. \quad (2.34)$$

The representations of equations (2.23) and (2.24) are obtained by noting that the exponential function can be expressed through $\exp(-t/\tau_{\text{dec}}) = \lim_{n \rightarrow \infty} (1 - t/\tau_{\text{dec}} n)^n$ and using $n = 1$ and $n = 2$, respectively.

As the numerical solution of $\tau(t)$ is provided by Smith & Verwichte [74] for different ratios of final to initial electron density $n_{e,\text{fin}}/n_{e,0}$, the contributions by each change of electron density and temperature can be identified. In the representation introduced by Smith & Verwichte [74], $y(t) = \nu_{e,0} t n_{e,\text{fin}} / n_{e,0} - \tau(t)$, the solution $y(t)$ for the case of a doubled electron density, $n_{e,\text{fin}} = 2n_{e,0}$, is exactly twice as large as the solution in the case of a constant electron density, i.e. $y(n_{e,\text{fin}} = 2n_{e,0}) = 2y(n_{e,\text{fin}} = n_{e,0})$. As

such, the contributions by electron density and temperature are additive, while the density contribution considers the ratio of density increase to initial density, i.e. $\Delta n_e = n_{e,\text{fin}} - n_{e,0}$. Introducing different time scales of exponential change for density and temperature, the parameter $\tau(t)$ is obtained as

$$\frac{\tau(t)}{\nu_{e,0}} = \frac{\Delta n_e}{n_{e,0}} \left[t - \tau_{\text{dec},n} \left\{ 1 - e^{-\frac{t}{\tau_{\text{dec},n}}} \right\} \right] + \left[t - \tau_{\text{dec},T} \left\{ 1 - e^{-\frac{t}{\tau_{\text{dec},T}}} \right\} \right]. \quad (2.35)$$

In the case of the density contribution, the integral relation of equation (2.21), $\tau(t) = \nu_{e,0} \int_{t_0}^t n_e(\tilde{t}) d\tilde{t}/n_{e,0}$, allows direct evaluation of τ for an exponential change of the density. However, following this approach, the density contribution identified in equation (2.35) cannot be obtained. Instead, the expression for $\tau(t)$ derived from numerical calculations implies a different relation,

$$\tau(t) = \nu_{e,0} \int_{t_0}^t \left[\frac{n_e(\tilde{t})}{n_{e,0}} - 1 \right] d\tilde{t}. \quad (2.36)$$

A similar expression is obtained for the contribution of an exponentially changing temperature. In total, the parameter $\tau(t)$ in the case of arbitrary evolution of electron density and temperature can be expressed as

$$\tau(t) = \nu_{e,0} \int_{t_0}^t \left[\frac{n_e(\tilde{t})}{n_{e,0}} - \frac{T_e(\tilde{t})}{T_{e,0}} \right] d\tilde{t}. \quad (2.37)$$

Noticeably, in the case of an instantaneous drop of the temperature, above expression simplifies to equation (2.21). Intriguingly, equation (2.21) implies $\tau(t) = \int_{t_0}^t \nu_e(\tilde{t}) d\tilde{t}$ (see equation (2.17) for the definition of ν_e). Yet, this relation appears not to hold in the case of exponentially changing density and temperature.

The validity of expression (2.37) in the case of an arbitrary temperature evolution still has to be determined. Only in the case of an exponential change of density and temperature on identical time scales τ_{dec} , the evolution of $\tau(t)$ obtained in numerical calculations is reproduced. In other cases, additional numerical calculations are required for validation. However, since a validation of expression (2.37) is outside the scope of this work, further numerical calculations are left for future work.

For applications of the model for hot-tail runaway electron generation by Smith & Verwichte [74], an integral expression for the parameter $\tau(t)$ for arbitrary evolution of electron density and temperature would be particularly useful. With the current approximation of $\tau(t)$, the time scale τ_{dec} of exponential change has to be determined before evaluating the hot-tail density. Applied in integrated simulations of background plasma, material injection and runaway electron generation, this restriction requires performing simulations twice. In a first simulation, the time scale τ_{dec} is determined, whereas the hot-tail density is calculated in a second simulation. The availability of an integral relation for the parameter $\tau(t)$ as in equation (2.37) would accelerate simulations of this kind.

2.1.5 Avalanche generation

In a close-range collision between an existing runaway and a thermal electron, the energy exchanged can be sufficient to transfer the thermal electron into the runaway region of momentum space, thus creating a secondary runaway electron in the process. Upon further acceleration in an applied electric field, the secondary runaway electron can in turn transfer parts of its energy to thermal electrons and as such create new runaway electrons itself. Throughout this *avalanche* like process, the number of runaway electrons increases exponentially. Experimental evidence of runaway electron multiplication was e.g. observed at the TEXTOR tokamak [65].

A suitable theoretical description of avalanche generation was obtained by Rosenbluth & Putvinski [76] from the gyrokinetic relativistic Fokker-Planck equation as

$$\Gamma_{\text{av}} = n_{\text{RE}} \frac{e}{m_e c \ln \Lambda_{\text{rel}}} \sqrt{\frac{\pi}{3}} \sqrt{\frac{\gamma}{Z_{\text{eff}} + 5}} [E_{\parallel} - E_c] \quad (2.38a)$$

$$\left/ \sqrt{1 - \frac{E_c}{E_{\parallel}} + \frac{4\pi}{3\gamma} \frac{(Z_{\text{eff}} + 1)^2}{Z_{\text{eff}} + 5} \left(\frac{E_{\parallel}^2}{E_c^2} + \frac{4}{\gamma^2} - 1 \right)} \right.^{-1},$$

$$\gamma = (1 + 1.46 \sqrt{\epsilon} + 1.72 \epsilon)^{-1}. \quad (2.38b)$$

Here, the quantity $\epsilon = r/R$ describes the inverse aspect ratio of the tokamak with minor radius r and major radius R . In the limit of large electric fields $E_{\parallel} > E_c$, the last factor of equation (2.38), i.e. the large square root, approaches unity. As such, the avalanche growth rate close to the magnetic axis at $r = 0$ is simplified to the expression $\Gamma_{\text{av}} = n_{\text{RE}} e E_{\parallel} / m_e c \ln \Lambda_{\text{rel}} \sqrt{Z_{\text{eff}} + 5}$ and thus increases linearly with runaway density n_{RE} and applied field E_{\parallel} . For constant plasma parameters, the runaway electron density therefore increases exponentially on the avalanche multiplication time scale $n_{\text{RE}} / \Gamma_{\text{av}}$. In the limit of high electric fields, a doubling of the runaway population on sub-ms time scales relevant for disruptions requires fields in excess of 100 V m^{-1} (see figure 2.10(a)). Suitable conditions for significant runaway multiplication to occur therefore exist only following the loss of thermal energy in the cold plasma with temperatures well below 10 eV (assuming $E_{\parallel} = j_0 / \sigma$; cf. equation (2.28)). Prior to the loss of thermal energy, the electric fields necessary would (far) exceed the Dreicer electric field (see equation (2.15)), resulting in electron slide-away instead of avalanche multiplication.

The model by Rosenbluth & Putvinski [76] has been used extensively in fluid modeling of runaway electron formation (see e.g. references 64, 81, 97) and is therefore considered in this work and included in the module `runawayelectrongeneration`. However, interactions between runaway electrons and partially ionized impurities are not properly taken into account by this model. In their presence, Rosenbluth & Putvinski [76] suggested to use the critical electric field including the total density of electrons, i.e. E_c^{tot} . Yet, in the high-field limit, the impact of non-fully ionized impurities on avalanche generation vanishes.

In recent work by Hesslow et al [77], the presence of non-fully ionized impurities was observed to noticeably increase avalanche multiplication in contrast to predictions by Rosenbluth & Putvinski [76]. Although collision frequencies are greatly enhanced under these conditions [94], the simultaneous increase of available target electrons by additional bound electrons results in a significant net increase of the avalanche generation rate [77], the effect of which is described by

$$\Gamma_{\text{av}} = n_{\text{RE}} \frac{e}{m_e c \ln \Lambda_{\text{rel}}} \frac{n_e^{\text{tot}}}{n_e} \frac{E_{\parallel} - E_c^{\text{eff}}}{\sqrt{\bar{\nu}_d(p_c^{\text{eff}}) \bar{\nu}_s(p_c^{\text{eff}}) + 4}}. \quad (2.39)$$

This expressions simplifies to the expression by Rosenbluth & Putvinski [76] (see equation (2.38)) in a fully ionized plasma in the high-field limit, where $\bar{\nu}_d \bar{\nu}_s = 1 + Z_{\text{eff}}$. Recall, that momentum-dependent expressions for the generalized deflection and slowing-down frequencies, $\bar{\nu}_d$ and $\bar{\nu}_s$ respectively, are given in equations (2.11) and (2.12) in section 2.1.2. Importantly, the effective critical momentum p_c^{eff} both frequencies depend upon is in turn a function of these frequencies through $p_c^{\text{eff}} = \sqrt[4]{\bar{\nu}_d(p_c^{\text{eff}}) \bar{\nu}_s(p_c^{\text{eff}}) / \sqrt{E_{\parallel} / E_c}}$, thus requiring iterative calculation starting with $p_c^{\text{eff}} = 1$.

Considering the impact of partially ionized impurities on electron runaway through the model by Hesslow et al [77], the avalanche generation rate is significantly increased in the presence of additional non-fully ionized impurities. As such, significant multiplication on sub-ms time scales is achieved at much lower electric fields than predicted by Rosenbluth & Putvinski [76] (see figure 2.10(a)). In the case of impurities with high atomic charge, such as argon, impurity amounts well below the hydrogen content are already sufficient to significantly enhance runaway multiplication (see figure 2.10(b)). Therefore, consideration of these effects is expected to be important in self-consistent simulations of background plasma evolution, material injection and runaway electron generation.

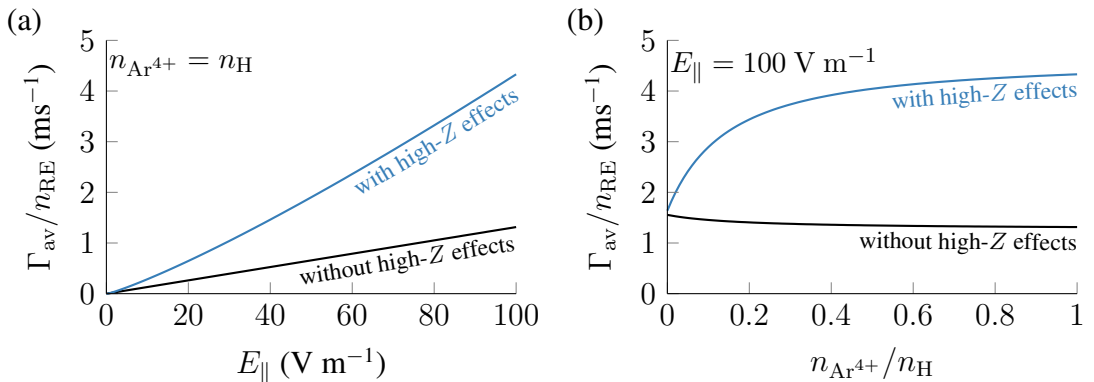


Figure 2.10: Avalanche runaway electron growth rate $\Gamma_{\text{av}}/n_{\text{RE}}$ considering the impact of partially ionized impurities on electron runaway (blue; see equation (2.39)) and neglecting their impact (black; see equation (2.38)) in a plasma consisting of H and Ar^{4+} ions for (a) a variation of the applied electric field E_{\parallel} and (b) a variation of the plasma ion composition. The remaining plasma parameters are chosen as $n_e = 10^{20} \text{ m}^{-3}$, $T_e = 10 \text{ eV}$ and $B = 0$ (as in the previous figures). In (a), an equal content of hydrogen and argon ions is used. In (b), the electric field is set to $E_{\parallel} = 100 \text{ V m}^{-1}$.

Throughout this work, the process of avalanche runaway generation is described using the model by Hesslow et al [77]. The model by Rosenbluth & Putvinski [76] is applied to assess the impact of partially ionized impurities on runaway multiplication in transport simulations. As such, I implemented expression (2.39) in the module `runawayelectrongeneration`. Here, the effective critical momentum p_c^{eff} is calculated iteratively with an accuracy of 10^{-8} , starting at $p_c^{\text{eff}} = 1$. The implementation was verified against a Matlab implementation by Hesslow et al [84], which they kindly provided. In the process, the implementation of the generalized deflection and slowing-down frequencies of equations (2.11) and (2.12) was also verified.

2.2 From magnetic flux surfaces to a radial coordinate

To describe electron runaway at different locations in a tokamak, a coordinate system for the plasma has to be defined. As the tokamak magnetic geometry has in good approximation the shape of a torus, each point can be described through a set of coordinates (r, ϕ, θ) and a parameter R , which are linked to Cartesian coordinates (x, y, z) through

$$x(r, \phi, \theta) = [R + r \cos \theta] \cos \phi, \quad (2.40a)$$

$$y(r, \phi, \theta) = [R + r \cos \theta] \sin \phi, \quad (2.40b)$$

$$z(r, \theta) = r \sin \theta. \quad (2.40c)$$

Here, R is a parameter describing the major radius of the tokamak. The coordinates (r, ϕ, θ) denote respectively minor radius, toroidal angle and poloidal angle. The dimensionality of the description can be reduced by making use of symmetries of the magnetic equilibrium. In a tokamak plasma, the equilibrium consists of nested surfaces of constant magnetic flux [12]. Using this property, a normalized coordinate can be defined to describe the radial dimension of the plasma in this work, required in the framework of 1.5D transport modeling. Furthermore, the properties of the magnetic equilibrium can be used to construct a quantity related to the stability of the plasma.

Inside magnetic confinement fusion devices, a magnetic equilibrium is achieved, when the plasma pressure p is balanced by magnetic forces,

$$\mathbf{j} \times \mathbf{B} = \nabla p, \quad (2.41)$$

with current density \mathbf{j} and magnetic field \mathbf{B} . From this relation, it follows by dotting with \mathbf{B} that $\mathbf{B} \cdot \nabla p = 0$ – the magnetic field lines are located on surfaces of constant pressure. As such, the magnetic equilibrium is described by a set of closed, nested, toroidal surfaces (see figure 2.11). The magnetic flux within each surface is similarly constant on surfaces of constant pressure. Thus, these surfaces are referred to in the following as flux surfaces.

Individual flux surfaces can be labeled by a flux coordinate. A natural choice for this purpose is the poloidal magnetic flux across a surface S_θ in the poloidal direction θ ,

$$\Psi = \int_{S_\theta} \mathbf{B} \cdot d\mathbf{S}_\theta = \int_{S_\theta} \mathbf{B} \cdot \hat{\mathbf{n}}_{S_\theta} dS_\theta = \int_{S_\theta} \mathbf{B} \cdot \hat{\mathbf{e}}_\theta dS_\theta. \quad (2.42)$$

The toroidal magnetic flux across a surface in the toroidal direction is defined similarly,

$$\Phi = \int_{S_\phi} \mathbf{B} \cdot \hat{\mathbf{e}}_\phi dS_\phi. \quad (2.43)$$

Using either flux quantity, a normalized flux coordinate ρ is constructed by requiring ρ to vanish on the magnetic axis and to take the value $\rho = 1$ at the last closed flux surface (LCFS). As such, the normalized poloidal magnetic flux ρ_θ and the normalized toroidal magnetic flux ρ_ϕ are obtained as

$$\rho_\theta = \sqrt{\frac{\Psi - \Psi_{\text{axis}}}{\Psi_{\text{LCFS}} - \Psi_{\text{axis}}}}, \quad \rho_\phi = \sqrt{\frac{\Phi - \Phi_{\text{axis}}}{\Phi_{\text{LCFS}} - \Phi_{\text{axis}}}}. \quad (2.44)$$

Both quantities are used regularly as a flux coordinate. The poloidal flux coordinate is calculated most accurately by equilibrium reconstruction tools in the edge region, wherefore ρ_θ is often chosen as a coordinate in edge plasma applications. Inside the central, confined plasma, reconstruction of Ψ often is inaccurate. Therefore, the toroidal flux coordinate ρ_ϕ is typically used in core physics studies. In this work, the spatio-temporal evolution of the confined plasma is investigated. As such, the toroidal flux coordinate ρ_ϕ is used throughout this work and referred to as ρ in the following. It should be noted, that a flux coordinate can also be defined from the volume enclosed by a flux surface through $\rho_V = \sqrt{V/V_{\text{LCFS}}}$.

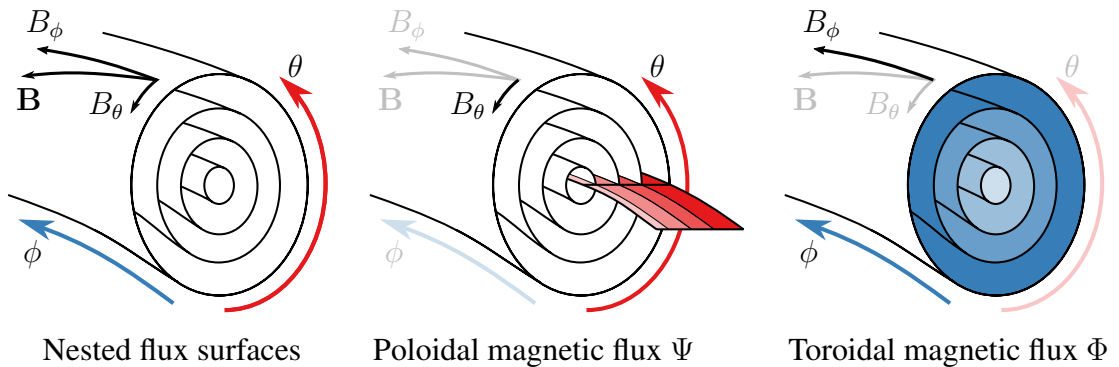


Figure 2.11: (Left) The tokamak magnetic equilibrium consists of closed, nested, toroidal surfaces. Magnetic field lines \mathbf{B} are located on these flux surfaces. As such, the magnetic field lines have only components in the poloidal direction θ and in the toroidal direction ϕ . (Middle) The poloidal magnetic flux Ψ is evaluated across surfaces in the poloidal direction, whereas (right) the toroidal magnetic flux Φ is evaluated across surfaces in the toroidal direction.

The properties of the magnetic equilibrium can also be used to construct a quantity related to the stability of the plasma. Following a magnetic field line on a flux surface around the torus, the winding ratio of toroidal rotations m to poloidal rotations n of the field line defines the safety factor $q = m/n$ of a tokamak plasma. This quantity is related to the stability of the plasma, where larger values correspond to greater stability [12]. The safety factor can also be expressed as the variation of the toroidal magnetic flux Ψ with the poloidal magnetic flux Φ through $q = d\Psi/d\Phi$. As such, it follows from the definition of the magnetic fluxes in equations (2.42) and (2.43) that the safety factor can in circular approximation be related to the ratios of magnetic field components and plasma radii through $q = rB_\phi/R_0B_\theta$, where r denotes the local minor radius and R_0 the major radius on the magnetic axis. A strict requirement for plasma stability is $q > 1$, known as the Kruskal-Shafranov limit [7].

2.3 ASDEX Upgrade runaway electron experiments

In this work, the transport model `ASTRA-STRAHL` is applied for self-consistent simulations of background plasma evolution, material injection and runaway electron generation of ASDEX Upgrade discharges, being the baseline experiment #33108 and similar discharges. Although the model is applicable not only to ASDEX Upgrade, but to tokamaks in general, describing ASDEX Upgrade runaway electron experiments and in particular discharge #33108 is important for determining relevant components for the model. After all, the phenomena to be modeled determine the model. As such, details on ASDEX Upgrade runaway electron experiments are discussed here.

In ASDEX Upgrade, the generation and mitigation of runaway electrons has been investigated over the past years [44–46]. In these experiments, artificial disruptions are induced by massive gas injection of neon or argon from a gas valve into a healthy plasma. Throughout several experimental campaigns, discharge #33108 has been used as a reference scenario and, as such, has also been studied computationally. Therefore, ASDEX Upgrade discharge #33108 is investigated throughout this work. In this particular discharge, argon is injected from the low-field-side valve located in toroidal sector 13/16. The valve's gas reservoir and feed line with a combined volume of 100 cm^3 were filled before the experiment with argon at a pressure of 0.73 bar, corresponding to a particle content of 1.75×10^{21} atoms.

The target plasma for material injection is chosen as a low density, high temperature plasma. As described in previous sections, both the critical electric field for runaway and the Dreicer electric field are reduced under these conditions (see equations (2.5) and (2.15)), thus facilitating the generation of runaway electrons in these scenarios. In ASDEX Upgrade discharge #33108, the average electron density prior to injection amounts to $2.84 \times 10^{19} \text{ m}^{-3}$. The electron temperature close to the magnetic axis is increased to above 10 keV just before injection through application of strongly localized, on-axis electron cyclotron resonance heating of 2.625 MW during the last 100 ms prior to injection. The radial profiles of electron density and temperature prior to injection

are shown in figure 2.12. For the simulation of discharge #33108, these profiles are set as initial conditions in ASTRA-STRahl. The study of runaway electron generation in these scenarios is further facilitated by investigating circular plasmas, which are vertically stable as opposed to elongated plasmas typically studied in ASDEX Upgrade [43–46].

Injection of material from the valve is typically triggered at $t_{\text{inj}} = 1$ s into the discharge. The material is ejected ballistically from the valve with the speed of sound. Given the finite time required to open the valve’s orifice, as well as the finite time of flight from valve to plasma boundary, noticeable amounts of impurities at the LCFS are only observed after a small delay in the order of a few milliseconds after triggering the injection, being in the case of discharge #33108 after $t_{\text{LCFS}} = 1.0$ ms as inferred from bolometry measurements in front of the gas valve in sector 13/16*.

Once impurities have reached the confined plasma, it is cooled down locally to temperatures in the range of 1 to 10 eV through impurity radiation and ionization. As a result, increasing amounts of radiation are detected through bolometry (see figure 2.13(a)). In the process, the plasma conductivity decreases strongly in the cold plasma ($\sigma \propto T_e^{3/2}$; c.f. equation (2.28)). As the plasma current does not decay significantly on these sub-ms time scales (see figure 2.13(c)), the local plasma current diffuses inwards into regions, where the plasma is still hot. With the continuing penetration of neutral impurities, the cold plasma region extends inwards progressively, resulting in increasing levels of radiation measured (see figure 2.13(a)), as well as an eventual increase of the line-averaged electron density measured by CO₂ interferometry along a central, vertical chord in sec-

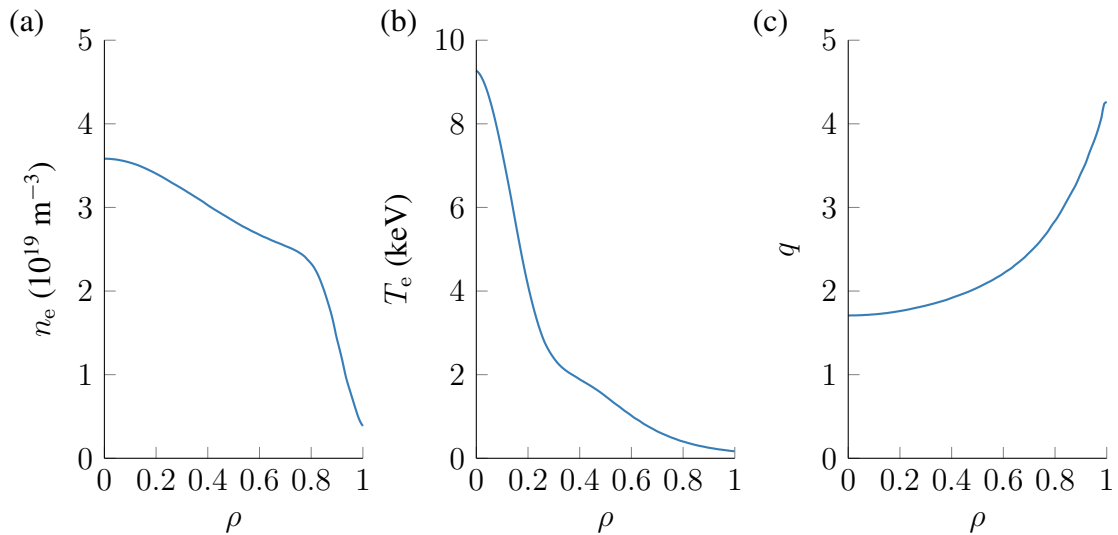


Figure 2.12: Radial profiles of (a) the electron density n_e , (b) the electron temperature T_e and (c) the safety factor q in ASDEX Upgrade discharge #33108 averaged over the last 50 ms prior to argon injection. These profiles are used as initial conditions in self-consistent modeling with ASTRA-STRahl.

* An overview image of the toroidal locations of gas valves and relevant diagnostics for runaway electron experiments in ASDEX Upgrade throughout its 16 sectors is provided in figure 1 by Pautasso et al [46]. An overview image of the lines of sights of relevant diagnostics in the poloidal cross section of sector 13/16 is provided in figure 3 by Linder et al [47].

tor 11/16 (see figure 2.13(b)). The current driven prior to injection in these locations accumulates in front of the cold gas front, forming a sheet of current.

When the neutral gas front reaches the location where the safety factor q has a rational value of 2, high-amplitude MHD modes with mode number $(m, n) = (2, 1)$ and higher harmonics are excited [106], being driven by the strongly pronounced current sheet. As a consequence, the plasma stored thermal energy is observed to be removed on sub-ms time scales, as inferred from soft x-ray measurements. This phase of the disruption is referred to as the *thermal quench* (TQ). Correspondingly, the initial phase of material injection between first occurrence at the LCFS and arrival at the $q = 2$ surface is referred to as *pre-thermal quench* phase. In discharge #33108, the onset of the thermal quench occurs around $t_{\text{TQ}} = 2.58$ ms after the valve trigger.

The loss of plasma stored energy during the thermal quench is accompanied by strongly enhanced (impurity) radiation (see figure 2.13(a)), which is considered responsible for the majority of thermal energy dissipation. Correspondingly, the line-averaged electron density increases rapidly during this phase (see figure 2.13(b)). Heat transport also contributes to removing thermal energy from the central plasma. Importantly, impurity radiation is observed throughout the entire core plasma on time scales faster than expected from impurity propagation with the speed of sound. It is therefore believed, that the violent MHD activity results in breakup of the magnetic surfaces and stochastization of magnetic field lines. Corresponding observations have recently been made in MHD simulations with JOREK for argon massive gas injection in JET [107]. As a result, the effective radial transport of heat and particles is strongly increased throughout the region of stochasticity. The same applies also to the current density, which is similarly redistributed. Flattening of the current density profile is accompanied by a sudden increase of the total plasma current, referred to as *current spike* (see figure 2.13(c)).

Following the complete loss of the plasma stored thermal energy, the plasma current decays in the cold plasma over a duration of several milliseconds. This phase of the disruption is referred to as *current quench* (CQ) phase, which in discharge #33108 starts at $t_{\text{CQ}} = 3.15$ ms after the valve trigger. Early into the current quench, strong impurity radiation is still observed, but vanishes over the course of a few milliseconds. Since strong electric fields are induced throughout the plasma as a result of the rapidly decaying plasma current, magnetic energy is dissipated within the plasma and lost through impurity radiation. Simultaneously, the strong electric fields induced can result in significant electron runaway, potentially replacing a substantial fraction of the predisturbance plasma current. In ASDEX Upgrade discharge #33108, an initial current of 763 kA is replaced by 225 kA of runaway electron current, as indicated by hard x-ray measurements (see figure 2.13(d)). Importantly, a significant hard x-ray signal is detected only at a late stage of the current quench. The end of the current quench is reached when all of the inductively driven current is removed, occurring in discharge #33108 at $t_{\text{RE}} = 7.72$ ms after the valve trigger. This also marks the onset of the runaway beam phase, where the population of runaway electrons generated may exist for hundreds of milliseconds. However, the runaway beam phase is not modeled in this work.

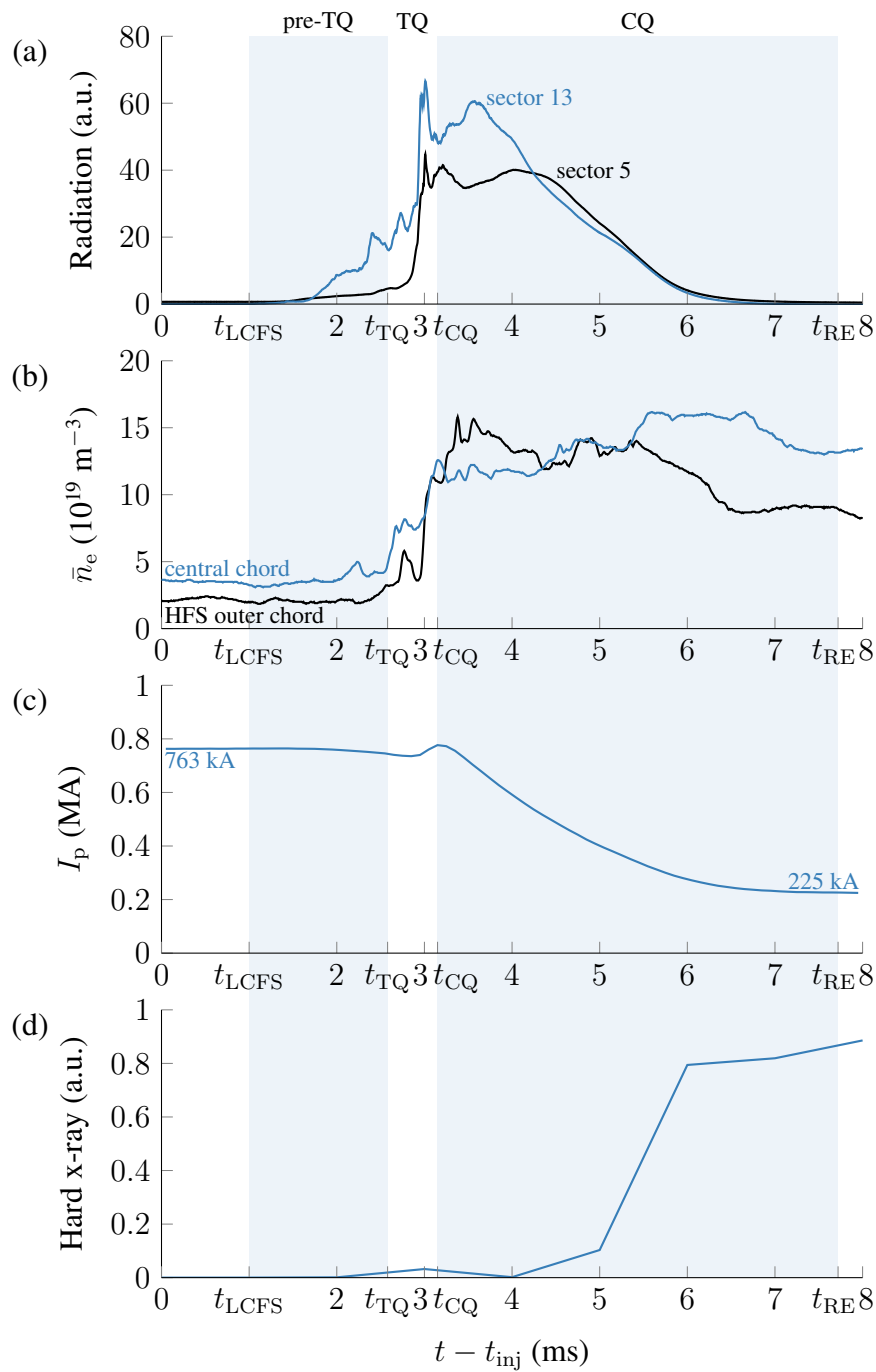


Figure 2.13: Temporal evolution of key quantities in ASDEX Upgrade discharge #33108 throughout the disruption induced by argon massive gas injection, being (a) the radiated power as measured by bolometry in sectors 13/16 (blue) and 5/16 (black), (b) the line-averaged electron density \bar{n}_e measured by CO₂ interferometry in sector 13/16 along the central chord (blue) and the high-field-side edge chord (black), (c) the plasma current I_p , as well as (d) the hard x-ray signal. The temporal evolution of these quantities is shown starting at the beginning of gas injection at t_{inj} . The characteristic phases of the disruption, being the pre-thermal quench, thermal quench (TQ) and current quench (CQ), are highlighted.

2.4 The macroscopic transport equation

To describe the self-consistent evolution of background plasma, material injected and runaway electrons, the framework of transport modeling is used in this work. As such, the spatio-temporal evolution of physical quantities inside tokamak type fusion devices can be described by solving (coupled) continuity equations for the quantities of interest,

$$\frac{\partial \mathcal{Y}(t, \mathbf{x})}{\partial t} = -\nabla_{\mathbf{x}} \cdot \mathbf{\Gamma} + S. \quad (2.45)$$

The temporal evolution of \mathcal{Y} , a quantity per unit volume, at location \mathbf{x} is determined by the flux $\mathbf{\Gamma}$ of this quantity and by additional sources S .

Even though fusion devices are naturally three-dimensional, the properties of the tokamak's magnetic equilibrium allow for a reduction of the dimensionality of the problem. In tokamak plasmas, many quantities are (almost) flux quantities, i.e. constant on flux surfaces. As such, these quantities do not depend on the poloidal or toroidal angle and can therefore be expressed as $\mathcal{Y}(\rho)$. Correspondingly, the dimensionality of the continuity equation is reduced to one,

$$\frac{\partial \mathcal{Y}(\rho)}{\partial t} = -\langle \nabla \cdot \mathbf{\Gamma} \rangle + S. \quad (2.46)$$

Note, that a dependence of these quantities on time is assumed, but not explicitly mentioned in the following. Importantly, the local flux $\mathbf{\Gamma}$ is not necessarily a flux quantity, but may vary poloidally, i.e. $\mathbf{\Gamma} = \mathbf{\Gamma}(\rho, \theta)$. Thus, evaluation of the continuity equation requires using the flux surface averaged flux density $\langle \nabla \cdot \mathbf{\Gamma} \rangle$. The local flux $\mathbf{\Gamma}$ can be expressed under consideration of diffusive \tilde{D} and advective $\tilde{\mathbf{v}}$ contributions as

$$\mathbf{\Gamma}(\rho, \theta) = \mathcal{Y}(\rho) \tilde{\mathbf{v}}(\rho, \theta) - \tilde{D}(\rho, \theta) \nabla \mathcal{Y}(\rho). \quad (2.47)$$

Performing the corresponding flux surface averages (for details see reference 108), the one-dimensional macroscopic transport equation for a flux quantity \mathcal{Y} is obtained as

$$\frac{1}{V'} \frac{\partial}{\partial t} (V' Y) = \frac{1}{V'} \frac{\partial}{\partial \rho} \left(V' \langle (\nabla \rho)^2 \rangle \left[D \frac{\partial Y}{\partial \rho} - v Y \right] \right) + S. \quad (2.48)$$

Here, all quantities are flux quantities, i.e. dependent only on the flux coordinate ρ and on time t . The magnetic geometry is described by the factor $V' \equiv \partial V / \partial \rho$, with V being the plasma volume, and the flux surface average of $(\nabla \rho)^2$. Although this transport equation is one-dimensional, it is occasionally referred to as a 1.5D transport equation as poloidal variation is taken into account through flux surface averages.

2.5 The transport code ASTRA

A tool for solving coupled macroscopic transport equations for plasma quantities is the 1.5D transport code *ASTRA*, the Automated System for *T*Ransport Analysis [80, 108]. It is not only a transport code, but also a flexible programming system to build numerical tools for transport modeling. For this purpose, *ASTRA* offers various modules describing physical processes and easily allows including new ones. As such, I used *ASTRA* in this work for the development of a toolkit for self-consistent simulations of background tokamak plasma, material injection and runaway electron generation.

Inside the core *ASTRA* routines, the macroscopic transport equation is evolved for the electron density n_e , the electron temperature T_e , the ion temperature T_i and the poloidal magnetic flux Ψ . The *ASTRA* solved transport equation is further amended to allow for a temporal variation of the on-axis toroidal magnetic field B_0 . In the case of the poloidal magnetic flux, the following equation is solved [108]:

$$\sigma_{\parallel} \left(\frac{\partial}{\partial t} - \frac{\dot{B}_0}{2B_0} \frac{\partial}{\partial \rho} \right) \Psi = \frac{j^2 R_0}{4\pi^2 \mu_0 \rho} \frac{\partial}{\partial \rho} \left(\frac{V'}{j} \left\langle \left(\frac{\nabla \rho}{r} \right)^2 \right\rangle \frac{\partial \Psi}{\partial \rho} \right) - \frac{V'}{2\pi \rho} j_{\text{ext}}. \quad (2.49)$$

Here, the quantities σ_{\parallel} and j describe respectively the plasma conductivity along magnetic field lines and the plasma current density. The vacuum permeability is denoted by μ_0 . The evolution of the poloidal magnetic flux is influenced by non-inductively driven current density j_{ext} , such as e.g. current density driven by other external means*, the transport-driven "bootstrap" current density† or, importantly for the purposes of this work, the runaway electron current density. Consequently, the feedback of the runaway electron population onto the evolution of the poloidal magnetic flux can easily be considered.

In the case of the electron density evolution, the following transport equation is solved:

$$\frac{1}{V'} \left(\frac{\partial}{\partial t} - \frac{\dot{B}_0}{2B_0} \frac{\partial}{\partial \rho} \right) (V' n_e) = -\frac{1}{V'} \frac{\partial}{\partial \rho} \Gamma_e + S_{n_e}. \quad (2.50)$$

The fluxes of particles Γ and heat q (see below) are described in reference 108 in more detail. A similar equation for the evolution of the main ion density is not solved. Instead, the evolution of the main ion density n_i and the corresponding particle flux is obtained from quasineutrality, i.e. $n_i = n_e/Z_i$, where Z_i is the ion charge. Finally, the evolution of the electron temperature is calculated from

$$\frac{3}{2} \frac{1}{V'^{\frac{5}{3}}} \left(\frac{\partial}{\partial t} - \frac{\dot{B}_0}{2B_0} \frac{\partial}{\partial \rho} \right) (V'^{\frac{5}{3}} n_e T_e) = -\frac{1}{V'} \frac{\partial}{\partial \rho} \left(q_e + \frac{5}{2} T_e \Gamma_e \right) + S_{T_e} \quad (2.51)$$

* As mentioned in the introduction in section 1.2, non-inductively driven current is necessary to overcome the tokamak's limitation of pulsed operation. Through injection of a neutral beam or electromagnetic waves, a significant toroidal current can be driven externally [7, 13].

† Details on this contribution following from neoclassical transport theory can be found e.g. in references 7 or 12.

and the evolution of the ion temperature from

$$\frac{3}{2} \frac{1}{V'^{\frac{5}{3}}} \left(\frac{\partial}{\partial t} - \frac{\dot{B}_0}{2B_0} \frac{\partial}{\partial \rho} \right) \left(V'^{\frac{5}{3}} n_i T_i \right) = - \frac{1}{V'} \frac{\partial}{\partial \rho} \left(q_i + \frac{5}{2} T_i \Gamma_i \right) + S_{T_i}. \quad (2.52)$$

Noticeably, the electron and ion temperatures are not evolved directly, but rather the electron and ion thermal energies are being evolved. As such, the evolution of the electron density and the temperatures is coupled. The electron energy content is increased through Joule heating by the plasma current, according to

$$S_J = \frac{1}{2\pi R_0} U_p j, \quad (2.53)$$

where the quantity U_p denotes the local plasma voltage. Electron and ion species in fusion experiments may be heated through external means, the power deposition of which can be described by optional modules integrated into ASTRA. Additionally, the heat exchange between electrons and ions, being

$$S_{ei} = \frac{3m_i}{m_e} n_e \nu_e [T_e - T_i], \quad (2.54)$$

can be considered. In the presence of impurity species, radiation S_{rad} dissipates electron thermal energy.

In transport simulations with ASTRA, not all of the physical quantities of equations (2.49) – (2.52) have to be evolved. Their evolution can alternatively be prescribed by various means, e.g. from an external file, from a user built model or from an initial value – whichever is suitable for the model to be developed. However, the poloidal magnetic flux has to be evolved according to equation (2.49) in all cases.

In this work, the evolution of the electron density $n_e(t)$ is calculated from the condition of quasineutrality, considering the evolution of impurity ion densities $n_k(t)$ of each impurity species k , as obtained by the impurity transport code STRAHL [92]. In the case of massive gas injection, the deuterium density can be assumed to remain constant at the pre-injection value $n_D(t_{\text{inj}})$, as the material introduced strongly increases the density of free electrons and thus far outweighs the deuterium content. The deuterium density is taken to be identical to the pre-injection electron density shown in figure 2.12(a)). As such, the evolution of the electron density is in this work described by

$$n_e(t) = n_D(t_{\text{inj}}) + \sum_k n_k(t) \langle Z_k(t) \rangle, \quad (2.55)$$

where $\langle Z_k \rangle$ denotes the average impurity charge of species k .

The ASTRA programming system further allows evolution of arbitrary, *auxiliary* quantities following the macroscopic transport equation (2.48), when providing transport or source terms. Importantly for this work, these quantities can be used to describe the evolution of different populations of runaway electrons. Details are provided in section 2.5.2.

2.5.1 The ASTRA magnetic equilibrium

For the evaluation of the ASTRA solved transport equations, information on the magnetic equilibrium is required for the factors ρ , $\nabla\rho$ and $\partial V/\partial\rho$. For this purpose, ASTRA provides options to calculate the magnetic equilibrium consistent with the evolution of the plasma. The simplest approach is the application of an ASTRA built-in 3-moment solver. Flux surfaces can be characterized by three quantities (the *moments*) related to the shape of the flux surface. These comprise the radial shift Δ of a flux surface's center with respect to the center of the outermost flux surface, referred to as Shafranov shift [12], as well as triangularity δ and elongation κ of the flux surface. Consequently, flux surfaces are not necessarily circular (in figure 2.11, circular flux surfaces are shown only as an example). Following the 3-moment approach, the radial r and vertical z coordinates of a flux surface with mid-plane minor radius a are parametrized by

$$r(a, \theta) = R_0 + \Delta(a) + a [\cos \theta - \delta(a) \sin^2 \theta], \quad (2.56a)$$

$$z(a, \theta) = a\kappa(a) \sin \theta. \quad (2.56b)$$

Up-down symmetry of the plasma with respect to the equatorial mid-plane at $z = 0$ is assumed. This parametrization is most suitable for magnetic equilibria, which do not deviate significantly from a circular shape. In the case of ASDEX Upgrade runaway electron experiments, the target plasma is usually chosen to be almost circular for reasons of stability [43–46]. As such, application of the ASTRA 3-moment solver is sufficient in this work.

It should be noted, that the magnetic equilibrium used in ASTRA can also be obtained from the equilibrium solver SPIDER [109]. This tool calculates the 2D magnetic equilibrium, being more accurate than the built-in 3-moment solver, especially in cases of non-circular equilibria. However, the computational cost can be significantly increased when using SPIDER in transport simulations with ASTRA.

2.5.2 Simulating electron runaway

Inside ASTRA, calculating the generation of runaway electrons is made possible by a wrapper routine referred to as REGIA, which couples the Fortran module discussed in section 2.1 to ASTRA. The wrapper routine ensures correct usage of data structures and physical units when exchanging data between ASTRA and the runaway electron module. As such, the generation of runaway electrons due to the Dreicer mechanism, hot-tail mechanism and avalanche mechanism can be calculated in ASTRA, thus constituting the mechanisms relevant for the study of electron runaway in ASDEX Upgrade experiments.

Each population of runaway electrons created due to one of the mechanisms described is evolved separately in ASTRA as one of the auxiliary quantities following equation (2.48). In the case of Dreicer and avalanche generation, the individual source terms S_i are set to the growth rates introduced in sections 2.1.3 and 2.1.5, respectively. Radial transport of these runaway electron populations is not considered. Only a small

diffusion coefficient with a magnitude of $10^{-3} \text{ m}^2 \text{ s}^{-1}$ is applied to ensure numerical stability if necessary. The absence of significant radial transport is motivated by the observation, that the bulk of the runaway population is generated when closed magnetic field lines have re-emerged. Therefore, transport across stochastic magnetic field lines is not considered. Following a similar argument, loss mechanisms for runaway electrons are not taken into account. Consequently, the runaway electron current calculated at the end of the current quench constitutes an upper bound for the runaway current generated. Problematically, radial transport of runaway electrons is neither well diagnosed in disruption experiments, nor sufficiently understood theoretically. However, once available, a suitable description of runaway transport can easily be implemented in ASTRA.

In the case of hot-tail runaway, the model describing runaway during rapid cooling yields the instantaneous density of runaway electrons, rather than the growth rate. As such, the density of hot-tail runaway electrons inside ASTRA is set equal to the density obtained with this model. Radial transport of hot-tail runaway electrons can therefore not be calculated with this approach. In future work under consideration of such processes [110], however, hot-tail runaway generation could alternatively be described by applying the temporal derivative of the hot-tail density obtained from equation (2.20) as source term inside ASTRA.

The generation of a substantial population of runaway electrons impacts the evolution of the poloidal magnetic flux Ψ inside ASTRA by adding the runaway electron carried current density to the externally driven current density j_{ext} (see equation 2.49). For this purpose, the runaway electrons generated are assumed to propagate with the speed of light, as the generation models employed provide only the growth rate of the number density of runaway electrons. The assumption of runaway propagation at the speed of light is justified by experimental observations that runaway electrons regularly reach energies in the range of tens of MeV, being well above the electron rest mass energy of 511 keV. Only during the initial phase of runaway generation, the average electron energy may not necessarily be deeply relativistic. However, in this phase, the runaway contribution to the overall current is small. Thus, the feedback of the runaway electron population on the poloidal magnetic flux is similarly small. Within this work, the choice of the average runaway electron velocity close to the speed of light was confirmed to have a minor impact on simulation results (see appendix B of Linder et al [93]), thus justifying this approach.

2.5.3 Simulating massive gas injection

In this work, ASTRA is used for simulations of massive material injection of argon into an ASDEX Upgrade discharge. The evolution of the impurities injected is, however, not calculated inside ASTRA, but rather inside the impurity radiation code STRAHL [92]. This tool is described in detail the following section 2.6. Still, settings specific to the application of simulating massive material injection are applied inside ASTRA.

In the light of material injection and subsequent disruptions occurring on time scales in the order of a few ms, the description of electron and ion heat can be simplified in

simulations starting at the onset of material injection. Transport mechanisms typically considered in integrated modeling of electron and ion heat, such as turbulent and neo-classical transport [111], can be neglected. However, a global heat diffusion coefficient of $\chi = 1 \text{ m}^2/\text{s}$, being in the order of the pre-injection power balance, is prescribed for evaluating the evolution of electron and ion heat to prevent formation of strongly localized hot plasma beamlets, as observed in other works of tokamak disruptions contrary to experimental evidence* [64, 112].

Furthermore, in ASDEX Upgrade runaway electron experiments, any external heating of the plasma is switched off with the onset of material injection. As such, consideration of external electron or ion heat source terms is not necessary. Therefore, source and sinks terms taken into account comprise Joule heating, electron-to-ion heat exchange and impurity radiation due to line radiation, continuum radiation and ionization power loss,

$$S_{T_e} = S_J - S_{ei} - S_{\text{rad}}, \quad S_{T_i} = S_{ei}. \quad (2.57)$$

As a result of massive material injection, the inward-propagating cold gas front triggers $(m, n) = (2, 1)$ MHD modes and higher harmonics through strong current density gradients upon reaching the flux surface with rational safety factor $q = 2$ [88, 106]. As outlined in the introduction in section 1.3, the occurrence of these modes marks the onset of a tokamak disruption. In ASDEX Upgrade and also in JET, this is accompanied by a rapid drop of the internal inductance and a sudden increase of the plasma current, being the current spike described previously. These observations point to a flattening of the current density j_p inside the $q = 2$ surface [46, 88].

In ASTRA, the effect of the $(2, 1)$ MHD modes on the current density is mimicked by flattening the q -profile inside the $q = 2$ surface under conservation of the total poloidal magnetic flux. The modes are assumed to be excited when the current density gradient at the $q = 2$ surface exceeds a threshold value, taken in this work as $(dj/d\rho)/j = 50$. As the safety factor is related to the current density through $q = 2B_\phi/\mu_0 j R$ [12], flattening the q -profile simultaneously flattens the current density profile in good approximation. Inside ASTRA, flattening the q -profile is easier to implement on a technical level. Using the normalized current density gradient as a condition for the onset of the $(2, 1)$ MHD modes is motivated by the assessment, that these MHD modes are driven by the plasma current [88]. The choice of a threshold value of $(dj/d\rho)/j = 50$ corresponds to the assumption, that the local current density decreases to zero over a radial distance of $\Delta\rho = 0.02$ or less. However, the exact numerical value within this order of magnitude is of lesser importance for the simulation results. In massive gas injection experiments, the formation of a pronounced current density sheet in front of the inward-propagating cold

* Describing the background plasma through the set of coupled transport equations, strongly localized current sheets may emerge, increasing locally Ohmic dissipation and consequently the temperature. As additional current diffuses into these regions as a result of the decreased plasma resistivity, Ohmic dissipation and temperature increases further, thus creating self-reinforcing hot plasma beamlets. Under experimental conditions, however, the strong current and temperature gradients would trigger instabilities preventing a further increase.

gas is observed as the current density contracts to regions where the plasma is still hot. Impurity propagation occurs with thermal velocity, being in the order of several 100 m s^{-1} depending on the gas species [29]. Thus, the strong, localized current density gradients also move inward on these time scales. As such, the actual choice of the threshold current density in ASTRA to mark the onset of the disruption is not particularly important, provided $(dj/d\rho)/j$ is in the aforementioned range.

It should be noted, that the approach of flattening the q -profile under conservation of the total poloidal magnetic flux cannot reproduce the current spike observed experimentally. However, it is believed, that this phenomenon can be accurately described by conserving instead the magnetic helicity [107, 113]. For the purposes of the work presented, omitting the effect of the current spike is assumed not to noticeably impact simulation results.

The onset of the $(2, 1)$ MHD modes results not only in the flattening of the current density, but also in the loss of the plasma stored thermal energy on sub-ms time scales. The breakup of magnetic surfaces during this phase is considered responsible for greatly enhanced radial transport. Within ASTRA, magnetic field line stochastization cannot be described, requiring instead non-linear MHD codes such as JOREK [85–87], M3D-C1 [114, 115] or NIMROD [116] for a proper treatment. However, the impact of broken magnetic surfaces can be mimicked in ASTRA through application of additional radial transport coefficients of the form

$$\mathcal{Y}_{\text{add}}(t) = \mathcal{Y}_{\text{add}}^{\text{max}} \exp\left(-\frac{t - t_{q=2}}{\tau_{\text{add}}}\right) \Theta(t - t_{q=2}) \quad (2.58)$$

inside the $q = 2$ surface. As closed magnetic flux surfaces re-emerge [117–119] quickly after the onset of the $(2, 1)$ MHD modes due to mode stabilization following the relaxation of the current density profile, enhanced radial transport is prescribed in ASTRA only

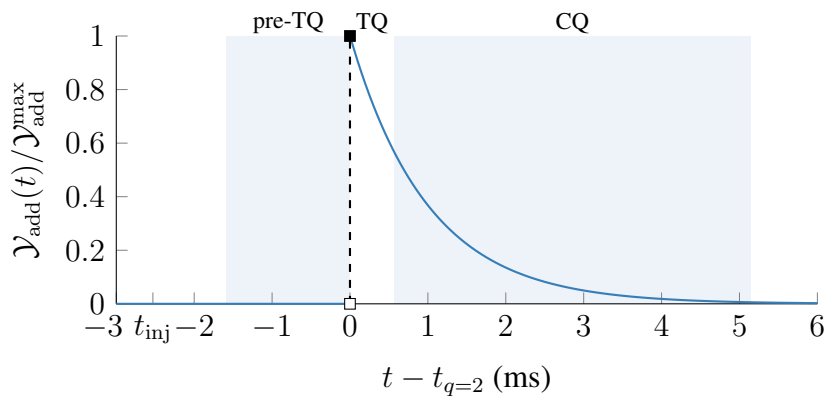


Figure 2.14: Temporal evolution of the additional transport coefficients prescribed in this work inside the $q = 2$ surface according to equation (2.58). Additional transport is assumed to occur once the cold gas, injected from t_{inj} onward, reaches the $q = 2$ surface at time $t_{q=2}$, thus causing breakup of the magnetic surfaces. The magnitude of additional transport is assumed to decrease exponentially on time scales $\tau_{\text{add}} = 1 \text{ ms}$ as magnetic surfaces re-emerge. Characteristic times are shown for ASDEX Upgrade #33108.

transiently. For this purpose, the magnitude of the additional coefficients decreases exponentially on time scales τ_{add} , taken in this work to be $\tau_{\text{add}} = 1.0$ ms. The stochastization of magnetic field lines affects both heat and impurity ion transport. After all, strong impurity radiation is observed experimentally in the central plasma throughout the thermal quench. In this work, the following maximum additional transport coefficients are applied for simulating argon injection in ASDEX Upgrade:

$$D_{\text{add}}^{\text{max}} = 100 \text{ m}^2 \text{ s}^{-1}, \quad v_{\text{add}}^{\text{max}} = -1000 \text{ m s}^{-1}, \quad \chi_{\text{add}}^{\text{max}} = 100 \text{ m}^2 \text{ s}^{-1}. \quad (2.59)$$

The magnitudes of these parameters are set to reproduce experimental observations of key parameters of ASDEX Upgrade discharge #33108. However, noticeably, only order of magnitude values have been used rather than fine-tuning these parameters. The temporal evolution of these additional transport coefficients is shown in figure 2.14. The applicability of this approach has to be assessed further with non-linear MHD codes.

2.5.4 Improvements to ASTRA

Preparing self-consistent simulations of artificial disruptions with ASTRA, I amended the ASTRA programming system by additional subroutines, modules and scripts to streamline simulation and development workflows. The most relevant improvements are described in this technical section in the following. Please note, modifications are with respect to ASTRA version 7 from 2018.

Including complex subroutines

ASTRA offers the possibility to include user-built subroutines when setting up a transport model. For this purpose, a directory `sbr` in the ASTRA working directory is provided, where Fortran files named identically as the subroutine to be included can be stored. Upon execution of ASTRA with a specific model file, ASTRA analyses the model file regarding user-built subroutines included and recompiles the model executable if changes in the corresponding Fortran file are discovered. A compiled object of the subroutine is stored inside a static library `user.a`, located in a compiler specific subdirectory of the directory `.usr`. As such, simple subroutines can easily be included in a transport model. However, this approach discourages the use of nested, multi-file subroutines, as changes in additional files the subroutine to be included depends upon may not be detected.

Application of complex subroutines within ASTRA is enabled by introducing an additional, automated workflow during setup of the model executable. When calling ASTRA, the user does not actually start a precompiled executable, but rather a C shell script to assemble the model, compile it into an executable if necessary and run the executable created. As such, an additional workflow is introduced into the ASTRA C shell script to compile complex user-built subroutines into single compiled objects for linking. For this purpose, an additional script is called from within the ASTRA script to first identify all user-built subroutines included in the model file provided. The additional script then checks if

a Fortran file with identical name is located in the directory `src` (including subdirectories) created for this purpose. If a corresponding file is found, `make` is called to create an object as specified in a makefile located at `src/makefiles/makefile.mk`. A general rule is specified in the makefile for subroutines to be included in the physical model. Here, a corresponding object is compiled under consideration of additional prerequisites specified for each subroutine individually and explicitly in the makefile. The object created is then stored in the static library `user.a`. Finally, the Fortran file of the subroutine included in the model is copied into the directory `sbr` to force `ASTRA` into recompiling the model executable under consideration of the changes made to the subroutine.

The approach of separately compiling user-built subroutines has the advantage, that the corresponding Fortran file is recompiled also when any of its dependencies have been updated. As such, user-built subroutines can use additional subroutines which are not intended to be included inside a physical model. Furthermore, each additional subroutine may be located in a separate Fortran file and may also be grouped according to functionality. For example, a subdirectory `src/math` is introduced for subroutines performing mathematical operations such as interpolation, integration or solving systems of linear equations. In this case, a single object `math.o` is created containing all related subroutines and stored in the static library `user.a`. Following this approach, grouping related subroutines in single objects additionally ensures clarity of the static library. The necessity of this approach for compiling user-built subroutines is illustrated in a following section regarding storage of `ASTRA` results in `netCDF` files.

Simulation specific run directory

The `ASTRA` executable, with the specified model and data files, is run by default in the `ASTRA` working directory. When performing file I/O (input/output) operations only at the beginning and end of a simulation, e.g. to calculate steady-state plasma profiles, multiple instances of the same `ASTRA` executable can in principle be run in parallel using different input data. However, in the case of continuous file I/O operations, only serial execution of the same executable with different initial input data is possible to avoid corruption of simulation specific I/O files by a different simulation running in parallel. As the impurity radiation code `STRAHL` is not incorporated in the `ASTRA` executable, but instead executed separately each specified time step by `ASTRA`, multiple `ASTRA-STRAHL` simulations cannot be carried out in parallel with the default versions of `ASTRA` and the `STRAHL` wrapper routine. The necessity of performing `ASTRA` simulations in serial execution arises for all user-built subroutines performing continuous file I/O operations.

Performing multiple `ASTRA` simulations with continuous file I/O operations in parallel is enabled by introducing simulation specific unique run directories through an additional subroutine. Upon being called, this subroutine creates a run directory in a predefined location. For the simulations presented in this work, for example, the `work` directory of IPP's `TOK` cluster is used. The run directory's unique name consists of the model file's name, the data file's name and a four digit integer. For example, the base case simulation

presented by Linder et al [93] has the unique name `re_Ar_mgi.aug33108.0437`. On successive calls of this additional subroutine throughout the simulation, the location of the simulation's run directory is returned. Each user-built subroutine requiring continuous file I/O operations makes use of this unique run directory throughout this work.

Storing simulation results

Performing ASTRA simulations using its graphical user interface, plasma profiles of the current time step can easily be stored in a text file at the click of a button. However, as such, the temporal evolution of plasma profiles is challenging to capture throughout a long simulation. More importantly, profiles cannot be stored when executing ASTRA in the background without a graphical user interface. Thus, to allow easily storing arbitrary radial profiles and scalar values throughout an ASTRA simulation, a subroutine is introduced which stores these quantities in a netCDF file with netCDF-4/HDF5 format located in the simulation's run directory. As added benefit, ASTRA simulation results can easily be shared and processed further when provided as netCDF-4 files.

The profiles and scalars to be stored are specified each in two-column text files named `profiles_use.dat` and `scalars_use.dat`, located in the directory `dat/netcdf`. For each profile or scalar to be included, the two columns describe the netCDF dataset's name to be used and ASTRA's variable name. As such, data located in ASTRA's custom arrays `CAR` or working arrays `WORK` can also be stored in the netCDF file. When including the corresponding subroutine in the ASTRA model file, the storage interval can be specified through the time interval between subroutine calls.

When removing or including additional quantities in one of the two text files, changes are detected automatically by `make` in the additional workflow discussed. In this case, the source code of the netCDF subroutine is updated automatically and the corresponding object recompiled. Following this approach, the user does not have to manually modify the source code as would have been required when storing the netCDF subroutine in the directory `sbr`.

Coupling to STRAHL

In the simulations of artificial disruptions presented in this work, the evolution of impurities injected is calculated by the coupled code STRAHL, discussed in detail in the following section 2.6. In light of the requirement to perform multiple ASTRA-STR AHL simulations in parallel, the wrapper subroutine to STRAHL is updated to make use of the unique simulation run directories introduced. For this purpose, STRAHL calculations are performed for a given ASTRA simulation within the corresponding unique run directory. As such, all input and output files required are located inside this directory. Further, non-technical details of the coupling between ASTRA and STRAHL are provided in section 2.6.3.

Batch job submission

Execution of an ASTRA simulation is typically started immediately upon calling ASTRA on the machine a user is logged on to. However, it may be favorable to perform a simulation only when sufficient computational resources are available or on a different machine. For example in the case of the simulations presented in this work, model development is typically performed on IPP's interactive TOK-I cluster, whereas production type simulations should be carried out on a separate batch cluster (for details of the clusters, see section 2.7). Therefore, to perform longer ASTRA simulations on the batch cluster, a set of scripts is provided in the directory `.exe` for submission of an ASTRA simulation to the job queuing system using the slurm workload manager. Instead of starting a simulation by calling `.exe/astra`, an ASTRA job can be submitted to the batch system through `.exe/sbatch_astra`. The corresponding batch script is defined in `.exe/sbatch_job_astra` and can be modified as required by the simulation, changing e.g. the number of nodes or amount of memory required. Execution of the actual ASTRA simulation on the batch cluster is performed as specified in the script `.exe/sbatch_run_astra`. Multiple longer ASTRA simulations can easily be performed in parallel on the batch cluster without blocking the limited resources of the interactive cluster.

2.6 The impurity transport code STRAHL

The impurity transport code STRAHL [92] allows to calculate the density evolution of impurities for individual charge states, as well as the corresponding impurity radiation. Similarly as ASTRA, STRAHL evaluates the macroscopic transport equation (2.48) for this purpose using cylindrical coordinates [92],

$$\frac{\partial n}{\partial t} = D\rho^2 \frac{\partial^2 n}{\partial \rho^2} + \left[\left[\rho'' + \frac{\rho'}{r} \right] D + \rho'^2 \frac{\partial D}{\partial \rho} \right] \frac{\partial n}{\partial \rho} - v\rho' \frac{\partial n}{\partial \rho} - \left[\frac{v}{r} + \rho' \frac{\partial v}{\partial \rho} \right] n + S, \quad (2.60)$$

with $\rho' \equiv \partial\rho/\partial r$ and $\rho'' \equiv \partial^2\rho/\partial r^2$. Importantly, atomic processes of the impurity charge states can be taken into account, such as electron-impact ionization and recombination, as well as charge exchange reactions among plasma species. During the evaluation of the transport equation, the atomic processes considered are treated as sources S . For a charge state i of impurity species k , the source is given by

$$S_{k,i} = n_e \alpha_{k,i-1}^{\text{ion}} n_{k,i-1} - \left[n_e \alpha_{k,i}^{\text{ion}} + n_e \alpha_{k,i}^{\text{rec}} + n_H \alpha_{k,i}^{\text{CX}} \right] n_{k,i} + n_e \alpha_{i,k+1}^{\text{rec}} n_{k,i+1}. \quad (2.61)$$

The reaction rates of ionization α^{ion} , recombination α^{rec} and charge exchange α^{CX} processes are described by tabulated coefficients from ADAS [120]. By considering these atomic processes, the evolution of neighboring impurity charge states is coupled. The resulting set of equations is solved using an unconditionally stable numerical method by

Lackner et al [121], where the temporal evolution is performed in two half-steps. In the first step, impurity densities are evolved from low to high ionization stages considering ionization implicitly and recombination explicitly. In the second step, evolution is performed in reversed order treating ionization explicitly and recombination implicitly.

For the transport of impurities due to diffusive and convective processes, it is possible to employ coefficients describing neoclassical effects through the built-in code NEOART [122]. The corresponding coefficients can be calculated using either charge-state-resolved impurity densities or the total impurity density with averaged charge. Additionally, arbitrary transport coefficients can be prescribed externally.

The tool STRAHL was developed to also allow to study trace amounts of impurities in diffusion dominated processes, particularly in the scrape-off layer outside the LCFS under consideration of particle influx from divertor and due to recycling. For this purpose, the STRAHL simulation domain is extended beyond the LCFS. Although its treatment of atomic processes makes STRAHL in principle a suitable tool for the study of material injection within this work, the original purpose of STRAHL hinders its application to massive gas injection scenarios, where massive amounts of neutral material, far outweighing the plasma's main ion content, are injected. Therefore, the original version of STRAHL cannot be used for the studies presented in this work. To still use STRAHL to describe the evolution of impurities, I modified STRAHL as required for this study. The most relevant modifications are described in the following.

2.6.1 Treatment of neutral impurities

In the original version of STRAHL, the densities of neutral impurities are not evolved following the macroscopic transport equation, but used merely as a source term for the first ionization stage of impurities k . The content of neutrals is not kept track of. As such, any neutrals not ionized are purged at the end of the current time step of a simulation. Performing STRAHL simulations, the neutral influx $\Gamma_{k,0}$ has to be provided instead of the neutral density. Furthermore, the radial profile $S_{k,0}(\rho)$ of the neutral source is assumed to follow a Gaussian distribution, centered at ρ_{src} and falling off over an inner and outer length scale of λ_{in} and λ_{out} , respectively, according to

$$\frac{S_{k,0}(\rho)}{\Gamma_{k,0}} = \frac{\exp\left(-\frac{(\rho-\rho_{\text{src},k})^2}{2\lambda_{\text{in},k}^2}\right)}{g_{\text{in},k}\sqrt{2\pi}\lambda_{\text{in},k}}\Theta(\rho_{\text{src},k}-\rho) + \frac{\exp\left(-\frac{(\rho-\rho_{\text{src}})^2}{2\lambda_{\text{out},k}^2}\right)}{g_{\text{out},k}\sqrt{2\pi}\lambda_{\text{out},k}}\Theta(\rho-\rho_{\text{src},k}). \quad (2.62)$$

The geometric factors g are adjusted inside STRAHL, such that the volume integral of above expressions over the simulation domain yields the neutral influx $\Gamma_{k,0}$ specified. This not only allows prescribing a neutral source in the form of a Gaussian distribution, but also allows applying a point source ($\lambda_{\text{in},k} \rightarrow 0$, $\lambda_{\text{out},k} \rightarrow 0$), a step function (letting only one $\lambda_k \rightarrow 0$) or a flat profile ($\lambda_{\text{in},k} \rightarrow \infty$, $\lambda_{\text{out},k} \rightarrow \infty$). In addition to the neutral source

profile above, STRAHL allows application of an edge neutral source, decaying inwards exponentially over the ionization length scale for neutrals with a specified energy.

For simulations of massive gas injection, the treatment of neutrals as described above is not suitable. Since fixed amounts of impurities are injected into the main plasma in experiments of massive gas injection, the total impurity content, including neutrals, has to be kept track of throughout a simulation. Furthermore, neutral impurities may not necessarily be ionized immediately upon deposition, especially in radial locations where the plasma temperature has already collapsed. Instead, in the case of massive gas injection, neutral atoms propagate (further) into the plasma center at the speed of sound. The neutral source profile throughout the injection process is thus not expected to follow a Gaussian distribution described merely by the three parameters $\rho_{\text{src},k}(t)$, $\lambda_{\text{in},k}(t)$ and $\lambda_{\text{out},k}(t)$.

To enable simulations of massive material injection with STRAHL, I modified the treatment of neutral impurities inside this tool. Following this update, the neutral population of

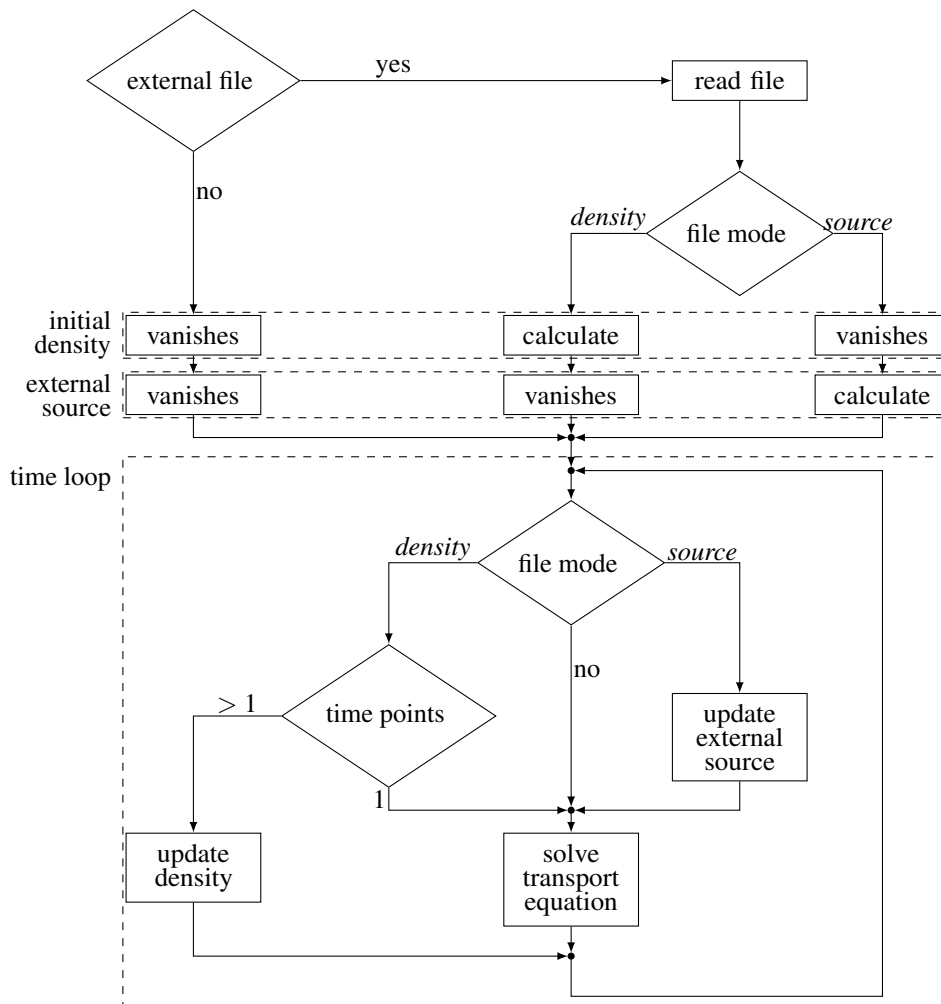


Figure 2.15: The density evolution of externally injected neutral particles can be influenced by providing (time-dependent) radial profiles from an external file. Depending on the file mode, either the density or the source profile of externally provided neutrals is updated accordingly during initialization and during the time loop.

impurities is evolved according to the macroscopic transport equation (2.48), thus ensuring conservation of the neutral particle content and as such of the total impurity content. Furthermore, two populations of neutral impurities are introduced, each evolved according to expression (2.48). In cold plasmas, impurity ions may recombine to neutral particles. However, recombined impurity neutrals likely have a different momentum space distribution as externally injected neutral particles, thus motivating the approach of using two neutral populations within STRAHL.

The population of externally injected neutrals is evolved applying the Gaussian deposition profile of equation (2.62) as a source term. To increase the flexibility of describing material deposition, an arbitrary neutral profile can be prescribed from an external file (see figure 2.15 for an overview flowchart). When prescribed in *source mode*, the (time-dependent) profile included is used as an additional source term during evaluation of the density of externally provided neutrals. Prescribing the external file in *density mode*, the density profile of externally injected neutrals is initialized at the start of the simulation with the profile provided and updated according to the external file when providing time-dependent profiles. Following this approach, radially non-uniform material deposition schemes can be considered in STRAHL, provided e.g. by external tools. For the simulations presented in this work, Gaussian deposition profiles of equation (2.62) are used.

For the study of massive gas injection, the externally provided neutral particles are assumed to propagate inwards with thermal velocity $v = -\sqrt{T_{k,0}/m_k}$, where $T_{k,0}$ denotes the energy of the neutral particles, as specified in the STRAHL parameter file. As such, the process of massive gas injection can be described by a Gaussian source of neutral particles according to equation (2.62) at ambient temperature $T_{k,0} \approx 300$ K, located just outside the LCFS, using inner and outer length scales of $\lambda_{\text{in},k} = 0$ and $\lambda_{\text{out},k} \rightarrow \infty$, respectively.

2.6.2 The discretization scheme

In early STRAHL simulations of purely convective impurity transport, the results contained numerical artifacts in the form of oscillating impurity densities (see figure 2.16(a)). However, for simulations of massive gas injection scenarios, an accurate treatment of convective transport is required, as the material deposited through massive gas injection propagates inwards through pure convection. The reason for the oscillatory behavior observed in early STRAHL simulations lies within the numerical scheme used by STRAHL, being a first-order, central finite difference scheme. As such, the first and second spatial derivatives of the density n_i^j at the spatial grid point i at time point j are expressed as

$$\frac{\partial n_i^j}{\partial \rho} = \frac{n_{i+1}^j - n_{i-1}^j}{2\Delta\rho}, \quad \frac{\partial^2 n_i^j}{\partial \rho^2} = \frac{n_{i+1}^j - 2n_i^j + n_{i-1}^j}{\Delta\rho^2}. \quad (2.63)$$

Here, the spacing of the computational grid is denoted by $\Delta\rho$ for the normalized radial coordinate. By considering for the evaluation at grid point i only directly neighboring grid points within this scheme, the matrix equation of the corresponding transport problem can be solved using the fast Thomas algorithm (also known as tridiagonal matrix

algorithm). However, in the case of advection dominated transport, this central finite difference scheme is known to yield oscillating solutions [123].

The dominant transport mechanism can easily be identified through evaluation of the Péclet number $Pe = v\Delta r/D$, where Δr is the spacing of the radial grid (such that Pe is adimensional), which describes the ratio of the advective to diffusive transport rate. From eigenvalue analysis of the matrix equation corresponding to the central finite difference scheme [123], oscillations are found to occur when

$$|Pe| = \frac{|v|\Delta r}{D} > 2. \quad (2.64)$$

Consequently in the presence of strong advective transport (see figure 2.16(a)), numerical oscillations can be reduced by decreasing the spacing Δr (or rather $\Delta\rho$) of the numerical grid and introducing a small, but finite diffusion coefficient D (see figure 2.16(b)). The numerical values of the additional diffusion or grid spacing necessary to effectively reduce numerical oscillations depend on the simulation parameters. For particularly large advection, the computational grid may have to be increased dramatically, thus increasing

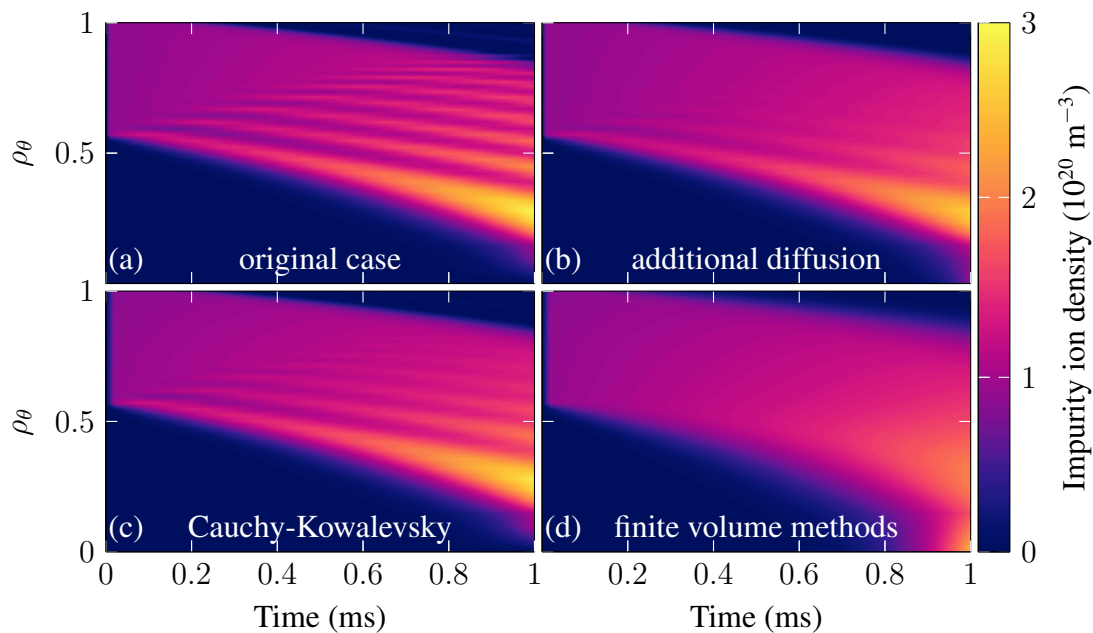


Figure 2.16: STRAHL simulations of argon deposition and propagation, showing the spatio-temporal evolution of the total ion density. Material is introduced in the outer half radius at the onset of the simulation and propagates inwards advectively with $v = -200 \text{ m s}^{-1}$. A simulation grid of 51 radial points and a constant time step of $\Delta t = 10^{-2} \text{ ms}$ is used. In (a), the density evolution is calculated using the original version of STRAHL. In (b), diffusive transport with $D = 0.2 \text{ m}^2 \text{ s}^{-1}$ is additionally considered. The density evolution in (c) is calculated using a version of STRAHL, where the Cauchy-Kowalevsky procedure has been applied, introducing numerical diffusion of around $D \approx v^2\Delta t/2 = 0.2 \text{ m}^2 \text{ s}^{-1}$. In (d), the numerical scheme of STRAHL has been replaced by a finite volume scheme with adaptive upwinding.

the computational cost. Alternatively, larger (potentially undesired) diffusion can be applied. Choosing insufficient values for these parameters, the numerical oscillations may not be removed, but merely damped (see figure 2.16(b)).

As an alternative to reducing the Péclet number Pe by introducing additional diffusion, numerical oscillations can be reduced through application of the Cauchy-Kowalevsky procedure to the macroscopic transport equation. For this purpose, the density n_i^{j+1} at time $t^{j+1} = t^j + \Delta t$ is expressed as Taylor expansion in Δt according to [124]

$$n_i^{j+1} = n_i^j + \Delta t \frac{\partial n_i^j}{\partial t} + \frac{\Delta t^2}{2} \frac{\partial^2 n_i^j}{\partial t^2} + \mathcal{O}(\Delta t^3). \quad (2.65)$$

Considering for illustrative purposes the one-dimensional advection equation with constant advection v in the absence of diffusion or sources, i.e. $\frac{\partial}{\partial t} n_i^j = -v \frac{\partial}{\partial \rho} n_i^j$, the second temporal derivative is obtained as $\frac{\partial^2}{\partial t^2} n_i^j = v^2 \frac{\partial^2}{\partial \rho^2} n_i^j$. Using this result in above Taylor expansion, the expression

$$n_i^{j+1} = n_i^j + \Delta t \left[-v \frac{\partial n_i^j}{\partial \rho} + \frac{v^2 \Delta t}{2} \frac{\partial^2 n_i^j}{\partial \rho^2} \right] + \mathcal{O}(\Delta t^3) \quad (2.66)$$

is obtained. Comparing it with the Taylor expansion up to first order in Δt of the one-dimensional advection-diffusion equation, i.e. $\frac{\partial}{\partial t} n_i^j = -v \frac{\partial}{\partial \rho} n_i^j + D \frac{\partial^2}{\partial \rho^2} n_i^j$, being

$$n_i^{j+1} = n_i^j + \Delta t \left[-v \frac{\partial n_i^j}{\partial \rho} + D \frac{\partial^2 n_i^j}{\partial \rho^2} \right] + \mathcal{O}(\Delta t^2), \quad (2.67)$$

the Cauchy-Kowalevsky procedure reduces numerical oscillations by introducing numerical diffusion of magnitude $D = v^2 \Delta t / 2$. As such, the Péclet number is modified as $Pe = 2\Delta r / v \Delta t$. A thorough treatment of the STRAHL transport equation (2.60) yields the modified diffusion \tilde{D} and advection \tilde{v} coefficients

$$\tilde{D} = D + \frac{v^2 \Delta t}{2}, \quad \tilde{v} = v \left[1 - \frac{\Delta t}{2} \left[\frac{v}{r} + \rho' \frac{\partial v}{\partial \rho} \right] \right], \quad (2.68)$$

which I implemented for the first-order central finite difference scheme in STRAHL to assess the suitability of this method*. Even though the Cauchy-Kowalevsky procedure can improve numerical stability (see figure 2.16(c)), it introduces limitations for the minimum time step. Demanding $|Pe| \leq 2$ for stability limits the time step to $\Delta t \geq \Delta r / |v|$. In the example shown in figure 2.16(c), the time step Δt was chosen too small to effectively remove the numerical oscillations. As such, the Cauchy-Kowalevsky procedure exhibits the same drawbacks as the previous method discussed, being increased computational costs due to a larger computational grid and introduction of (undesired) numerical diffusion.

* When applying the Cauchy-Kowalevsky procedure to the first-order central finite difference scheme, the discretization obtained is also referred to as *Lax-Wendroff scheme* [124].

An effective method for preventing the occurrence of numerical oscillations can be designed by recalling, that these are caused by discretizing the first spatial derivative through a first-order central finite difference scheme. Applying instead a forward or backward scheme (depending on the sign of v), numerical oscillations can be avoided. However, this scheme has a lower accuracy and introduces numerical damping. As cases with low Péclet number $|Pe| < 2$ are numerically stable using a central scheme, the discretization of $\partial n / \partial \rho$ may be chosen depending on the value of the Péclet number. This approach is referred to as *adaptive upwinding*. For this purpose, the adaptive upwinding parameter $K \in [-1, 1]$ is introduced and the first spatial derivative discretized as

$$\frac{\partial n}{\partial \rho} = \frac{1}{2\Delta\rho} [[1 + K] n_{i-1} - 2K n_i - [1 - K] n_{i+1}]. \quad (2.69)$$

In the case $K = 0$, the central scheme is re-obtained, whereas for $K = \pm 1$ a forward/backward discretization is applied. The parameter K has to be related to the Péclet number such that $K(Pe = 0) = 0$ and $K(|Pe| = \infty) = \text{sgn}(Pe)$ to ensure removing the numerical oscillations. Suitable methods are exponential fitting or an approximation thereof [123], being respectively

$$K = \frac{e^{Pe} + 1}{e^{Pe} - 1} - \frac{2}{Pe}, \quad (2.70a)$$

$$K = \max(0, 1 - 2/|Pe|) \text{sgn}(Pe). \quad (2.70b)$$

The latter expression takes the stability boundary of the central finite difference scheme into account. Both methods are illustrated in figure 2.17. Following this approach, the discretization applied is generally a mixture of a central scheme and upwinding. Given the simplicity of the latter expression (2.70b), this relation is used in the following. Here,

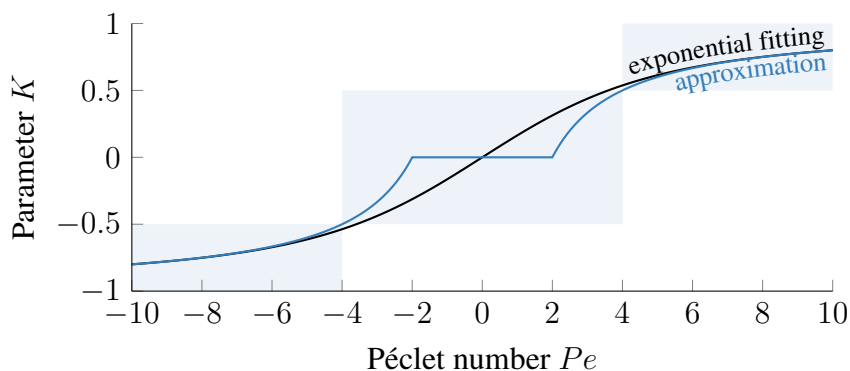


Figure 2.17: Adaptive upwinding parameter K for the discretization of the first derivative $\partial n / \partial \rho$ in equation (2.69) as a function of the Péclet number Pe using exponential fitting (black; see equation (2.70a)) and an approximation thereof (blue; see equation (2.70b)). In cases of strong diffusion with $|Pe| < 4$, the central scheme dominates the discretization, whereas in cases of large advection with $|Pe| > 4$ upwinding dominates.

the central scheme dominates the discretization in cases of strong diffusion with $|Pe| < 4$, whereas in cases of large advection with $|Pe| > 4$ upwinding dominates.

Even though the introduction of adaptive upwinding in the discretization scheme prevents the occurrence of numerical oscillations, the forward scheme for the discretization of the first spatial derivative $\partial n / \partial \rho$ has a lower accuracy and, even worse, introduces numerical damping. Furthermore, the first-order finite difference scheme used does generally not conserve the particle content*. However, as this property is a requirement for assessing the amount of injected material in simulations of massive gas injection, a discretization scheme different from the first-order finite difference scheme is needed. Ideally, a scheme is to be applied which relies for the density evolution only on directly neighboring grid points, such that the fast Thomas algorithm can be continued to be used.

Conservation of the particle content can be ensured by application of a finite volume discretization. For this purpose, a discretization is derived from the conservative form of the transport equation in cylindrical coordinates. Consider a numerical grid where the grid points i at radial position r_i are embedded in cells $\Omega_i = [r_{i-\frac{1}{2}}, r_{i+\frac{1}{2}}]$ with vertices $r_{i\pm\frac{1}{2}} = \frac{1}{2}(r_i + r_{i\pm 1})$. Vertices are located in the middle between grid points, corresponding to a vertex centered scheme. The cell averaged density $\bar{n}(r_i, t)$ is then given by

$$\bar{n}(r_i, t) = \frac{\int_{\Omega_i} r n(r, t) dr}{\int_{\Omega_i} r dr} = \frac{2}{r_{i+\frac{1}{2}}^2 - r_{i-\frac{1}{2}}^2} \int_{r_{i-\frac{1}{2}}}^{r_{i+\frac{1}{2}}} r n(r, t) dr. \quad (2.71)$$

Applying this scheme, the conservative form of the differential equation is obtained as

$$\frac{\partial \bar{n}(r_i)}{\partial t} = \frac{2}{g_i} \left[r D \frac{\partial n}{\partial r} - r v n \right]_{i-\frac{1}{2}}^{i+\frac{1}{2}} + \bar{S}_i, \quad (2.72)$$

where the abbreviation $g_i = r_{i+\frac{1}{2}}^2 - r_{i-\frac{1}{2}}^2$ has been introduced. Using a vertex centered scheme, quantities at the cell boundaries $i \pm \frac{1}{2}$ are evaluated as the average of both cells,

$$D_{i\pm\frac{1}{2}} = \frac{1}{2} [\bar{D}_i + \bar{D}_{i\pm 1}], \quad (2.73a)$$

$$v_{i\pm\frac{1}{2}} = \frac{1}{2} [\bar{v}_i + \bar{v}_{i\pm 1}], \quad (2.73b)$$

$$\left. \frac{\partial n}{\partial r} \right|_{i\pm\frac{1}{2}} = \mp \frac{\bar{n}_i - \bar{n}_{i\pm 1}}{\Delta r_{i\pm}}. \quad (2.73c)$$

The distance between neighboring grid points is denoted with $\Delta r_{i\pm} = \mp(r_i - r_{i\pm 1})$. In the case of the density $n_{i\pm\frac{1}{2}}$ at the cell boundaries from the advection contribution, using the cell average would correspond to a first order central scheme. However, as discussed before, in the case of large Péclet numbers $|Pe|$, this scheme introduces numerical oscillations.

* The non-conservation of the particle inventory using a first-order finite difference scheme can be demonstrated e.g. in simulations of advective only transport using a constant velocity field changing sign between grid points l and $l + 1$, such that $v_i = v$ for $i \leq l$ and $v_i = -v$ for $i \geq l + 1$.

tions. Note, that for the evaluation of the diffusion $D_{i\pm\frac{1}{2}}$ and advection $v_{i\pm\frac{1}{2}}$ coefficients, this restriction does not apply, as these quantities are merely evaluated instead of evolved. Thus, adaptive upwinding is to be used to express the density at the cell boundaries, giving

$$n_{i\pm\frac{1}{2}} = \frac{1}{2} \left[\left[1 \mp K_{1\pm\frac{1}{2}} \right] \bar{n}_{i\pm 1} + \left[1 \pm K_{i\pm\frac{1}{2}} \right] \bar{n}_i \right], \quad (2.74)$$

where the parameter $K_{i\pm\frac{1}{2}}$ is to be evaluated using expression (2.70b) at the cell boundaries.

For the discretization of the temporal derivative $\partial\bar{n}/\partial t$, the θ -method is applied, being

$$\frac{\partial\bar{n}_i}{\partial t} = \frac{n_i^{j+1} - n_i^j}{\Delta t} = \theta F(n_i^{j+1}) + (1 - \theta)F(n_i^j). \quad (2.75)$$

From stability analysis, unconditional stability of this scheme is known to be achieved for $\theta \geq \frac{1}{2}$ [123]. As the approach of applying $\theta = \frac{1}{2}$, known also as *Crank-Nicolson method*, is used in the original version of STRAHL, it is also applied for the discretization of the conservative form of the transport equation. Introducing further the abbreviations $\tilde{D}_{i\pm} = r_{i\pm\frac{1}{2}}D_{i\pm\frac{1}{2}}/g_i\Delta r_{i\pm}$ and similarly $\tilde{v}_{i\pm} = r_{i\pm\frac{1}{2}}v_{i\pm\frac{1}{2}}/2g_i$, the complete finite volume discretization for STRAHL is obtained as

$$\begin{aligned} \frac{\bar{n}_i^{j+1} - \bar{n}_i^j}{\Delta t} = & \bar{S}_i + \left[\tilde{D}_{i-} + \tilde{v}_{i-} \left[1 + K_{i-\frac{1}{2}} \right] \right] \left[\bar{n}_{i-1}^{j+1} + \bar{n}_{i-1}^j \right] \\ & - \left[\tilde{D}_{i-} - \tilde{v}_{i-} \left[1 - K_{i-\frac{1}{2}} \right] \right] \left[\bar{n}_i^{j+1} + \bar{n}_i^j \right] \\ & - \left[\tilde{D}_{i+} + \tilde{v}_{i+} \left[1 + K_{i+\frac{1}{2}} \right] \right] \left[\bar{n}_i^{j+1} + \bar{n}_i^j \right] \\ & + \left[\tilde{D}_{i+} - \tilde{v}_{i+} \left[1 - K_{i+\frac{1}{2}} \right] \right] \left[\bar{n}_{i+1}^{j+1} + \bar{n}_{i+1}^j \right]. \end{aligned} \quad (2.76)$$

For the inner most grid point on the magnetic axis at $r_0 = 0$, a Neumann boundary condition is chosen, requiring the density derivative to vanish, i.e. $\partial n/\partial\rho = 0$. Additionally, advection is assumed to be absent on the magnetic axis, i.e. $v_0 = 0$. Evaluating the lower integration bound of the conservative form of the transport equation (2.72) at $r = 0$ accordingly, the discretization of the inner most grid point $i = 0$ is obtained as,

$$\begin{aligned} \frac{\bar{n}_0^{j+1} - \bar{n}_0^j}{\Delta t} = & \bar{S}_0 - \left[\tilde{D}_{0+} + \tilde{v}_{0+} \left[1 + K_{\frac{1}{2}} \right] \right] \left[\bar{n}_0^{j+1} + \bar{n}_0^j \right] \\ & + \left[\tilde{D}_{0+} - \tilde{v}_{0+} \left[1 - K_{\frac{1}{2}} \right] \right] \left[\bar{n}_1^{j+1} + \bar{n}_1^j \right]. \end{aligned} \quad (2.77)$$

Outside the simulation domain, the particle density is assumed to decay exponentially over a length scale λ . As such, a Robin boundary condition is used by STRAHL, being $\partial n/\partial\rho = -n\lambda$. To incorporate this condition in the discretization of the transport problem, a virtual grid point is introduced at index $b+1$. The density at this point is thus given by $\bar{n}_{b+1} = [1 - \Delta r_{b-}/\lambda] \bar{n}_b$, using the same grid spacing as between the points b and $b-1$. Applying additionally identical transport coefficients at the virtual point, i.e. $D_{b+1} = D_b$

and $v_{b+1} = v_b$, and positioning the point at $r_{b+1} = r_b + \Delta r_{b-}$, the discretization for the simulation boundary is obtained as

$$\begin{aligned} \frac{\bar{n}_b^{j+1} - \bar{n}_b^j}{\Delta t} = & \bar{S}_b + \left[\tilde{D}_{b-} + \tilde{v}_{b-} \left[1 + K_{b-\frac{1}{2}} \right] \right] [\bar{n}_{b-1}^{j+1} + \bar{n}_{b-1}^j] \\ & - \left[\tilde{D}_{b-} - \tilde{v}_{b-} \left[1 - K_{b-\frac{1}{2}} \right] \right] [\bar{n}_b^{j+1} + \bar{n}_b^j] \\ & - \left[\tilde{D}_{b+} \frac{\Delta r_{b-}}{\lambda} + \tilde{v}_{b+} \left[2 - \left[1 - K_{b+\frac{1}{2}} \right] \frac{\Delta r_{b-}}{\lambda} \right] \right] [\bar{n}_b^{j+1} + \bar{n}_b^j]. \end{aligned} \quad (2.78)$$

This concludes the description of the finite volume discretization for STRAHL.

The discretization of the transport equation used in STRAHL by means of finite volume methods was developed by myself based on the work by Hundsdorfer & Verwer [123]. I adopted the approach presented to the specific requirements of STRAHL and replaced the previously employed finite difference scheme in the code.

Using a finite volume discretization with adaptive upwinding in STRAHL, the issue of numerical oscillations discussed at the beginning of this section is successfully resolved (see figure 2.16(d)). Furthermore, the new scheme ensures conservation of the particle content in STRAHL, thus being suitable for the simulation of massive gas injection scenarios. As such, the updated version of STRAHL is used throughout the remainder of this work. On a side note, the improved numerical scheme presented has, by now, also been implemented in the STRAHL [92] main branch, as well as in the derived tool AURORA [125, 126].

2.6.3 Coupling to ASTRA

The tool STRAHL is coupled to ASTRA to enable self-consistent simulations of the evolution of background plasma and impurities. In light of the modifications made to STRAHL and additional features required with respect to previous applications (see e.g. the work by Fable et al [106]), I rewrote the existing wrapper routine calling STRAHL from within ASTRA. At its core, the wrapper routine produces the (text) input files required by STRAHL at each time step, initiates a STRAHL simulation over the duration of the ASTRA time step and collects the STRAHL results from a netCDF-file.

The wrapper routine itself is controlled by an input file, where parameters constant throughout the simulation are specified and read by the routine at the beginning of the simulation. The options include i.a. the constant STRAHL time step, treatment of the computational grid, options for the application of NEOART, connection lengths for recycling and specifications of the impurity species present.

During an ASTRA simulation, profiles of the electron temperature and density are passed to STRAHL to calculate the rate coefficients of the atomic processes considered. Additionally, the computational grid used by ASTRA is provided and applied identically in STRAHL. This approach allows easier exchange of kinetic profiles between both tools,

removing the necessity of profile interpolation. For this purpose, I updated STRAHL to perform calculations on an externally provided grid. The option to use one of the grids defined by STRAHL is kept, but not used in this work. Furthermore, geometric information such as the total plasma volume V and the normalized radial coordinate ρ_V are passed to STRAHL, as the transport equation employs cylindrical coordinates based on ρ_V .

To calculate neoclassical impurity transport coefficients with NEOART inside STRAHL, the wrapper routine was amended to provide the required geometric profiles as specified in the STRAHL manual [92]. Previously, these factors were made available only when calculating the magnetic equilibrium inside ASTRA with the code SPIDER. However, as argued in section 2.5.1, application of SPIDER is not necessary, as the magnetic equilibrium of massive gas injection experiments in ASDEX Upgrade is well described using the 3-moment approach. To allow combined usage of the 3-moment solver and NEOART, the required geometric factors are calculated in the ASTRA wrapper routine calling STRAHL.

After STRAHL has performed an impurity transport simulation, the results are stored, by default, in a netCDF-file. The wrapper routine reads this file and extracts relevant quantities for subsequent use in ASTRA. Charge state resolved impurity densities are stored in a common block variable to allow access by other modules, such as the routine REGIA. Recall, state-of-the-art runaway generation models calculate screening and deflection frequencies by considering all individual charge states present (see section 2.1.2). Furthermore, the total impurity ion density and average charge are calculated to construct the free electron density inside ASTRA's core routines. For the evolution of the plasma current, the effective plasma charge is additionally calculated. Finally, the wrapper routine collects from the STRAHL output file the impurity radiation calculated, which consists of line radiation, continuum radiation and ionization power loss. The impurity radiation is then used as a sink term during the evaluation of the electron temperature evolution. Additional variables are collected by the wrapper routine from the netCDF file and stored in the ASTRA output file for postsimulation analysis.

2.6.4 Simulating massive gas injection

The injection of massive amounts of material in ASDEX Upgrade using argon massive gas injection is simulated by STRAHL in this workflow. The material is deposited 1 cm outside the LCFS using a Gaussian source with inner and outer length scales of $\lambda_{\text{in}} = 0$ and $\lambda_{\text{out}} = 1$ m. As such, calculating the propagation of the material from valve to LCFS is not necessary, thus simplifying the problem. For a more complete description of material propagation up to the LCFS, tools focusing on this problem, such as IMAGINE [127], could be employed in future work. Depositing the material just outside the LCFS in STRAHL, the delay between valve trigger and arrival at the LCFS has to be taken into account. The delay is inferred experimentally from bolometry measurements to be 1 ms.

The strength of the argon source decreases with time, as the valve is progressively emptied. As such, the source strength is related to the valve's argon content N_{Ar} through $S_{\text{Ar}} = -dN_{\text{Ar}}/dt$. Under the assumption of one-dimensional ideal flow, the outflow of

argon from the valve can be described by the continuity equation [43]

$$\frac{dN_{\text{Ar}}}{dt} + n_{\text{Ar}}|_{\text{nozzle}} v_{\text{Ar}}|_{\text{nozzle}} A_v(t) = 0. \quad (2.79)$$

In the case of sonic gas expansion under conservation of entropy, the density $n_{\text{Ar}}|_{\text{nozzle}}$ and flow velocity $v_{\text{Ar}}|_{\text{nozzle}}$ at the valve's nozzle are related to the in-vessel argon content and temperature through $n_{\text{Ar}}|_{\text{nozzle}} = N_{\text{Ar}} \left(\frac{2}{\kappa+1}\right)^{\frac{1}{\kappa-1}} / V_v$ and $v_{\text{Ar}}|_{\text{nozzle}} = \sqrt{\frac{2\kappa}{\kappa+1} \frac{k_B T_v}{m_{\text{Ar}}}}$ [128], respectively. The quantity V_v denotes the valve's constant volume consisting of a gas reservoir with 85 cm³ and a feed line of 15 cm³ volume in ASDEX Upgrade. The quantity k_B denotes the Boltzmann constant. For argon, the isentropic expansion factor κ amounts to $\kappa = 5/3$. The valve itself is at ambient temperature of $T_v \approx 300$ K.

Once the valve is triggered at time t_{inj} , the gas valve opens over a finite opening time $\tau_v = 1$ ms. In this period, the cross sectional area of the valve's aperture is assumed to increase linearly as $A_v(t) = \tilde{A}_v(t - t_{\text{inj}})/\tau_v$. As such, the source rate during opening of the valve and with opened valve is obtained from above continuity equation as

$$S_{\text{Ar}} = \frac{N_{\text{Ar},0}}{\tilde{\tau}} \begin{cases} \frac{t-t_{\text{inj}}}{\tau_v} \exp\left(-\frac{(t-t_{\text{inj}})^2}{2\tilde{\tau}\tau_v}\right), & t_{\text{inj}} \leq t \leq t_{\text{inj}} + \tau_v \\ \exp\left(-\frac{\tau_v}{2\tilde{\tau}}\right) \exp\left(-\frac{(t-[t_{\text{inj}}+\tau_v])^2}{\tilde{\tau}}\right), & t > t_{\text{inj}} + \tau_v \end{cases} \quad (2.80a)$$

$$\tilde{\tau} = \frac{V_v}{\tilde{A}_v} \left(\frac{\kappa+1}{2}\right)^{\frac{2\kappa-1}{\kappa-1}} \sqrt{\frac{m_{\text{Ar}}}{\kappa T_v}}. \quad (2.80b)$$

The argon content prior to injection is denoted by $N_{\text{Ar},0}$. As an example, the temporal evolution of the argon source strength at the LCFS for ASDEX Upgrade discharge #33108 is shown in figure 2.18. Following the injection of material, the neutral impurities deposited propagate inwards with thermal velocity $\sqrt{k_B T_v / m_{\text{Ar}}}$, as discussed in section 2.6.1.

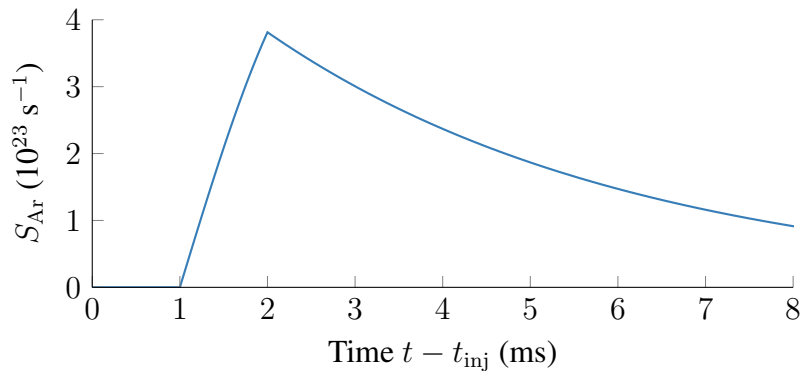


Figure 2.18: Temporal evolution of the argon source strength S_{Ar} at the LCFS in ASDEX Upgrade discharge #33108. Before the discharge, the gas valve was filled with an argon content of $0.73 \text{ bar} \times 100 \text{ cm}^3$. When triggering the valve at time t_{inj} , the valve opens its nozzle over a duration of $\tau_v = 1$ ms. Due to a finite time of flight, the gas injected reaches the LCFS with a delay of 1 ms.

2.7 Simulation specific details

The simulations presented were carried out on the TOK batch cluster and on the interactive TOK-I cluster of IPP Garching. The batch cluster includes 124 nodes, each equipped with 2 Intel Xeon Gold 6130 CPUs consisting of 16 cores and with 192 GB of memory. The interactive cluster is limited to 8 nodes, each having 24 cores (2 Intel Xeon E5-2680 v3 CPUs) and 0.75 TB of memory. As the core ASTRA routines allow only serialized execution of the tool, the simulations were performed using one core and 1 GB of memory. Within the code STRAHL, I have furthermore parallelized execution of the neoclassical code NEOART with `openMP`. Yet, the speed-up in wall-clock time achieved on the batch cluster was far less than expected. Thus, the simulations were performed single-threaded.

The confined tokamak plasma between the magnetic axis at $\rho = 0$ and LCFS at $\rho = 1$ is described by ASTRA-STRAHL using 401 equally spaced radial grid points. The ASTRA adaptive simulation time step is kept within 10^{-8} s and 10^{-3} s in production-type runs (although the upper limit is never reached). In STRAHL, a fixed time step of 10^{-8} s is used. Convergence scans of the simulation results with respect to a variation of these numerical parameters were performed prior to carrying out production-type simulations. ASDEX Upgrade disruptions were modeled over a duration of 8 ms of plasma evolution. On the specified architecture, production-type simulations took between 20 and 40 hours.

Additionally, I performed exploratory simulations on the interactive TOK-I cluster for qualitative studies, model development and code testing. In these simulations, both the minimum ASTRA time step and the STRAHL fixed time step were increased to 10^{-6} s, while using the same amount of radial grid points. Results of production-type simulations are still well reproduced in simulations using the larger minimum time step. Importantly, modeling ASDEX Upgrade disruptions over a duration of 8 ms of plasma evolution is achieved in only 15 to 30 minutes.



Summary of included papers

3.1 Paper #1

O. Linder, E. Fable, F. Jenko, G. Papp, G. Pautasso, the ASDEX Upgrade Team and the EUROfusion MST1 Team,
Self-consistent modeling of runaway electron generation in massive gas injection scenarios in ASDEX Upgrade,
Nuclear Fusion **60**, 096031 (2020).

<https://doi.org/10.1088/1741-4326/ab9dcf>
[arXiv:2003.00725](https://arxiv.org/abs/2003.00725) [physics.plasm-ph]

In this paper, first-time simulations with the coupled transport codes ASTRA–STRAHL [80, 92] of the spatio-temporal evolution of background plasma, material injected and runaway electron generation are performed throughout an ASDEX Upgrade disruption induced by massive gas injection. The temporal evolution of key plasma parameters, such as the line averaged free electron density and the plasma current, is calculated in agreement with experimental observations of ASDEX Upgrade discharge #33108 throughout the various stages of the disruption, being the pre-thermal quench, the thermal quench and the current quench. The study thus demonstrates the suitability of describing the underlying processes through a 1.5D approach, despite the complexity and 3D nature of material injection.

The work presented also shows the importance of additional transport mechanisms during breakup and reconnection of magnetic surfaces for the propagation of the material injected. Only under the assumption of rapid redistribution of material inside the $q = 2$ rational magnetic flux surface in the presence of magnetic reconnection [106] (the effects of which are described by a 0D model), experimental observations of the rapid increase of the free electron density and the decay of the plasma current can be explained. Simultaneously, neoclassical processes for the transport of ionized impurities are found to be relevant for the propagation of impurities during the current quench.

The study further illustrates the necessity of evolving the impurity species distribution based on electron-impact ionization and recombination rates, e.g. from ADAS [120], instead of assuming steady-state conditions (coronal equilibrium) among the impurity ionization stages for each time point considered. Comparing the coronal impurity distribution calculated postdisruption using the simulation's kinetic profiles with the impurity distribution obtained in self-consistent simulations, the coronal assumption is shown to overestimate the rate of change of the impurity distribution in the presence of changing plasma conditions on sub-ms time scales. Hence, a coronal distribution of impurities should not be used in integrated simulations of material injection and runaway electron generation, due to the sensitivity of electron runaway on the impurity composition.

Finally, the paper highlights the importance of considering the impact of partially ionized impurities on electron runaway in self-consistent simulations of tokamak disruptions. In simulations under application of simple models describing electron runaway in the absence of these effects [62, 76], the runaway current obtained disagrees qualitatively with

measurements of plasma current decay and hard x-ray radiation, as significant primary runaway is predicted to occur too early into the disruption. Utilizing recently developed reduced-kinetic models [77, 84] instead, a runaway response consistent with experimental observations is obtained, thus emphasizing the importance of the impact of partially ionized impurities on electron runaway.

Aforementioned paper included was written by me. To perform the studies conducted, I extended the tool's capabilities by creating a `Fortran` module containing several reduced models for electron runaway* and including it inside `ASTRA`. I enabled simulations of massive gas injection using `STRAHL` by modifying the code for the treatment of (multiple) neutral impurity species, implementing a finite volume scheme and updating the coupling between `ASTRA` and `STRAHL` accordingly.

The simulations discussed in the paper were performed from start to finish by me, i.e. simulation design, setup, execution, storage and analysis. For comparison with experiment, I retrieved the necessary measurement data and processed these according to comparison requirements. I developed a collection of additional tools and scripts for each step of the simulation workflow to allow for automation and consistent execution of the workflow.

The paper itself was written entirely by me, including all sections and appendices. All figures embedded were created from simulation and experimental data by me; where necessary through application of self-developed data processing scripts. As first author I was responsible for the submission and peer-review procedure of the manuscript.

* The standalone `Fortran` module is available at <https://github.com/o-linder/runawayelectrongeneration>.

3.2 Paper #2

O. Linder, G. Papp, E. Fable, F. Jenko, G. Pautasso, the ASDEX Upgrade Team and the EUROfusion MST1 Team,
Electron runaway in ASDEX Upgrade experiments of varying core temperature,
Journal of Plasma Physics **87**, 905870301 (2021).
<https://doi.org/10.1017/S0022377821000416>
arXiv:2101.04471 [physics.plasm-ph]

In this paper, the work on simulating the spatio-temporal evolution of background plasma, material injection and runaway electron generation presented in paper #1 (see section 3.1) is expanded upon by considering an additional mechanism for electron runaway, being hot-tail runaway during the thermal collapse of the plasma. For this purpose, I improved and implemented an analytical model [74] describing the hot-tail population in the coupled transport codes `ASTRA-STRahl`.

In simulations of argon injection in ASDEX Upgrade discharge #33108, primary runaway generation mechanisms are found to produce only a small seed population of runaway electrons, being in total around 3 kA compared to the postdisruption runaway current of 331 kA calculated. The exact strength of primary generation is only of secondary importance, as similar postdisruption runaway currents are obtained when neglecting one of the primary generation mechanisms. Electron runaway in ASDEX Upgrade is therefore caused predominantly by avalanche multiplication. Similar observations have been made in zero spatial dimension kinetic simulations with the tool `CODE` [101].

In a set of 17 `ASTRA-STRahl` simulations with varying predisruption central electron temperature based on ASDEX Upgrade discharge #33108, the postdisruption runaway electron current is found insensitive to a variation of the temperature below 9 keV. The same behavior is observed experimentally across a database of 70 ASDEX Upgrade discharges with material injection parameters similar to #33108. However, the runaway current of around 330 kA calculated in self-consistent simulations is larger than measured experimentally, being around 190 kA. This difference suggests the presence of runaway electron loss mechanisms not accounted for in the model employed. In the case of predisruption temperatures above 9 keV, simulations predict an increase of the runaway current due to an increasing hot-tail population, constituting up to 9% of the postdisruption current for the largest temperatures of 20 keV considered. However, in ASDEX Upgrade experiments in this temperature range, no postdisruption runaway electron current is measured. As the models employed predict significant primary and secondary generation under these conditions, the experimentally observed absence of runaway electrons suggests the complete loss of the runaway seed during the thermal quench and subsequent magnetic reconnection, prompting further studies with non-linear MHD codes and additional experiments of ASDEX Upgrade in this temperature regime.

Aforementioned paper included was written by me. I improved and implemented the analytical model for the hot-tail population [74] inside the standalone `Fortran` module introduced in paper #1 (see section 3.1). To extract characteristic quantities of the thermal quench required by this hot-tail model, I created appropriate analysis scripts. I adapted the simulation workflow set up for the study presented in paper #1 for the specific requirements of the hot-tail model.

The study presented in this paper was designed and corresponding simulations performed by me from start to finish, covering setup, execution and analysis. Throughout the simulation workflow, I employed the tools I had developed for the study presented in paper #1 and expanded them as necessary. For comparison of simulation results with experimental measurements, I created aforementioned database of 70 ASDEX Upgrade discharges using a self-developed analysis workflow to extract key quantities of interest from experimental signals.

The manuscript of this publication was written by me, covering all sections and appendices. I created all figures included in the paper using simulation and experimental data. For this purpose, I also utilized self-developed scripts for data processing. Submission of the manuscript, as well as correspondence during the peer-review process was handled by me.

The background features several light blue, curved lines that sweep across the page from the left side towards the right, creating a sense of motion and depth. The lines vary in thickness and curvature, with some being more pronounced than others.

Discussion 4

In this dissertation, the generation of runaway electrons following the injection of massive amounts of material in tokamak-type fusion reactors is investigated computationally with the coupled transport codes *ASTRA-TRAHL*. In this context, the first self-consistent transport simulations of simultaneous background plasma evolution, material injection and runaway electron generation are performed in agreement with experimental measurements of an ASDEX Upgrade discharge. The simulations presented cover the entire artificially induced disruption from the onset of material injection up to the end of the current quench. The findings of these studies are reported in two publications by Linder et al [47, 93].

4.1 Material deposition

The scope of the simulations performed constitutes a novel approach for the investigation of runaway electron generation in tokamak plasmas. In particular, the thorough treatment of impurity deposition and propagation in this work is shown to be essential. Key experimental observations in ASDEX Upgrade discharge #33108 such as the increase of the line-averaged electron density and decrease of the plasma current can only be reproduced when accurately modeling the deposition and propagation of impurities. Regarding the generation of runaway electrons, theoretical work [77, 84, 94, 95] emphasizes the high importance of the impact of partially ionized impurities on electron runaway, thus advocating for a thorough treatment of impurities in simulations of runaway electron generation. The simulations presented in this dissertation are able to show that impurity deposition and propagation can be successfully described through one-dimensional transport modeling. Here, the density evolution of neutral impurities deposited just outside the LCFS is explicitly calculated from the macroscopic transport equation under the assumption of inward propagation at the speed of sound. The transport of impurity ions is identified to be caused by neoclassical effects and by rapid redistribution during breakup of the magnetic surfaces due to MHD activity.

Compared to previous studies, the treatment of impurities in this work constitutes a step forward, as the aspect of impurity deposition has been treated only superficially in preceding modeling exercises. Focusing more on simulating the generation of runaway electrons, a common choice for the deposition of impurities is the application of a spatially uniform (neutral) impurity density profile [82, 129]. Alternatively, impurity density profiles shaped as the predisturbance electron density profile and ramped-up exponentially in time have been employed [81]. Impurity density profiles have also been obtained from the condition that impurity radiation balances Ohmic heating during the current quench phase [71]. While motivated by experimental observations of material deposition time scales [81, 129], by the material delivery scheme [129] or by energy conservation [71], the alternative methods described are challenging to apply to scenarios of massive gas injection from a valve throughout the entire disruption.

A promising approach for describing the deposition of material has been presented previously with *ASTRA-TRAHL* by Fable et al [106]. In their work, massive gas injection

was modeled by depositing neutral material outside the LCFS and obtaining the evolution of the neutral impurity density inside the confined plasma from the stationary continuity equation. Applied only during the pre-thermal quench, these simulations demonstrated the suitability of a one-dimensional treatment of impurity deposition in transport simulations by reproducing experimental observations in this phase. As such, the work presented by Fable et al [106] inspired the treatment of neutral impurity deposition within this dissertation. However, by obtaining the impurity density from the stationary continuity equation, the effective propagation velocity of the material has to be analyzed postdisruption. Simulation results obtained are invalid if propagation occurs at velocities exceeding the speed of sound [106]. This issue is resolved in the work presented in this dissertation by calculating the spatio-temporal evolution of the neutral impurity density through the transport equation under the assumption of inward propagation at thermal velocities for impurities deposited by massive gas injection. Following this approach, impurity deposition and the neutral density profile can be calculated throughout the entire disruption.

The neutral particle source employed in this work describes the deposition of material by massive gas injection. The source strength at the valve's nozzle is obtained from a continuity equation for the valve's particle content under the assumption of ideal, isentropic flow in one dimension through a converging nozzle [128]. For simplicity, the source is located just outside the LCFS in the simulations presented. However, a more accurate treatment of neutral impurity deposition can be obtained by explicitly modeling the propagation from the gas valve to the LCFS, as carried out e.g. by the code *IMAGINE* [127]. For this purpose, the simulation domain has to be extended radially up to the location of the valve. Apart from solving coupled transport equations for electron heat, ion heat and the neutral impurity density, continuity equations describing the conservation of the neutral particle momentum and energy are considered by *IMAGINE*. These constraints have also been considered for the derivation of the source strength [128] used in this work. Yet additionally in *IMAGINE*, charge exchange reactions between impurity neutrals and plasma ions are taken into account. The relevance of these processes has recently been highlighted in studies of impurity density measurements at the pedestal in ASDEX Upgrade [130]. Following the approach employed by *IMAGINE*, a more accurate description of the neutral particle source for deposition by massive gas injection can be obtained. A corresponding treatment of impurity deposition could be employed in future work with *ASTRA-STRahl*, e.g. by implementing such a model directly in *STRahl*.

By evolving the population of deposited neutral particles according to the macroscopic transport equation in *ASTRA-STRahl*, deposition schemes other than massive gas injection can also be investigated in this framework. For the ITER tokamak, material deposition by shattered pellet injection is currently planned [17], wherefore this scheme is being investigated in present-day devices [37, 38]. Calculating the ablation rate of the shards injected with external tools, e.g. with the model presented by Bosviel et al [131] and applied by Kim et al [132], the spatio-temporal evolution of the neutral source profile could be prescribed in *STRahl*, thus enabling investigation of shattered pellet injection scenarios with *ASTRA-STRahl* in future work.

4.2 Breakup of magnetic surfaces

In massive gas injection scenarios in ASDEX Upgrade, $(m, n) = (2, 1)$ MHD modes and higher harmonics are excited by strong current density gradients [88, 107] when the inward propagating cold gas front reaches the $q = 2$ surface [106]. As a result, the well confining structure of nested magnetic surfaces is perturbed or replaced by ergodic zones due to fast magnetic reconnection [113]. In this environment, the radial transport of heat and ions is strongly enhanced as particles travel along stochastic magnetic field lines [7]. Eventually, closed magnetic flux surfaces re-emerge [117–119] as MHD modes are stabilized following the relaxation of the current density profile, thus reducing radial transport to typical levels.

The process of breakup and re-emergence of magnetic flux surfaces cannot be modeled in the one-dimensional transport codes `ASTRA-STRahl`, requiring instead treatment by non-linear MHD codes, such as `JOEK` [85–87], `M3D-C1` [114, 115] or `NIMROD` [116]. However, simultaneously, the impact of MHD activity during the thermal quench on the transport of heat and ions cannot be neglected. In self-consistent transport simulations with `ASTRA-STRahl` in the absence of these effects, the loss of thermal energy on sub-ms time scales cannot be reproduced [47]. In other transport studies of runaway electron generation, modeling the impact of MHD activity on the plasma was circumvented e.g. by starting the simulation only after the temperature has collapsed [71] or by assuming an exponential decay of the temperature during the thermal quench [82].

In the work presented in this dissertation, the impact of MHD activity during the thermal quench is taken into account by flattening the current density profile and prescribing additional, transient transport coefficients for heat and particles. In massive gas injection experiments in ASDEX Upgrade or JET, the occurrence of a current spike during the thermal quench suggests the flattening of the current density profile [46, 88]. This process is mimicked inside `ASTRA` by flattening the current density profile under conservation of the total poloidal magnetic flux. This approach, however, is not suitable for additionally reproducing the current spike. Instead, the magnetic helicity is constant throughout the flattening of the current density [113], as observed in recent `JOEK` simulations of massive gas injection in JET [107]. In future work with `ASTRA-STRahl`, this effect has to be taken into account. The increase of the total plasma current during the late phase of the thermal quench is associated with a change of the electric field in the cold plasma. As such, impurity ionization and runaway electron generation might be affected as well under these conditions. Considering the current spike in self-consistent simulations is therefore believed to describe experimental observations more realistically.

The approach of prescribing transient transport coefficients during breakup of magnetic surfaces in `ASTRA-STRahl` is found suitable to induce the loss of plasma stored energy on sub-ms time scales. However, as the corresponding coefficients are not derived from first principles, the required magnitude has to be determined from agreement between simulation and the experiment to be modeled. In the case of heat transport, a maximum transient heat diffusion coefficient of $\chi = 100 \text{ m}^2 \text{ s}^{-1}$ is identified to be sufficient, as

conjectured by Fehér et al [64]. A maximum diffusion coefficient of similar magnitude is used for the transport of particles in this work. The approach chosen to mimic the impact of the breakup of magnetic surfaces on the plasma, as well as the validity of the numerical values used has to be assessed in future work with non-linear MHD codes. In recent JOREK simulations of argon massive gas injection in JET, rapid redistribution of impurity ions in the central plasma following the onset of MHD mode activity was observed [107]. As such, the approach chosen for impurity redistribution within this work is qualitatively supported by more complex modeling. Furthermore, the method employed in this work is observed to cause the loss of plasma stored energy on sub-ms time scales. Hence, with the model of additional, transient transport coefficients, the work presented in this dissertation successfully describes tokamak disruptions from the onset of material injection up to the end of the current quench.

4.3 Agreement with experimental observations

The self-consistent simulations of impurity argon injection in ASDEX Upgrade discharge #33108 presented in this work are shown to reproduce key experimental observations of the discharge modeled. Corresponding simulations have first been reported by Linder et al [47] considering runaway generation due to only the Dreicer mechanism and avalanche multiplication. In follow-up studies taking also hot-tail generation into account [93], agreement between simulation and experiment is still obtained.

The simulations discussed reproduce key experimental observations. Importantly, the strong increase of the line-averaged electron density during the thermal quench is described well (see figure 4.19(a)). Application of additional, transient transport coefficients

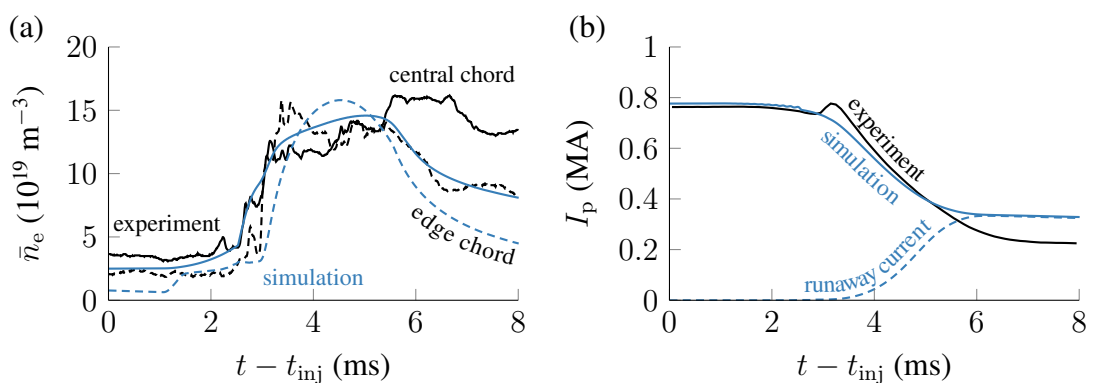


Figure 4.19: Temporal evolution of key quantities in self-consistent ASTRA-STRAHL simulations (blue) of ASDEX Upgrade discharge #33108 throughout the artificial disruption compared to experimental measurements (black), being (a) the line-averaged electron density \bar{n}_e along the central chord (solid) and the high-field-side edge chord (dashed), as well as (b) the plasma current I_p (solid) and the runaway electron current (dashed). The temporal evolution of these quantities is shown starting at the beginning of gas injection at t_{inj} .

was required to mimic the impact of the breakup of magnetic surfaces on the redistribution of heat and particles during the thermal quench. The coefficients employed are set only to an order of magnitude, as the increase of the line-averaged electron density can be reproduced within reasonable bounds under a variation of these coefficients by up to 50%. Furthermore, the comparison of the line-averaged electron density between simulation and experiment is not straight-forward due to the three-dimensional nature of material injection. Following deposition, the gas redistributes toroidally slower than radially, given the different dimensions of toroidal circumference and minor radius. Thus in the presence of plasma rotation, the measured line-averaged electron density can exhibit oscillations. Correspondingly in several discharges, the signal measured along edge or central chord contains pronounced density oscillations with periods in the range of 1.0 ms to 1.5 ms, coinciding with experimental measurements of the plasma rotation period. As such, comparison between simulation and experiment has to be performed with care, aiming at reproducing the general trend of the line-averaged electron density measured. For this additional reason, refinement of the transient transport coefficient prescribed is not reasonable. Yet importantly, the model presented is capable of accurately describing the occurrence of the thermal quench, as supported by the corresponding increase of the line-averaged electron density simulated. Simultaneously, the occurrence of the thermal quench is also successfully inferred from a synthetic soft x-ray signal in comparison with measurements by soft x-ray photo diodes [133] along central lines of sight.

The response of the line-averaged electron density during the other phases of the disruption is also described well by the simulations (see figure 4.19(b)). Following the onset of material injection, the electron density simulated along both chords rises slowly, thus being in agreement with measurements. After occurrence of the thermal quench and the accompanying strong increase of the electron density, simulations predict a continued, but slow rise of the density during the early stage of the current quench, as thermal energy is further introduced through Ohmic heating. Only during the late stage of the current quench, impurities simulated recombine too quickly compared to experimental observations, resulting in reduced electron densities as well as in reduced levels of impurity radiation. As such, the model for impurity transport inside ASTRA-STRAHL requires further refinement in future work to accurately describe the prolonged occurrence of elevated levels the line-averaged electron density. Alternatively, the introduction of loss mechanisms for runaway electrons could resolve this discrepancy, as discussed further below in section 4.4.

The plasma current calculated in self-consistent ASTRA-STRAHL simulations also agrees well with experimental observations. Following the onset of material injection, the total Ohmic current simulated decreases slowly at rates consistent with the experiment. However, as discussed above, the current spike measured experimentally cannot be captured in the simulations, as the current density is flattened at the onset of the thermal quench under conservation of the total poloidal magnetic flux instead of the magnetic helicity. In future ASTRA-STRAHL simulations, corresponding modifications are needed, as described in the previous section 4.2. During the current quench following, the plasma

current obtained in the simulations decays at a similar rate as measured experimentally. Importantly, a current decay rate consistent with experimental observations can be obtained only when accurately describing the increase of the line-averaged electron density during the thermal quench. Across several ASDEX Upgrade discharges, the maximum current decay rate is experimentally observed to increase as larger amounts of impurities are deposited in the confined plasma [46]. Therefore in simulations of ASDEX Upgrade discharge #33108, comparable amounts of impurities are implied to be present in the central plasma as in the experiment performed, resulting in comparable decay rates of the plasma current. The postdisruption runaway current calculated is, however, larger than observed experimentally due to the absence of loss mechanisms for runaway electrons. The topic of runaway electron generation is discussed in more detail in section 4.4.

Despite the good agreement between simulation and experiment regarding the evolution of the line-averaged electron density and the plasma current, the comparison of simulation results with further experimental measurements between the onset of material injection and the end of the current quench is challenging, given the limited number and temporal resolution of available measurements. Problematically, tokamak disruptions rapidly change plasma conditions on sub-ms time scales, thus being too fast for plasma diagnostics designed to operate during steady-state core plasma operation. Yet, the experimental data available imply good agreement between self-consistent ASTRA-STRAHL simulations of argon massive gas injection in ASDEX Upgrade discharge #33108 and experimental observations.

Similar transport studies as the ones presented in this dissertation, comparing simulations of massive material injection and experiment, have not been carried out before. As mentioned above, previous work with ASTRA-STRAHL studied only the pre-thermal quench in ASDEX Upgrade [106]. Other studies, however, focused predominantly on the aspect of runaway electron generation in the framework of one-dimensional transport modeling, simplifying experimental aspects in the process, such as e.g. material deposition or the loss of plasma stored thermal energy. Still, tools like GO [81] proved capable of correctly calculating the plasma current evolution for JET discharges. Given the threat of runaway electrons for future high-current devices, several studies have investigated runaway electron generation in ITER following massive material injection in the framework of transport modeling [71, 82]. However, as the ITER tokamak is not operational yet, comparison of simulations with experimental results is not possible.

Using non-linear MHD codes, recent JOREK simulations of argon massive gas injection in JET pulse 85943 up to the thermal quench phase were able to match the evolution of the plasma current (including the occurrence of the current spike) and qualitatively reproduce the measured impurity radiation [107]. These results are a promising step towards JOREK simulations covering the entire disruption from material injection up to established runaway electron beam, but simultaneously demonstrate that this endeavor is challenging. Simulations of massive gas injection were also performed by the MHD code NIMROD with a focus on the toroidal redistribution of material in DIII-D to achieve uniform impurity radiation [134, 135]. Earlier NIMROD simulations were able to repro-

duce experimental aspects of massive gas injection in Alcator C-Mod and DIII-D [136]. However, it should be noted that MHD simulations are computationally expensive, taking weeks or months on HPC systems until completion instead of hours or days on a single core as in the case of the transport codes ASTRA–STRAHL.

In the light of the modeling efforts carried out using other (transport) tools, the model presented in this dissertation for self-consistent simulations with the toolkit ASTRA–STRAHL constitutes a major step forward, being validated against experimental observations and thus drastically improving the modeling capabilities of massive gas injection scenarios.

4.4 Investigation of electron runaway

In self-consistent simulations of artificial disruptions in ASDEX Upgrade with the coupled-transport codes ASTRA–STRAHL, the generation of runaway electrons is studied in response to the injection of massive amounts of material. The capabilities of the model presented are demonstrated by Linder et al (2020) [47] considering runaway generation due to the Dreicer mechanism and avalanche multiplication. In subsequent studies by Linder et al (2021) [93], electron runaway due to the hot-tail mechanism [74] is additionally taken into account and further investigations are carried out. Since the hot-tail mechanism is found to contribute only a small population of seed runaway electrons, the findings of the previous work are not challenged. As such, the discussion of runaway electron generation in the following is based on the results presented by Linder et al (2021) [93].

The simulations presented are shown to be capable of describing runaway dynamics in agreement with experimental observations (see figure 4.19(b)), resulting in the generation of a pronounced runaway electron beam of several hundred kA at the end of the disruption. The dynamics of runaway generation is strongly influenced by details of material deposition and propagation. During the initial phase of injection, a small seed population of runaway electrons is created by the Dreicer mechanism in the vicinity of the cold gas front propagating inwards. As the Ohmic current diffuses to regions of still hot plasma, a growing current density sheet forms in front of the cold gas cloud. The strong electric fields of up to 5% E_D induced in the process facilitate the generation of runaway electrons due to the Dreicer mechanism (cf. section 2.1.3) outside the $q = 2$ during the pre-thermal quench (see figure 4.20). Upon reaching the $q = 2$ surface, the interior current density profile is flattened, resulting in electric fields of only around 3% E_D and thus terminating favorable conditions for Dreicer runaway generation. In the presence of the rapid, radiation induced temperature decay, runaway electrons are created by the hot-tail mechanism and to reduced extent by the Dreicer mechanism inside the $q = 2$ surface (see figure 4.20). Up to the end of the thermal quench, comparable amounts of primary runaway electrons in the order of a few kA are generated by the two mechanisms. The small seed of runaway electrons is amplified during the decay of the residual Ohmic current by avalanche multiplication. Throughout the current quench, the growing population of runaway electrons

progressively reduces the electric field induced by removing poloidal magnetic flux [113]. Through this negative feedback on the evolution of the poloidal magnetic flux (see also equation (2.49)), the disruption is eventually terminated and a runaway electron current of several hundred kA is established (see figure 4.20).

The runaway current generated in ASDEX Upgrade disruptions is calculated to be dominated by avalanche generated runaway electrons with primary mechanisms providing only a small seed population (see figure 4.20). Similar observations have recently been made for ASDEX Upgrade by means of kinetic modeling with the full- f solver CODE [101]. In their work, the postdisruption runaway current obtained is created predominantly by avalanche multiplication of a small seed population of hot-tail runaway electrons. The contribution from the Dreicer mechanism is calculated to be negligible, in contrast to the findings of the work presented in this dissertation. In ASTRA-STRAHL simulations, Dreicer runaway generation is observed to be related to the one-dimensional, inward propagation of the material injected. The CODE simulations mentioned, however, performed calculations of runaway electron generation in zero dimensions in position space, prescribing on-axis values of plasma quantities throughout the simulation to represent plasma conditions on the magnetic axis. As such, the one-dimensional effect of inward material propagation cannot be described with this approach, explaining the differences in Dreicer contributed runaway electron seed population. Even though the treatment of the electron population in kinetic tools considering two dimensions in momentum space is generally superior to the application of reduced kinetic models in a transport framework, an accurate treatment of the one-dimensional position space evolution of background plasma quantities is also important for the generation of runaway electrons. However, as the Dreicer generated runaway population is small in the case of ASDEX Upgrade discharge #33108, overall differences in the postdisruption runaway

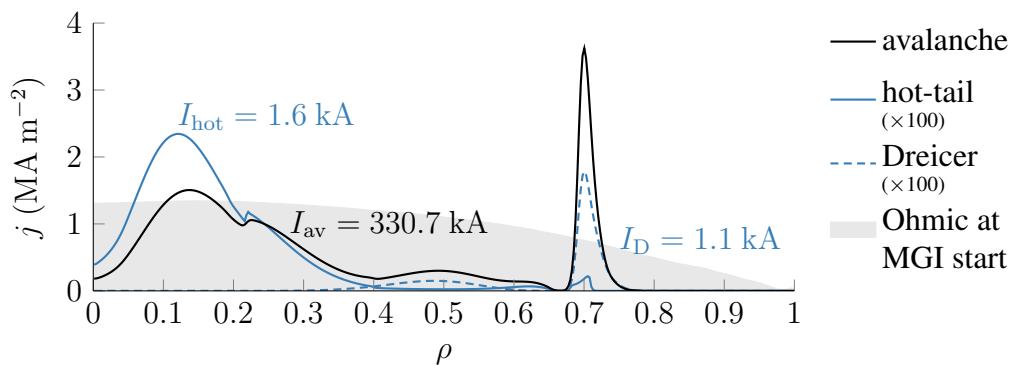


Figure 4.20: Radial profiles of the runaway electron current densities j at the end of the current quench in self-consistent ASTRA-STRAHL simulations of ASDEX Upgrade discharge #33108, generated by avalanche multiplication (solid black), the hot-tail mechanism (solid blue) and the Dreicer mechanism (dashed blue). For comparison, the Ohmic current density profile at the start of massive gas injection (MGI) is shown (filled gray). Note, that the current density profiles of the primary runaway electron populations are scaled by a factor of $\times 100$ for easier comparison.

electron current between kinetic tools and a transport modeling approach are small. This is also related to finite amounts of poloidal magnetic flux available for the generation of runaway electrons and their negative feedback on the evolution of the poloidal magnetic flux, as discussed above. As such, self-consistent simulations using reduced kinetic models can provide valuable insights into runaway electron dynamics.

An important effect still to be considered in `ASTRA-STRAHL` simulations is the loss of runaway electrons by magnetic fluctuations, especially during breakup of the magnetic surfaces. Corresponding effects have not been considered in this work for now. As such, the postdisruption runaway current calculated is consistently larger than observed experimentally in the ASDEX Upgrade reference discharge #33108, being in the order of 330 kA instead of 220 kA (see figure 4.19(b)). However, it should be noted that postdisruption runaway beams in excess of 300 kA have also been observed experimentally for target plasmas similar to #33108 (see e.g. figure 9 of Linder et al (2021) [93]), with the highest runaway current exceeding 400 kA. Still, consideration of runaway losses could improve agreement between simulation and experimental observations. For this purpose, the impact of magnetic perturbations on runaway could be taken into account in future work to describe losses and radial transport of runaway electrons [110, 137]. In the code `GO`, the runaway electron current obtained in simulations of JET [81] and ITER [137] can be greatly reduced in the presence of magnetic fluctuations.

Consideration of runaway electron losses would not only improve the description of the runaway electron population with respect to experimental observations, but could also resolve discrepancies observed between the simulated line-averaged electron density response and experimental measurements. In the simulations performed, the electron density starts to decrease again too early into the current quench. This might be, in parts, caused by the presence of a too small Ohmic current density, resulting in insufficient amounts of Ohmic heating and thus impurity ionization. In the presence of runaway electron losses, however, a larger Ohmic current would persist for a longer period, thus also prolonging the occurrence of high line-averaged electron densities. As such, consideration of runaway electron loss mechanisms is presumed to increase overall agreement between simulations and experiments for multiple quantities.

The model presented can also be applied to study the impact of non-fully ionized impurities on electron runaway. In recent theoretical work [77, 84, 94, 95], the presence of partially ionized impurities is identified to affect electron runaway by increasing electron-ion friction, but also by increasing the amount of target electrons for avalanche multiplication. These effects are, however, not taken properly into account in classical formulae describing Dreicer generation [62] and avalanche multiplication [76], considering only the total density of electrons. In `GO` simulations of JET-like [84] and ITER cases [77], consideration of these effects produces runaway electron currents differing (significantly) from classical estimates. Especially the avalanche multiplication factor [77] is greatly enhanced in the presence of partially ionized impurities. In self-consistent simulations, however, the situation might be different, given the feedback of the runaway current on the poloidal magnetic flux, the electric field, Ohmic heating and thus impurity ioniza-


tion. Still, performing ASTRA–STRAHL simulations using either state-of-the-art runaway generation models [77, 84] or their classical counterparts [62, 76], the main findings of the respective publications describing the impact of partially ionized impurities [77, 84] are reproduced. The strength of the Dreicer mechanism is considerably reduced, while avalanche multiplication is enhanced when taking the impact of non-fully ionized impurities into account. Combining these effects, similar postdisruption runaway currents are obtained in each ASTRA–STRAHL simulation due to the negative feedback of the runaway current on the evolution of the poloidal magnetic flux. As such, these simulations imply at first that the impact of partially ionized impurities on electron runaway is in total not important in self-consistent simulations. However, the dynamics of electron runaway in the absence of these effects is inconsistent with other experimental observations such as hard x-ray measurements. As such, self-consistent simulations of background plasma evolution, material injection and runaway electron generation emphasize the importance of the impact of partially ionized impurities on electron runaway.

Finally, using ASDEX Upgrade scenarios similar to discharge #33108, the impact of a variation of the predisruption core electron temperature on electron runaway is investigated with ASTRA–STRAHL. For central temperatures below 9 keV, the postdisruption runaway current obtained responds only weakly to a variation of the temperature. Experimentally, a similar trend is observed. At higher temperatures, simulations predict a noticeable increase of the hot-tail runaway population and consequently of the postdisruption runaway current. Experimentally, however, runaway beams can be produced less reliably and only at reduced runaway currents in this temperature region. As such, the runaway electron seed appears to be subjected to greatly enhanced losses above a certain temperature threshold.

The difficulty of reliably generating runaway beams in scenarios with predisruption core temperatures above 9 keV appears to be a phenomenon restricted to ASDEX Upgrade. In the DIII-D tokamak, an increase of the runaway current generated is observed for increasing predisruption temperatures in scenarios of argon pellet injection [138]. In complementary kinetic simulations, an increase of the hot-tail runaway seed is obtained under these conditions, in agreement with experimental observations, as higher temperatures accelerate pellet ablation and thus the thermal quench [138]. As ASTRA–STRAHL simulations similarly predict an increase of the hot-tail runaway current for increasing temperatures, the runaway generation models employed appear to correctly describe the expected runaway electron response. Therefore, discrepancies between simulation and ASDEX Upgrade experiments point towards additional phenomena at play, such as the complete loss of the runaway seed. As these effects are likely related to MHD activity, these phenomena cannot easily be modeled inside ASTRA–STRAHL, requiring non-linear MHD codes such as JOREK instead. However, considering runaway loss mechanisms discussed above within ASTRA–STRAHL could still shed light onto runaway electron loss under these conditions.

In other computational studies investigating the generation of runaway electrons at varying temperatures [129], it was observed that the runaway population generated de-

creases above a threshold temperature of around 5 keV, in contrast to the findings of the work presented in this dissertation. The decrease of the hot-tail current calculated [129] can be related to the decrease of impurity radiation at higher temperatures under the assumption of a steady-state distribution of impurity charge states. Under these conditions, the time scale of the temperature decay is increased, therefore reducing the hot-tail runaway population. However, as shown by Linder et al (2020) [47], the impurity charge state distribution during a disruption is not adequately described by a steady-state distribution. As such, accurate modeling of individual impurity charge states is found relevant also for the study of scenarios with varying pre-disruption electron temperature in self-consistent transport simulations.



5 Summary & conclusion

The generation of a large population of relativistic runaway electrons following the sudden loss of plasma stored energy in future high-current fusion reactors poses a serious threat for the structural integrity of these devices. Yet through injection of massive amounts of material, runaway electron generation can be hindered. In this dissertation, I presented a computational toolkit based on the coupled 1.5D transport codes ASTRA-STRAHL [80, 92] to investigate electron runaway in response to massive material injection by means of self-consistent simulations of background plasma evolution, material injection and runaway electron generation. The findings of this work are reported in two publications by Linder et al [47, 93].

To enable self-consistent simulations, the ASTRA flexible programming system was used for the development of a computational model, referred to in the following as ASTRA-STRAHL [47, 80, 92]. The spatio-temporal evolution of plasma temperatures and poloidal magnetic flux is calculated inside ASTRA, while impurities are treated inside the impurity radiation code STRAHL [92] under consideration of electron-impact ionization and recombination. I amended the tool STRAHL in the process to allow for the treatment of neutral particles, as required for simulations of massive material injection. Furthermore, I changed the STRAHL numerical scheme to a finite volume scheme with adaptive upwinding to ensure conservation of particles and to remove numerical artifacts in simulations of advection dominated transport. Within ASTRA, I chose to describe runaway electron generation by state-of-the-art reduced-kinetic models under consideration of the impact of partially ionized impurities on electron runaway [77, 84, 94, 95]. To assess the importance of these effects in self-consistent simulations, classical analytical formulae [62, 76] are applied alternatively in ASTRA. I implemented the models describing runaway electron generation in a standalone Fortran module publicly available at <https://github.com/o-linder/runawayelectrongeneration>.

I successfully applied the toolkit developed in self-consistent simulations of argon massive gas injection in the representative ASDEX Upgrade discharge #33108. The simulations of background plasma evolution, material injection and runaway electron generation reproduce key experimental observations, such as increase of the line-averaged electron density during the thermal quench or the decay of the plasma current during the current quench. As such, I presented the very first transport simulations correctly describing the distinct phases of the artificially induced disruption, being pre-thermal quench, thermal quench and current quench. Consequently, the approach of applying a 1.5D transport framework to model the inherently three dimensional process of massive gas injection is demonstrated to be suitable to capture experimental trends, presumably due to flux surface averaged treatment and fast equilibration along magnetic field lines.

Throughout the simulations presented, an accurate treatment of material deposition and propagation was identified to be crucial to describe experimental measurements. The inward propagation of neutral material at the speed of sound during the pre-thermal quench results in the formation of a substantial current sheet and consequently in electron runaway. These phenomena cannot be described using zero dimensional modeling. As the cold gas reaches the $q = 2$ rational flux surface, $(m, n) = (2, 1)$ MHD modes and higher

harmonics are excited, enhancing the radial transport of heat and ionized material in the process. Only when describing this effect through the application of additional, transient impurity transport coefficients, the plasma stored thermal energy is lost in the simulations on experimental sub-ms time scales. Under these conditions, the rapid increase of line-averaged electron density and impurity radiation during the thermal quench is successfully described by the simulations. During the subsequent decay of the residual Ohmic current, neoclassical transport processes were identified to also contribute noticeably to impurity transport. Throughout the simulations, individual impurity charge states have to be evolved explicitly through rate equations, as a steady-state charge state distribution was observed in postsimulation analysis to overpredict impurity ionization and recombination during thermal quench and current quench, respectively. Through this thorough treatment of material deposition and propagation, 1.5D transport simulations successfully describe experimental observations.

The generation of runaway electrons in ASDEX Upgrade discharge #33108 was identified to be dominated by avalanche multiplication of a small seed population of runaway electrons. Generation due to the Dreicer mechanism occurs predominantly outside the $q = 2$ flux surface during the pre-thermal quench phase, as the neutral material injected pushes a substantial Ohmic current density sheet inwards. With the plasma stored thermal energy lost on sub-ms time scales, runaway electrons are generated by the hot-tail mechanism in the central plasma, mostly around a radial position of $\rho = 0.12$. On-axis impurity accumulation prevents formation of a hot-tail population centered around the magnetic axis, as identified through evaluation of the simple expression (2.33) I derived to estimate the postquench hot-tail runaway density. Based on the hot-tail generation model by Smith & Verwichte [74], I also derived expression (2.37) to generalize an important parameter of their model to allow evaluation of the hot-tail density without prior knowledge of postquench plasma parameters. The validity of this approach will have to be assessed with kinetic modeling in future work. In the simulations performed, both primary generation mechanisms provide only a small seed runaway electron population of a few kA. During the current quench, avalanche multiplication results in the formation of a substantial postdisruption runaway electron current, being in the order of experimental measurements.

Importantly, the self-consistent simulations presented can only reproduce experimental observations of runaway electron generation under consideration of the impact of partially ionized impurities on electron runaway. Neglecting these effects, significant generation occurs too early into the disruption, while avalanche multiplication is noticeably reduced. Although both approaches yield a comparable postdisruption runaway electron current, only simulations using state-of-the-art runaway electron generation models are consistent with experimental observations.

In simulations of ASDEX Upgrade scenarios with varying core temperature, the post-disruption runaway current is observed to be insensitive to a variation of the temperature below central temperatures of around 9 keV, thus reproducing experimental trends. However, as runaway losses are not considered in this work, the postdisruption current calcu-

lated is consistently larger than in the experiment. For predischruption temperatures beyond 9 keV, an increase of the runaway current is predicted, while runaway beams are only rarely generated experimentally in this temperature range. This discrepancy suggests the complete loss of the seed population during the thermal quench, requiring further investigation with non-linear MHD codes.

Throughout this work, runaway electron radial transport and loss mechanisms [110, 137], e.g. due to magnetic fluctuations, have not been taken into account and will therefore have to be considered in light of the discrepancies discussed above in future work. Furthermore, the current density is to be flattened at the onset of the thermal quench under conservation of the magnetic helicity in order to reproduce the current spike seen in experiments of massive gas injection. Consideration of these effects for runaway electron generation in ASTRA-STRAHL is expected to further improve agreement between simulations and experiment, thus enabling predictive simulation for future devices. For this purpose, models for material deposition by shattered pellet injection could be implemented in ASTRA-STRAHL to assess the efficacy of different delivery schemes.

Given the success of ASTRA-STRAHL in reproducing experimental observations in massive gas injection scenarios, the thorough treatment of background plasma evolution, material injection and runaway electron generation has by now inspired other tools to apply similar methods as employed by ASTRA-STRAHL, for example the European transport solver within the European framework for integrated modeling [139–141] or the tool DREAM [142] currently under development. As such, the approach presented in this work constitutes a significant step forward for self-consistent simulations of runaway electron generation in massive material injection scenarios.

Bibliography

- [1] A. S. Eddington. The internal structure of the stars. *Science* **52**, 233 (1920).
- [2] C. F. v. Weizsäcker. Zur Theorie der Kernmassen. *Z. Phys.* **96**, 431 (1935).
- [3] H. A. Bethe. Energy production in stars. *Phys. Rev.* **55**, 434 (1939).
- [4] E.G. Adelberger, A. Garcia, R.G. Hamish Robertson, K.A. Snover, A.B. Balantekin, K. Heeger, M.J. Ramsey-Musolf, D. Bemmerer, A. Junghans, C.A. Bertulani et al. Solar fusion cross sections. II. The pp chain and CNO cycles. *Rev. Mod. Phys.* **83**, 195 (2011).
- [5] S. Basu, W.J. Chaplin, Y. Elsworth, R. New and A.D. Serenelli. Fresh insights on the structure of the solar core. *Astrophys. J.* **699**, 1403 (2009).
- [6] H.-S. Bosch and G.M. Hale. Improved formulas for fusion cross-sections and thermal reactivities. *Nucl. Fusion* **32**, 611 (1992).
- [7] J. Freidberg. *Plasma Physics and Fusion Energy*. Cambridge University Press, Cambridge, 1st edition, 2007.
- [8] P.K. Kaw and I. Bandyopadhyay. The Case for Fusion. In M. Kikuchi, K. Lackner and M.Q. Tran, *Fusion Physics*. International Atomic Energy Agency, Vienna, 2012.
- [9] W.M. Nevins and R. Swain. The thermonuclear fusion rate coefficient for p-¹¹B reactions. *Nucl. Fusion* **40**, 865 (2000).
- [10] C.M. Braams and P.E. Stott. *Nuclear Fusion: Half a Century of Magnetic Confinement Fusion Research*. Institute of Physics Publishing, Bristol, 2002.
- [11] V.D. Shafranov. The initial period in the history of nuclear fusion research at the Kurchatov Institute. *Phys.-Uspekhi* **44**, 835 (2001).
- [12] J. Wesson. *Tokamaks*. Oxford University Press, Oxford, 3rd edition, 2004.
- [13] A. Bock, E. Fable, R. Fischer, M. Reich, D. Rittich, J. Stober, M. Bernert, A. Burckhart, H. Doerk, M. Dunne et al. Non-inductive improved H-mode operation at ASDEX Upgrade. *Nucl. Fusion* **57**, 126041 (2017).
- [14] T. Sunn Pedersen, A. Dinklage, Y. Turkin, R. Wolf, S. Bozhenkov, J. Geiger, G. Fuchert, H.-S. Bosch, K. Rahbarnia, H. Thomsen et al. Key results from the first plasma operation phase and outlook for future performance in Wendelstein 7-X. *Phys. Plasmas* **24**, 055503 (2017).

- [15] A. Kallenbach for the ASDEX Upgrade Team and the EUROfusion MST1 Team. Overview of ASDEX Upgrade results. *Nucl. Fusion* **57**, 102015 (2015).
- [16] H. Meyer for the AUG Team: D. Aguiam, C. Angioni, C.G. Albert, N. Arden, R. Arredondo Parra, O. Asunta, M. de Baar, M. Balden, V. Bandaru, K. Behler et al. Overview of physics studies on ASDEX Upgrade. *Nucl. Fusion* **59**, 112014 (2019).
- [17] ITER Organization. *ITER Research Plan within the Staged Approach*. Number ITR-18-003. ITER Organization, September 2018.
- [18] L. Spitzer Jr. The stellarator concept. *Phys. Fluids* **1**, 253 (1958).
- [19] A. Dinklage, C.D. Beidler, P. Helander, G. Fuchert, H. Maaßberg, K. Rahbarnia, T. Sunn Pedersen, Y. Turkin, R.C. Wolf, A. Alonso et al. Magnetic configuration effects on the Wendelstein 7-X stellarator. *Nat. Phys.* **14**, 855 (2018).
- [20] H. Zohm. Assessment of DEMO challenges in technology and physics. *Fusion Eng. Des.* **88**, 428 (2013).
- [21] F. Warmer, V. Bykov, M. Drevlak, A. Häußler, U. Fischer, T. Stange, C.D. Beidler, R.C. Wolf and the W7-X Team. From W7-X to a HELIAS fusion power plant: On engineering considerations for next-step stellarator devices. *Fusion Eng. Des.* **123**, 47 (2017).
- [22] EUROfusion. *European Research Roadmap to the Realisation of Fusion Energy*. EUROfusion, September 2018.
- [23] R. Betti and O.A. Hurricane. Inertial-confinement fusion with lasers. *Nat. Phys.* **12**, 435 (2016).
- [24] ITER Physics Basis Editors, ITER Physics Expert Group Chairs and Co-Chairs and ITER Joint Central Team and Physics Integration Unit. Chapter 1: Overview and summary. *Nucl. Fusion* **39**, 2137 (1999).
- [25] R. Aymar, P. Barabaschi and Y. Shimomura (for the ITER Team). The ITER design. *Plasma Phys. Control. Fusion* **44**, 519 (2002).
- [26] M. Lehnen. Loads due to disruptions and prospects for mitigation. Contribution at the 6th IAEA DEMO Programme Workshop, Moscow, Russian Federation, 1.-4.10.2019.
- [27] A.H. Boozer. Magnetic surface loss and electron runaway. *Plasma Phys. Control. Fusion* **61**, 024002 (2019).
- [28] ITER Physics Expert Group on Disruptions, Plasma Control, and MHD and ITER Physics Basis Editors. Chapter 3: MHD stability, operational limits and disruptions. *Nucl. Fusion* **39**, 2251 (1999).
- [29] T.C. Hender, J.C. Wesley, J. Bialek, A. Bondeson, A.H. Boozer, R.J. Buttery, A. Garofalo, T.P. Goodman, R.S. Granetz, Y. Gribov et al. Chapter 3: MHD stability, operational limits and disruptions. *Nucl. Fusion* **47**, S128 (2007).

-
- [30] G.F. Matthews, B. Bazylev, A. Baron-Wiechec, J. Coenen, K. Heinola, V. Kiptily, H. Maier, C. Reux, V. Riccardo, F. Rimini et al. Melt damage to the JET ITER-like Wall and divertor. *Phys. Scr.* **T167**, 014070 (2016).
- [31] R.A. Tinguely, R.S. Granetz, M. Hoppe and O. Embréus. Measurements of runaway electron synchrotron spectra at high magnetic fields in Alcator C-Mod. *Nucl. Fusion* **58**, 076019 (2018).
- [32] M. Lehnen, K. Aleynikova, P.B. Aleynikov, D.J. Campbell, P. Drewelow, N.W. Eidietis, Yu. Gasparyan, R.S. Granetz, Y. Gribov, N. Hartmann et al. Disruptions in ITER and strategies for their control and mitigation. *J. Nucl. Mater.* **463**, 39 (2015).
- [33] C.M. Greenfield, R. Nazikian, M.S. Foster, J. Canik, J. Hughes, W. Solomon, M.E. Fenstermacher, O. Schmitz, L. Baylor and G. Jackson. *Fusion Energy Sciences Workshop on Transients in Tokamak Plasmas: Report on Scientific Challenges and Research Opportunities in Transient Research*. U.S. Department of Energy Office of Fusion Energy Sciences, 2015.
- [34] L.R. Baylor, S.J. Meitner, T.E. Gebhart, J.B.O. Caughman, J.L. Herfindal, D. Shiraki and D.L. Youchison. Shattered pellet injection technology design and characterization for disruption mitigation experiments. *Nucl. Fusion* **59**, 066008 (2019).
- [35] N. Commaux, L.R. Baylor, T.C. Jernigan, E.M. Hollmann, P.B. Parks, D.A. Humphreys, J.C. Wesley and J.H. Yu. Demonstration of rapid shutdown using large shattered deuterium pellet injection in DIII-D. *Nucl. Fusion* **50**, 112001 (2010).
- [36] N. Commaux, L.R. Baylor, S.K. Combs, N.W. Eidietis, T.E. Evans, C.R. Foust, E.M. Hollmann, D.A. Humphreys, V.A. Izzo, A.N. James et al. Novel rapid shutdown strategies for runaway electron suppression in DIII-D. *Nucl. Fusion* **51**, 103001 (2011).
- [37] C. Reux, C. Paz-Soldan, P. Aleynikov, V. Bandaru, O. Ficker, S. Silburn, M. Hoelzl, S. Jachmich, N. Eidietis, M. Lehnen et al. Demonstration of safe termination of megaampere relativistic electron beams in tokamaks. *Phys. Rev. Lett.* **126**, 175001 (2021).
- [38] G. Papp, M. Dibon, A. Herrmann, M. Bernert, T. Eberl, T. Lunt, G. Pautasso, M. Hoelzl, W. Zeidner, V. Rohde et al. ASDEX Upgrade SPI: design, status and plans. Contribution at the IAEA (Virtual) Technical Meeting on Plasma Disruptions and their Mitigation, Saint-Paul-lez-Durance, France, 20.-23.07.2020.
- [39] G. Pautasso, K. Büchl, J.C. Fuchs, O. Gruber, A. Herrmann, K. Lackner, P.T. Lang, K.F. Mast, M. Ulrich, H. Zohm et al. Use of impurity pellets to control energy dissipation during disruption. *Nucl. Fusion* **36**, 1291 (1996).
- [40] R. Yoshino, T. Kondoh, Y. Neyatani, K. Itami, Y. Kawano and N. Isei. Fast plasma shutdown by killer pellet injection in JT-60U with reduced heat flux on the divertor

- plate and avoiding runaway electron generation. *Plasma Phys. Control. Fusion* **39**, 313 (1997).
- [41] P.L. Taylor, A.G. Kellman, T.E. Evans, D.S. Gray, D.A. Humphreys, A.W. Hyatt, T.C. Jernigan, R.L. Lee, J.A. Leuer, S.C. Luckhardt et al. Disruption mitigation studies in DIII-D. *Phys. Plasmas* **6**, 1872 (1999).
- [42] V.M. Timokhin, V.Yu. Sergeev and B.V. Kuteev. Study of discharge quenching in the T-10 tokamak by injecting high- z impurity pellets. *Plasma Phys. Rep.* **27**, 181 (2001).
- [43] G. Pautasso, C.J. Fuchs, O. Gruber, C.F. Maggi, M. Maraschek, T. Pütterich, V. Rohde, C. Wittmann, E. Wolfrum, P. Cierpka et al. Plasma shut-down with fast impurity puff on ASDEX Upgrade. *Nucl. Fusion* **47**, 900 (2007).
- [44] G. Pautasso, A. Mlynek, M. Bernert, K. Mank, A. Herrmann, R. Dux, H.W. Müller, A. Scarabosio, M. Sertoli and the ASDEX Upgrade Team. Assimilation of impurities during massive gas injection in ASDEX Upgrade. *Nucl. Fusion* **55**, 033015 (2015).
- [45] G. Pautasso, M. Bernert, M. Dibon, B. Duval, R. Dux, E. Fable, J.C. Fuchs, G.D. Conway, L. Giannone, A. Gude et al. Disruption mitigation by injection of small quantities of noble gas in ASDEX Upgrade. *Plasma Phys. Control. Fusion* **59**, 014046 (2017).
- [46] G. Pautasso, M. Dibon, M. Dunne, R. Dux, E. Fable, P. Lang, O. Linder, A. Mlynek, G. Papp, M. Bernert et al. Generation and dissipation of runaway electrons in ASDEX Upgrade experiments. *Nucl. Fusion* **60**, 086011 (2020).
- [47] O. Linder, E. Fable, F. Jenko, G. Papp, G. Pautasso, the ASDEX Upgrade team and the EUROfusion MST team. Self-consistent modeling of runaway electron generation in massive gas injection scenarios in ASDEX Upgrade. *Nucl. Fusion* **60**, 096031 (2020).
- [48] D.G. Whyte, T.C. Jernigan, D.A. Humphreys, A.W. Hyatt, C.J. Lasnier, P.B. Parks, T.E. Evans, P.L. Taylor, A.G. Kellman, D.S. Gray et al. Disruption mitigation with high-pressure noble gas injection. *J. Nucl. Mater.* **313-316**, 1239 (2003).
- [49] E.M. Hollmann, T.C. Jernigan, M. Groth, D.G. Whyte, D.S. Gray, M.E. Austin, B.D. Bray, D.P. Brennan, N.H. Brooks, T.E. Evans et al. Measurements of impurity and heat dynamics during noble gas jet-initiated fast plasma shutdown for disruption mitigation in DIII-D. *Nucl. Fusion* **45**, 1046 (2005).
- [50] M. Bakhtiari, Y. Kawano, H. Tamai, Y. Miura, R. Yoshino and Y. Nishida. Fast plasma shutdown scenarios in the JT-60U tokamak using intense mixed gas puffing. *Nucl. Fusion* **42**, 1197 (2002).
- [51] S. Coda, M. Agostini, R. Albanese, S. Alberti, E. Alessi, S. Allan, J. Allcock, R. Ambrosino, H. Anand, Y. Andrébe et al. Physics research on the TCV tokamak

- facility: from conventional to alternative scenarios and beyond. *Nucl. Fusion* **59**, 112023 (2019).
- [52] K.H. Finken, G. Manka, A. Krämer-Flecken and R. Jaspers. Mitigation of disruptions by fast helium gas puffs. *Nucl. Fusion* **41**, 1651 (2001).
- [53] M. Lehnen, P. Aleynikov, B. Bazylev, D.J. Campbell, S. Carpentier-Chouchana, P.C. de Vries, F. Escourbiac, Y. Gribov, G.T.A. Huijsmans, R. Khayrutdinov et al. Plasma disruption management in ITER. Contribution at the 26th IAEA Fusion Energy Conf., Kyoto, Japan, 17.-22.10.2016, EX/P6-39.
- [54] B.N. Breizman, P. Aleynikov, E.M. Hollmann and M. Lehnen. Physics of runaway electrons in tokamaks. *Nucl. Fusion* **59**, 083001 (2019).
- [55] O. Embréus. *Kinetic modelling of runaways in plasma*. PhD thesis, Chalmers University of Technology, January 2019.
- [56] J.R. Martín-Solís, A. Loarte, E.M. Hollmann, B. Esposito, V. Riccardo, FTU Team, DIII-D Team and JET EFDA Contributors. Inter-machine comparison of the termination phase and energy conversion in tokamak disruptions with runaway current plateau formation and implications for ITER. *Nucl. Fusion* **54**, 083027 (2014).
- [57] C.T.R. Wilson. The acceleration of β -particles in strong electric fields such as those of thunderstorms. *Math. Proc. Camb. Philos. Soc.* **22**, 534 (1925).
- [58] A.V. Gurevich, G.M. Milikh and R. Roussel-Dupre. Runaway electron mechanism of air breakdown and preconditioning during a thunderstorm. *Phys. Lett. A* **165**, 463 (1992).
- [59] J. Kuijpers, P. van der Post and C. Slottje. Runaway acceleration in a radio flare. *Astron. Astrophys.* **103**, 331 (1981).
- [60] J. Decker, E. Hirvijoki, O. Embréus, Y. Peysson, A. Stahl, I. Pusztai and T. Fülöp. Numerical characterization of bump formation in the runaway electron tail. *Plasma Phys. Control. Fusion* **58**, 025016 (2016).
- [61] B. Coppi, F. Pegoraro, R. Pozzoli and G. Rewoldt. Slide-away distributions and relevant collective modes in high-temperature plasmas. *Nucl. Fusion* **16**, 309 (1976).
- [62] J.W. Connor and R.J. Hastie. Relativistic limitations of runaway electrons. *Nucl. Fusion* **15**, 415 (1975).
- [63] A. Stahl, M. Landremann, O. Embréus and T. Fülöp. Norse: A solver for the relativistic non-linear FokkerPlanck equation for electrons in a homogeneous plasma. *Comput. Phys. Commun.* **212**, 269 (2017).
- [64] T. Fehér, H.M. Smith, T. Fülöp and K. Gál. Simulation of runaway electron generation during plasma shutdown by impurity injection in ITER. *Plasma Phys. Control. Fusion* **53**, 035014 (2011).

- [65] R. Jaspers, K.H. Finken, G. Mank, F. Hoenen, J.A. Boedo, N.J. Lopes Cardozo and F.C. Schüller. Experimental investigation of runaway electron generation in TEXTOR. *Nucl. Fusion* **33**, 1775 (1993).
- [66] C. Paz-Soldan, N.W. Eidietis, R. Granetz, E.M. Hollmann, R.A. Moyer, J.C. Wesley, J. Zhang, M.E. Austin, N.A. Crocker, A. Wingen et al. Growth and decay of runaway electrons above the critical electric field under quiescent conditions. *Phys. Plasmas* **21**, 022514 (2014).
- [67] B. Esposito, L. Boncagni, P. Buratti, D. Carnevale, F. Causa, M. Gospodarczyk, JR Martin-Solis, Z. Popovic, M. Agostini, G. Apruzzese et al. Runaway electron generation and control. *Plasma Phys. Control. Fusion* **59**, 014044 (2017).
- [68] S. Coda, J. Ahn, R. Albanese, S. Alberti, E. Alessi, S. Allan, H. Anand, G. Anastassiou, Y. Andrébe, C. Angioni et al. Overview of the TCV tokamak program: scientific progress and facility upgrades. *Nucl. Fusion* **57**, 102011 (2017).
- [69] H. Dreicer. Electron and ion runaway in a fully ionized gas. I. *Phys. Rev.* **115**, 238 (1959).
- [70] H. Dreicer. Electron and ion runaway in a fully ionized gas. II. *Phys. Rev.* **117**, 329 (1960).
- [71] J.R. Martín-Solís, A. Loarte and M. Lehnen. Formation and termination of runaway beams in iter disruptions. *Nucl. Fusion* **57**, 066025 (2017).
- [72] S.C. Chiu, M.N. Rosenbluth, R.W. Harvey and V.S. Chan. Fokker-Planck simulations my1b of knock-on electron runaway avalanche and bursts in tokamaks. *Nucl. Fusion* **38**, 1711 (1998).
- [73] R.W. Harvey, V.S. Chan, S.C. Chiu, T.E. Evans, M.N. Rosenbluth and D.G. Whyte. Runaway electron production in DIII-D killer pellet experiments, calculated with the CQL3D/KPRAD model. *Phys. Plasmas* **7**, 4590 (2000).
- [74] H.M. Smith and E. Verwichte. Hot tail runaway electron generation in tokamak disruptions. *Phys. Plasmas* **15**, 072502 (2008).
- [75] Y.A. Sokolov. "Multiplication" of accelerated electrons in a tokamak. *JETP Lett.* **29**, 218 (1979).
- [76] M.N. Rosenbluth and S.V. Putvinski. Theory for avalanche of runaway electrons in tokamaks. *Nucl. Fusion* **37**, 1355 (1997).
- [77] L. Hesslow, O. Embréus, O. Vallhagen and T. Fülöp. Influence of massive material injection on avalanche runaway generation during tokamak disruptions. *Nucl. Fusion* **59**, 084004 (2019).
- [78] A. Stahl, O. Embréus, G. Papp, M. Landreman and T. Fülöp. Kinetic modelling of runaway electrons in dynamic scenarios. *Nucl. Fusion* **56**, 112009 (2016).
- [79] M. Hoppe, L. Hesslow, O. Embréus, L. Unnerfelt, G. Papp, I. Pusztai, T. Fülöp, O. Lexell, T. Lunt, E. Macusova et al. Spatiotemporal analysis of the runaway

- distribution function from synchrotron images in an ASDEX Upgrade disruption. *J. Plasma Phys.* **87**, 855870102 (2021).
- [80] E. Fable, C. Angioni, A.A. Ivanov, K. Lackner, O. Maj, S. Yu Medvedev, G. Pautasso, G.V. Pereverzev, W. Treutterer and the ASDEX Upgrade Team. Dynamical coupling between magnetic equilibrium and transport in tokamak scenario modelling, with application to current ramps. *Plasma Phys. Control. Fusion* **55**, 074007 (2013).
- [81] G. Papp, T. Fülöp, T. Fehér, P.C. de Vries, V. Riccardo, C. Reux, M. Lehnen, V.V. Kiptily, B. Alper and JET EFDA contributors. The effect of ITER-like wall on runaway electron generation in JET. *Nucl. Fusion* **53**, 123017 (2013).
- [82] O. Vallhagen, O. Embreus, I. Pusztai, L. Hesslow and T. Fülöp. Runaway dynamics in the DT phase of ITER operations in the presence of massive material injection. *J. Plasma Phys.* **86**, 475860401 (2020).
- [83] L. Hesslow. *Kinetic modeling of runaway-electron dynamics in partially ionized plasmas*. PhD thesis, Chalmers University of Technology, September 2020.
- [84] L. Hesslow, L. Unnerfelt, O. Vallhagen, O. Embreus, M. Hoppe, G. Papp and T. Fülöp. Evaluation of the Dreicer runaway growth rate in the presence of high- Z impurities using a neural network. *J. Plasma Phys.* **85**, 475850601 (2019).
- [85] G.T.A. Huysmans and O. Czarny. MHD stability in X-point geometry: simulation of ELMs. *Nucl. Fusion* **47**, 659 (2007).
- [86] O. Czarny and G. Huysmans. Bézier surfaces and finite elements for MHD simulations. *J. Comput. Phys.* **227**, 7423 (2008).
- [87] M. Hoelzl, G.T.A. Huijsmans, S.J.P. Pamela, M. Bécoulet, E. Nardon, F.J. Artola, B. Nkongha, C.V. Atanasiu, V. Bandaru, A. Bhole et al. The JOREK non-linear extended MHD code and applications to large-scale instabilities and their control in magnetically confined fusion plasmas. *Nucl. Fusion* **61**, 065001 (2021).
- [88] E. Nardon, A. Fil, M. Hoelzl, G. Huijsmans and JET Contributors. Progress in understanding disruptions triggered by massive gas injection via 3D non-linear MHD modelling with JOREK. *Plasma Phys. Control. Fusion* **59**, 014006 (2017).
- [89] E. Nardon, D. Hu, M. Hoelzl, D. Bonfiglio and the JOREK Team. Fast plasma dilution in ITER with pure deuterium shattered pellet injection. *Nucl. Fusion* **60**, 126040 (2020).
- [90] V. Bandaru, M. Hoelzl, F.J. Artola, G. Papp and G.T.A. Huijsmans. Simulating the nonlinear interaction of relativistic electrons and tokamak plasma instabilities: Implementation and validation of a fluid model. *Phys. Rev. E* **99**, 063317 (2019).
- [91] V. Bandaru, M. Hoelzl, C. Reux, O. Ficker, S. Silburn, M. Lehnen, N. Eidietis, JOREK Team and JET Contributors. Magnetohydrodynamic simulations of run-

- away electron beam termination in JET. *Plasma Phys. Control. Fusion* **63**, 035024 (2021).
- [92] R. Dux, A.G. Peeters, A. Gude, A. Kallenbach, R. Neu and ASDEX Upgrade Team. Z dependence of the core impurity transport in ASDEX Upgrade H mode discharges. *Nucl. Fusion* **39**, 1509 (1999).
- [93] O. Linder, G. Papp, E. Fable, F. Jenko, G. Pautasso, the ASDEX Upgrade Team and the EUROfusion MST1 Team. Electron runaway in ASDEX Upgrade experiments of varying core temperature. *J. Plasma Phys.* **87**, 905870301 (2021).
- [94] L. Hesslow, O. Embréus, G.J. Wilkie, G. Papp and T. Fülöp. Effect of partially ionized impurities and radiation on the effective critical electric field for runaway generation. *Plasma Phys. Control. Fusion* **60**, 074010 (2018).
- [95] L. Hesslow, O. Embréus, M. Hoppe, T.C. DuBois, G. Papp, M. Rahm and T. Fülöp. Generalized collision operator for fast electrons interacting with partially ionized impurities. *J. Plasma Phys.* **84**, 905840605 (2018).
- [96] I.N. Bronshtein, K.A. Semendyayev, G. Musiol and H. Muehlig. *Handbook of Mathematics*. Springer-Verlag, Berlin, Heidelberg, 4th edition, 2004.
- [97] P. Helander, L.-G. Eriksson and F. Andersson. Runaway acceleration during magnetic reconnection in tokamaks. *Plasma Phys. Control. Fusion* **44**, B247 (2002).
- [98] A.V. Gurevich. On the theory of runaway electrons. *Sov. Phys. JETP* **12**, 904 (1961).
- [99] A.N. Lebedev. Contribution to the theory of runaway electrons. *Sov. Phys. JETP* **21**, 931 (1965).
- [100] M.D. Kruskal and I.B. Bernstein. Technical Report MATT-Q-20 (unpublished), Princeton Plasma Physics Laboratory, 1962.
- [101] K. Insulander Björk, G. Papp, O. Embréus, L. Hesslow, T. Fülöp, O. Vallhagen, A. Lier, G. Pautasso, A. Bock, the ASDEX Upgrade Team et al. Kinetic modelling of runaway electron generation in argon-induced disruptions in ASDEX Upgrade. *J. Plasma Phys.* **86**, 855860401 (2020).
- [102] R.W. Harvey, Yu.V. Petrov, Charlson C. Kim, C.B. Forest, L.L. Lao and P.B. Parks. Time-dependent runaway electron simulations: AmpereFaraday equations implemented in CQL3D. *Nucl. Fusion* **59**, 106046 (2019).
- [103] Yu.V. Petrov, P.B. Parks and R.W. Harvey. Numerical simulation of the hot-tail runaway electron production mechanism using CQL3D and comparison with Smith-Verwichte analytical model. *Plasma Phys. Control. Fusion* **63**, 035026 (2021).
- [104] I. Svenningsson. *Hot-tail runaway electron generation in cooling fusion plasmas*. Master's thesis, Chalmers University of Technology, June 2020.
- [105] H.M. Smith, T. Fehér, T. Fülöp, K. Gál and E. Verwichte. Runaway electron generation in tokamak disruptions. *Plasma Phys. Control. Fusion* **51**, 124008 (2009).

-
- [106] E. Fable, G. Pautasso, M. Lehnen, R. Dux, M. Bernert, A. Mlynek and the ASDEX Upgrade Team. Transport simulations of the pre-thermal-quench phase in ASDEX Upgrade massive gas injection experiments. *Nucl. Fusion* **56**, 026012 (2016).
- [107] E. Nardon, D. Hu, F.J. Artola, D. Bonfiglio, M. Hoelzl, A. Boboc, P. Carvalho, S. Gerasimov, G. Huijsmans, V. Mitterauer et al. Thermal quench and current profile relaxation dynamics in massive-material-injection-triggered tokamak disruptions. *Plasma Phys. Control. Fusion* **63**, 115006 (2021).
- [108] G.V. Pereverzev and P.N. Yushmanov. *ASTRA - Automated System for TRansport Analysis*. Number IPP 5/98. Max-Planck-Institut für Plasmaphysik, February 2002.
- [109] A.A. Ivanov, R.R. Khayrutdinov, S.Yu. Medvedev and Yu.Yu. Poshekhonov. New adaptive grid plasma evolution code SPIDER. Contribution at the 32nd EPS Conference on Plasma Physics, Tarragona, Spain, 27.06-01.07.2005, P5.063.
- [110] K. Särkimäki, O. Embreus, E. Nardon, T., Fülöp and JET contributors. Assessing energy dependence of the transport of relativistic electrons in perturbed magnetic fields with orbit-following simulations. *Nucl. Fusion* **60**, 126050 (2020).
- [111] O. Linder, J. Citrin, G.M.D. Hogeweij, C. Angioni, C. Bourdelle, F.J. Casson, E. Fable, A. Ho, F. Koechl, M. Sertoli et al. Flux-driven integrated modelling of main ion pressure and trace tungsten transport in ASDEX Upgrade. *Nucl. Fusion* **59**, 016003 (2019).
- [112] S. Putvinski, N. Fujisawa, D. Post, N. Putvinskaya, M.N. Rosenbluth and J. Wesley. Impurity fueling to terminate Tokamak discharges. *J. Nucl. Mater.* **241-243**, 316 (1997).
- [113] A.H. Boozer. Runaway electrons and ITER. *Nucl. Fusion* **57**, 056018 (2017).
- [114] S.C. Jardin, N. Ferraro, X. Luo, J. Chen, J. Breslau, K.E. Jansen and M.S. Shephard. The M3D-C¹ approach to simulating 3D 2-fluid magnetohydrodynamics in magnetic fusion experiments. *J. Phys.: Conf. Ser.* **125**, 012044 (2008).
- [115] N.M. Ferraro, S.C. Jardin, L.L. Lao, M.S. Shephard and F. Zhang. Multi-region approach to free-boundary three-dimensional tokamak equilibria and resistive wall instabilities. *Phys. Plasmas* **23**, 056114 (2016).
- [116] C.R. Sovinec, A.H. Glasser, T.A. Gianakon, D.C. Barnes, R.A. Nebel, S.E. Kruger, S.J. Plimpton, A. Tarditi, M.S. Chu and the NIMROD Team. Nonlinear magnetohydrodynamics with high-order finite elements. *J. Comp. Phys.* **195**, 355 (2004).
- [117] M. Hoelzl, D. Hu, E. Nardon, G.T.A. Huijsmans, JOREK Team and ASDEX Upgrade Team. First predictive simulations for deuterium shattered pellet injection in ASDEX Upgrade. *Phys. Plasmas* **27**, 022510 (2020).
- [118] C. Sommariva, E. Nardon, P. Beyer, M. Hoelzl, G.T.A. Huijsmans, D. van Vugt and JET Contributors. Test particles dynamics in the JOREK 3D non-linear MHD

- code and application to electron transport in a disruption simulation. *Nucl. Fusion* **58**, 016043 (2017).
- [119] V.A. Izzo, E.M. Hollmann, A.N. James, J.H. Yu, D.A. Humphreys, L.L. Lao, P.B. Parks, P.E. Sieck, J.C. Wesley, R.S. Granetz et al. Runaway electron confinement modelling for rapid shutdown scenarios in DIII-D, Alcator C-Mod and ITER. *Nucl. Fusion* **51**, 063032 (2011).
- [120] H.P. Summers. The ADAS User Manual, version 2.6, 2004. <https://www.adas.ac.uk>.
- [121] K. Lackner, K. Behringer, W. Engelhardt and R. Wunderlich. An algorithm for the solution of impurity diffusion under finite reaction rates. *Z. Naturforschung* **37a**, 931 (1982).
- [122] A.G. Peeters. Reduced charge state equations that describe Pfirsch Schlüter impurity transport in tokamak plasma. *Phys. Plasmas* **7**, 268 (2000).
- [123] W. Hundsdorfer and J.G. Verwer. *Numerical Solution of Time-Dependent Advection-Diffusion-Reaction Equations*. Springer-Verlag, Berlin, 1st edition, 2003.
- [124] E. Sonnendrücker. *Lecture notes: Numerical methods for hyperbolic systems*. Technische Universität München, Sommersemester 2013.
- [125] F. Sciortino, N.M. Cao, N.T. Howard, E.S. Marmor and J.E. Rice. Particle transport constraints via Bayesian spectral fitting of multiple atomic lines. *Rev. Sci. Instrum.* **92**, 053508 (2021).
- [126] F. Sciortino, T. Odstrčil, A. Cavallaro, S. Smith, O. Meneghini, R. Reksoatmodjo, O. Linder, J.D. Lore, N.T. Howard, E.S. Marmor et al. Modeling of particle transport, neutrals and radiation in magnetically-confined plasmas with Aurora. *Plasma Phys. Control. Fusion* **63**, 112001 (2021).
- [127] A. Fil. *Modeling of massive gas injection triggered disruptions in tokamak plasmas*. PhD thesis, Aix-Marseille University, September 2015.
- [128] H. Pauly. *Atom, Molecule, and Cluster Beams I. Basic Theory, Production and Detection of Thermal Energy Beams*. Springer-Verlag, Berlin Heidelberg, 2000.
- [129] P. Aleynikov and B.N. Breizman. Generation of runaway electrons during the thermal quench in tokamaks. *Nucl. Fusion* **57**, 046009 (2017).
- [130] R. Dux, M. Cavedon, A. Kallenbach, R.M. McDermott, G. Vogel and the ASDEX Upgrade team. Influence of CX-reactions on the radiation in the pedestal region at ASDEX Upgrade. *Nucl. Fusion* **60**, 126039 (2020).
- [131] N. Bosviel, P. Parks and R. Samulyak. Near-field models and simulations of pellet ablation in tokamaks. *Phys. Plasmas* **28**, 012506 (2021).
- [132] C.C. Kim, Y. Liu, P.B. Parks, L.L. Lao, M. Lehnen and A. Loarte. Shattered pellet injection simulations with NIMROD. *Phys. Plasma* **26**, 042510 (2019).

-
- [133] V. Igochine, A. Gude, M. Maraschek and the ASDEX Upgrade Team. *Hotlink based Soft X-ray Diagnostic on ASDEX Upgrade*. Number IPP 1/338. Max-Planck-Institut für Plasmaphysik, May 2010.
- [134] V.A. Izzo. Impurity mixing and radiation asymmetry in massive gas injection simulations of DIII-D. *Phys. Plasmas* **20**, 056107 (2013).
- [135] V.A. Izzo, P.B. Parks, N.W. Eidietis, D. Shiraki, E.M. Hollmann, N. Commaux, R.S. Granetz, D.A. Humphreys, C.J. Lasnier, R.A. Moyer et al. The role of MHD in 3D aspects of massive gas injection. *Nucl. Fusion* **55**, 073032 (2015).
- [136] V.A. Izzo, D.G. Whyte, R.S. Granetz, P.B. Parks, E.M. Hollmann, L.L. Lao and J.C. Wesley. Magnetohydrodynamic simulations of massive gas injection into Alcator C-Mod and DIII-D plasmas. *Phys. Plasmas* **15**, 056109 (2008).
- [137] P. Svensson, O. Embreus, S.L. Newton, K. Särkimäki, O. Vallhagen and T. Fülöp. Effects of magnetic perturbations and radiation on the runaway avalanche. *J. Plasma Phys.* **87**, 905870207 (2021).
- [138] C. Paz-Soldan, P. Aleynikov, E.M. Hollmann, A. Lvovskiy, I. Bykov, X. Du, N.W. Eidietis and D. Shiraki. Runaway electron seed formation at reactor-relevant temperature. *Nucl. Fusion* **60**, 056020 (2020).
- [139] G.I. Pokol, S. Olasz, B. Erdos, G. Papp, M. Aradi, M. Hoppe, T. Johnson, J. Ferreira, D. Coster, Y. Peysson et al. Runaway electron modelling in the self-consistent core European Transport Simulator. *Nucl. Fusion* **59**, 076024 (2019).
- [140] S. Olasz, O. Embreus, M. Hoppe, M. Aradi, D. Por, T. Jonsson, D. Yadikin, G.I. Pokol and EU-IM Team. Validity of models for Dreicer generation of runaway electrons in dynamic scenarios. *Nucl. Fusion* **61**, 066010 (2021).
- [141] G.L. Falchetto, D. Coster, R. Coelho, B.D. Scott, L. Figini, D. Kalupin, E. Nardon, S. Nowak, L.L. Alves, J.F. Artaud et al. The European Integrated Tokamak Modelling (ITM) effort: achievements and first physics results. *Nucl. Fusion* **54**, 043018 (2014).
- [142] M. Hoppe, O. Embreus and T. Fülöp. DREAM: A fluid-kinetic framework for tokamak disruption runaway electron simulations. *Comput. Phys. Commun.* **268**, 108098 (2021).



Included papers

Paper #1

O. Linder, E. Fable, F. Jenko, G. Papp, G. Pautasso, the ASDEX Upgrade Team and the EUROfusion MST1 Team,
Self-consistent modeling of runaway electron generation in massive gas injection scenarios in ASDEX Upgrade,
Nuclear Fusion **60**, 096031 (2020).

<https://doi.org/10.1088/1741-4326/ab9dcf>

arXiv:2003.00725 [physics.plasm-ph]

Self-consistent modeling of runaway electron generation in massive gas injection scenarios in ASDEX Upgrade

O. Linder¹, E. Fable, F. Jenko, G. Papp², G. Pautasso, the ASDEX Upgrade team^a and the EUROfusion MST1 team^b

Max-Planck-Institut für Plasmaphysik, Boltzmannstr. 2, 85748 Garching, Germany

E-mail: Oliver.Linder@ipp.mpg.de

Received 3 March 2020, revised 29 May 2020

Accepted for publication 17 June 2020

Published 18 August 2020



Abstract

We present the first successful simulation of an induced disruption in ASDEX Upgrade from massive material injection (MMI) up to established runaway electron (RE) beam, thus covering pre-thermal quench, thermal quench and current quench (CQ) of the discharge. For future high-current fusion devices such as ITER, the successful suppression of REs, e.g. through MMI, is of critical importance to ensure the structural integrity of the vessel. To computationally study the interplay between MMI, background plasma response, and RE generation, a toolkit based on the 1.5D transport code coupling ASTRA–STRAHL is developed. Electron runaway is described by state-of-the-art reduced kinetic models in the presence of partially ionized impurities. Applied to argon MMI in ASDEX Upgrade discharge #33 108, key plasma parameters measured experimentally, such as temporal evolution of the line averaged electron density, plasma current decay rate and post-CQ RE current, are well reproduced by the simulation presented. Impurity ions are transported into the central plasma by the combined effect of neoclassical processes and additional effects prescribed inside the $q = 2$ rational surface to explain experimental time scales. Thus, a thermal collapse is induced through strong impurity radiation, giving rise to a substantial RE population as observed experimentally.

Keywords: runaway electrons, tokamaks, disruptions, massive material injection

(Some figures may appear in colour only in the online journal)

1. Introduction

In the presence of sufficiently strong electric fields, plasma electrons surmount the collective collisional drag and experience net acceleration up to relativistic energies; a process referred to as electron runaway. Eventually, pitch-angle scattering and radiative losses due to Bremsstrahlung and synchrotron radiation hinder further gain of energy in the relativistic regime. These so called runaway electrons (RE) are created not only naturally in astrophysical or atmospheric plasmas, but also in human-made high-temperature laboratory plasmas.

In current carrying fusion devices, a significant population of runaway electrons may be generated following the sudden loss of both magnetic confinement and thermal energy, referred to as a disruption. In the cold post-disruption plasma, the plasma current and consequently the magnetic field generated by the same collapse, giving rise to electric fields sufficiently strong for the high-energy tail of the electron population to run away. Runaway electrons created in the process can potentially damage plasma facing components (PFC) severely upon impact by depositing both kinetic energy $W_{\text{kin}} \propto \langle p_{\text{RE}}^2 \rangle I_{\text{RE}}$ and magnetic energy $W_{\text{mag}} \propto I_{\text{RE}}^2$, with p_{RE} being the RE momentum and I_{RE} the RE carried current. Significant RE-induced damage of PFCs has been reported, e.g. at JET [1, 2], where RE currents close to 1 MA caused melting of substantial amounts of Be at the inner limiter of the ITER-like wall.

^a See Meyer *et al* 2019 (<https://doi.org/10.1088/1741-4326/ab18b8>) for the ASDEX Upgrade team.

^b See Labit *et al* 2019 (<https://doi.org/10.1088/1741-4326/ab2211>) for the EUROfusion MST1 team.

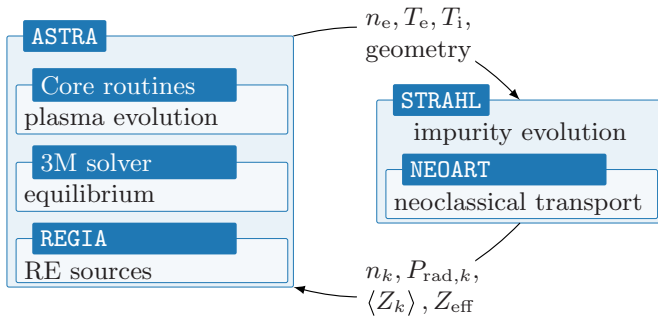


Figure 1. Overview of the model employed in this work. The transport code ASTRA evolves the main plasma in a magnetic equilibrium obtained by the built-in 3-moment solver. Kinetic profiles are passed to STRAHL to calculate the evolution of impurity species under consideration of neoclassical transport coefficients obtained through NEOART inside STRAHL. Impurity densities, radiation and average charge of each species k , as well as the plasma effective charge are passed back to ASTRA. In this environment, RE sources are calculated by REGIA and the runaway population is evolved by ASTRA.

In ITER and other future high-current devices, REs pose an even greater threat to the structural integrity of the plasma vessel [3]. A large fraction of the pre-disruptive current I_p of up to 16 MA may be carried by suprathermal electrons post-disruption due to long exponentiation of a post-disruption RE seed, giving rise to runaway currents in excess of 10 MA. Simultaneously, the RE stored magnetic energy increases significantly compared to present-day devices, given the quadratic scaling with the current carried, $W_{\text{mag}} \propto I_{\text{RE}}^2$. Under these conditions, the PFCs of high-current devices may be damaged severely by deconfined REs.

To protect the plasma vessel of ITER during a disruption, massive material injection (MMI) into the plasma center on a ms-timescale is envisioned, thus evenly distributing the plasma stored thermal energy across the first wall through radiation. In the cold post-injection plasma, the noticeably increased density of plasma electrons enhances the collisional drag experienced by the electron population and prevents the formation of a considerable RE beam under ideal conditions.

Currently, the feasibility of MMI for RE suppression is being investigated in dedicated experiments across multiple machines using massive gas injection (MGI), e.g. at ASDEX Upgrade (AUG) [4] and TCV [5], or shattered pellet injection (SPI), e.g. at DIII-D [6]. Yet, extrapolation from present-day small and large machines to ITER is ambitious, given the exponential sensitivity of RE generation on the pre-disruptive plasma current [7]. At the same time, elaborate models describing RE generation are being derived theoretically [8–10].

To complement experimental and theoretical studies of electron runaway in tokamak disruptions following MGI, the coupled 1.5D transport code toolkit ASTRA–STRAHL is presented in this work, allowing self-consistent simulations of the interactions between background plasma, impurity species and runaway electrons. The model is then applied for the simulation of argon (Ar) MGI in AUG discharge #33 108.

Simulations of RE generation and mitigation by MGI have also been carried out for ITER [11], applying a Monte Carlo Fokker-Planck solver to model RE generation [12]. In the work presented in this manuscript, state-of-the-art reduced kinetic models, being a neural network for the Dreicer growth rate [13], constructed from calculations by the full- f continuum Fokker-Planck solver CODE [14], as well as an analytical description of avalanche generation [10], are applied for the first time in a transport code. Both models have also been implemented in the disruption code GO [15].

A description of the computational model employed in this work is provided in section 2, covering i.a. the treatment of the impurity species and the theoretical models for RE generation incorporated into the tool. Experimental aspects of AUG discharge #33 108 are discussed in section 3. Simulations of Ar MGI with ASTRA–STRAHL for this discharge are presented in section 4. Final conclusions are drawn in section 5.

2. Model description

The interaction between the tokamak background deuterium plasma, injected material and REs in artificially induced disruptions in AUG MGI scenarios is studied by transport modeling of particles and heat with the 1.5D transport code ASTRA [16] coupled to the impurity transport and radiation code STRAHL [17]. This toolset was previously used i.a. for the study of the pre-thermal quench (TQ) of AUG MGI experiments [18], but is enhanced to simulate MGI up to the RE plateau phase, as outlined in sections 2.2–2.4. An overview of the tool structure is shown in figure 1; the details explained in the following. ASTRA–STRAHL may thus be used to model RE generation in tokamak MGI experiments. However, restrictions concerning the treatment of REs may apply depending on the machine (discussed in section 2.4).

2.1. Background plasma evolution

The evolution of the background plasma is performed by ASTRA through evaluation of the macroscopic transport equation

$$\frac{\partial Y}{\partial t} = \frac{1}{V'} \frac{\partial}{\partial \rho} \left(V' \langle (\Delta \rho)^2 \rangle \left\{ D \frac{\partial Y}{\partial \rho} - v Y \right\} \right) + \sum_j S_j \quad (1)$$

for any of the evolved fluid quantities $Y(\rho, t)$ in the presence of diffusion D , advection v and sources/sinks S_j . Here, ρ is the toroidal flux-surface label. Hence, the quantities $\Delta \rho$ and $V' = \partial V / \partial \rho$ describe the magnetic geometry, where V is the volume of a flux-surface. In this work, the transport equations for electron temperature T_e , ion temperature T_i , poloidal magnetic flux Ψ and RE density n_{RE} are solved. The electron density n_e is obtained through quasi-neutrality from the ion densities $n_k(t)$ of each impurity species k evolved by STRAHL; i.e. $n_e(t) = n_D + \sum_k \langle Z_k \rangle n_k(t)$, with average charge $\langle Z_k \rangle$. The deuterium population n_D is set to remain at the level prior to MGI. The initial profiles of the quantities being evolved are

taken from experimental reconstruction. In the case of the initial profile of the poloidal magnetic flux, the reconstructed safety factor q is used.

For the evolution of the electron temperature, the impurity radiation P_{rad} is used as a sink term. A global heat diffusion coefficient of the order of the power balance, i.e. $\chi_e = 1 \text{ m}^2 \text{ s}^{-1}$, is applied to prevent the formation of strongly localized hot plasma beamlets during simulations, as e.g. observed in other studies [19, 20]. Apart from this, the overall T_e -evolution is unaffected by a reasonable choice of χ_e in these scenarios, since radiated losses far outweigh conductive ones [20]. Following the same argument, turbulent transport is not taken into account. The temperature evolution of electrons and ions is coupled through heat exchange, described by $P_{\text{ei}} = 3(T_e - T_i)n_e m_e / m_i \tau_e$ [16] (τ_e being the electron collision time).

The transport calculations for aforementioned quantities are performed in a realistic magnetic geometry obtained from the equilibrium solver SPIDER [21] or from a simple 3-moment solver, built into ASTRA. Applying the latter solver, the radial r and vertical z coordinates of flux-surfaces inside a tokamak of major radius R_0 are parametrized by [16]

$$\left. \begin{aligned} r(a, \theta) &= R_0 + \Delta(a) + a \{ \cos \theta - \delta(a) \sin^2 \theta \}, \\ z(a, \theta) &= a \kappa(a) \sin \theta, \end{aligned} \right\} \quad (2)$$

with mid-plane minor radius a of a flux-surface and poloidal angle θ . The Shafranov shift is denoted by $\Delta(a)$, the triangularity by $\delta(a)$ and elongation by $\kappa(a)$. Since AUG MGI experiments are typically performed in circular discharges to ensure vertical stability of the plasma during disruption, application of the 3-moment solver is sufficient for this study.

It should be noted, that the impact of MHD phenomena on the magnetic equilibrium is not included in the simulations. In particular, the occurrence of a spike of the total plasma current observed in Ar MGI experiments at AUG when the cold gas front reaches the $q = 2$ surface is not taken into account. However, the impact of this MHD phenomenon on the plasma species may be mimicked by application of increased transport coefficients inside the $q = 2$ surface. An estimate of the required magnitude can be obtained through comparison with experimental observations of kinetic profiles, as will be described in section 4.3.

2.2. Impurity transport modeling

The evolution of impurity species is calculated for each individual charge state by STRAHL from transport equations as used in ASTRA (see equation (1)). The computational grid is provided by ASTRA to simplify the exchange of (kinetic) profiles between both codes. Additionally, electron density and temperature profiles are passed to STRAHL to evaluate reaction rates of atomic processes for a given impurity species. These electron-atom interactions, most importantly ionization and recombination, are described through tabulated rate coefficients from ADAS [22]. During evaluation of the impurity evolution, reaction rates obtained are prescribed as sources/sinks

S_j . For each impurity species k , charge state i resolved impurity densities $n_{k,i}$, total impurity radiation $P_{\text{rad},k}$ and average impurity ion charge $\langle Z_k \rangle = \sum_{i \geq 1} Z_{k,i} n_{k,i} / \sum_{i \geq 1} n_{k,i}$ are passed to ASTRA and are applied as described in section 2.1. Additionally, the effective charge $Z_{\text{eff}} = \{n_D + \sum_{k,i} Z_{k,i}^2 n_{k,i}\} / n_e$ of the plasma under consideration of all plasma ions is returned.

The diffusive and convective impurity transport coefficients D and v are calculated in the case of neoclassical transport by the code NEOART [23]. Geometric quantities for the calculation are provided by ASTRA. Increased simulation performance is achieved by parallelizing calls to NEOART for individual grid points with openMP and by applying STRAHL-specific optimization. Further transport mechanisms can be considered through externally provided transport coefficients. In this work, an additional global impurity diffusion with $D = 1 \text{ m}^2 \text{ s}^{-1}$ is applied; giving $D/\chi_e \sim 1$ as observed in gyrokinetic studies of impurity transport [24].

To enable the treatment of strongly advective particle transport, where the (local) Péclet number $\mu = v \Delta \rho / D \rightarrow \infty$, the 1st order central finite difference scheme used for the spatial discretization of the STRAHL transport equation is replaced with a finite volume discretization. The order of the scheme is kept to allow for continued application of the fast tridiagonal matrix algorithm during evaluation of the matrix equations. The numerical scheme used for discretization is chosen depending on the parameter $K = \max(0, 1 - 2/|\mu|) \cdot \text{sign}(\mu)$ [25]. In diffusion dominated cases ($K \rightarrow 0$), a central scheme is applied, whereas in advection dominated cases ($K \rightarrow \infty$) upwinding is used. This approach prevents introducing numerical oscillations in the case $|\mu| \rightarrow \infty$, while simultaneously preventing application of an inaccurate scheme for $|\mu| \rightarrow 0$. As a result, impurity transport simulations with arbitrary Péclet number are enabled in STRAHL. As additional benefit of the finite volume scheme, particle conservation is ensured. Numerical details of the scheme are outlined in A.

2.3. Neutral particle modeling

Neutral impurities are treated similarly in STRAHL as their ionized counterparts. However, to distinguish between recombined impurity ions and externally deposited neutrals with different distribution functions $f(\rho, \mathbf{v}, t)$, multiple neutral impurity populations are employed within STRAHL. External neutral particles can be initialized at the start of the simulation with an arbitrary density profile or may be deposited gradually at an arbitrary location within the simulation domain throughout the course of the simulation. Once deposited, external neutrals are assumed to propagate inwards with thermal velocity $v_{\text{th}} = \sqrt{T/m}$ until being ionized eventually. Depending on the temperature evolution during the simulation, ions may recombine to neutrals.

For the simulation of MGI in this work, the source of neutrals is set just outside the last closed flux surface. Consequently, the propagation from gas valve to the plasma edge is not modeled. Instead, experimental experience is used to estimate the neutral flow rate and flight time from gas valve to plasma boundary.

2.4. Runaway electron modeling

The density of runaway electrons n_{RE} is treated in ASTRA as a separate species, following the same transport equations as described by equation (1). Source terms S_j for RE generation considered in this study include the Dreicer mechanism and the avalanche mechanism. The former process describes small-angle momentum space diffusion of thermal electrons beyond the critical momentum for electron runaway (primary generation), whereas the latter one covers large-angle knock-on collisions of existing REs with the thermal bulk, thus creating secondary REs. Additional mechanisms for primary generation are not considered in this work. In AUG's non-nuclear environment, tritium β^- -decay and Compton scattering of high energy photons originating from activated wall material do not pose a relevant source of REs.

Rapid cooling of the plasma in AUG may increase RE formation, as the high-energy tail of the electron distribution equilibrates slower and may therefore exceed the critical energy for runaway under these conditions. Still, this mechanism, referred to as hot-tail generation [26, 27], is not taken into account given the lack of suitable numerical models. Although being described by kinetic models, e.g. CODE [14], application of kinetic solvers in transport simulations is unpractical due to computational costs. Simultaneously, fluid approximations, such as e.g. the work presented by Smith and Verwichte [28] or Fehér *et al* [20], underestimate the hot-tail population by up to an order of magnitude [14]. Although being highly sensitive to the evolution of the electric field [29], its impact on the hot-tail population is not considered by these fluid models [30]. However, as finite magnetic flux is converted [7] into predominantly secondary REs in the AUG disruption studied in this work (see e.g. section 4.5), as well as in similar AUG discharges [31], a variation of the seed population in the presence of dominating avalanche amplification is expected to result in similar post-disruption RE currents [32].

Both the Dreicer and the avalanche RE sources considered can be described by widely used equations. An analytic expression for Dreicer generation in the presence of an electric field E_{\parallel} (here, parallel to the magnetic field lines) was derived by Connor and Hastie [33],

$$S_{\text{D}} = k_{\text{D}} n_{\text{e}} \nu_{\text{e}} \left(\frac{E_{\parallel}}{E_{\text{D}}} \right)^{-h} \exp \left(-\lambda \frac{E_{\text{D}}}{E_{\parallel}} - \eta \sqrt{\frac{E_{\text{D}}}{E_{\parallel}}} \right), \quad (3)$$

where the unknown constant k_{D} is of order unity and is therefore taken as $k_{\text{D}} = 1$. The quantity ν_{e} denotes the thermal electron-electron collision frequency, being $\nu_{\text{e}} = n_{\text{e}} e^4 \ln \Lambda / 4\pi \varepsilon_0^2 m_{\text{e}}^{1/2} T_{\text{e}}^{3/2}$. Setting $\varepsilon = E_{\parallel} / E_{\text{c}}$, the remaining numerical factors are given by

$$\left. \begin{aligned} h &= \frac{Z_{\text{eff}} + 1}{16} \left\{ 1 + 2 \frac{\varepsilon - 2}{\varepsilon - 1} \sqrt{\frac{\varepsilon}{\varepsilon - 1}} \right\} + \frac{2}{\varepsilon - 1}, \\ \lambda &= 2\varepsilon \left\{ \varepsilon - \frac{1}{2} - \sqrt{\varepsilon(\varepsilon - 1)} \right\}, \\ \eta &= \varepsilon \sqrt{\frac{Z_{\text{eff}} + 1}{4(\varepsilon - 1)}} \left\{ \frac{\pi}{2} - \arcsin \left(1 - \frac{2}{\varepsilon} \right) \right\}. \end{aligned} \right\} \quad (4)$$

The characteristic fields, being the Dreicer field $E_{\text{D}} = n_{\text{e}} e^3 \ln \Lambda / 4\pi \varepsilon_0^2 T_{\text{e}}$ and the critical field $E_{\text{c}} = E_{\text{D}} T_{\text{e}} / m_{\text{e}} c^2$, describe runaway of electrons at thermal and relativistic velocities, respectively. The critical field E_{c} constitutes the minimum field for net acceleration of electrons. For $E_{\parallel} > E_{\text{c}}$, more energy is gained from the electric field during one collision time ν_{e}^{-1} than transferred to low energy electrons. Consequently, the RE growth rate of equation (3) vanishes for $E_{\parallel} / E_{\text{c}} \rightarrow 1^+$, as the exponent $h \rightarrow -\infty$ and $E_{\parallel} \ll E_{\text{D}}$ under these conditions.

An expression for generation of runaway electrons due to the avalanche mechanism was initially obtained by Rosenbluth and Putvinski [34]

$$\left. \begin{aligned} S_{\text{av}} &= n_{\text{RE}} \frac{e^2}{m_{\text{e}} \Lambda_{\text{c}}} \sqrt{\frac{\pi \gamma}{3(Z_{\text{eff}} + 5)}} \{E_{\parallel} - E_{\text{c}}\} \\ &\times \left(1 - \varepsilon + \frac{\frac{4\pi}{3\gamma} (Z_{\text{eff}} + 1)^2}{(Z_{\text{eff}} + 5) \left\{ \varepsilon^2 + \frac{4}{\gamma^2} - 1 \right\}} \right)^{-\frac{1}{2}}, \\ \gamma &= (1 + 1.46\sqrt{\varepsilon} + 1.72\varepsilon)^{-1}, \end{aligned} \right\} \quad (5)$$

where ε denotes the inverse tokamak aspect ratio. The quantity $\ln \Lambda_{\text{c}} = \ln \Lambda_0 + \frac{1}{2} \ln(m_{\text{e}} c^2 / T_{\text{e}})$ describes the Coulomb logarithm for collisions between relativistic and thermal electrons [9], replacing the Coulomb logarithm $\ln \Lambda_0$ for thermal-thermal collisions in the expression by Rosenbluth and Putvinski [34]. Although above expression for S_{av} is accurate for large fields, the growth rate in the vicinity of the critical field is underestimated [34].

The two models discussed are valid only for plasmas consisting of fully ionized species. Yet following MGI, already low- Z to medium- Z impurities are only partially ionized, particularly in a cold post-TQ plasma. Under these conditions, Rosenbluth and Putvinski [34] suggested to generalize the expression of the critical electric field E_{c} by including half the bound electrons. An improved description is achieved by taking the impact of partially ionized impurities on RE dynamics directly into account. Increased friction, pitch-angle scattering and radiation losses enhance significantly both the critical field E_{c} and the avalanche growth rate S_{av} [8–10] beyond the classical formulae of Rosenbluth and Putvinski [34]. In the presence of partially ionized impurities, the avalanche growth rate can be expressed as [10]

$$S_{\text{av}} = k_{\text{av}} n_{\text{RE}} \frac{e^2}{m_{\text{e}} \ln \Lambda_{\text{c}}} \frac{n_{\text{e}}^{\text{tot}}}{n_{\text{e}}} \frac{E_{\parallel} - E_{\text{c}}^{\text{eff}}}{\sqrt{4 + \bar{\nu}_{\text{s}}(p_*) \bar{\nu}_{\text{D}}(p_*)}}. \quad (6)$$

A description of the effective critical field $E_{\text{c}}^{\text{eff}}$, the slowing-down frequency $\bar{\nu}_{\text{s}}$ and the generalized deflection frequency $\bar{\nu}_{\text{D}}$ is provided by Hesslow *et al* [8]. Since the effective critical momentum p_* for runaway generation is itself a function of $\bar{\nu}_{\text{s}}$ and $\bar{\nu}_{\text{D}}$ through $p_* = \sqrt[4]{\bar{\nu}_{\text{s}}(p_*) \bar{\nu}_{\text{D}}(p_*)} / \sqrt{E_{\parallel} / E_{\text{c}}}$, a closed form of equation (6) cannot be given.

In contrast to the increase of the avalanche growth rate, the steady-state flux of electrons into the runaway region as obtained by kinetic simulations with the linearized Fokker-Planck solver CODE [14] is noticeably reduced in the presence

of partially ionized impurity ions for $E/E_D \lesssim 0.1$ [9]. Albeit useful, application of kinetic solvers in 1D transport simulations for the calculation of RE growth rates is unfeasible due to computational costs. Therefore a neural network for the calculation of the Dreicer growth rate has been created recently from CODE simulations covering an experimentally relevant region of parameter space using a set of 8 input parameters [13]. Although training of the network was carried out using only Ar and Ne impurities, input parameters were chosen sufficiently general to allow for application to other impurity species. The neural network obtained shows good agreement with CODE results and may therefore be applied in fluid simulations [13].

For the calculation of Dreicer and avalanche growth rates inside ASTRA, the models discussed are incorporated into a stand-alone Fortran module¹ and can therefore be used in any Fortran program. A wrapper routine, referred to as REGIA (Runaway Electron Generation In Astra), is employed in ASTRA to call the requested module routines and convert quantities to ASTRA units. Since the expressions by Hesslow *et al* [10, 13] provide an improved description of Dreicer and avalanche generation over the classical formulae, both the neural network for S_D and equation (6) for S_{av} are applied throughout this study. The implementation of both models was verified directly against the work of Hesslow *et al* [10, 13]. For the calculation of impurity related quantities, REGIA selects from the impurity densities obtained through STRAHL all charge states l which contribute noticeably to the overall electron density or are present in noticeable amounts, i.e. $n_l \cdot \max(Z_l, 1) \geq 10^{-4} n_e$.

The possibility to use the analytical expressions of Connor and Hastie [33], and Rosenbluth and Putvinski [34], i.e. equations (3) and (5), is kept to allow for an assessment of the differences between these models and hence of the importance of partially ionized impurities on the RE population obtained in self-consistent MGI simulations. The implementation of the analytical Dreicer and avalanche sources from equations (3) and (5) was verified successfully against calculations by the disruption code G0 [15]. For this purpose, simulations of a thermal collapse with prescribed exponential temperature decay on time scales $\tau \in [0.1 \text{ ms}, 10.0 \text{ ms}]$ to on-axis post-disruption temperatures $T_{e,f} \in [1 \text{ eV}, 100 \text{ eV}]$ in a clean plasma were carried out. The RE currents obtained by both tools show reasonable agreement within a few % in the region of parameter space $(\tau, T_{e,f})$ relevant for disruptions in AUG.

The transport of runaways across magnetic flux surfaces is set to occur diffusive with $D = 10^{-3} \text{ m}^2 \text{ s}^{-1}$ to ensure numerical stability of the simulations without impacting simulation results. Rapid radial transport due to stochastic magnetic field lines during magnetic reconnection is not considered, as the bulk of the RE population is generated only once nested flux surfaces have re-emerged. Other transport mechanisms are expected to be of minor importance, given the fast time

scale of the current quench (CQ) and hence RE generation within a few ms in AUG. RE dissipation mechanisms are thus considered important only after the CQ during the RE beam phase of a disruption. However, this aspect is not covered in this work.

From the RE density n_{RE} obtained by ASTRA through evaluation of the transport equation (equation (1)) under consideration of sources S_j and transport D , the runaway carried current density is constructed, $j_{RE} = cen_{RE}$, and added to Ohmic current density and bootstrap current density to construct the total plasma current density, i.e. $j_p = j_\Omega + j_{BS} + j_{RE}$, thus affecting Ψ -evolution in ASTRA. Hereby, the REs are assumed to travel with the speed of light, which gives a less than 1% deviation for REs with $E_{kin} > 6.1 m_e c^2 = 3.1 \text{ MeV}$. This assumption may not hold in the early phase of a disruption as electrons have to perform in excess of 10^3 revolutions in the tokamak to extract these amounts of energy from the strong induced electric fields. Simultaneously, the RE contribution to the total current and hence impact on Ψ -evolution is negligible. Only at a later stage of the CQ, sufficient amounts of REs are present to noticeably impact Ψ -evolution. At this stage, however, REs are expected to have gained enough energy from the electric field to justify the assumption that REs travel with the speed of light.

The model discussed is thus suitable to study RE generation in MGI experiments in small to mid-sized machines with non-nuclear environment. As radial transport of REs is currently treated to be negligible, application to scenarios where the plasma current decays on time scales exceeding tens of ms may provide additional challenges. Additionally, RE generation in DT-scenarios (e.g. ITER during fusion power operation or upcoming DT-campaign of JET) cannot be modeled as generation mechanisms due to nuclear processes (tritium decay, Compton scattering) are not taken into account at present.

3. Experimental scenario

Simulations of the interplay between deuterium plasma, impurity MGI and REs are performed for AUG discharge #33 108. This particular discharge was tailored for the study of RE generation and mitigation and has been used as a reference case for proceeding RE experiments in multiple experimental campaigns.

In the discharge chosen, Ar is injected into an L-mode limiter plasma with an initial plasma current of 763 kA and an applied on-axis magnetic field of 2.5 T. Vertical stability of the plasma during the artificial disruption is facilitated through the circular shape of the plasma. The pre-disruption plasma density was kept low with an average of $\langle n_e \rangle = 2.84 \times 10^{19} \text{ m}^{-3}$ to reduce the collisional drag on (seed) runaways and thus to facilitate generation of a substantial RE beam during the disruption. Current conversion was further enhanced by applying 2.625 MW of on-axis ECRH provided by four of the gyrotrons in the last 100 ms prior to MGI, i.e. between $t = 0.9 \text{ s}$ and

¹ The Fortran module for the calculation of runaway electron Dreicer and avalanche growth rates is available at <https://github.com/olinder/runawayelectrongeneration>.

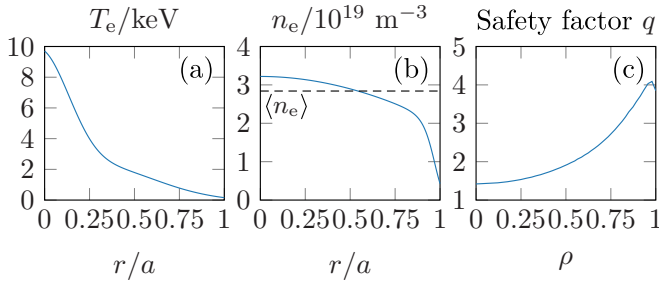


Figure 2. Profiles averaged between $t = 0.95$ s and $t = 1.00$ s prior to Ar MGI in AUG #33 108 of (a) electron temperature T_e obtained from electron cyclotron emission (ECE) and Thomson scattering (TS) measurements, (b) electron density n_e from TS and interferometry, (c) the safety factor q .

$t = 1.0 \text{ s}^2$. In the process, a strongly peaked electron temperature profile is established, with on-axis temperatures in excess of 10 keV. As a result, the Dreicer electric field E_D is reduced in the central plasma, thus enhancing the primary source of runaways through the exponential sensitivity on $-E_D/E_{\parallel}$ (see equation (3)) and contributing to generation of a considerable RE beam during the disruption. The profiles of electron temperature T_e , electron density n_e and safety factor q averaged between $t = 0.95$ s and $t = 1.00$ s are shown in figure 2. These profiles are set as initial conditions in the simulations discussed in the following section 4.

3.1. Diagnostics

The evolution of the plasma following injection of Ar is captured by several diagnostics. The line integrated electron density \bar{n}_e is obtained from CO_2 interferometers along two vertical lines of sight, covering the central plasma (chord V-1) and the high-field-side (HFS) outer plasma (chord V-2) in sector 11 of the AUG vessel (see figure 3; see figure 1 of reference [4] for an overview of AUG sectors, including MGI-relevant diagnostics). Radiation measurements are carried out with the Absolute eXtreme UltraViolet diagnostic (AXUV), a diode array consisting of 48 vertical channels (although only the relevant first 32 channels are shown in figure 3), and can be used to reconstruct the propagation of the deposited material. The occurrence of the TQ can be determined by measurements of soft x-ray (SXR) radiation in the plasma center using one vertical and one horizontal channel of the available SXR photo diodes.

3.2. Ar MGI

In AUG #33 108, Ar is injected from the low-field-side (LFS) valve located in sector 13 (see figure 3) into the vessel. The valve's gas reservoir of 85 cm^3 and feed line of 15 cm^3 were filled with 0.73 bar of Ar at ambient temperature, corresponding to 1.75×10^{21} Ar atoms - around 7 times the deuterium content of the confined plasma. Injection of material

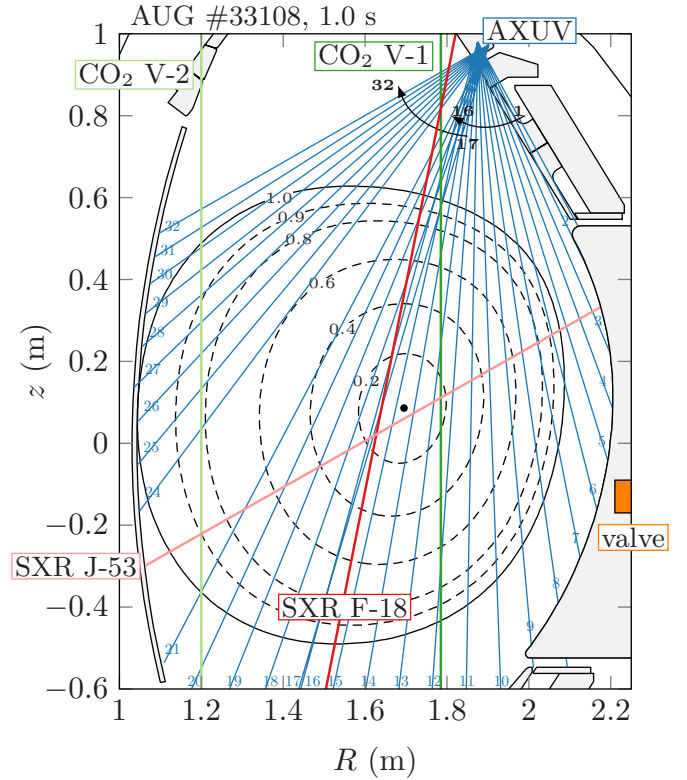


Figure 3. Line of sights of the relevant diagnostics for the analysis of AUG #33 108, being two vertical CO_2 interferometers (green), the AXUV photodiodes (blue) and two central SXR channels (red). Ar is injected from the LFS valve (orange) in sector 13. The magnetic equilibrium at the onset of Ar MGI at $t_{\text{MGI}} = 1.0$ s is illustrated by flux surfaces of normalized poloidal flux ρ_{θ} .

is triggered at $t_{\text{MGI}} = 1.0$ s. At the same time, ECRH heating is shut off. The flow of Ar out of the valve is reconstructed in 0D under the assumption of ideal flow from the continuity equation $dN_{\text{Ar}}/dt + v_{\text{Ar}}N_{\text{Ar}}A_v(t)/V_v = 0$ (see appendix A of reference [35] for details). A finite opening time of 1 ms of the valve's aperture of size A_v is assumed [18]. The Ar flow obtained is illustrated in figure 4(a). A more complete treatment of material injection is e.g. achieved by the 1D code IMAGINE [36]. Throughout the remainder of this work, the temporal evolution t will be given with respect to t_{MGI} instead of the beginning of the discharge.

The material injected reaches the last closed flux surface (LCFS) at the LFS at $t = 1$ ms, as indicated by the increase of UV radiation measured by channels #5 and #6 of the AXUV diagnostic in sector 13 (see figure 5). Over the following 1 ms, the AXUV signal increases across the remaining channels, as part of the Ar gas ionizes and redistributes poloidally. Ar propagates further inwards (see increase of the line averaged electron density \bar{n}_e in figure 4(b)) and causes a thermal collapse of the plasma between $t = 2.85$ ms and $t = 3.13$ ms, as determined from SXR measurements (see figure 4(d)). The accompanying increase of radiation is detected by the AXUV arrays both in sector 13 and 5 (see figure 4(c) and figure 5), as well as by SXR measurements of the central plasma (see figure 4(d)). During the TQ, the plasma current is observed to

² In this section, the time t is given with respect to the beginning of the discharge.

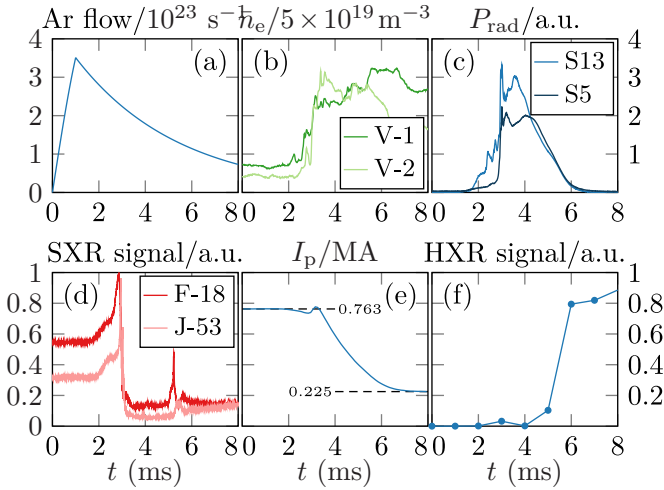


Figure 4. Temporal evolution of experimentally obtained and derived quantities of AUG #33 108 following the MGI trigger at $t_{\text{MGI}} = 1.0$ s, being (a) the calculated Ar flow from the valve, (b) measurements of the line integrated electron density \bar{n}_e by the CO₂ interferometers, (c) the total radiated power P_{rad} calculated from AXUV measurements in sectors 13 and 5, (d) the signals of two central SXR measurements, (e) the reconstructed plasma current I_p and (f) HXR measurements as an indication for the RE population.

increase by 41 kA (see figure 4(e)), presumably due to magnetic reconnection, triggered by the cold gas front reaching the $q = 2$ rational surface [18] as the loop voltage exhibits non-monotonic behavior in this phase. Over the 2.5 ms following the TQ, the remnant core plasma continues to radiate strongly. Simultaneously, the plasma current decreases rapidly from an initial value of 763 kA down to 225 kA. The remaining current is carried by relativistic electrons, as indicated by a strong increase of the signal of the hard x-ray (HXR) diagnostic (see figure 4(f)).

4. MGI simulations

4.1. Scenario specific simulation settings

Argon MGI in AUG discharge #33 108 is simulated with the model presented in section 2. The source of Ar is set 1 cm outside the LCFS since the propagation of material from the valve to the core plasma is not modeled. Instead, the experimentally observed delay of 1 ms between valve trigger and detection of Ar at the LFS-LCFS (see figure 5) is applied to the calculated flow rate of Ar from the valve (see figure 4(a)) and used as source rate in the simulation. The neutral Ar injected from the valve at ambient temperature propagates into the core plasma with thermal velocity, being $v_{\text{th}} = \sqrt{T/m} = 246$ m s⁻¹.

The simulations presented in the following are carried out using a numerical grid consisting of 201 points inside ASTRA. A minimum and maximum time step of 10^{-5} ms and 1 ms respectively are chosen to capture the transient dynamics of Ar MGI, while allowing efficient calculation of the later stages of the induced disruption. Applying larger values for the

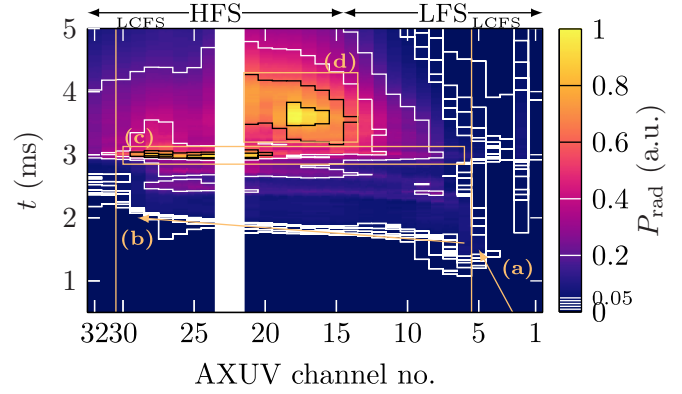


Figure 5. Radiation measurements of the individual channels of the AXUV photodiodes in sector 13 (see figure 3 for their line-of-sights). Channels 1 to 14 capture LFS radiation, i.e. their lines-of-sight intersect the equatorial plane beyond the magnetic axis, whereas channels 15 to 32 cover the HFS. Core radiation is captured by channels 6 to 30. Note, that this classification is valid only in the very early phase of the disruption. The Ar injected reaches the LFS-LCFS at $t = 1$ ms (a), ionizes and re-distributes poloidally (b), eventually causing a thermal collapse at $t = 3$ ms (c), followed by strong central radiation (d).

minimum time step impacts simulation results due to exponentiation of the RE population. The time step is varied by ASTRA adaptively throughout the simulation to ensure a maximum change of the profiles evolved of 1% during a single time step. The electron and ion heat transport equations are solved applying a fixed boundary condition of $T_e = T_i = 0.5$ eV for technical reasons, i.e. to ensure sufficiently large temperatures necessary for equilibrium calculations and thus for the stability of the simulations.

Calculations of the impurity evolution inside STRAHL are performed on the same numerical grid as used in ASTRA, while being expanded outside the LCFS to resolve the Ar source. A constant time step of 10^{-5} ms is set to ensure resolving the fast dynamics of the atomic processes involved. The convergence of ASTRA-STR AHL simulation results was ensured by examining the impact of varying values for both the minimum time step used in ASTRA as well as for the constant time step used in STRAHL.

4.2. Impurity Ar evolution

In the simulations performed, neutral Ar deposited outside the LCFS propagates into the core plasma with thermal velocity $v_{\text{th}} = 246$ m s⁻¹, ionizes and radiatively cools down the local plasma to a few eV in the process (see figure 6(a) and (b)). As a result of the combined effect of depletion of neutrals in the gas plume through ionization and replenishment through the external source, the effective inward propagation velocity v_{eff} of the neutral gas front is noticeably reduced from the thermal velocity down to on average 78 m s⁻¹.

The transport of ionized Ar is governed by neoclassical mechanisms in these simulations. At the periphery of the cold gas front, the neoclassical diffusion coefficient increases up

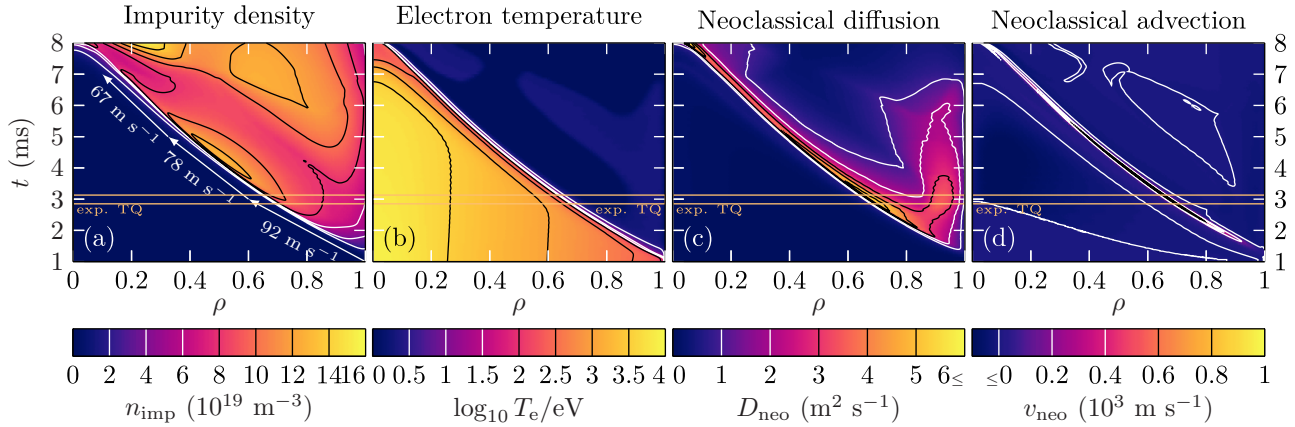


Figure 6. Spatio-temporal plasma evolution of AUG #33 108 in a simulation of Ar MGI, where the transport of impurity ions is treated solely neoclassically: (a) impurity density of both neutral and ionized Ar, as well as effective inward propagation velocity v_{eff} , (b) logarithmic electron temperature, (c) neoclassical diffusion coefficient and (d) neoclassical drift velocity. In the experiment, the TQ is observed to occur between $t = 2.85$ ms and $t = 3.13$ ms (orange ribbon); cf figure 4(d) and figure 5.

to on average $D_{\text{neo}} = 4.0 \text{ m}^2 \text{ s}^{-1}$ (see figure 6(c)), gradually decreasing towards the edge³. Simultaneously, an outward drift of on average $v_{\text{neo}} = 540 \text{ m s}^{-1}$ occurs in the region of largest impurity density gradients, thus being highly localized (see figure 6(d)). The resulting net neoclassical fluxes are in consequence noticeably smaller than the influx of neutrals. The inward propagation of the cooling front is therefore primarily driven by incoming neutrals.

Under consideration of aforementioned impurity transport mechanisms, the plasma stored energy is lost on longer time scales than experimentally observed. Whereas the TQ is detected to occur between $t = 2.85$ ms and $t = 3.13$ ms in AUG #33 108 (see figure 4(d)), the plasma stored energy is gradually lost over the duration of 5.2 ms in the simulation performed, with the central electron temperature collapsing only at around $t = 6.3$ ms (see figure 6(b)). Similarly, the sudden rise of the line integrated electron density prior to the TQ (see figure 4(b)) cannot be captured. Hence, the penetration of material into the plasma core occurs too slow under consideration of only neutral propagation with thermal velocity and neoclassical impurity transport to reproduce experimental observations. Consequently, additional transport mechanisms are considered to dominate impurity and plasma evolution.

To demonstrate the necessity for the consideration of additional transport mechanisms, the inward propagation of neutral Ar is unrealistically assumed to occur with $v_{\text{th}} = 1000 \text{ m s}^{-1}$ in a following simulation; corresponding to a gas temperature of 4800 K in the valve. Yet under these conditions, ionization of incoming neutrals reduces the average effective propagation velocity of the gas plume down to on average $v_{\text{eff}} = 114 \text{ m s}^{-1}$. Being not significantly faster than the effective propagation velocity calculated for the simulation of Ar at room temperature, the plasma evolution obtained is qualitatively similar for

³ Note, that the neoclassical transport coefficients D_{neo} and v_{neo} are the averages of individual transport coefficients from all charge states i with finite density, $n_{\text{imp},i} \geq 10^3 \text{ m}^{-3}$. Averaged coefficients are shown only for illustrative purposes; transport calculations for individual charge states are performed applying the corresponding coefficients obtained by NEOART.

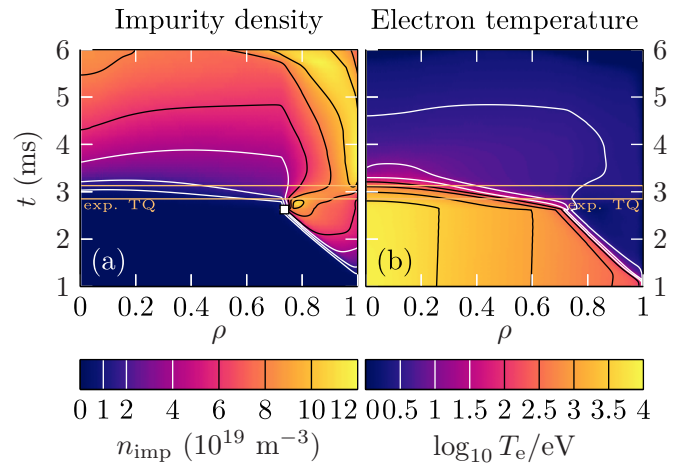


Figure 7. Spatio-temporal plasma evolution of AUG #33 108 in a simulation of Ar MGI with impurity mixing: (a) impurity density of both neutral and ionized Ar, (b) logarithmic electron temperature. The neutral Ar deposited penetrates the core plasma up to $\rho = 0.74$ at $t = 2.6$ ms (white square in (a)).

both values of the valve temperature. The choice of the initial neutral velocity has therefore no significant influence on the occurrence of a fast TQ (or rather lack of therefore) in the simulations, advocating the consideration of additional transport mechanisms.

4.3. Impurity mixing

The experimentally observed plasma response to Ar MGI can be reproduced by impurity transport simulations under the assumption of rapid redistribution of ionized material (see figures 7 and 8). In AUG #33 108, an $(m, n) = (2, 1)$ mode and higher harmonics are excited as the cold gas front reaches the $q = 2$ surface [18], eventually triggering magnetic reconnection and resulting in rapid redistribution of impurities inside the $q = 2$ surface.

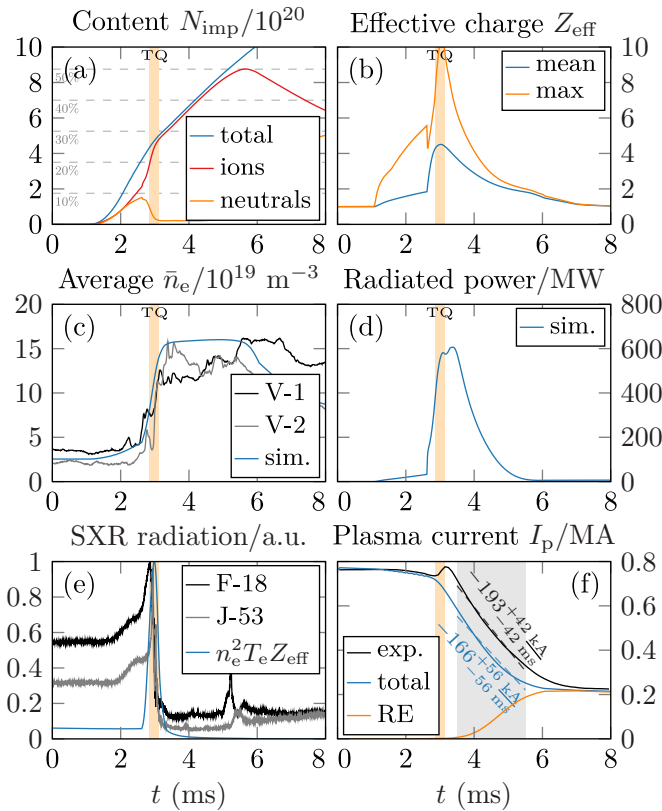


Figure 8. Temporal evolution of plasma parameters in an Ar MGI simulation with impurity mixing: (a) content of the total, ionized and neutral impurity Ar inside the LCFS, (b) volume averaged and maximum effective charge, (c) line averaged electron density compared to measurements of the two CO₂ chords, (d) radiated power, (e) line averaged value of $n_e^2 T_e Z_{\text{eff}}$ as proxy for the measured SXR radiation [37] to determine the onset of the TQ⁷ compared to two central channels of the SXR diagnostic, (f) total and RE plasma current compared to experimental reconstruction. The rate of current decay is averaged between $t = 3.5$ ms and $t = 5.5$ ms (gray region).

The rapid redistribution of impurity ions due to MHD phenomena can be mimicked in 1D transport simulations by applying increased transport coefficients inside the $q = 2$ surface to the impurity ion population when the cold gas front reaches this particular rational surface at $t_{q=2}$. Since the process of magnetic reconnection is a transient phenomenon, the transport coefficients prescribed decrease exponentially on time scales τ_{add} , i.e. in the case of the diffusion coefficient $D_{\text{add}}(t) = D_{\text{add}}^{\text{max}} \exp(-\{t - t_{q=2}\}/\tau_{\text{add}}) \cdot \Theta(t - t_{q=2})$ and similarly for the pinch velocity. In the simulations presented, $D_{\text{add}}^{\text{max}} = 100 \text{ m}^2 \text{ s}^{-1}$, $v_{\text{add}}^{\text{max}} = -200 \text{ m s}^{-1}$ and $\tau_{\text{add}} = 1.0$ ms are applied. Outside the $q = 2$ surface, no additional transport is applied. The numerical values for the additional transport coefficients are obtained by manually varying these parameters across several simulations (not shown). The final set of values is then chosen from the simulation showing best agreement with experimental observations of the line integrated electron density evolution $\bar{n}_e(t)$ and plasma current evolution $I_p(t)$, including the final RE current I_{RE} (see figures 4(b) and (e)). The heat transport coefficient is additionally increased by

$\chi_{\text{add}} = 10 \text{ m}^2 \text{ s}^{-1}$ for both electrons and ions in the entire simulation domain to prevent the occurrence of strongly localized hot plasma beamlets in the simulation during this phase of the discharge. Compared to neoclassical impurity transport discussed (see figure 6(c)), the additional transport is significantly increased.

Alternatively to the rapid redistribution of impurities, the TQ may be triggered by assuming significantly increased heat transport ($\chi > 100 \text{ m}^2 \text{ s}^{-1}$) inside the $q = 2$ surface. Even though the loss of thermal energy occurs significantly faster in simulations of this case, both the obtained line integrated electron density \bar{n}_e and the plasma current decay rate $|dI_p/dt|$ fall noticeably below experimental measurements. Consequently, the rapid redistribution of impurity ions is a necessary assumption to reproduce experimental observations of AUG #33 108.

On a side note, another manifestation of the MHD phenomena triggered by the cold gas front is the occurrence of a sudden increase of the total plasma current, the so called ‘ I_p spike’, at $t = 3.15$ ms (see figure 4(e)). However being focused on the simulation of material propagation and RE generation, reproducing the increase in total plasma current in the simulations goes beyond the scope of this work. Consequently, the evolution of the total plasma current cannot be captured by the simulations performed. However, the current decay rate dI_p/dt is well reproduced during the CQ (see figure 8(f)).

4.4. Plasma evolution with rapid Ar redistribution

In the presence of the additional transport coefficients introduced in section 4.3 ($D_{\text{add}}^{\text{max}} = 100 \text{ m}^2 \text{ s}^{-1}$, $v_{\text{add}}^{\text{max}} = -200 \text{ m s}^{-1}$, $\tau_{\text{add}} = 1.0$ ms), experimental observations are reproduced by the Ar MGI simulation carried out (see figures 7 and 8). The neutral Ar deposited outside the LCFS propagates into the core plasma. Upon reaching the $q = 2$ surface at $\rho_{q=2} = 0.72$ and $t_{q=2} = 2.62$ ms, the additional impurity transport coefficients prescribed to mimic the impact of magnetic reconnection rapidly transport ionized Ar into the central plasma. A considerable amount of impurity ions, $n_{\text{Ar}} \geq 10^{19} \text{ m}^{-3}$, is present at the magnetic axis after 0.42 ms at $t \geq 3.04$ ms.

Given the exponential decay of the additional transport coefficients on a time scale of $\tau_{\text{add}} = 1$ ms, the associated transport alone is insufficient to obtain the level of central impurity accumulation necessary to reproduce experimental observations of the artificial disruption. Here, neoclassical impurity transport provides a substantial contribution to redistribute impurities in the plasma center. Omitting this mechanism in a separate simulation, the impurity content inside the $q = 2$ surface is reduced by as much as 60% during rapid impurity redistribution. Even though sufficient to induce a fast TQ on experimental time scales and to reproduce the increase of the line averaged electron density observed, the plasma current decays too slow under these conditions. This suggests, that in the experiment, a significant fraction of the impurity ions are present in the central plasma, where the remnant plasma current is located, thus accelerating current decay. Still, in the absence of neoclassical transport processes, experimental conditions may be recovered by increasing the additional transport coefficients applied, e.g.

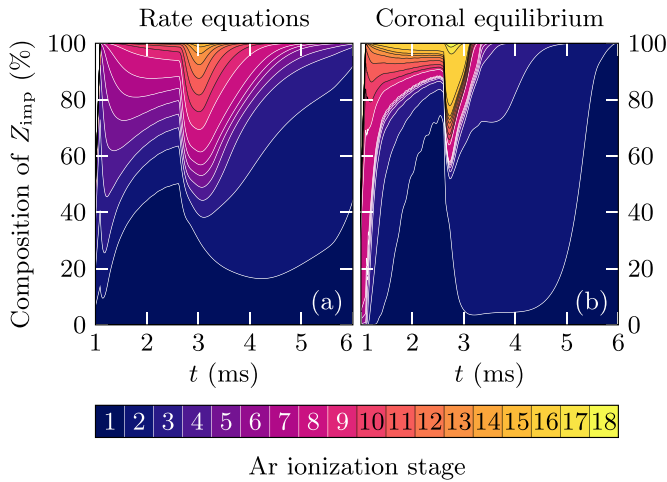


Figure 9. Normalized contributions $\int Z_j n_j dV / \sum_i \int Z_i n_i dV$ of individual Ar charge states j to the global average impurity ion ionization state $Z_{\text{imp}} = \sum_i \int Z_i n_i dV / \sum_i \int n_i dV$ in regions where $\sum_i n_i \geq 10^{16} \text{ m}^{-3}$ obtained (a) through evolution of the charge state distribution according to rate equations and (b) through evaluation of the steady state charge state distribution (coronal equilibrium) according to the electron temperature evolution obtained in case (a). Impurity Ar is injected into the vessel at $t = 1$ ms.

$D_{\text{add}}^{\text{max}} = 100 \text{ m}^2 \text{ s}^{-1} \rightarrow 200 \text{ m}^2 \text{ s}^{-1}$ and $v_{\text{add}}^{\text{max}} = -200 \text{ m s}^{-1} \rightarrow -1000 \text{ m s}^{-1}$, thus emphasizing the importance of neoclassical impurity transport for impurity redistribution inside the $q = 2$ surface.

Even though neoclassical processes alone are also insufficient to cause a thermal collapse of the plasma on experimentally observed time scales (see section 4.2), the rapid redistribution of impurity ions through application of additional transport coefficients modifies the plasma profiles favorably for inward neoclassical transport. As the steepness of the ion density gradient greatly decreases in the process of redistribution, the magnitude of the outward neoclassical pinch is significantly reduced, even reversing direction (with low magnitude). Furthermore, neoclassical diffusion contributions are considerably increased compared to the case without additional transport (see figure 6(c)), being on average inside the $q = 2$ surface of the order of $\langle D_{\text{neo}} \rangle = 20 \text{ m}^2 \text{ s}^{-1}$.

In the process of propagating into the hot central plasma, the Ar is ionized to high ionization states, reaching in the vicinity of the magnetic axis up to $Z_{\text{imp}} = 12.8$ and rapidly increasing the density of plasma electrons (see figures 8(b) and (c)). Given the time scale of material deposition and penetration in MGI experiments, numerical evolution of the individual impurity charge state densities from rate equations is mandatory in simulations of these scenarios as the charge state distribution is not in steady state (coronal equilibrium) throughout the simulation (see figure 9). Evaluating in post-processing the steady state impurity ion distribution for the electron temperature evolution obtained in the simulation presented (see figure 7(b)), the steady state Ar population calculated adapts too quickly to changing plasma conditions as compared to simulation results. In regions of hot plasma, i.e. in front of the cold gas front and inside the $q = 2$ surface during rapid redistribution, impurity ionization is significantly

overestimated. Particularly overpopulated are the ionization stages Ar^{8+} (Ne-like Ar) and Ar^{16+} (He-like Ar). Similarly, recombination to singly ionized Ar in the wake of the cold gas front and in the post-TQ plasma occurs too fast. Consequently, application of the steady state Ar charge state distribution is not suitable to describe the charge state evolution in MGI simulations. Instead, numerical evolution by STRAHL through rate equations is required to adequately describe the impurity charge state evolution on time scales relevant for MGI.

As a consequence of the rapid redistribution of impurities, the majority of the plasma thermal energy is lost through strong radiation within 0.68 ms between $t = t_{q=2}$ and $t = 3.30$ ms. In the resulting cold post-TQ plasma of a few eV, the Ar recombines to low ionization stages, thus decreasing the free electron density in the central plasma. Yet, neutral Ar deposited in the core plasma following the TQ still becomes ionized in the outer half of the plasma, thus keeping the line averaged electron density approximately constant in the 2.43 ms following the TQ. The plasma temperature of a few eV is maintained throughout this phase despite further radiative losses through Ohmic heating by the remaining, decaying plasma current as a result of strong parallel electric fields induced. Only after the majority of the Ohmic current has decayed at $t = 5.72$ ms, the remainder of the plasma stored energy is lost through impurity radiation and the plasma temperature approaches 1 eV. In this environment, Ar recombination back to neutral particles occurs, decreasing the line averaged electron density.

The plasma evolution described agrees qualitatively with experimental observations of AUG #33 108. By assuming rapid redistribution of ionized Ar inside the $q = 2$ surface, the magnitude and time scale of the increase in line averaged electron density following Ar MGI as detected by the two CO_2 interferometers is reproduced in the simulation (see figure 8(c)). Similarly, the duration of the TQ as reconstructed from the evolution of the line averaged quantity $n_e^2 T_e Z_{\text{eff}}$ as a proxy for SXR radiation matches estimates from the SXR diagnostics (see figure 8(e)). Yet, the onset of the TQ obtained in the simulation is slightly delayed by 0.12 ms with respect to experimental estimates. During the CQ following, the averaged current decay rate of $-166_{-56}^{+56} \text{ kA/ms}$ calculated agrees with experimental reconstructions of $-193_{-42}^{+42} \text{ kA/ms}$ within errorbars, both being averaged between $t = 3.5$ ms and $t = 5.5$ ms (see figure 8(f)). Here, the spike of the total plasma current observed experimentally might impact the rate of current decay. Due to the selection procedure of the additional transport coefficients $D_{\text{add}}^{\text{max}}$ and $v_{\text{add}}^{\text{max}}$, the post-CQ RE current measured in AUG #33 108 is matched by the simulation presented. As a result, the plasma evolution during Ar MGI is captured by the simulation throughout the different phases of the disruption.

4.5. RE evolution

Throughout the artificially induced disruption by Ar MGI discussed in the previous section 4.4, the generation of REs is simulated (see figure 10). The source mechanisms considered

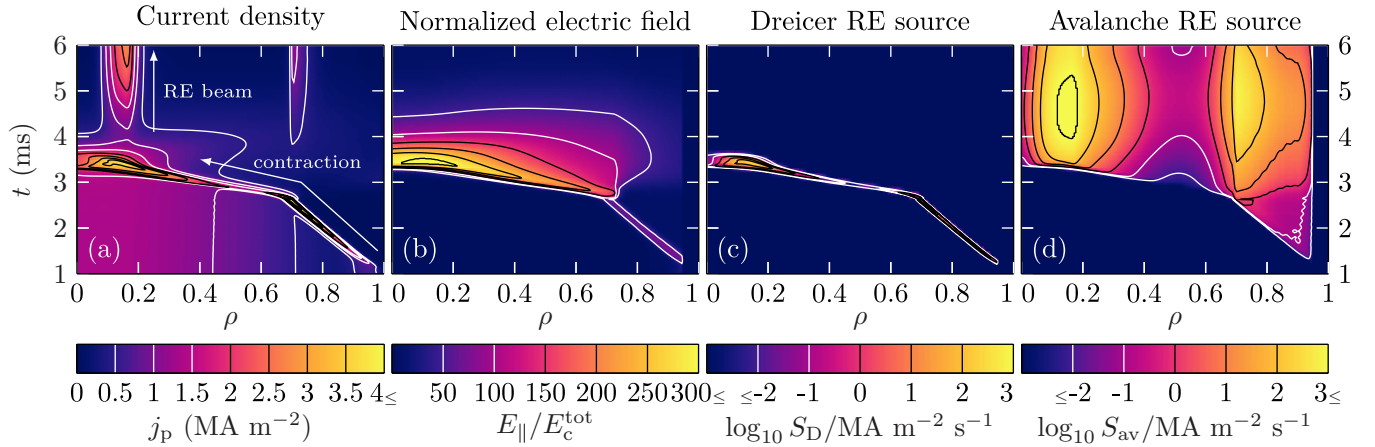


Figure 10. Spatio-temporal response of RE related quantities to Ar MGI in simulations of AUG #33 108: (a) total plasma current density, (b) parallel electric field normalized to the total critical electric field $E_c^{\text{tot}} = E_c n_e^{\text{tot}}/n_e$, (c) logarithmic Dreicer RE source and (d) logarithmic avalanche RE source. The parallel electric field normalized to the Dreicer field, E_{\parallel}/E_D , evolves similar as the logarithmic Dreicer source and is thus not shown.

are highly sensitive to the evolution of the plasma kinetic profiles through (in a simple, analytical picture) exponential dependence on both the electron density and temperature in the case of primary generation, i.e. $S_D \propto \exp(-n_e/T_e)$ (see equation (3)), and on the electron density in the case of avalanche multiplication, i.e. $n_{\text{RE}}(t) \propto \exp(-n_e)$ (see equation (5)). Therefore, the deposition and propagation of impurity ions in the plasma core strongly influences the amount of REs generated in the process. Yet, the final RE current can be reproduced in MGI simulations with reasonable agreement to experimental observations if the additional transport coefficients prescribed are chosen such that the evolution of the line averaged electron density is well approximated in the simulation.

Analyzing the response of the plasma and RE current densities to Ar MGI in the simulation including additional transport coefficients (see figure 10), the edge Ohmic current starts to contract as the material starts to propagate into the confined core; cooling down the plasma to a few eV and reducing the plasma conductivity in the process. Simultaneously, the local electric field E_{\parallel} increases significantly to counter the change in magnetic flux. Even though increasing well above levels E_{\parallel}/E_D for substantial primary RE generation, these conditions do not last locally sufficiently long to generate relevant amounts of primary RE at a given radial location, let alone secondary REs through avalanching (see $\rho \gtrsim 0.8$ in figure 10). Note that the simulations presented do not employ a RE seed population.

Noticeable amounts of REs are generated only after the neutral gas front has reached the $q = 2$ surface at $t_q = 2$, triggering the prescription of additional transport coefficients in the simulation discussed. With increased propagation of the cooling front towards the plasma center, contraction of the current density is accelerated, inducing increasingly stronger electric fields. Given the eventual strong localization of Ohmic current density in the plasma center, the net power loss through impurity radiation is considerably decreased by Ohmic heating in the vicinity of $\rho = 0.16$, keeping the electron temperature in

this region transiently between 10 eV and 20 eV for 0.21 ms (see figure 7(b)). In this environment, sufficient amounts of primary REs are generated to achieve significant avalanche multiplication in the presence of the still strong electric fields, $E_{\parallel} \gg E_c$, of the cold post-TQ plasma of a few eV. This effect is also observed in the vicinity of $\rho = 0.70$. As a result of the selection procedure for the additional transport coefficients, the final RE current is well reproduced by the simulation, being 217 kA, i.e. 4% below the experimental value $I_{\text{RE}}^{\text{exp}} = 225$ kA. Given the greater strength of the avalanche source compared to the Dreicer source (see figures 10(c) and (d)), the post-CQ RE current consists almost entirely of secondary REs, constituting 99% of the total RE current. The Dreicer mechanism provides only a seed population for avalanche multiplication of REs.

The simulation discussed was performed calculating both the primary and secondary RE source from expressions by Hesslow *et al* [10, 13]. Employing the analytical formulae of Connor and Hastie [33], and Rosenbluth and Putvinski [34] instead (equations (3) and (5)), a larger RE current is obtained at the end of the CQ, being 295 kA, i.e. +31% $I_{\text{RE}}^{\text{exp}}$. In this case, the Dreicer mechanism not only provides a seed population for avalanche multiplication, but contributes a substantial fraction of 35% to the total RE current. Furthermore, a noticeable RE current is obtained earlier in the simulation, exceeding 1 kA at $t = 1.36$ ms as opposed to $t = 2.55$ ms when employing the CODE neural network instead. The associated considerable increase of the Dreicer growth rate under application of the analytical expression of equation (3) [33] is expected as several effects reducing the flux of thermal electrons into the runaway region of momentum space are not considered in this model, being partial screening of impurities and the energy dependence of the Coulomb logarithm [13].

Simultaneously, the strength of the avalanche source is reduced applying the expression of Rosenbluth and Putvinski [34] of equation (5), as the nuclear charge of impurity ions is assumed to be screened completely by bound electrons in

this model. However as discussed by Hesslow *et al* [9], collision rates are enhanced in the presence of partially ionized impurities, leading to a stronger than linear dependence of S_{av} on $E_{||}$ for large electric fields under consideration of both free and bound electrons, thus increasing the growth rate beyond levels predicted by equation (5). Nevertheless, despite a larger RE seed population and a longer multiplication time in simulations employing the analytical formulae of equations (3) and (5), a comparable avalanche current is obtained in simulations of both cases.

It should be noted, that the additional transport coefficients employed are chosen to match the final RE current, as well as the evolution of plasma current $I_p(t)$ and line averaged electron density $\bar{n}_e(t)$, under application of the RE generation models by Hesslow *et al* [10, 13]. However, experimental conditions can also be reproduced describing the RE sources by the analytic expressions of equations (3) and (5) by setting e.g. $D_{add}^{max} = 100 \text{ m}^2 \text{ s}^{-1} \rightarrow 200 \text{ m}^2 \text{ s}^{-1}$ and $v_{add}^{max} = -200 \text{ m s}^{-1} \rightarrow -400 \text{ m s}^{-1}$. For this choice of parameters, application of the CODE neural network and equation (6) underestimates the RE current generated, being 173 kA ($-23\% I_{RE}^{exp}$). Yet, the overall evolution of the RE current is qualitatively similar for both choices of transport coefficients discussed for each set of the RE generation models. The relative importance of the RE generation mechanisms is unaffected.

Despite employing different models for RE generation and application of varying additional transport coefficients D_{add}^{max} and v_{add}^{max} , the final RE currents obtained in the simulations discussed are of similar magnitude, being within ${}_{-23\%}^{+35\%} I_{RE}^{exp}$, as the available poloidal magnetic flux is dissipated by the total RE generation following the disruption. Consideration of a hot-tail source is hence not expected to modify simulation results significantly. Application of the analytical formulae of Connor and Hastie [33], and Rosenbluth and Putvinski [34] to described RE generation therefore yields a reasonable estimate for the order of magnitude of the post-disruption RE current in MGI scenarios.

Still, the evolution of the RE current during the CQ is captured only under application of the models by Hesslow *et al* [10, 13], where a substantial RE current is obtained after around 4 ms (see figure 8(f)). Experimentally, the hard x-ray signal increases after 5 ms (see figure 4(f)); note the temporal resolution of 1 ms), thus being delayed by around 1 ms compared to the RE current simulated. Given the finite time required for newly generated REs to extract relevant amounts of energy from the electric field (requiring in excess of 10^3 revolutions in the tokamak; see section 2.4), a delay of 1 ms between occurrence of a noticeable RE current in the simulation and detection of a hard x-ray radiation in the experiment appears reasonable. Consequently, the RE current evolution obtained applying the models by Hesslow *et al* [10, 13] is in line with measurements of hard x-ray radiation. Applying the analytical formulae of Connor and Hastie [33], and Rosenbluth and Putvinski [34] instead, a significant RE current is present already at around 2.5 ms. Following above argument regarding the delay between RE current and hard x-ray signal, the RE current evolution of simulations using the analytical

formulae is contrary to experimental observations of HXR radiation.

5. Conclusion

In this work, we presented the toolkit ASTRA-STRahl for self-consistent 1.5D transport simulations of background plasma, impurity species and runaway electrons in MGI scenarios of tokamak plasmas. The model was applied successfully to study the interactions between aforementioned species in simulations of Ar MGI in AUG #33 108, covering all distinct phases of the artificially induced disruption, i.e. the pre-thermal quench, the thermal collapse and the conversion of Ohmic current to runaway electrons. Despite the complexity and the 3D nature of MGI, the evolution of key plasma parameters, such as line integrated electron density and plasma current, can be reproduced in a 1D framework with good agreement compared to experimental observations. The validity of the 1D approach is likely due to the combination of a flux-surface averaged treatment of an arbitrary magnetic geometry by ASTRA, fast equilibration along magnetic field lines and the strong localization of the impurity radiation up to the thermal quench.

The propagation of impurities into the central plasma is driven by rapid redistribution as a result of presumably MHD activity, triggered by the cold gas reaching the $q = 2$ rational surface. Still, neoclassical processes provide a non-negligible contribution to inward impurity ion transport. Considering only neoclassical effects, the cold gas front propagates too slow with $v_{eff} \ll v_{th}$ to induce a thermal quench on experimental time scales as propagation is driven primarily by incoming neutrals. The additional transport necessary can be described reasonably well by a simple 0D model of exponentially decaying coefficients for diffusive and convective transport, thus requiring few free parameters. For the simulation of AUG #33 108, the choices $D_{add}^{max} = 100 \text{ m}^2 \text{ s}^{-1}$, $v_{add}^{max} = -200 \text{ m s}^{-1}$ and $\tau_{add} = 1 \text{ ms}$ were found suitable to reproduce experimental observations. The applicability of these values for simulations of other AUG discharges will have to be investigated in future work.

The generation of REs in AUG #33 108 is described reasonably well in the simulation presented, reproducing the final RE current obtained experimentally. Consideration of the impact of partially ionized impurities on RE generation through application of the models by Hesslow *et al* [10, 13] is necessary to explain both current and HXR measurements. Simulations evolving the RE population based on the commonly used formulae by Connor and Hastie [33], and Rosenbluth and Putvinski [34] cannot capture these experimental observations, highlighting the importance of a thorough treatment of RE generation.

An open question is the impact of the hot-tail mechanism not considered in this work. Even though the Dreicer source is suspected to compensate the absence of a hot-tail source, further simulations under application of a suitable model for hot-tail generation are needed eventually. Given the lack of suitable models, investigating the impact of the

hot-tail mechanism on the scenario discussed will be left for future work. Similarly, given the sensitivity of runaway generation mechanisms on plasma and impurity parameters, the 1D treatment of the inherently 3D process of material injection introduces further uncertainties in this work. Here, additional experimental measurements could constrain the impurity propagation assumed in this work.

Application of the model presented to Ar MGI in AUG #33 108 demonstrates the suitability of this toolkit for the further study of MMI in tokamak plasmas, in particular of MGI in AUG discharges. Future work will have to investigate if not only individual discharges, but parametric trends observed experimentally can be reproduced. Here, the impact of varying impurity amounts, species and composition on RE generation is to be studied in MGI scenarios. Eventually, the impurity deposition model employed is to be extended by an SPI model, thus allowing MMI simulations of ITER relevant scenarios.

Acknowledgments

This work was supported by the EUROfusion - Theory and Advanced Simulation Coordination (E-TASC). This work has been carried out within the framework of the EUROfusion Consortium and has received funding from the Euratom research and training programme 2014-2018 and 2019-2020 under grant agreement No 633053. The views and opinions expressed herein do not necessarily reflect those of the European Commission.

Appendix A Finite volume scheme of STRAHL

The first order central finite difference scheme used in STRAHL is replaced by a vertex centered finite volume discretization of the same order to enable simulations with arbitrary Péclet number μ . Starting from the STRAHL transport equation in cylindrical coordinates,

$$\frac{\partial n}{\partial t} = \frac{1}{r} \frac{\partial}{\partial r} \left(D \frac{\partial n}{\partial r} - v n \right) + S, \quad (\text{A1})$$

the conservative form of the transport equation for the density $\bar{n}_i(r_i, t) = \int_{\Omega_i} r n(r, t) dr / \int_{\Omega_i} r dr$ averaged over the cell $\Omega_i = [r_{i-\frac{1}{2}}, r_{i+\frac{1}{2}}]$ is

$$\frac{\partial \bar{n}_i}{\partial t} = \frac{2}{r_{i+\frac{1}{2}}^2 - r_{i-\frac{1}{2}}^2} \left[r D \frac{dn}{dr} - r v n \right]_{r_{i-\frac{1}{2}}}^{r_{i+\frac{1}{2}}} + \bar{S}_i. \quad (\text{A2})$$

Quantities at the cell boundaries are evaluated as the average of both cells, i.e. $X_{i\pm\frac{1}{2}} = [X_i + X_{i\pm 1}] / 2$. For the transport coefficients, the following substitutions are applied:

$$\left. \begin{aligned} \tilde{D}_{i\pm} &= \frac{r_{i\pm\frac{1}{2}}}{g_i \Delta r_{i\pm}} D_{i\pm\frac{1}{2}}, & \tilde{v}_{i\pm} &= \frac{r_{i\pm\frac{1}{2}}}{2g_i} v_{i\pm\frac{1}{2}}, \\ g_i &= r_{i+\frac{1}{2}}^2 - r_{i-\frac{1}{2}}^2, & \Delta r_{i\pm} &= \mp (r_i - r_{i\pm 1}). \end{aligned} \right\} \quad (\text{A3})$$

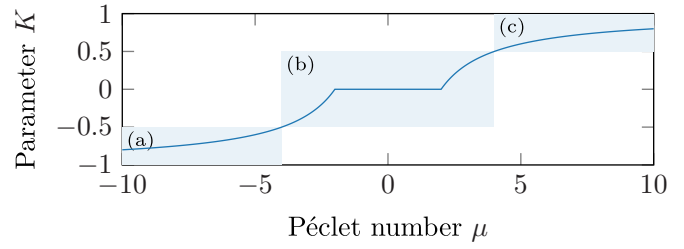


Figure A1. The discretization method applied is adjusted through the parameter K (see equation (A5)). For cases of strong advection with $|\mu| > 4$ ((a) and (c)), the backward/forward scheme dominates the discretization, whereas for strong diffusion with $|\mu| < 4$ (b), the central scheme dominates (see equation (A4)).

The temporal derivative is discretized applying the θ -method, such that $\partial \bar{n}_i / \partial t = \theta F(\bar{n}_i^{j+1}) + (1 - \theta) F(\bar{n}_i^j)$. Unconditional stability of the scheme is ensured for $\theta \geq 1/2$ and therefore $\theta = 1/2$ is chosen. For a time step size τ , i.e. $t^{j+1} = t^j + \tau$, the complete discretization is obtained as

$$\begin{aligned} \bar{n}_i^{j+1} + \bar{n}_i^j &= \tau \bar{S}_i \\ &+ \tau \left\{ \tilde{D}_{i-} + \left[1 + K_{i-\frac{1}{2}} \right] \tilde{v}_{i-} \right\} \cdot \left(\bar{n}_{i-1}^{j+1} + \bar{n}_{i-1}^j \right) \\ &- \tau \left\{ \tilde{D}_{i-} - \left[1 - K_{i-\frac{1}{2}} \right] \tilde{v}_{i-} \right\} \cdot \left(\bar{n}_i^{j+1} + \bar{n}_i^j \right) \\ &+ \tau \left\{ \tilde{D}_{i+} - \left[1 + K_{i+\frac{1}{2}} \right] \tilde{v}_{i+} \right\} \cdot \left(\bar{n}_i^{j+1} + \bar{n}_i^j \right) \\ &+ \tau \left\{ \tilde{D}_{i+} - \left[1 - K_{i+\frac{1}{2}} \right] \tilde{v}_{i+} \right\} \cdot \left(\bar{n}_{i+1}^{j+1} + \bar{n}_{i+1}^j \right). \end{aligned} \quad (\text{A4})$$

Depending on the Péclet number $\mu_i = v_i \Delta r_i / D_i$, the spatial discretization is changed adaptively from a central scheme ($|\mu_i| \rightarrow 0$) to upwinding ($|\mu_i| \rightarrow \infty$) through the parameter (see figure A1)

$$K_i = \max(0, 1 - 2/|\mu_i|) \cdot \text{sgn}(\mu_i). \quad (\text{A5})$$

The scheme presented is applied for the discretization inside the STRAHL simulation domain. To treat the left and right boundary, the discretization is adjusted in accordance with the existing STRAHL boundary conditions.

ORCID iDs

O. Linder <https://orcid.org/0000-0002-5637-2861>

G. Papp <https://orcid.org/0000-0003-0694-5446>

References

- [1] Reux C., Plyusnin V., Alper B., Alves D. and Bazylev B. et al 2015 Runaway electron beam generation and mitigation during disruptions at JET-ILW *Nucl. Fusion* **55** 093013
- [2] Matthews G.F., Bazylev B., Baron-Wiechec A., Coenen J. and Heinola K. et al 2016 Melt damage to the JET ITER-like Wall and divertor *Phys. Scr.* **T167** 014070
- [3] Hender T.C., Wesley J.C., Bialek J., Bondeson A. and Boozer A.H. et al 2007 Chapter 3: MHD stability, operational limits and disruptions *Nucl. Fusion* **47** S128

- [4] Pautasso G., Bernert M., Dibon M., Duval B. and Dux R. *et al* 2017 Disruption mitigation by injection of small quantities of noble gas in ASDEX Upgrade *Plasma Phys. Control. Fusion* **59** 014046
- [5] Coda S., Agostini M., Albanese R., Alberti S. and Alessi E. *et al* 2019 Physics research on the TCV tokamak facility: from conventional to alternative scenarios and beyond *Nucl. Fusion* **59** 112023
- [6] Commaux N., Baylor L.R., Jernigan T.C., Hollmann E.M., Parks P.B. *et al* 2010 Demonstration of rapid shutdown using large shattered deuterium pellet injection in DIII-D *Nucl. Fusion* **50** 112001
- [7] Boozer A.H. 2019 Magnetic surface loss and electron runaway *Plasma Phys. Control. Fusion* **61** 024002
- [8] Hesslow L., Embréus O., Wilkie G.J., Papp G. and Fülöp T. 2018 Effect of partially ionized impurities and radiation on the effective critical electric field for runaway generation *Plasma Phys. Control. Fusion* **60** 074010
- [9] Hesslow L., Embréus O., Hoppe M., DuBois T.C. and Papp G. *et al* 2018 Generalized collision operator for fast electrons interacting with partially ionized impurities *J. Plasma Phys.* **84** 905840605
- [10] Hesslow L., Embréus O., Vallhagen O. and Fülöp T. 2019 Influence of massive material injection on avalanche runaway generation during tokamak disruptions *Nucl. Fusion* **59** 084004
- [11] Konovalov S., Aleynikov P., Aleynikova K., Gribov Y. and Huijsmans G.T.A. *et al* 2014 Integrated modelling of ITER disruption mitigation *Contribution at the 25th IAEA Int. Conf. on Fusion Energy* 13.-18.10. St. Petersburg Russian Federation, TH/P3-31
- [12] Aleynikov P., Aleynikova K., Breizman B., Huijsmans G.T.A., Konovalov S., Putvinski S. and Zhogolev V. 2014 Kinetic modelling of runaway electrons and their mitigation in ITER *Proc. 25th Int. Conf. on Fusion Energy* (St Petersburg, Russia, 13–18 October 2014) (Vienna: IAEA) TH/P3-38 (http://www-naweb.iaea.org/napc/physics/FEC/FEC2014/fec2014-preprints/319_THP338.pdf)
- [13] Hesslow L., Unnerfelt L., Vallhagen O., Embréus O. and Hoppe M. *et al* 2019 Evaluation of the Dreicer runaway generation rate in the presence of high-Z impurities using a neural network *J. Plasma Phys.* **85** 475850601
- [14] Stahl A., Embréus O., Papp G., Landreman M. and Fülöp T. 2016 Kinetic modelling of runaway electrons in dynamic scenarios *Nucl. Fusion* **56** 112009
- [15] Papp G., Fülöp T., Fehér T., de Vries P.C. and Riccardo V. *et al* 2013 The effect of ITER-like wall on runaway electron generation in JET *Nucl. Fusion* **53** 123017
- [16] Fable E., Angioni C., Ivanov A.A., Lackner K. and Maj O. *et al* 2013 Dynamical coupling between magnetic equilibrium and transport in tokamak scenario modelling, with application to current ramps *Plasma Phys. Control. Fusion* **55** 074007
- [17] Dux R., Peeters A.G., Gude A., Kallenbach A. and Neu R. *et al* 1999 Z dependence of the core impurity transport in ASDEX Upgrade H mode discharges *Nucl. Fusion* **39** 1509
- [18] Fable E., Pautasso G., Lehnen M., Dux R. and Bernert M. *et al* 2016 Transport simulations of the pre-thermal-quench phase in ASDEX Upgrade massive gas injection experiments *Nucl. Fusion* **56** 026012
- [19] Putvinski S., Fujisawa N., Post D., Putvinskaya N. and Rosenbluth M.N. *et al* 1997 Impurity fueling to terminate Tokamak discharges *J. Nucl. Mater.* **316** 241–3
- [20] Fehér T., Smith H.M., Fülöp T. and Gál K. 2011 Simulation of runaway electron generation during plasma shutdown by impurity injection in ITER *Plasma Phys. Control. Fusion* **53** 035014
- [21] Ivanov A.A., Khayrutdinov R.R., Medvedev S.Y. and Poshekhnov Y.Y. 2005 New adaptive grid plasma evolution code SPIDER *32nd EPS Conf. on Plasma Phys.* (Tarragona, Spain, 27 June - 1 July 2005) P5.063 (http://epsppd.epfl.ch/Tarragona/pdf/P5_063.pdf)
- [22] Summers H.P. The ADAS User Manual version 2.6. (www.adas.ac.uk)
- [23] Peeters A.G. 2000 Reduced charge state equations that describe Pfirsch Schlüter impurity transport in tokamak plasma *Phys. Plasmas* **7** 268
- [24] Angioni C., Bilato R., Casson F.J., Fable E. and Mantica P. *et al* 2017 Gyrokinetic study of turbulent convection of heavy impurities in tokamak plasmas at comparable ion and electron heat fluxes *Nucl. Fusion* **57** 022009
- [25] Hundsdorfer W. and Verwer J.G. 2003 *Numerical Solution of Time-Dependent Advection-Diffusion-Reaction Equations* (Berlin: Springer) 1st edn
- [26] Chiu S.C., Rosenbluth M.N., Harvey R.W. and Chan V.S. 1998 Fokker-Planck simulations mylb of knock-on electron runaway avalanche and bursts in tokamaks *Nucl. Fusion* **38** 1711
- [27] Harvey R.W., Chan V.S., Chiu S.C., Evans T.E. and Rosenbluth M.N. *et al* 2000 Runaway electron production in DIII-D killer pellet experiments, calculated with the CQL3D/KPRAD model *Phys. Plasmas* **7** 4590
- [28] Smith H.M. and Verwichte E. 2008 Hot tail runaway electron generation in tokamak disruptions *Phys. Plasmas* **15** 072502
- [29] Harvey R.W., Petrov Y.V., Kim C.C., Forest C.B. and Lao L.L. *et al* 2019 Time-dependent runaway electron simulations: Ampère–Faraday equations implemented in CQL3D *Nucl. Fusion* **59** 106046
- [30] Breizman B.N., Aleynikov P., Hollmann E.M. and Lehnen M. 2019 Physics of runaway electrons in tokamaks *Nucl. Fusion* **59** 083001
- [31] Insulander Björk K., Papp G., Embréus O., Hesslow L. and Fülöp T. *et al* 2020 Kinetic modelling of runaway electron generation in argon-induced disruptions in ASDEX Upgrade *J. Plasma Phys.* (arXiv:2005.01606)
- [32] Papp G., Stahl A., Drevlak M., Fülöp T. and Lauber P.W. *et al* 2015 Towards self-consistent runaway electron modeling *42nd EPS Conf. on Plasma Physics* (Lisbon, Portugal, 22–26 July 2015) P1.173 (<http://ocs.ciemat.es/EPS2015PAP/pdf/P1.173.pdf>)
- [33] Connor J.W. and Hastie R.J. 1975 Relativistic limitations of runaway electrons *Nucl. Fusion* **16** 415
- [34] Rosenbluth M.N. and Putvinski S.V. 1997 Theory for avalanche of runaway electrons in tokamaks *Nucl. Fusion* **37** 1355
- [35] Pautasso G., Fuchs C.J., Gruber O., Maggi C.F. and Maraschek M. *et al* 2007 Plasma shut-down with fast impurity puff on ASDEX Upgrade *Nucl. Fusion* **47** 900
- [36] Fil A. 2015 Modeling of massive gas injection triggered disruptions in tokamak plasmas *PhD thesis* Aix-Marseille University
- [37] Igochine V., Gude A., Maraschek M. and the ASDEX Upgrade Team 2010 *Hotlink based Soft X-ray Diagnostic on ASDEX Upgrade* IPP 1/338 Max-Planck-Institut für Plasmaphysik, May


Paper #2

O. Linder, G. Papp, E. Fable, F. Jenko, G. Pautasso, the ASDEX Upgrade Team and the EUROfusion MST1 Team,
Electron runaway in ASDEX Upgrade experiments of varying core temperature,

Journal of Plasma Physics **87**, 905870301 (2021).

<https://doi.org/10.1017/S0022377821000416>

arXiv:2101.04471 [physics.plasm-ph]

Copyright © The Author(s), 2021. Published by Cambridge University Press under the terms of the Creative Commons Attribution license CC BY 4.0 (<http://creativecommons.org/licenses/by/4.0/>), which permits unrestricted re-use, distribution, and reproduction in any medium, provided the original work is properly cited. Reprinted without changes. 

Electron runaway in ASDEX Upgrade experiments of varying core temperature

O. Linder^{1,†,‡}, G. Papp^{1,§}, E. Fable¹, F. Jenko¹, G. Pautasso¹, the ASDEX Upgrade Team[‡] and the EUROfusion MST1 Team[§]

¹Max-Planck-Institut für Plasmaphysik, 85748 Garching, Germany

(Received 13 January 2021; revised 29 March 2021; accepted 30 March 2021)

The formation of a substantial postdisruption runaway electron current in ASDEX Upgrade material injection experiments is determined by avalanche multiplication of a small seed population of runaway electrons. For the investigation of these scenarios, the runaway electron description of the coupled 1.5-D transport solvers ASTRA-STRAHL is amended by a fluid model describing electron runaway caused by the hot-tail mechanism. Applied in simulations of combined background plasma evolution, material injection and runaway electron generation in ASDEX Upgrade discharge #33108, both the Dreicer and hot-tail mechanism for electron runaway produce only ~ 3 kA of runaway current. In colder plasmas with core electron temperatures $T_{e,c}$ below 9 keV, the postdisruption runaway current is predicted to be insensitive to the initial temperature, in agreement with experimental observations. Yet in hotter plasmas with $T_{e,c}$ above 10 keV, hot-tail runaway can be increased by up to an order of magnitude, contributing considerably to the total postdisruption runaway current. In ASDEX Upgrade high-temperature runaway experiments, however, no runaway current is observed at the end of the disruption, despite favourable conditions for both primary and secondary runaway.

Key words: fusion plasma, runaway electrons, plasma simulation

1. Introduction

In future current-carrying fusion devices, the formation of a substantial population of runaway electrons during the sudden loss of thermal confinement poses a significant threat to the integrity of the plasma vessel. Already in present-day devices, beams of lost runaway electrons are observed to damage plasma facing components, e.g. at JET (Matthews *et al.* 2016) or at Alcator C-Mod (Tinguely *et al.* 2018). However, in high-current devices, a larger runaway current is expected due to increased avalanche multiplication (Boozer 2019). As the total energy carried by a runaway beam grows quadratically with the runaway current (Martín-Solís *et al.* 2014), the threat to high-current fusion devices is amplified. Therefore, runaway electron generation has to be suppressed and potential disruptions mitigated (Breizman *et al.* 2019).

[†] Email address for correspondence: oliver.linder@ipp.mpg.de

[‡] See author list of H. Meyer *et al.* 2019 *Nucl. Fusion* **59**, 112014.

[§] See author list of B. Labit *et al.* 2019 *Nucl. Fusion* **59**, 086020.

Suppression of electron runaway may be achieved through massive material injection, as proposed for ITER (Lehnen *et al.* 2015). This scheme is currently being investigated across several machines using massive gas injection (MGI), e.g. at ASDEX Upgrade (AUG) (Pautasso *et al.* 2017, 2020) or TCV (Coda *et al.* 2019), and shattered pellet injection (SPI), e.g. at DIII-D (Commaux *et al.* 2010; Paz-Soldan *et al.* 2020) and JET (Reux *et al.* 2021). Given the unfavourable scaling of the runaway electron threat to future devices due to increased avalanche multiplication, experimental investigation is complemented by theoretical and computational studies to aid in extrapolation from present to future devices (Breizman *et al.* 2019).

Owing to the complexity of the runaway electron problem, different computational tools are used for the investigation of different aspects of electron runaway. The most accurate description is achieved by kinetic tools, such as the full- f Fokker–Planck solver CODE (Stahl *et al.* 2016), where the runaway fluxes are determined through evolution of the momentum-space electron distribution. However, the simultaneous spatio-temporal evolution of the background plasma or impurities injected is challenging to calculate in these frameworks (Hoppe *et al.* 2021). For this purpose, 1-D transport codes such as ASTRA-STRAHL (Dux *et al.* 1999; Fable *et al.* 2013; Linder *et al.* 2020) or GO (Papp *et al.* 2013; Vallhagen *et al.* 2020) can be applied. Here, electron runaway is described through a fluid treatment, as a kinetic description greatly increases the computational cost. For a description of the 3-D spatio-temporal evolution of the magnetic field during disruptions, non-linear magnetohydrodynamic (MHD) codes such as JOREK (Bandaru *et al.* 2019) are used.

The recent development of sophisticated reduced kinetic models describing electron runaway due to momentum-space diffusion of thermal electrons (Hesslow *et al.* 2019b) and knock-on collisions of existing runaways with the thermal bulk (Hesslow *et al.* 2019a) has accelerated modelling efforts. Applied inside the transport code ASTRA-STRAHL, simulations of the spatio-temporal evolution of runaway electron population, background plasma and material injected have recently been found capable of describing AUG disruptions, as demonstrated modelling AUG discharge #33108 (Linder *et al.* 2020).

In this work, we investigate runaway electron (seed) generation in AUG experiments of varying core temperature between 4 and 20 keV by means of ASTRA-STRAHL simulations. For this purpose, we expand upon the findings by Linder *et al.* (2020), performing coupled simulations of background plasma evolution, material injection and electron runaway. As kinetic modelling using CODE suggests formation of a seed population of runaway electrons predominantly due to rapid cooling (Insulander Björk *et al.* 2020; Hoppe *et al.* 2021), the runaway electron generation models used in ASTRA-STRAHL are amended by a model by Smith & Verwichte (2008) describing this effect. The toolkit ASTRA-STRAHL is then applied for the investigation of the (seed) runaway electron population in simulations of AUG discharge #33108. Throughout the simulations performed, the preinjection on-axis electron temperature is varied between 4 and 20 keV, as SPI experiments in DIII-D suggest a growing seed runaway population as the electron temperature increases (Paz-Soldan *et al.* 2020). The simulation results obtained are compared against measurements of AUG disruption experiments.

This paper is organized as follows. A brief description of the model employed is provided in § 2, with experimental aspects of AUG discharge #33108 covered in § 3. More details on both parts can be found in Linder *et al.* (2020). Simulations of runaway electron generation in the AUG discharge chosen are presented in § 4. The impact of a variation of the preinjection on-axis electron temperature on the postdisruption runaway electron current calculated is discussed in § 5. Finally, a conclusion is provided in § 6. Additionally, a simplified model for the hot-tail runaway electron current density at the

end of the thermal quench is presented in [Appendix A](#); the impact of the average runaway electron velocity on the postdisruption runaway current is discussed in [Appendix B](#).

2. Model description

The spatio-temporal evolution of the main tokamak plasma, material introduced through MGI, and runaway electrons generated in the process can be described by the coupled 1.5-D transport codes ASTRA (Fable *et al.* 2013) and STRAHL (Dux *et al.* 1999). The suitability of this toolkit for the simulation of runaway electron generation during MGI has recently been demonstrated by Linder *et al.* (2020). Building on the model presented, the capabilities of ASTRA-STRAHL are expanded to additionally consider electron runaway due to the hot-tail mechanism. Therefore, only a brief overview of ASTRA-STRAHL is given, with details described in Linder *et al.* (2020).

2.1. The coupled transport codes ASTRA-STRAHL

The evolution of the main plasma and impurity species introduced is calculated by ASTRA and STRAHL, respectively, following the macroscopic transport equation

$$\frac{\partial Y}{\partial t} = \left(\frac{\partial V}{\partial \rho} \right)^{-1} \frac{\partial}{\partial \rho} \left(\frac{\partial V}{\partial \rho} \langle (\Delta \rho)^2 \rangle \left\{ D \frac{\partial Y}{\partial \rho} - v Y \right\} \right) + \sum_j S_j \quad (2.1)$$

for a fluid quantity Y in the presence of diffusion D , convection v and sources S_j . The quantity ρ denotes the toroidal flux-surface label, with V being the flux-surface volume.

Inside ASTRA, the poloidal magnetic flux Ψ , both the electron temperature T_e and ion temperature T_i and the density n_{RE} of runaway electrons are evolved. In the case of electron heat transport, sources S_j due to Ohmic heating, electron-to-ion heat transport and impurity radiation from STRAHL (line radiation and Bremsstrahlung) are taken into account throughout the entirety of the simulations and assumed to outweigh radial transport (Fehér *et al.* 2011) (confirmed by the simulations presented). Consequently, turbulent radial transport is neglected. The electron density n_e is calculated from quasi-neutrality, i.e. $n_e(t) = n_D + \sum_k \langle Z_k \rangle n_k(t)$ where n_D denotes the density of deuterium, the main plasma species. The densities n_k and average charges $\langle Z_k \rangle$ of the impurities k are evolved by STRAHL. The magnetic equilibrium is obtained from the ASTRA built-in 3-moment solver, applicable for circular discharges of MGI experiments in AUG (Pautasso *et al.* 2017, 2020).

The impurity densities $n_{k,i}$ are evolved by STRAHL for each charge state i under consideration of electron impact ionization and recombination rates from ADAS (Summers 2004). Neutrals originating from a gas valve are deposited in the simulation domain just outside the last closed flux surface (LCFS) and propagate into the core plasma with thermal velocity $v_{k,0} = v_{th} = \sqrt{T/m}$, T and m being the neutral impurity temperature and mass, respectively. The source strength $-dN_k/dt$ is determined from the continuity equation $dN_k/dt + v_{k,0}N_kA_v(t)/V_v = 0$ for a valve with particle inventory N_k , aperture size $A_v(t)$ and volume V_v . Impurity transport due to neoclassical processes is described by NEOART (Peeters 2000).

Following the injection of impurities, (2, 1) MHD modes and higher harmonics are triggered as the cold gas front reaches the flux surface with safety factor $q = 2$ (Fable *et al.* 2016) at time $t_{q=2}$. As a result, the current density inside the $q = 2$ surface is redistributed, which is achieved in the simulations by flattening the q -profile to $q = 2$ under conservation of the total poloidal magnetic flux. During the breakup of the magnetic surfaces, the transport of ionized material and heat is greatly enhanced until closed flux surfaces have re-emerged. To mimic this effect inside ASTRA, additional transport coefficients of the

form

$$X_{\text{add}}(t) = X_{\text{add}}^{\text{max}} \exp\left(-\frac{t - t_{q=2}}{\tau_{\text{add}}}\right) \Theta(t - t_{q=2}) \quad (2.2)$$

are applied for both diffusive and convective transport inside the $q = 2$ surface with $D_{\text{add}}^{\text{max}} = 100 \text{ m}^2 \text{ s}^{-1}$, $v_{\text{add}}^{\text{max}} = -1000 \text{ m s}^{-1}$, $\chi_{\text{add}}^{\text{max}} = 100 \text{ m}^2 \text{ s}^{-1}$ (Fehér *et al.* 2011) and $\tau_{\text{add}} = 1.0 \text{ ms}$. The evolution of plasma parameters in ASTRA-STRAHL simulations applying this approach for discharge AUG #33108 studied in this work has been compared in detail to experimental observations in the publication by Linder *et al.* (2020), where application of these coefficients was found necessary to reproduce the experimentally observed increase of the line-averaged electron density. Please note, that in this work, the additional transport coefficients are set to generic values (instead of a refined fit) as experimental observations are adequately described under a moderate variation of these coefficients by up to 50%. In the simulations of varying preinjection on-axis electron temperature between 4 and 20 keV discussed in § 5, transport coefficients of identical magnitude are prescribed, since the MHD modes triggered are largely current driven. As such, a (strong) dependence of the mode amplitude on predisruption temperature and pressure is not expected. A more detailed investigation on this subject is planned for future work.

The simulations presented in this work are carried out employing a radial grid of 401 points inside ASTRA, extending from the magnetic axis up to the LCFS. For STRAHL calculations, the grid is expanded to additionally include the scrape-off layer. Both minimum and constant time step in ASTRA and STRAHL, respectively, are set to 10^{-5} ms to resolve transient events. The suitability of these simulation settings was ensured by means of convergence scans of radial and temporal resolution in prestudy simulations.

2.2. Runaway electron generation

The process of electron runaway is described by reduced fluid models, providing sources S_j for the evolution of the runaway electron density n_{RE} inside ASTRA¹. Mechanisms for runaway electron generation considered in this work include hot-tail generation due to rapid cooling (see § 2.2.1), Dreicer generation due to momentum-space diffusion of thermal electrons (see § 2.2.2) and avalanche generation due to knock-on collision of existing runaway with thermal electrons (see § 2.2.3). Further mechanisms due to nuclear processes (Vallhagen *et al.* 2020) are not taken into account given AUG's non-nuclear environment. Feedback of the runaway electron population on the poloidal magnetic flux evolution $\Psi(t)$ is considered by adding the runaway electron current density to the total plasma current density under the assumption that runaway electrons propagate with a velocity $\langle v_{\text{RE}} \rangle$ equal to the speed of light c , i.e. $\langle v_{\text{RE}} \rangle = c$.

2.2.1. Hot-tail generation

In events of rapid plasma cooling, as in the case of tokamak disruptions, electron runaway may occur. Under these conditions, the high-energy tail of the electron energy distribution function equilibrates slower than the thermal bulk and may thus exceed the critical energy for runaway (Chiu *et al.* 1998; Harvey *et al.* 2000). The runaway electron population generated due to this process can be described by reduced fluid models, e.g. by the work of Smith & Verwichte (2008) and Fehér *et al.* (2011). However, compared with kinetic simulations with the full- f continuum Fokker–Planck solver CODE (Stahl *et al.* 2016), these reduced models are found to underestimate the hot-tail density by up to an order of magnitude as the impact of the electric field on the underlying electron

¹The runaway electron generation models discussed are implemented as a standalone Fortran module, available at <https://github.com/o-linder/runawayelectrongeneration>.

distribution function is not taken into account by these models (Breizman *et al.* 2019; Harvey *et al.* 2019). Simultaneously, the computational cost of kinetic solvers renders application in transport simulations impractical. Therefore, cheaper and more accurate models are currently being developed by Svenningsson (2020), which, however, are not available yet for practical applications with varying effective plasma charge Z_{eff} . For this reason, the model by Smith & Verwichte (2008) is applied in this work for the calculation of the hot-tail runaway electron population. Note, that in a recent validation of this model by Petrov, Parks & Harvey (2021) with the Fokker–Planck solver CQL3D, an additional Z_{eff} -dependent factor of order unity was proposed for the definition of the critical velocity.

According to the model by Smith & Verwichte (2008), the hot-tail runaway electron density n_{hot} at time t is obtained from the velocity-space integral across the runaway region as

$$n_{\text{hot}}(t) = \frac{4n_{e,0}}{\sqrt{\pi}v_{\text{th},0}^3} \int_{v_c(t)}^{\infty} (v^2 - v_c(t)^2) \exp\left(-\left[\frac{v^3}{v_{\text{th},0}^3} + 3\tau(t)\right]^{2/3}\right) dv, \quad (2.3)$$

where v_{th} denotes the thermal velocity, $v_{\text{th}}^2 = 2T_e/m_e$, and v_c the critical velocity for electron runaway, $v_c^2 = e^3 n_e \ln \Lambda / 4\pi \varepsilon_0^2 m_e E_{\parallel}$ with $\ln \Lambda$ being the Coulomb logarithm for thermal-thermal collisions, i.e. $\ln \Lambda = 16.1 - 0.5 \log(n_e/10^{19} \text{ m}^{-3}) + \log(T_e/\text{keV})$. The constants m_e , e and ε_0 denote, respectively, the electron mass, the elementary charge and the vacuum permittivity. Quantities evaluated at the onset of rapid cooling are denoted by indices ‘0’. The parameter $\tau(t)$ is a normalized time, i.e. $\tau(t) = \nu_0 \int_{t_0}^t n_e(\tilde{t}) d\tilde{t} / n_{e,0}$, with the thermal-thermal collision frequency $\nu = n_e e^4 \ln \Lambda / 4\pi \varepsilon_0^2 m_e^2 v_{\text{th}}^3$.

The expression (2.3) introduced by Smith & Verwichte (2008) for the hot-tail density assumes an instantaneous drop of the electron temperature from $T_{e,0}$ to the final temperature $T_{e,\text{fin}}$. However, motivated by an exponential decay of the temperature on time scales t_{dec} due to plasma cooling (Smith & Verwichte 2008), the hot-tail density evolution under assumption of an exponential decay of the temperature, i.e.

$$T_e(t) = (T_{e,0} - T_{e,\text{fin}}) \exp\left(-\frac{t - t_0}{t_{\text{dec}}}\right) + T_{e,\text{fin}}, \quad (2.4)$$

can be described by modifying the expression for $\tau(t)$. In the work by Smith & Verwichte (2008), the temporal evolution of this parameter is obtained through numerical integration of a high moment of the kinetic equation for a two-component distribution function. In the case of an exponential electron density evolution, the numerical solution obtained for $\tau(t)$ is well approximated by $\tau(t) = \nu_0(t - t_0 - t_{\text{dec}})\Theta(t - t_0 - t_{\text{dec}})n_{e,\text{fin}}/n_{e,0}$ for $t - t_0 > 3 t_{\text{dec}}$ (Smith & Verwichte 2008). However, to describe $\tau(t)$ more accurately during the initial phase of rapid cooling, an alternative expression is introduced and used throughout this work

$$\tau(t) = \nu_0 \frac{n_{e,\text{fin}}}{n_{e,0}} \begin{cases} \frac{(t - t_0)^2}{4t_{\text{dec}}}, & t - t_0 < 2t_{\text{dec}} \\ (t - t_0 - t_{\text{dec}}), & t - t_0 \geq 2t_{\text{dec}} \end{cases}. \quad (2.5)$$

For evaluation of the hot-tail density, a closed form of expression (2.3) cannot be provided, necessitating numerical integration. Inside ASTRA, the integral is evaluated using Kepler’s rule as the integrand falls off monotonically and sufficiently fast for $v \rightarrow \infty$. The hot-tail runaway electron density n_{hot} obtained can be used inside ASTRA directly for subsequent calculations of the runaway electron current density and secondary runaway generation, eliminating the necessity to evaluate the macroscopic transport equation (2.1) for the hot-tail population. However, importantly, evaluation of the instantaneous hot-tail

population through (2.3) requires characterization of parameters at onset and end of the thermal quench, being the time t_0 of the onset of the thermal quench, the electron temperature $T_e(t_0)$, the temperature decay time scale t_{dec} , as well as the electron density at onset and end of the thermal quench, i.e. $n_e(t_0)$ and $n_e(t_{\text{fin}})$. As onset and end of the thermal quench cannot be determined during a simulation, the required parameters are calculated in postsimulation analysis (see § 2.3) and applied in a subsequent simulation for the calculation of the hot-tail population. Convergence of the parameters obtained has to be assessed and simulations repeated if convergence is not met. Note, that in the simulations presented in this work, one iteration to determine the thermal quench parameters was sufficient to achieve an averaged iteration accuracy of less than 1 % across all grid points, being in all cases less than 5 %.

2.2.2. Dreicer generation

The process of electron runaway due to momentum-space diffusion of thermal electrons in the presence of partially ionized mid- to high- Z impurities cannot be described by analytical reduced fluid models, as a result of the complicated energy dependence of collision frequencies at near-thermal energies (Hesslow *et al.* 2019b). Analytical expressions under consideration of fully ionized impurities only (Connor & Hastie 1975) have been demonstrated to overestimate electron runaway under certain conditions (Hesslow *et al.* 2019b). Applied in transport simulations of runaway electron generation during MGI, a noticeably increased seed population in contrast to experimental observations is obtained (Linder *et al.* 2020). Therefore, instead of reduced fluid models, a neural network model for the calculation of Dreicer growth rates (Hesslow *et al.* 2019b) is utilized in this work.

The neural network by Hesslow *et al.* (2019b) is based on simulations of CODE. Training of the network was performed with argon and neon impurities, generalized for application to other species using eight input parameters x . The Dreicer source rate S_D is thus obtained through evaluation of

$$S_D = \nu n_e \exp(\mathcal{F}(\mathbf{W}_5, \mathcal{F}(\mathbf{W}_4, \mathcal{F}(\mathbf{W}_3, \mathcal{F}(\mathbf{W}_2, \mathcal{F}(\mathbf{W}_1, x, \mathbf{b}_1), \mathbf{b}_2), \mathbf{b}_3), \mathbf{b}_4), \mathbf{b}_5)), \quad (2.6)$$

$$\mathcal{F}(W, x, b) = \tanh(Wx + b), \quad (2.7)$$

with weights \mathbf{W}_i and biases \mathbf{b}_i (see Hesslow *et al.* (2019b) for details).

2.2.3. Avalanche generation

The generation of secondary runaway electrons due to knock-on collisions of existing runaways with thermal electrons in the presence of partially ionized impurities can be described through a reduced fluid model by Hesslow *et al.* (2019a). The avalanche source rate S_{av} is calculated from

$$S_{\text{av}} = n_{\text{RE}} \frac{e}{m_e c \ln \Lambda_c} \frac{n_e^{\text{tot}}}{n_e} \frac{E_{\parallel} - E_c^{\text{eff}}}{\sqrt{4 + \bar{\nu}_{\text{slow}}(p_{\star}) \bar{\nu}_{\text{defl}}(p_{\star})}}, \quad (2.8)$$

with the relativistic Coulomb logarithm $\ln \Lambda_c = \ln \Lambda - 0.5 \ln(T/m_e c^2)$. The total electron density n_e^{tot} comprises both free plasma electrons n_e and electrons bound to impurity ions. In the presence of partially ionized impurities, the critical electric field $E_c = n_e e^3 \ln \Lambda_c / 4\pi \epsilon_0^2 m_e c^2$ for runaway is increased, the effect of which is described by the effective critical electric field E_c^{eff} defined in Hesslow *et al.* (2018b). Expressions for the slowing-down frequency $\bar{\nu}_{\text{slow}}$ and for the generalized deflection frequency $\bar{\nu}_{\text{defl}}$ are found in Hesslow *et al.* (2018a) and Hesslow *et al.* (2018b). Noticeably, the effective critical

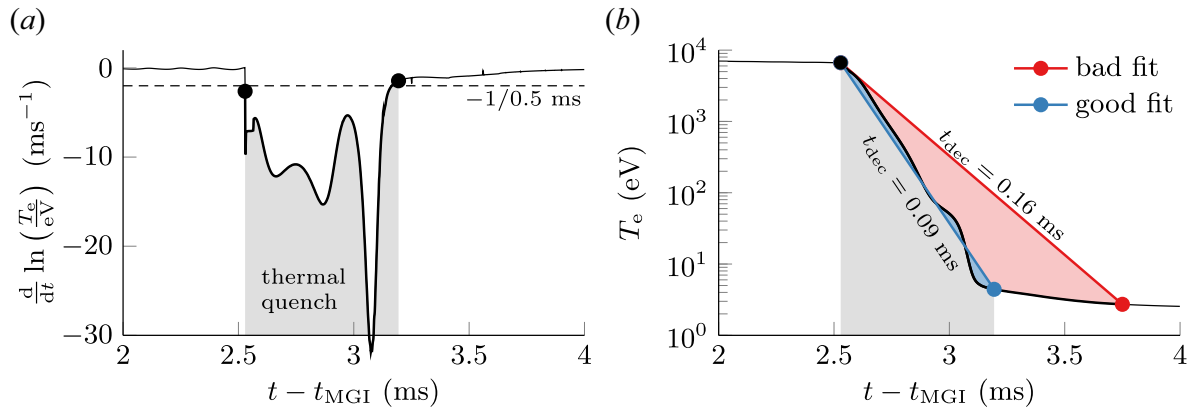


FIGURE 1. The occurrence of a thermal quench is determined from the electron temperature evolution starting at the onset of MGI at t_{MGI} . (a) The temporal derivative of the logarithmic temperature falling below a threshold of $-1/0.5$ ms marks the onset of the quench. (b) The end is obtained from an exponential fit of the electron temperature, illustrated for both a suitable (blue) and a poor (red) choice of the decay time scale t_{dec} .

momentum p_{\star} depends on both frequencies through $p_{\star} = \sqrt[4]{\bar{v}_{\text{slow}}(p_{\star})\bar{v}_{\text{defl}}(p_{\star})}/\sqrt{E_{\parallel}/E_c}$, thus requiring numerical evaluation of these parameters.

2.3. Determining thermal quench parameters

The calculation of characteristic quantities of the thermal quench for the evaluation of the hot-tail runaway population during the thermal quench (see § 2.2.1) is performed in postsimulation analysis. Onset t_0 and end t_{fin} of the thermal quench are determined from the electron temperature evolution. The required values for both the electron temperature and density are then obtained through evaluation of these quantities at t_0 and t_{fin} , respectively.

The time t_0 of the onset of the thermal quench is defined as the time when the instantaneous logarithmic temperature change $d \ln(T_e(t)/\text{eV})/dt$ falls below a threshold value $-1/\tilde{t}_{\text{dec}} = -1/0.5$ ms, with \tilde{t}_{dec} being the instantaneous temperature decay time (see figure 1a). Both the end t_{fin} of the thermal quench and the temperature decay time scale t_{dec} are determined through a linear fit $\ln \tilde{T}_e(t)$ of the logarithmic electron temperature evolution (see figure 1b). Under the assumption $T_e(t_0) \gg T_e(t_{\text{fin}})$, the ansatz for $T_e(t)$ of (2.4) can be reduced to $\ln(T_e(t)/T_e(t_0)) = -(t - t_0)/t_{\text{dec}}$, thus yielding the time scale t_{dec} . The end of the thermal quench is defined as the last time point where $\tilde{T}_e(t_{\text{fin}}) = T_e(t_{\text{fin}})$, i.e. before the fit falls off below the actual temperature. The quality of the fit is evaluated for $t \in [t_0, t_{\text{fin}}]$.

3. ASDEX Upgrade runaway electron experiments

3.1. Reference scenario

Simulations of runaway electron generation are performed for artificially disrupted ASDEX Upgrade experiments through MGI (Pautasso *et al.* 2017, 2020). The plasma parameters chosen in this work are based on ASDEX Upgrade discharge #33108 (for details see Linder *et al.* 2020). In this experiment, argon (Ar) was injected at $t_{\text{inj}} = 1.0$ s after breakdown from a gas valve of volume 100 cm^3 and initial Ar pressure of 0.73 bar into an L-mode limiter plasma with low average electron density of $\langle n_e \rangle = 2.8 \times 10^{19} \text{ m}^{-3}$ and high peaked electron temperature of $T_e(\rho = 0) = 9.3 \text{ keV}$ at the magnetic axis. A peaked temperature profile is achieved through application of 2.6 MW of on-axis electron cyclotron resonance heating (ECRH) during the last 0.1 s prior to MGI. As a result of

Quantity	AUG #33108	Similar shots
$I_{p,0}$ (MA)	0.76	0.60–0.90
p_{Ar} (bar)	0.73	0.60–0.85
B_{tor} (T)	2.50	2.30–2.70
q_{95}	3.79	3.50–4.10

TABLE 1. Characteristic parameters for runaway electron experiments in AUG, being the predisruptive plasma current $I_{p,0}$, the valve Ar pressure p_{Ar} , the toroidal magnetic field B_{tor} and the edge safety factor q_{95} . Values for the reference discharge AUG #33108 are given, as well as criteria for selecting similar shots from all AUG runaway electron experiments performed.

Ar injection, the plasma stored energy is removed through impurity radiation and the plasma current decreases from initially 763 kA down to 225 kA, carried by relativistic electrons. Additional characteristic parameters of AUG #33108, as well as criteria for selecting similar runaway electron shots for analysis in § 5.5, are listed in table 1.

3.2. Gaussian process regression for experimental fitting

Reconstruction of experimental profiles often requires fitting of measured data. Application of a probabilistic approach under consideration of uncertainties allows a reliable estimate of experimental quantities. Therefore, Gaussian process regression (GPR) techniques are employed in this work through application of a toolset by Ho *et al.* (2019), based on work by Chilenski *et al.* (2015). Using these tools, reconstruction of preinjection electron temperature profiles $T_e(t_{inj}, \rho)$ from electron cyclotron emission (ECE) and Thomson scattering (TS) measurements is performed in § 5.1 for the entire plasma radius and in § 5.5 for a better reconstruction of the on-axis value $T_e(t_{inj}, 0)$. An estimation of the experimentally measured runaway electron current as a function of $T_e(t_{inj}, 0)$ is also performed using GPR.

Applying Bayesian probability theory, robust reconstruction of these profiles, as well as of associated gradients and uncertainties, is performed from covariance functions $k(x, x')$ utilizing normally distributed weights. Where stated in this work, profile estimation through GPR is performed using a rational quadratic covariance function

$$k(x, x') = \sigma^2 \left(1 + \frac{(x - x')^2}{2\alpha l^2} \right)^\alpha \quad (3.1)$$

with variance σ^2 and characteristic length scale l . The hyperparameter α describes length scale mixing. When simpler estimates are sufficient, plasma profiles are instead reconstructed using an mtanh function (Schneider 2012).

4. Electron runaway in ASDEX Upgrade #33108

Coupled transport simulations of Ar injection, background plasma evolution and runaway electron generation are performed with ASTRA-STRAHL for AUG discharge #33108. The evolution of the Ar-induced disruption throughout the simulation is described in § 4.1. The generation of a seed population is discussed in § 4.2, whereas the avalanche multiplication following is covered in § 4.3. The spatio-temporal evolution of the runaway electron current density contributions and the Ohmic current density is illustrated, in

addition to this paper, in a supplementary movie available at <https://doi.org/10.1017/S0022377821000416>.

4.1. Simulation of thermal and current quench

Simulating AUG discharge #33108, the impurities injected reach the LCFS at $t = 1.0$ ms after the valve trigger. Note that in this section, the time t is given with respect to the time t_{inj} of the start of material injection. The cold gas front propagates further into the central plasma and in the process locally cools down the plasma through strong impurity radiation. As a result, the Ohmic current (with density j_{Ω}) contracts inwards where the plasma temperature has not collapsed yet (see supplementary movie). Eventually, strong current density gradients $dj_{\Omega}/d\rho$ at the $q = 2$ surface at $\rho = 0.7$ excite $(m, n) = (2, 1)$ MHD modes and higher harmonics, thus causing rapid redistribution of heat and material inside the $q = 2$ surface. In the process, the remaining plasma stored energy is dissipated globally through impurity radiation on a sub-ms time scale, decreasing the electron temperature and therefore also the plasma conductivity. Following the law of induction, strong electric fields are generated. In this environment, a seed population of runaway electrons is created due to both the hot-tail and Dreicer mechanisms. During the slower decay of the residual Ohmic current, the runaway seed population is amplified by the avalanche mechanism, establishing a significant runaway electron current at the end of the current quench, being 333 kA in the simulation.

4.2. The runaway seed population

Seed runaway electrons are generated due to the hot-tail and Dreicer mechanisms until the end of the thermal quench in the simulations performed. In the case of Dreicer generation, runaway occurs primarily in the vicinity of the $q = 2$ surface at around $\rho = 0.7$ prior to the thermal quench (see [figure 2](#)). As the material injected begins to propagate into the plasma centre, cooling it down in the process, the Ohmic current contracts inwards to locations where the temperature has not collapsed yet. As a result, a high Ohmic current density is located in front of the cold gas, growing in magnitude as the material propagates inwards further (see supplementary movie). The maximum Ohmic current density is observed in the vicinity of the $q = 2$ surface. As the cold gas front reaches this location, $(2, 1)$ MHD modes are triggered. In the process, the current density is flattened inside the $q = 2$ surface. As follows from the relation

$$\frac{E_{\parallel}}{E_{\text{D}}} = \frac{m_e v}{n_e e^2 j_{\Omega}} \frac{4\pi \varepsilon_0^2 T_e}{n_e e^3 \ln \Lambda} = \frac{\sqrt{m_e}}{en_e \sqrt{8T_e}} j_{\Omega}, \quad (4.1)$$

strong electric fields E_{\parallel} normalized to the Dreicer electric field $E_{\text{D}} = n_e e^3 \ln \Lambda / 4\pi \varepsilon_0^2 T_e$ are induced at locations of high Ohmic current density j_{Ω} , amounting to around 5% E_{D} in the vicinity of the $q = 2$ surface. With the generation of Dreicer runaway electrons being, in a simple picture, exponentially sensitive to $-E_{\text{D}}/E_{\parallel}$ (Connor & Hastie 1975), a seed population of up to 18 kA m⁻² is established in the vicinity of the $q = 2$ surface.

During the thermal quench following, the electric field inside the $q = 2$ surface increases up to $\sim 3\%$ E_{D} as the rapidly decaying Ohmic current is distributed inside the $q = 2$ surface more evenly. However, due to the aforementioned exponential sensitivity, only a small population of additional runaway electrons is generated. Until the end of the thermal quench, the Dreicer mechanism produces a runaway current of 1.1 kA, constituting only around 0.3% of the total postdisruption runaway current. Consequently, the Dreicer mechanism is relevant only for establishing a small seed population of runaways.

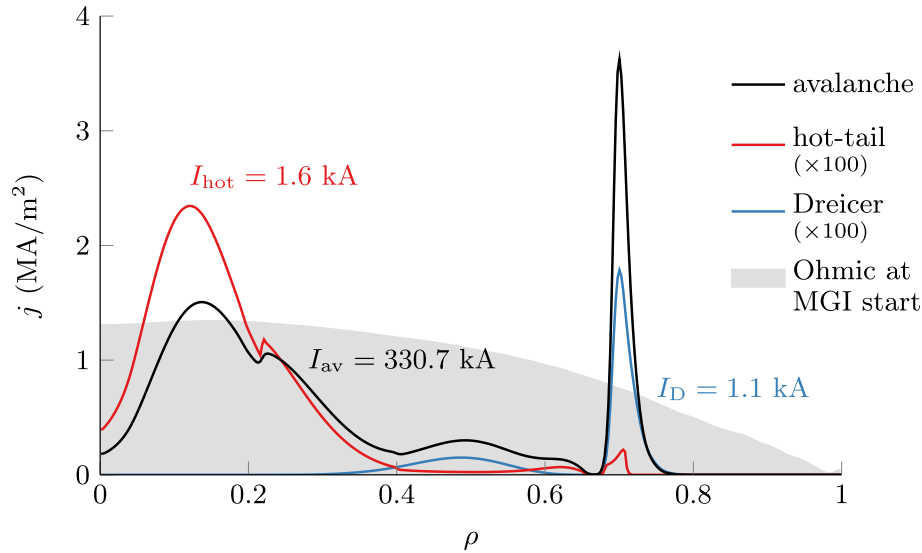


FIGURE 2. Radial distribution of the postdisruption runaway electron current densities j at the end of the current quench in simulations of AUG #33108, generated by the avalanche mechanism (black), by the hot-tail mechanism (red) and by the Dreicer mechanism (blue). The runaway electron current densities are compared against the Ohmic current density j_{Ω} at the start of MGI. Note, that the current densities of the hot-tail and Dreicer mechanism generated seed populations shown are multiplied by a factor of $\times 100$ given their small magnitude compared to the avalanche generated runaway current density. Additionally, the current I carried by each population is shown next to the corresponding current density profile. The spatio-temporal evolution of the runaway electron current density is additionally shown in a supplementary movie of this figure.

The hot-tail mechanism for the generation of runaways becomes important during rapid decrease of the electron temperature. Prior to the thermal quench during the inward propagation of the cold gas front, these conditions are not met. Only with the onset of the thermal quench, a noticeable population of hot-tail runaways is created inside the $q = 2$ surface (see figure 2). Importantly, significant generation of more than 1 kA m^{-2} of hot-tail current density occurs predominantly inside $\rho = 0.4$, i.e. in the region where on-axis ECRH was applied prior to MGI. At the end of the thermal collapse, a total hot-tail current of 1.6 kA is obtained, being around 0.5 % of the postdisruption runaway current. Consequently, the hot-tail mechanism also provides only a small seed population of runaways in AUG #33108.

The largest hot-tail current density $\max j_{\text{hot}}$ is observed off-axis at $\rho = 0.12$, while the on-axis current density amounts to only around $\max(j_{\text{hot}})/6$ despite a larger prequench temperature. This seemingly contradictory behaviour can be understood by evaluating the dominant contributions of the hot-tail model of (2.3), thus obtaining the simplified expression (see (A 9) of Appendix A)

$$n_{\text{hot}}^{\text{simple}}(t_{\text{fin}}) = \frac{2n_{e,0}}{\sqrt{\pi}} \exp \left(-4 \left\{ \tilde{\nu} \ln \Lambda(t_0) \frac{n_{e,\text{fin}} t_{\text{dec}}}{T_{e,0}^{3/2}} \right\}^{2/3} \right). \quad (4.2)$$

Hence, in a simple estimate, the postquench hot-tail density is exponentially sensitive to the prequench electron temperature $T_{e,0}$, to the decay time scale t_{dec} , and to the postquench electron density $n_{e,\text{fin}}$. Analysing the radial distribution of these quantities for AUG #33108 (see figure 3a), the decay time is observed to be uniformly around $t_{\text{dec}} \sim 0.1 \text{ ms}$. Therefore, the hot-tail population is predominantly determined by the ratio $n_{e,\text{fin}}^{2/3}/T_{e,0}$. Inside $\rho = 0.4$,

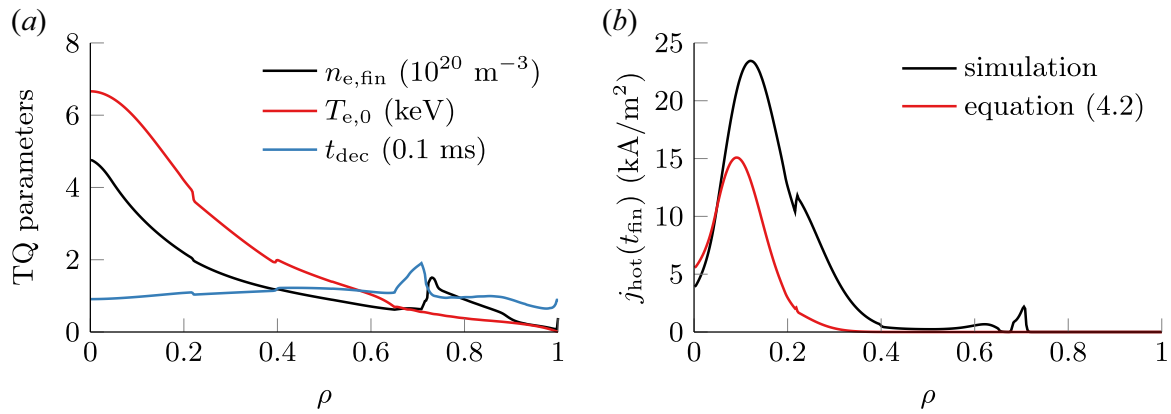


FIGURE 3. For simulations of AUG #33108, (a) parameters of the thermal quench (TQ), i.e. electron density at the end (black), electron temperature at the onset (red) as well as the temperature decay time scale (blue). (b) The postquench hot-tail current density obtained through simulations (black) is compared against an analytical estimate from (4.2) (red).

this ratio decreases as the electron temperature peaks due to preinjection ECRH. With higher prequench temperature, as well as due to inward impurity propagation, the impurity contributed free electron density postquench is increased as well, peaking close to the magnetic axis, and thus increasing the ratio $n_{e,fin}^{2/3}/T_{e,0}$ close to the magnetic axis. As a result, the largest hot-tail population is observed off-axis.

The simple analysis following (4.2) is capable of reproducing the general trend of the hot-tail density obtained through evaluating the full expression (2.3) in simulations (see figure 3b). Consequently, the dependencies discussed are also valid for the complete model. It should be noted that the simplified model underestimates the hot-tail density especially in the outer half-radius. This behaviour occurs because factors appearing in a more general model (see (A 7)) were simplified based on AUG disruption parameters of the central plasma. Application of the more general simplified model of (A 7) yields an estimate of the hot-tail density larger than observed in simulations.

Following this analysis, the postquench hot-tail population observed is strongly influenced by both the prequench electron temperature, as well as by impurity deposition and propagation. A reduction of the hot-tail seed population can consequently be achieved by reducing the plasma temperature, slowing down the thermal quench, or depositing impurities predominantly in regions of highest temperatures.

4.3. Runaway electron multiplication

The vast majority of the runaway current observed in simulations of AUG #33108, being 331 kA or 99.1 % of the postdisruption runaway current, originates from secondary runaway electrons (see figure 2), generated during knock-on collisions of thermal electrons with existing runaways from the small seed population. The radial distribution of the avalanche generated runaway current density is thus a scaled-up superposition of the seed populations. Consequently, the postdisruption runaway population is located primarily in the vicinity of the $q = 2$ surface, as well as close to the magnetic axis at $\rho \sim 0.1$. Due to diffusion of the electric field during the current quench, the postdisruption runaway current density exceeds the pre-disruption Ohmic current density at these locations. As a result of impurity redistribution during the disruption and the associated impact on the evolution of the residual Ohmic current density, favourable conditions for avalanche multiplication exist predominantly close to, but inside the $q = 2$ surface. Therefore,

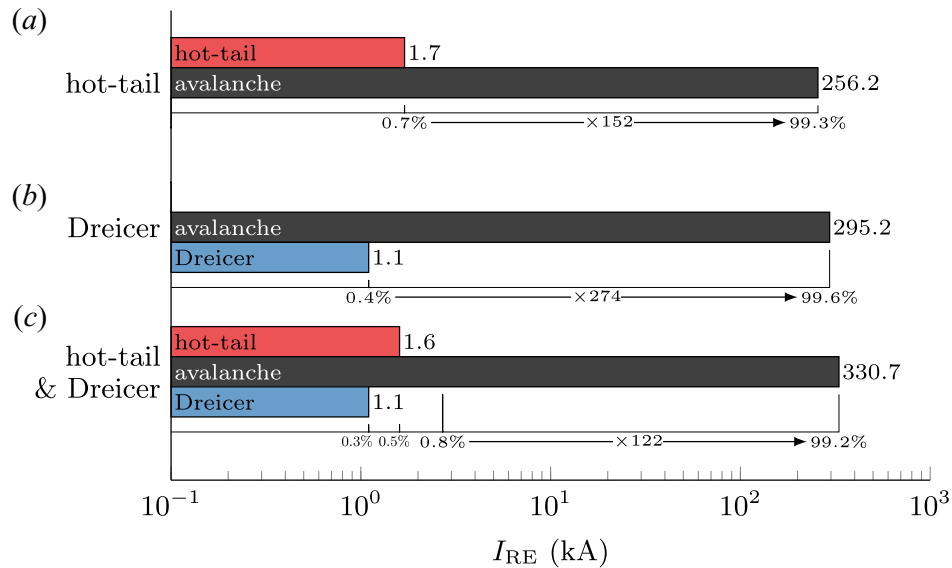


FIGURE 4. Comparison of the postdisruption runaway current contributions I_{RE} from seed and avalanche mechanisms in simulations of AUG #33108 utilizing selected source mechanisms, being (1) only the hot-tail mechanism (a), (2) only the Dreicer mechanism (b), and (3) both the hot-tail and the Dreicer mechanism (c). Both the absolute runaway currents, as well as the relative strength of each generation mechanism are specified. Additionally, the avalanche multiplication factor for each simulation is listed.

avalanche multiplication of the Dreicer generated seed population is stronger than for the hot-tail seed.

The importance of the avalanche mechanism for electron runaway in AUG #33108 has also been observed by Insulander Björk *et al.* (2020) in simulations with the full- f solver CODE. In their work, however, the small seed population was determined to consist almost entirely of hot-tail generated runaways with virtually no contribution from the Dreicer mechanism. Thus, to assess the impact of the individual source mechanisms on runaway multiplication in this framework, simulations of AUG #33108 are repeated with only one of the primary generation mechanisms enabled.

In simulations considering either only the hot-tail or the Dreicer mechanism as a source for primary runaways, the seed population is reduced to 1.7 kA (−37%) and 1.1 kA (−59%), respectively, compared with a seed population of 2.7 kA obtained in the case of employing both mechanisms (see figure 4). Yet, the postdisruption runaway current obtained in both cases is not reduced proportionally, being 258 kA (−23%) and 296 kA (−11%), respectively. As the residual Ohmic current decays at similar time scales independent of the seed mechanisms employed, the postdisruption runaway current is thus determined by the avalanche multiplication time and seed population. Given the more favourable conditions for avalanche multiplication in the vicinity of the $q = 2$ surface as discussed above, the smaller Dreicer generated runaway seed produces a larger secondary population than in the case utilizing only a hot-tail seed. Importantly, a comparable postdisruption runaway current is obtained in all three cases. Therefore, based on the simulations presented, the exact composition of the primary runaway seed seems to be of secondary importance in the case of AUG #33108, as avalanche generation during the current quench dominates the dynamics.

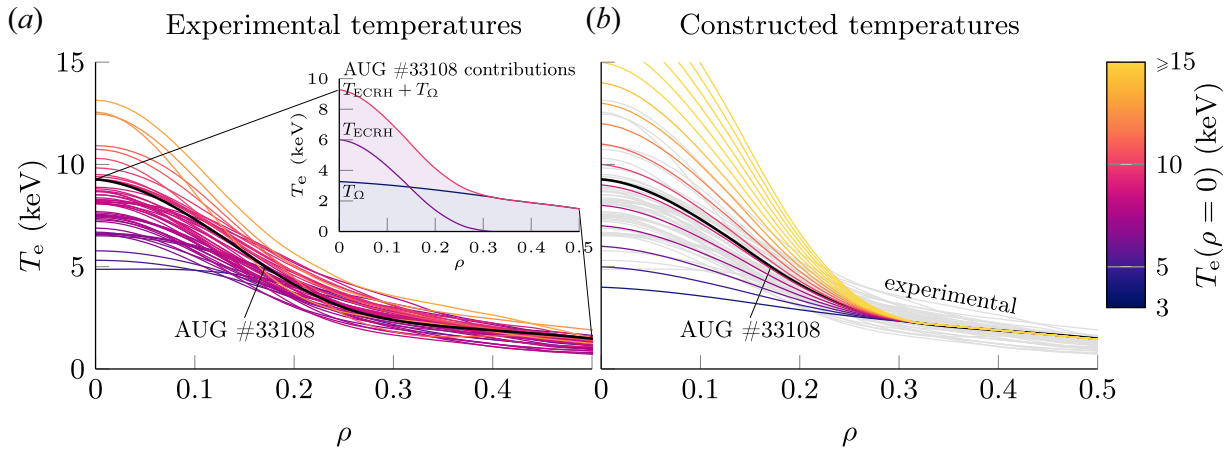


FIGURE 5. (a) Electron temperature profiles of AUG disruption experiments similar to discharge #33108 (see table 1), constructed by GPR using ECE and TS measurement from the last 50 ms prior to MGI. The temperature profile of AUG #33108 can be decomposed into a contribution T_{Ω} due to Ohmic heating and into a localized contribution T_{ECRH} due to on-axis ECRH. (b) Electron temperature profiles for the scan presented in § 5 are constructed by using the profile of AUG #33108 and scaling the ECRH contribution T_{ECRH} , thus assuming application of varying amounts of ECRH to this baseline shot. The experimental temperature profiles of the discharges selected are shown for reference in grey. The temperature profiles are colour-coded by their on-axis values $T_e(\rho = 0)$.

5. Impact of predisruption temperature on runaway

The predisruption electron temperature is an important parameter for hot-tail runaway electron generation during the thermal quench, as discussed in § 4.2. With increasing temperature, an exponentially increased hot-tail seed is expected to be generated. Simultaneously, increased impurity ionization is expected to occur under these conditions, potentially countering the increase of the hot-tail seed through enhanced friction. This behaviour is analysed computationally in this section by varying the preinjection, on-axis electron temperature in the range $T_e(\rho = 0) \in [4, 20 \text{ keV}]$ in simulations of AUG #33108.

5.1. Set-up of electron temperature profiles

In AUG runaway electron experiments, on-axis ECRH is applied in the last 0.1 s prior to impurity injection to achieve high electron temperatures in the vicinity of the magnetic axis. For AUG discharges similar to AUG #33108, the electron temperature profiles obtained through Gaussian process regression of measurements by ECE and TS thus exhibit a peaked central temperature profile of varying magnitude (see figure 5a). For locations around midradius and beyond, the local temperature and the on-axis temperature are, however, not clearly correlated. This observation motivates the approach of constructing different experimentally relevant electron temperature profiles for this investigation based on the temperature profile of AUG #33108 under the assumption of applying varying amounts of on-axis ECRH.

In contrast to using experimental temperature profiles of discharges with a desired preinjection on-axis temperature, this approach ensures applying temperature profiles consistent with each other throughout the temperature range considered, thus removing the impact peculiarities of the individual temperature profiles might have on the simulation results. Furthermore, this approach allows investigation of cases not covered (yet) experimentally, particularly at temperatures beyond 10 keV, while still ensuring experimental relevance.

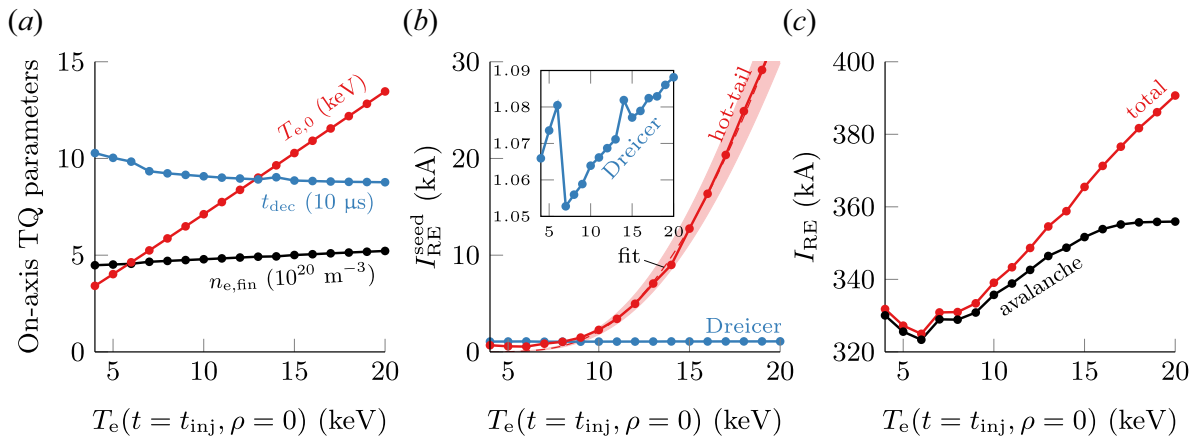


FIGURE 6. Simulations of AUG #33108 with increasing preinjection on-axis electron temperature $T_e(t = t_{inj}, \rho = 0)$, showing (a) on-axis thermal quench parameters, being the postquench electron density (black), the electron temperature at the onset of the thermal quench (red) and the temperature decay time scale (blue). The runaway current obtained at the end of the disruption is shown for (b) the seed runaway population I_{RE}^{seed} , generated by the hot-tail mechanism (red) and by the Dreicer mechanism (blue), as well as for (c) the avalanche generated runaway current (black) and the total runaway current (red). The hot-tail current in panel (b) is approximated by a function $I_{hot}^{fit} = a_0 \exp(-a_1/T_{e,0})$ (dashed red) of (5.2), with fitting parameters a_0 and a_1 .

To construct the temperatures profiles used, the experimental temperature profile of AUG #33108 is separated into a contribution $T_\Omega(\rho)$ due to Ohmic heating and into a contribution $T_{ECRH}(\rho)$ due to ECRH (see figure 5a). Given the localized application, the ECRH contribution is non-vanishing only inside $\rho = 0.35$. Profiles with an arbitrary electron temperature T_{ax} at the magnetic axis are thus obtained by scaling the ECRH contribution, according to

$$T_e(\rho) = \frac{T_{ax} - T_\Omega(0)}{T_{ECRH}(0)} T_{ECRH}(\rho) + T_\Omega(\rho). \quad (5.1)$$

The temperature profiles constructed are consequently not modified beyond $\rho = 0.35$. The profiles used throughout this scan in the range $T_e(\rho = 0) \in [4, 20 \text{ keV}]$ are shown in figure 5(b). Compared to the temperature profiles of the discharges selected (illustrated in the same figure), the experimentally observed peaked temperature profiles are well described by the approach chosen. Therefore, the scan presented in the following describes experimentally relevant cases.

5.2. Impact on the runaway seed

Increasing the preinjection on-axis electron temperature $T_e(t_{inj}, 0)$ in simulations of AUG #33108 from 4 keV up to 20 keV, the hot-tail current generated is observed to grow exponentially from a minimum value of 0.6 kA up to 33.7 kA (see figure 6b). For the smallest choices of $T_e(t_{inj}, 0)$, runaway occurs predominantly around $\rho \sim 0.7$, shifting towards $\rho \sim 0.1$ with increasing $T_e(t_{inj}, 0)$ (see figure 7a). Here, the minimum hot-tail current is observed for $T_e(t_{inj}, 0) = 6 \text{ keV}$. Significant hot-tail runaway eventually occurs for preinjection on-axis temperatures beyond 10 keV (such that the hot-tail current constitutes more than 1% of the postdisruption runaway current), generating in all cases considered a seed current density noticeably smaller than the local predisruption Ohmic current density j_Ω (see figure 7). In the region of parameter space with $T_e(t_{inj}, 0) > 10 \text{ keV}$,

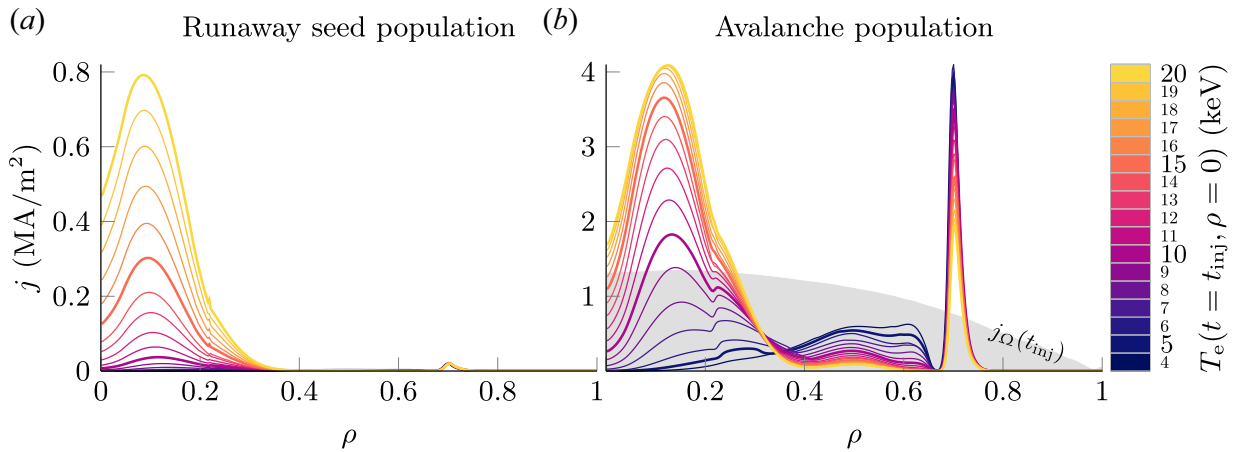


FIGURE 7. Radial profiles of (a) the runaway electron seed current densities j_{seed} and (b) the postdisruption runaway electron current densities j_{av} generated by the avalanche mechanism in simulations of AUG #33108 with varying preinjection on-axis electron temperatures $T_e(t = t_{\text{inj}}, \rho = 0)$ ranging from 4 to 20 keV. For reference, the Ohmic current density j_{Ω} at the start of MGI is shown (grey) in panel (b).

the hot-tail current obtained is well approximated by a function based on the simplified estimate of the hot-tail population (see (4.2)),

$$I_{\text{hot}}^{\text{fit}}(T_{e,0}(\rho = 0)) = (914 \pm 58) \exp \left(-4 \left\{ \frac{\tilde{\nu} \ln \Lambda(t_0) \langle n_{e,\text{fin}} t_{\text{dec}} \rangle}{T_{e,0}(\rho = 0)^{3/2}} \right\}^{2/3} \right) \text{ kA}, \quad (5.2)$$

using the on-axis temperature $T_{e,0}(\rho = 0)$ at the onset of the thermal quench as dependent variable. This estimate suggests an effective spatial average of the postquench electron density $n_{e,\text{fin}}$ and decay time scale t_{dec} of $\langle n_{e,\text{fin}} t_{\text{dec}} \rangle = (1.66 \pm 0.04) \times 10^{19} \text{ m}^{-3} \text{ ms}$. Consequently, the hot-tail runaway current grows with increasing preinjection temperature as anticipated following the above argument. Yet, the free electron density due to impurity ionization does not increase at a similar rate (see figure 6(a) for the on-axis values of thermal quench parameters), due to the increasing ionization potential of higher impurity ion charge states. At the same time, the decay time scale decreases slightly for larger temperatures, thus partially compensating the increase of the electron density. As a result, hot-tail runaway strongly increases in hotter plasmas. It should be noted that the opposite effect was observed by Aleynikov & Breizman (2017), where, different to the study presented in this manuscript, scenarios of instantaneous impurity deposition were investigated under the assumption of a steady-state impurity charge state distribution.

The impact of a variation of the preinjection on-axis electron temperature on electron runaway due to the Dreicer mechanism is, however, negligible (see figure 6(b)), varying only by approximately 3% throughout the temperature range considered. As discussed in § 4.2, Dreicer generation occurs as a result of the contracting Ohmic current predominantly in the vicinity of the $q = 2$ surface, i.e. where the preinjection temperature profile is considered unaffected by a variation of on-axis ECRH. Consequently, the Dreicer generated runaway current is approximately constant in the scenario considered.

5.3. Runaway electron multiplication

Throughout the temperature range considered, the runaway current generated due to the avalanche mechanism increases (see figure 6(c)), but not in proportion to the strong increase of the hot-tail seed population. For preinjection on-axis temperatures below 10 keV,

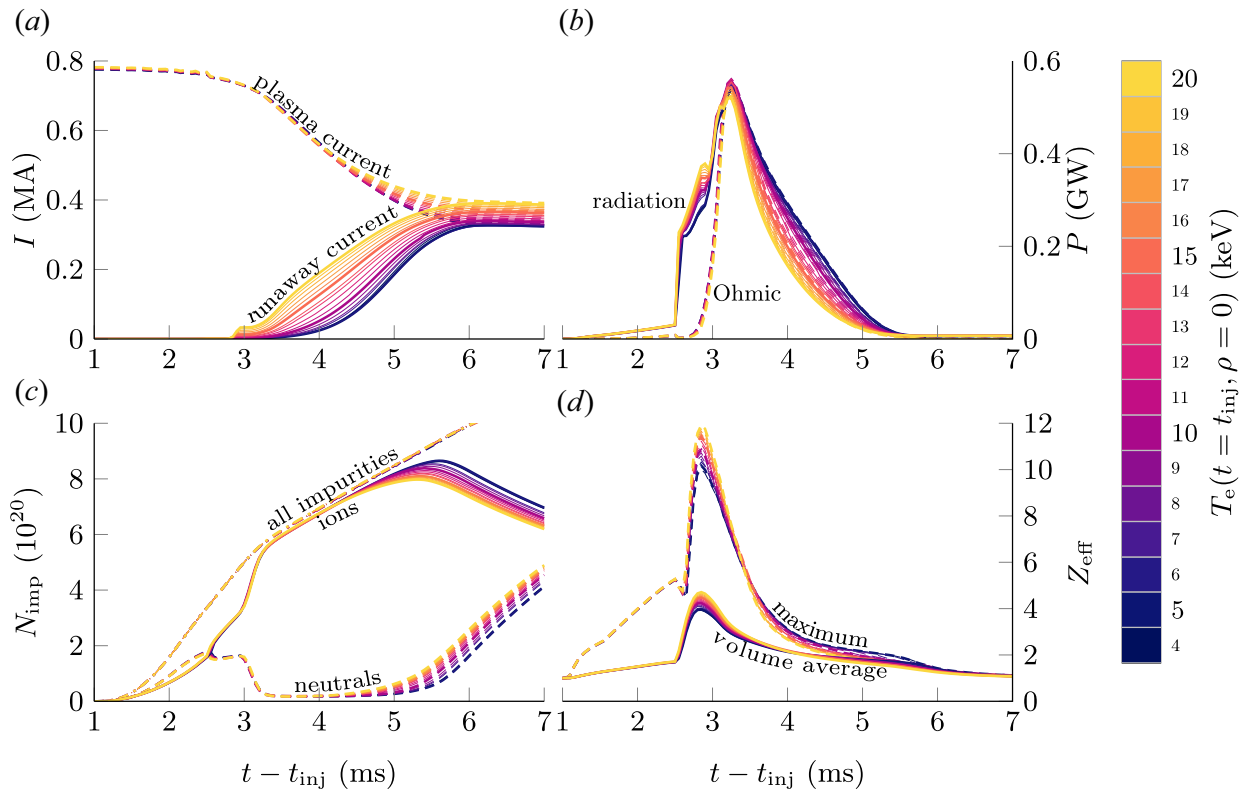


FIGURE 8. Temporal evolution of plasma parameters throughout the disruption in simulations of varying preinjection on-axis electron temperature $T_e(t_{inj}, 0)$, being (a) the current I of runaway electrons (solid) and of the plasma (dashed), (b) the power P of Ohmic heating (dashed) and radiation due to both line radiation and Bremsstrahlung (solid), (c) impurity content N_{imp} of ionized impurities (solid), neutral impurities (dashed) and all impurities (dash-dotted), (d) volume-averaged effective charge (solid) and maximum effective charge (dashed).

the small variation of the runaway seed population results in an approximately constant avalanche current of around 330 kA. With the significant increase of the hot-tail population for larger temperatures, the avalanche generated current grows as well with temperature, yet noticeably only by a similar amount. In the range between 9 and 14 keV, the avalanche multiplication factor of the additional hot-tail population amounts to only between 2 and 3, even approaching a factor of 1 for $T_{e,0} \rightarrow 20$ keV. Consequently for temperatures above 17 keV, the avalanche generated current reaches a constant value of 356 kA.

The radial distribution of the avalanche current density changes throughout the range of preinjection temperatures (see figure 7b) as a result of the increasing hot-tail seed population close to the magnetic axis. Occurring predominantly in the vicinity of the $q = 2$ surface and around midradius for lower temperatures, avalanche generation shifts towards the magnetic axis to around $\rho = 0.12$. Given the large hot-tail seed in this region, significant avalanching starts earlier into the current quench, thus accelerating the decay of the residual Ohmic current.

The total runaway electron current obtained at the end of the disruption increases roughly linearly for $T_{e,0} > 9$ keV (see figure 6c) due to the significantly growing hot-tail population. For the largest temperatures considered, the hot-tail seed constitutes almost 9% of the postdisruption runaway current. Consequently, the relative impact of avalanche multiplication decreases significantly with increasing temperature, as non-negligible amounts of the finite poloidal magnetic flux available for conversion to runaways (Boozer 2019) are consumed by a growing population of hot-tail runaways.

Consequently, avalanche multiplication in future devices such as ITER may be less than predicted in previous studies (Hesslow *et al.* 2019a).

5.4. Background plasma and impurity evolution

The variation of the preinjection, on-axis temperature in the simulations discussed affects not only the spatio-temporal evolution of the runaway population, but also the evolution of the background plasma and of the impurities injected (see figure 8 for selected quantities). With higher initial temperature, impurity radiation (including line radiation and Bremsstrahlung) during the thermal quench is enhanced to dissipate the increased plasma thermal energy (see figure 8b). However, as the temperature profiles are effectively modified only in the region $\rho < 0.3$ (see figure 5b), making up around 10% of the total plasma volume, the preinjection plasma stored thermal energy increases throughout the temperature range considered only by around 30%. The net energy lost, being the difference between Ohmic heating and impurity radiation, until the end of the thermal quench is increased by the same amount.

During the thermal quench, radiative losses far exceed 200 MW throughout the temperature range considered. As such, conductive heat transport plays a marginal role in removing heat from the central plasma. The thermal quench is therefore induced by impurity radiation in the simulations performed. The duration of the thermal quench is similar in all cases, as inferred from the occurrence of a balance between impurity radiation and Ohmic heating. This is also manifested by the temperature decay time scale (see figure 6a), which decreases only slightly as larger preinjection temperatures are applied. The content of impurities inside the core plasma is identical during the thermal quench throughout the temperature range considered (see figure 8c). Consequently, larger densities of high impurity ionization stages are present at the end of the thermal quench in cases of high initial temperature (see figure 8d).

The seed population of hot-tail runaway electrons generated during the thermal quench increases in the central plasma as larger initial temperatures are applied (see § 5.3). Consequently, noticeable avalanche generation starts earlier in the disruption in the high-temperature cases (see figure 8a). In the process, the residual Ohmic current is depleted quicker, providing reduced amounts of Ohmic heating to the cold postquench plasma (see figure 8b). As impurity radiation and Ohmic heating is balanced during the current quench, the impurities deposited in cases of hotter predisruption plasmas effectively recombine earlier into the current quench (see figures 8c,d). Nevertheless, the total length of the disruptions simulated is comparable throughout the temperature range considered, with the postdisruption runaway current being established at around 6 ms after the MGI valve trigger.

5.5. Comparison with experimental observations

For a comparison of the postdisruption runaway current for varying preinjection temperatures between the ASTRA-STRAHL simulations discussed above and AUG experiments, discharges similar to AUG experiment #33108 are selected out of all runaway electron experiments performed in AUG. The selection is based on the preinjection plasma current, injection quantity, toroidal magnetic field and edge safety factor, according to the criteria listed in table 1. The experimentally measured runaway current as a function of the preinjection temperature is shown for these discharges, as well as for all runaway electron experiments performed in AUG in figure 9. The preinjection, on-axis electron temperatures are determined applying GPR (see § 3.2) to central ECE measurements.

Experimental observations of the postdisruption runaway electron current as a function of the preinjection temperature show no clear correlation between both quantities

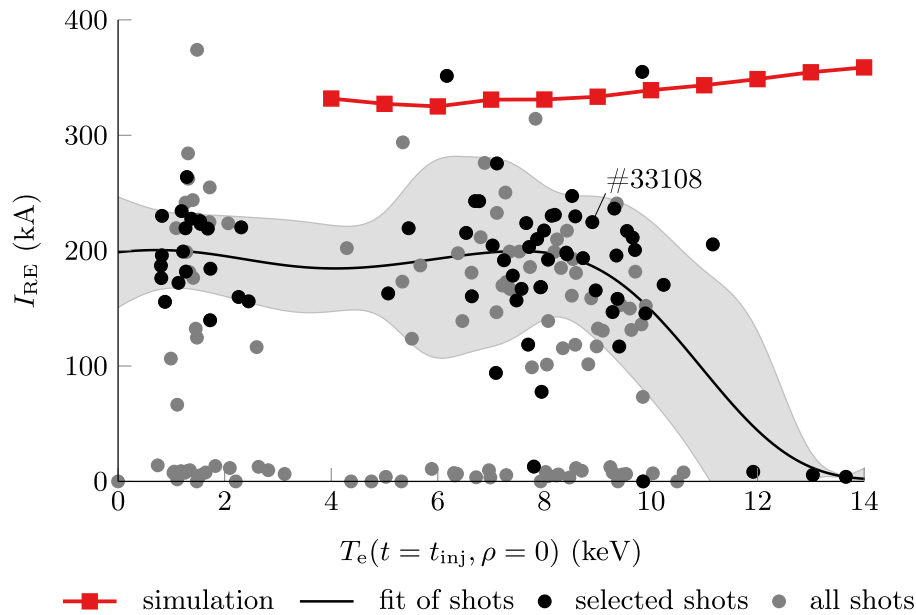


FIGURE 9. Postdisruption runaway electron current I_{RE} calculated in simulations of varying preinjection on-axis electron temperature $T_{e,0}$ (red squares) compared with the experimental dependence $I_{RE}(T_{e,0})$ of selected AUG shots similar to #33108 (black circles) and of all runaway electron experiments performed in AUG (grey circles). Gaussian process regression of shots similar to AUG #33108 shows the general trend observed experimentally (solid black), including uncertainties (filled grey).

(see figure 9). Runaway currents ranging from 150 to 250 kA are generated regularly, but may also be as large as 350 kA or may not be observed at all. Only for temperatures well above 10 keV, electron runaway does not occur. However, in this parameter region, only a small number of discharges has been performed. The experimentally observed relation between runaway current and postinjection temperature can be estimated applying GPR. Here, a runaway current of around 190 kA independent of the temperature is on average expected for temperatures below 9 keV.

In the ASTRA-STRAHL simulations of AUG discharge #33108 performed for varying preinjection temperatures, no strong temperature dependence of the postdisruption runaway current is observed for temperatures below 9 keV, similarly to the experimental estimate from Gaussian process regression. Yet, the calculated runaway current of around 330 kA is noticeably larger than the experimental average. Still, this behaviour is expected, as the assumption regarding the average runaway electron velocity, $\langle v_{RE} \rangle = c$, may somewhat overestimate the runaway current, especially from contributions of runaways generated late into the current quench. However, a reduction of $\langle v_{RE} \rangle / c$ will not proportionally reduce the postdisruption runaway current due to prolonged avalanche multiplication under these conditions (see Appendix B). As loss mechanisms for and radial transport of runaway electrons are also not considered in this work, the runaway current calculated is expected to be further overestimated. Thus, the simulations provide a pessimistic estimate of the runaway electron current. Under consideration of these effects, the relative contributions of individual generation mechanisms are expected to change only marginally, preserving the trends observed in the simulations. Importantly, neither in experiments, nor in simulations, a pronounced temperature dependence of the runaway current is observed for temperatures below 9 keV.

For temperatures above 10 keV, simulations predict a steadily increasing postdisruption runaway current, contrary to experimental observations of a vanishing runaway current. As runaway generation in all simulations occurs predominantly due to the avalanche mechanism, the absence of a postdisruption runaway current in the experiment suggests that no seed population is present at the end of thermal quench. After all, significant avalanche multiplication of a runaway seed is expected during the current quench, given that the parallel electric field typically far exceeds the effective critical electric field under these conditions. As the amount of material injected is similar in all experiments selected, the impurity friction experienced by highly energetic electrons is assumed not to be increased. Conditions for avalanche multiplication are therefore also expected suitable for preinjection temperatures above 10 keV.

Assuming favourable conditions for avalanche multiplication, the absence of a runaway seed population is due to either insufficient generation of primary runaways or due to the loss of the entire seed during breakup of the magnetic surfaces. However, the generation models employed in this work predict the formation of a noticeable seed population. Generation due to the Dreicer mechanism is driven by the contracting Ohmic current density in the vicinity of the $q = 2$ surface. Therefore, the modification of the central electron temperature profile affects electron runaway due to momentum-space diffusion in this particular region only insignificantly, even under consideration of radial broadening of the electron temperature profile during application of increasing amounts of ECRH. In the case of hot-tail runaway, an increase of the preinjection temperature strongly facilitates formation of a seed population, particularly under the assumption of radial broadening of the temperature profile. Thus, for preinjection temperatures beyond 10 keV, formation of a noticeable runaway seed is also expected to occur. Note that the exponential time scale t_{dec} and, more importantly, the variation thereof throughout the temperature range considered cannot be determined experimentally in AUG with the available diagnostics due to insufficient temporal resolution of the TS diagnostic and the ECE signal being in high-density cutoff.

The absence of a runaway current in AUG experiments with preinjection temperatures above 10 keV thus suggests, following the above argument, that the runaway seed is lost entirely during breakup of magnetic surfaces, i.e. before avalanche multiplication significantly increases the runaway population. Within ASTRA-STRAHL, this hypothesis cannot be tested as magnetic field line stochasticity and the associated runaway loss cannot be modelled self-consistently in this framework. Instead, non-linear MHD codes could be applied to investigate the existence of a transition in field line stochasticity in AUG disruptions when increasing the preinjection temperature to above 10 keV. Similarly, the signals of magnetic diagnostics in AUG disruption experiments of varying core temperature should be analysed in future work regarding changes in MHD activity.

It should be noted that, analysing AUG runaway experiments with preinjection temperatures above 10 keV, the low number of available discharges is not sufficient to rule out the existence of a postdisruption runaway current in this temperature region. After all, for the discharges selected, the absence of a postdisruption runaway current is also occasionally observed for temperatures below 10 keV. Therefore, further experiments with strongly increased temperatures are required to confirm or disprove the general absence of a postdisruption runaway current under these conditions.

The question of electron runaway at temperatures well above 10 keV is especially relevant for future fusion devices, such as ITER. If the runaway seed is indeed lost completely during high-temperature disruptions, the risk of producing a large runaway electron current would be greatly reduced. In the opposite case, the runaway seed

generated by the hot-tail mechanism is expected to contribute significantly to the overall plasma current. If, simultaneously, seed losses were to be increased (through external manipulation), poloidal flux could be removed effectively and thus avalanche multiplication hindered.

6. Conclusion

In this work, runaway electron generation in ASDEX Upgrade MGI experiments was investigated by means of 1.5-D transport simulations performed with the coupled codes ASTRA-STRAHL. The suitability of this approach for the study of electron runaway in ASDEX Upgrade has recently been demonstrated by Linder *et al.* (2020). For this study, the toolkit chosen has been extended by a model from Smith & Verwichte (2008) describing the hot-tail population during the thermal collapse of the plasma.

Applied in simulations of argon injection in ASDEX Upgrade discharge #33108, primary runaway generation mechanisms are calculated to both produce only a small seed population of comparable magnitude, being in total around 3 kA of fast electrons. Whereas electron runaway due to the Dreicer mechanism occurs as a result of the inward contracting Ohmic current predominantly in the vicinity of the $q = 2$ surface at $\rho \sim 0.7$ prior to thermal collapse, hot-tail runaway is encountered primarily in the central plasma during the thermal quench as the postcollapse hot-tail population is exponentially sensitive to the predisruption temperature, $n_{\text{hot}}(t_{\text{fin}}) \propto \exp(-1/T_{e,0})$. At the end of the disruption, a runaway current of 331 kA is obtained in the simulations, the vast majority generated by the avalanche mechanism. A similar impact of runaway generation mechanisms has also been observed in kinetic simulations with the full- f solver CODE (Insulander Björk *et al.* 2020). In the simulations presented in this work, similar postdisruption runaway electron currents are generated when neglecting one of the primary generation mechanisms. Thus, avalanche multiplication plays a significant role for the formation of a postdisruption runaway current in ASDEX Upgrade.

Investigating the impact of varying the central electron temperature prior to argon injection in these scenarios, the postdisruption runaway current is approximately constant for on-axis temperatures below 9 keV in both simulations and experiment, generating a runaway current of around 330 and 190 kA, respectively. Differences are assumed to be due to the absence of runaway loss mechanisms and an overestimation of the average runaway electron velocity, $\langle v_{\text{RE}} \rangle = c$. For larger temperatures up to 20 keV, simulations predict a strongly increased hot-tail population and consequently an increase of the postdisruption runaway current. Contradictorily, in the few ASDEX Upgrade discharges available in this parameter region, no postdisruption runaway current is detected. As the runaway electron models predict strong primary and secondary generation under these conditions, the absence of a postdisruption current in the experiment is considered to be caused by the loss of the entire seed population. Here, non-linear MHD codes could be applied to investigate if field line stochasticity drastically enhances seed losses. Furthermore, analysis of MHD activity inferred from measurements by magnetic diagnostics should be performed in future studies. Finally, further runaway electron experiments in ASDEX Upgrade are required to confirm or disprove the experimental trend observed.

In the simulations performed, the hot-tail mechanism provides only a small seed population of runaway electrons. Yet, the model by Smith & Verwichte (2008) employed is known to underestimate the hot-tail density (Stahl *et al.* 2016). Under application of more elaborate (kinetic) models, hot-tail runaway is thus suspected to be significantly increased. Simultaneously, in scenarios such as ASDEX Upgrade discharge #33108, the postdisruption runaway current is not expected to be drastically increased. However in

hotter predischruption plasmas, a more realistic description of hot-tail runaway could provide a substantial seed population. Simultaneously, magnetic perturbations could significantly reduce avalanche multiplication (Svensson *et al.* 2021). As this temperature range is relevant for future fusion devices, further investigation of primary runaway under these conditions is required. Here, reduced kinetic models, as, for example, being developed by Svenningsson (2020), could be employed in combination with radial runaway transport coefficients, e.g. by Särkimäki *et al.* (2020), to consider runaway losses.

Supplementary movie

Supplementary movie is available at <https://doi.org/10.1017/S0022377821000416>.

Acknowledgements

The authors would like to thank J. Hobirk for developing the high-temperature scenarios and M. Hoelzl for clarifying thoughts on MHD mode activity during the thermal quench.

Editor Tünde Fülöp thanks the referees for their advice in evaluating this article.

Funding

This work was supported by the EUROfusion - Theory and Advanced Simulation Coordination (E-TASC). This work has been carried out within the framework of the EUROfusion Consortium and has received funding from the Euratom research and training programme 2014-2018 and 2019-2020 under grant agreement No 633053. The views and opinions expressed herein do not necessarily reflect those of the European Commission.

Declaration of interests

The authors report no conflict of interest.

Appendix A. Approximation of the hot-tail density

The temporal evolution of the hot-tail runaway electron density $n_{\text{hot}}(t)$ throughout the thermal quench can be calculated with the model by Smith & Verwichte (2008). Yet to assess the density only at the end of the thermal quench at t_{fin} , evaluation of the model from onset of the quench at t_0 until t_{fin} is still required. Alternatively, a simple estimate can be obtained considering only the dominating contributions to the hot-tail density.

Considering the full expression (see (2.3))

$$n_{\text{hot}}(t) = \frac{4n_{e,0}}{\sqrt{\pi}v_{\text{th},0}^3} \int_{v_c(t)}^{\infty} (v^2 - v_c(t)^2) \exp\left(-\left[\frac{v^3}{v_{\text{th},0}^3} + 3\tau(t)\right]^{2/3}\right) dv, \quad (\text{A } 1)$$

the velocity distribution function is evaluated beyond the critical velocity for runaway $v_c^2 = e^3 n_e \ln \Lambda / 4\pi \epsilon_0^2 m_e E_{\parallel}$. Throughout the process of thermal collapse, an initially large $v_c(t_0) \gg v_{\text{th},0}$ will eventually approach $v_{\text{th},0}$, i.e. $v_c(t_{\text{fin}}) \rightarrow v_{\text{th},0}$, as the local electric field E_{\parallel} strongly increases. Simultaneously, the parameter $\tau(t)$ grows throughout the quench according to $\tau(t) = (t - t_{\text{dec}}) v_0 n_{e,\text{fin}} / n_{e,0}$. Consequently, the exponent of the exponential function of (A 1) starts typically far from unity, i.e. $v_c^3 / v_{\text{th},0}^3 + 3\tau \gg 1$. As the exponential function decreases rapidly for $v > v_c$, electrons with $v \gtrsim v_c$ contribute dominantly to the velocity-space integral. Under these assumptions, the argument of the exponential function in (A 1) can be approximated as

$$-\left[\frac{v^3}{v_{\text{th},0}^3} + 3\tau(t)\right]^{2/3} \approx -\left(\frac{v}{v_c(t)}\right)^2 \left[\left(\frac{v_c(t)}{v_{\text{th},0}}\right)^3 + 3\tau(t)\right]^{2/3}. \quad (\text{A } 2)$$

The solution of the velocity-space integral is thus readily obtained as

$$n_{\text{hot}}(t) = \frac{2n_{e,0}}{\sqrt{\pi}} \frac{\left(\frac{v_c(t)}{v_{\text{th},0}}\right)^3}{\left[\left(\frac{v_c(t)}{v_{\text{th},0}}\right)^3 + 3\tau(t)\right]^{2/3}} \exp\left(-\left[\left(\frac{v_c(t)}{v_{\text{th},0}}\right)^3 + 3\tau(t)\right]^{2/3}\right). \quad (\text{A } 3)$$

A similar approximation is derived in Smith & Verwichte (2008), where the numerator of the pre-exponential fraction is amended by $+3\tau(t)$. However, the resulting expression overestimates the hot-tail population, compared with evaluation of (A 1).

To obtain the postquench hot-tail population, the above expression has to be evaluated at time t^* , when the exponent of the exponential function reaches its maximum value. This in turn requires evaluation of the temporal evolution of the critical velocity $v_c(t)$. Considering an exponential decay of the electron temperature in the limit $T_{e,\text{fin}} \ll T_{e,0}$, i.e. $T_e(t) = T_{e,\text{fin}} + (T_{e,0} - T_{e,\text{fin}}) e^{-t/t_{\text{dec}}} \approx T_{e,0} e^{-t/t_{\text{dec}}}$, the evolution of the electric field required for $v_c(t)$ is obtained as

$$E_{\parallel}(t) = \frac{j_{\Omega,0}}{\sigma(t)} = \frac{e^2 \sqrt{m_e} \ln \Lambda}{8\sqrt{2}\pi\epsilon_0^2 T_e(t)^{3/2}} j_{\Omega,0} = E_{\parallel,0} \exp\left(\frac{3}{2} \frac{t}{t_{\text{dec}}}\right), \quad (\text{A } 4)$$

with σ being the plasma conductivity. Note, that the Ohmic current density $j_{\Omega}(t)$ is in good approximation constant throughout the part of the thermal collapse relevant for hot-tail runaway. Alternatively, the evolution of the electric field can be evaluated through $(d/dt)\{\sigma(t)E_{\parallel}(t)\} = -2RE_{\parallel}(t)/La^2$ (Hesslow *et al.* 2018b), with major radius R , minor radius a and inductance L . Using typical AUG parameters, deviations with respect to expression (A 4) become important only for $t/t_{\text{dec}} \gtrsim 5$, i.e. when the hot-tail population is already established. Thus, the ratio of velocities can be written as

$$\frac{v_c(t)}{v_{\text{th},0}} = \sqrt{\frac{en_{e,0}}{j_{\Omega,0}}} \sqrt{\frac{2T_{e,0}}{m_e}} \exp\left(-\frac{3}{4} \frac{t}{t_{\text{dec}}}\right) = \frac{v_{c,0}}{v_{\text{th},0}} \exp\left(-\frac{3}{4} \frac{t}{t_{\text{dec}}}\right) \quad (\text{A } 5)$$

and thus the exponent of the exponential function obtains its maximum value at time (see also Smith & Verwichte 2008)

$$t^* = \frac{4}{9} t_{\text{dec}} \left\{ 3 \log\left(\frac{v_{c,0}}{v_{\text{th},0}}\right) - \log\left(\frac{4}{3} \nu_0 \frac{n_{e,\text{fin}}}{n_{e,0}} t_{\text{dec}}\right) \right\}. \quad (\text{A } 6)$$

Applied in (A 3), the hot-tail population at the end of the thermal quench can be estimated as

$$n_{\text{hot}}(t_{\text{fin}}) \approx \frac{2n_{e,0}}{\sqrt{\pi}} \frac{\mathcal{F}^{1/3}}{\mathcal{G}^{2/3}} \exp\left(-(\mathcal{F}\mathcal{G})^{2/3}\right), \quad (\text{A } 7)$$

where

$$\mathcal{F} = \frac{4}{3} \nu_0 \frac{n_{e,\text{fin}}}{n_{e,0}} t_{\text{dec}}, \quad \mathcal{G} = 3 \log\left(\frac{v_{c,0}}{v_{\text{th},0}}\right) - \log \mathcal{F} - \frac{5}{4}. \quad (\text{A } 8a,b)$$

The radial variation of (A 7) is primarily determined by the contribution of \mathcal{F} in the exponent of the exponential function. To emphasize this dependence, further simplifications can be made by applying values for the disruption parameters as typically

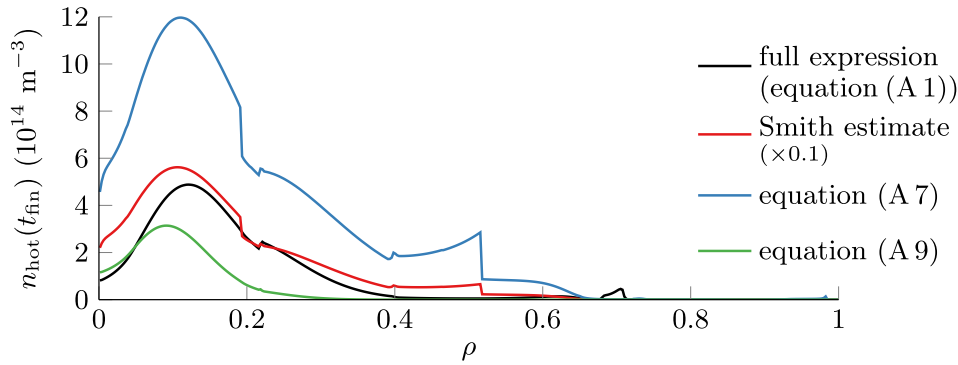


FIGURE 10. Hot-tail population of AUG #33108 calculated in simulations of ASTRA-STRAHL evaluating the full expression of (A 1) (black), see § 4, compared with analytical estimates from (23) of Smith & Verwichte (2008) (red), (A 7) (blue) and (A 9) (green). Note that the estimate using the approximation by Smith & Verwichte (2008) is scaled by a factor of $\times 0.1$.

occurring in AUG disruption experiments, yielding a pre-exponential factor of $\mathcal{F}/\mathcal{G}^2 \approx 1$ and inside the exponent $(4\mathcal{G}/3)^{2/3} \approx 4$. Writing the collision frequency as $\nu_0 n_{e,\text{fin}}/n_{e,0} \equiv \tilde{\nu} \ln \Lambda(t_0) n_{e,\text{fin}}/T_{e,0}^{3/2}$, the hot-tail runaway density can thus be expressed as

$$n_{\text{hot}}^{\text{simple}}(t_{\text{fin}}) = \frac{2n_{e,0}}{\sqrt{\pi}} \exp \left(-4 \left\{ \tilde{\nu} \ln \Lambda(t_0) \frac{n_{e,\text{fin}} t_{\text{dec}}}{T_{e,0}^{3/2}} \right\}^{2/3} \right). \quad (\text{A } 9)$$

Albeit being a simple estimate for the hot-tail population, key dependencies on thermal quench parameters are readily clear evaluating this expression. Estimates of the hot-tail population for the simulation of AUG discharge #33108 presented in § 4 are shown in figure 10 for the different analytical expressions introduced. The simple estimate of (A 9) agrees rather well with the hot-tail population obtained through evaluation of the full expression (A 1), thus illustrating the suitability of (A 9) to assess the dependence of the hot-tail population on parameters of the thermal quench.

Appendix B. Average runaway electron velocity

In the simulations presented, the runaway electron current density j_{RE} is calculated from the number density n_{RE} under the assumption that runaway electrons travel with the speed of light, i.e. the average runaway electron velocity $\langle v_{\text{RE}} \rangle = c$. For large kinetic energies $E_{\text{kin}} > 6.1 m_e c^2 = 3.1 \text{ MeV}$, this gives a less than 1% error. However, the validity of this assumption is often questioned. Therefore, it is demonstrated in this section that a reasonable choice of $\langle v_{\text{RE}} \rangle \sim c$ has only a minor impact on the amount of postdisruption runaway current generated.

In simulations of AUG #33108 of varying average runaway electron velocity, the postdisruption runaway electron current obtained is rather insensitive to a moderate modification of $\langle v_{\text{RE}} \rangle$, as shown in figure 11. Note, that these simulations presented were performed with decreased temporal resolution for illustrative purposes. Assuming an average velocity of 50% c , the postdisruption runaway current is reduced by 15%. Only for $\langle v_{\text{RE}} \rangle \lesssim 20\% c$, the runaway current calculated falls off quickly. Importantly, the associated kinetic energy of the runaway electrons is well below $m_e c^2$ for both choices of $\langle v_{\text{RE}} \rangle/c$ discussed, approaching even the pre-disruption thermal electron energy. However as the bulk of the runaway electron population is expected to reach kinetic energies above the rest mass energy, corresponding to $\langle v_{\text{RE}} \rangle > 87\% c$, the postdisruption runaway current is not significantly affected by a variation of $\langle v_{\text{RE}} \rangle$ within these bounds.

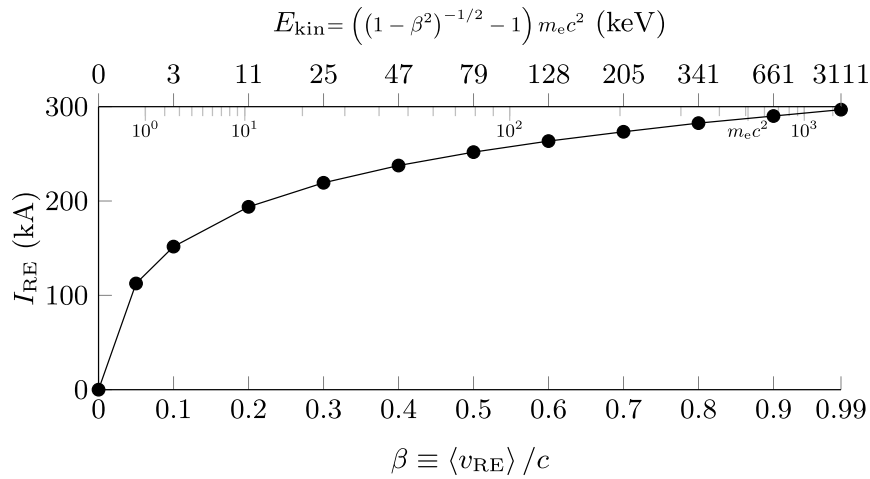


FIGURE 11. Postdisruption runaway electron current I_{RE} in simulations of AUG #33108 applying a varying average runaway electron velocity $\langle v_{RE} \rangle$. For reference, the corresponding kinetic electron energy E_{kin} is given. Note, that these simulations were carried out with decreased temporal resolution for illustrative purposes.

A variation of the average runaway electron velocity can also be considered as a variation of the strength of primary runaway electron generation under the assumption $\langle v_{RE} \rangle = c$. Writing $\beta \equiv \langle v_{RE} \rangle / c$, the macroscopic transport equation (2.1) for the primary runaway electron current density can be expressed as (neglecting radial transport)

$$\frac{\partial j_{seed}}{\partial t} = e \langle v_{RE} \rangle S_{seed} = e (c\beta) S_{seed} = ec (\beta S_{seed}), \quad (\text{B } 1)$$

hence describing either a variation of $\langle v_{RE} \rangle$ or of S_{seed} . Simultaneously, avalanche multiplication is described by

$$\frac{\partial j_{av}}{\partial t} = e \langle v_{RE} \rangle n_{RE} \tilde{S}_{av} = (j_{av} + j_{seed}) \tilde{S}_{av}, \quad (\text{B } 2)$$

thus not explicitly considering assumptions regarding the average runaway electron velocity. A variation of $\langle v_{RE} \rangle$ does therefore directly affect only the primary population. Hence, varying β within the range $[0, 1]$, the source strength S_{seed} can be considered scaled by this factor instead of $\langle v_{RE} \rangle$. Under these conditions of decreased primary generation, however, avalanche multiplication is not affected proportionally, as discussed in § 4.3.

REFERENCES

- ALEYNIKOV, P. & BREIZMAN, B. N. 2017 Generation of runaway electrons during the thermal quench in tokamaks. *Nucl. Fusion* **57**, 046009. <https://doi.org/10.1088/1741-4326/aa5895>.
- BANDARU, V., HOELZL, M., ARTOLA, F. J., PAPP, G. & HUIJSMANS, G. T. A. 2019 Simulating the nonlinear interaction of relativistic electrons and tokamak plasma instabilities: Implementation and validation of a fluid model. *Phys. Rev. E* **99**, 063317. <https://doi.org/10.1103/PhysRevE.99.063317>.
- BOOZER, A. H. 2019 Magnetic surface loss and electron runaway. *Plasma Phys. Control. Fusion* **61**, 024002. <https://doi.org/10.1088/1361-6587/aaf293>.
- BREIZMAN, B. N., ALEYNIKOV, P., HOLLMANN, E. M. & LEHNEN, M. 2019 Physics of runaway electrons in tokamaks. *Nucl. Fusion* **59**, 083001. <https://doi.org/10.1088/1741-4326/ab1822>.
- CHILENSKI, M. A., GREENWALD, M., MARZOUK, Y., HOWARD, N. T., WHITE, A. E., RICE, J. E. & WALK, J. R. 2015 Improved profile fitting and quantification of uncertainty in experimental measurements of impurity transport coefficients using Gaussian process regression. *Nucl. Fusion* **55**, 023012. <https://doi.org/10.1088/0029-5515/55/2/023012>.

- CHIU, S. C., ROSENBLUTH, M. N., HARVEY, R. W. & CHAN, V. S. 1998 Fokker-Planck simulations mylb of knock-on electron runaway avalanche and bursts in tokamaks. *Nucl. Fusion* **38**, 1711. <https://doi.org/10.1088/0029-5515/38/11/309>.
- CODA, S., AGOSTINI, M., ALBANESE, R., ALBERTI, S., ALESSI, E., ALLAN, S., ALLCOCK, J., AMBROSINO, R., ANAND, H., THE EUROFUSION MST1 TEAM, *et al.* 2019 Physics research on the TCV tokamak facility: from conventional to alternative scenarios and beyond. *Nucl. Fusion* **59**, 112023. <https://doi.org/10.1088/1741-4326/ab25cb>.
- COMMAUX, N., BAYLOR, L. R., JERNIGAN, T. C., HOLLMANN, E. M., PARKS, P. B., HUMPHREYS, D. A., WESLEY, J. C. & YU, J. H. 2010 Demonstration of rapid shutdown using large shattered deuterium pellet injection in DIII-D. *Nucl. Fusion* **50**, 112001. <https://doi.org/10.1088/0029-5515/50/11/112001>.
- CONNOR, J. W. & HASTIE, R. J. 1975 Relativistic limitations of runaway electrons. *Nucl. Fusion* **15**, 415. <https://doi.org/10.1088/0029-5515/15/3/007>.
- DUX, R., PEETERS, A. G., GUDE, A., KALLENBACH, A. & NEU, R. & THE ASDEX UPGRADE TEAM 1999 Z dependence of the core impurity transport in ASDEX Upgrade H mode discharges. *Nucl. Fusion* **39**, 1509. <https://doi.org/10.1088/0029-5515/39/11/302>.
- FABLE, E., ANGIONI, C., IVANOV, A. A., LACKNER, K., MAJ, O., MEDVEDEV, S. Y., PAUTASSO, G., PEREVERZEV, G. V. & TREUTTERER, W. & THE ASDEX UPGRADE TEAM 2013 Dynamical coupling between magnetic equilibrium and transport in tokamak scenario modelling, with application to current ramps. *Plasma Phys. Control. Fusion* **55**, 074007. <https://doi.org/10.1088/0741-3335/55/7/074007>.
- FABLE, E., PAUTASSO, G., LEHNEN, M., DUX, R., BERNERT, M. & MLYNEK, A. & THE ASDEX UPGRADE TEAM 2016 Transport simulations of the pre-thermal-quench phase in ASDEX Upgrade massive gas injection experiments. *Nucl. Fusion* **56**, 026012. <https://doi.org/10.1088/0029-5515/56/2/026012>.
- FEHÉR, T., SMITH, H. M., FÜLÖP, T. & GÁL, K. 2011 Simulation of runaway electron generation during plasma shutdown by impurity injection in ITER. *Plasma Phys. Control. Fusion* **53**, 035014. <https://doi.org/10.1088/0741-3335/53/3/035014>.
- HARVEY, R. W., CHAN, V. S., CHIU, S. C., EVANS, T. E., ROSENBLUTH, M. N. & WHYTE, D. G. 2000 Runaway electron production in DIII-D killer pellet experiments, calculated with the CQL3D/KPRAD model. *Phys. Plasmas* **7**, 4590. <https://doi.org/10.1063/1.1312816>.
- HARVEY, R. W., PETROV, Y. V., KIM, C. C., FOREST, C. B., LAO, L. L. & PARKS, P. B. 2019 Time-dependent runaway electron simulations: Ampere-Faraday equations implemented in CQL3D. *Nucl. Fusion* **59**, 106046. <https://doi.org/10.1088/1741-4326/ab38cb>.
- HESSLOW, L., EMBRÉUS, O., HOPPE, M., DUBOIS, T. C., PAPP, G., RAHM, M. & FÜLÖP, T. 2018a Generalized collision operator for fast electrons interacting with partially ionized impurities. *J. Plasma Phys.* **84**, 905840605. <https://doi.org/10.1017/S0022377818001113>.
- HESSLOW, L., EMBRÉUS, O., VALLHAGEN, O. & FÜLÖP, T. 2019a Influence of massive material injection on avalanche runaway generation during tokamak disruptions. *Nucl. Fusion* **59**, 084004. <https://doi.org/10.1088/1741-4326/ab26c2>.
- HESSLOW, L., EMBRÉUS, O., WILKIE, G. J., PAPP, G. & FÜLÖP, T. 2018b Effect of partially ionized impurities and radiation on the effective critical electric field for runaway generation. *Plasma Phys. Control. Fusion* **60**, 074010. <https://doi.org/10.1088/1361-6587/aac33e>.
- HESSLOW, L., UNNERFELT, L., VALLHAGEN, O., EMBRÉUS, O., HOPPE, M., PAPP, G. & FÜLÖP, T. 2019b Evaluation of the Dreicer runaway growth rate in the presence of high-Z impurities using a neural network. *J. Plasma Phys.* **85**, 475850601. <https://doi.org/10.1017/S0022377819000874>.
- HO, A., CITRIN, J., AURIEMMA, F., BOURDELLE, C., CASSON, F. J., KIM, H.-T., MANAS, P., SZEPESI, G. & WEISEN, H. & JET CONTRIBUTORS 2019 Application of Gaussian process regression to plasma turbulent transport model validation via integrated modelling. *Nucl. Fusion* **59**, 056007. <https://doi.org/10.1088/1741-4326/ab065a>.
- HOPPE, M., HESSLOW, L., EMBREUS, O., UNNERFELT, L., PAPP, G., PUSZTAI, I., FÜLÖP, T., LEXELL, O., LUNT, T., MACUSOVA, E., *et al.* 2021 Spatiotemporal analysis of the runaway distribution function from synchrotron images in an ASDEX Upgrade disruption. *J. Plasma Phys.* **87**, 855870102. <https://doi.org/10.1017/S002237782000152X>.

- INSULANDER BJÖRK, K., PAPP, G., EMBREUS, O., HESSLOW, L., FÜLÖP, T., VALLHAGEN, O., LIER, A., PAUTASSO, G., BOCK, A., THE ASDEX UPGRADE TEAM, *et al.* 2020 Kinetic modelling of runaway electron generation in argon-induced disruptions in ASDEX Upgrade. *J. Plasma Phys.* **86**, 855860401. <https://doi.org/10.1017/S0022377820000793>.
- LEHNEN, M., ALEYNIKOVA, K., ALEYNIKOV, P. B., CAMPBELL, D. J., DREWELow, P., EIDIETIS, N. W., GASPARYAN, Y., GRANETZ, R. S., GRIBOV, Y., HARTMANN, N., *et al.* 2015 Disruptions in ITER and strategies for their control and mitigation. *J. Nucl. Mater.* **463**, 39. <https://doi.org/10.1016/j.jnucmat.2014.10.075>.
- LINDER, O., FABLE, E., JENKO, F., PAPP, G. & PAUTASSO, G., THE ASDEX UPGRADE TEAM & THE EUROFUSION MST1 TEAM 2020 Self-consistent modeling of runaway electron generation in massive gas injection scenarios in ASDEX Upgrade. *Nucl. Fusion* **60**, 096031. <https://doi.org/10.1088/1741-4326/ab9dcf>.
- MARTÍN-SOLÍS, J. R., LOARTE, A., HOLLMANN, E. M., ESPOSITO, B. & RICCARDO, V., FTU TEAM, DIII-D TEAM & JET EFDA CONTRIBUTORS 2014 Inter-machine comparison of the termination phase and energy conversion in tokamak disruptions with runaway current plateau formation and implications for ITER. *Nucl. Fusion* **54**, 083027. <https://doi.org/10.1088/0029-5515/54/8/083027>.
- MATTHEWS, G. F., BAZYLEV, B., BARON-WIECHEC, A., COENEN, J., HEINOLA, K., KIPTILY, V., MAIER, H., REUX, C., RICCARDO, V., RIMINI, F., *et al.* 2016 Melt damage to the JET ITER-like Wall and divertor. *Phys. Scr.* **T167**, 014070. <https://doi.org/10.1088/0031-8949/T167/1/014070>.
- PAPP, G., FÜLÖP, T., FEHÉR, T., DE VRIES, P. C., RICCARDO, V., REUX, C., LEHNEN, M., KIPTILY, V., PLYUSNIN, V. V., ALPER, B., *et al.* 2013 The effect of ITER-like wall on runaway electron generation in JET. *Nucl. Fusion* **53**, 123017. <https://doi.org/10.1088/0029-5515/53/12/123017>.
- PAUTASSO, G., BERNERT, M., DIBON, M., DUVAL, B., DUX, R., FABLE, E., FUCHS, J. C., CONWAY, G. D., GIANNONE, L., GUDE, A., *et al.* 2017 Disruption mitigation by injection of small quantities of noble gas in ASDEX Upgrade. *Plasma Phys. Control. Fusion* **59**, 014046. <https://doi.org/10.1088/0741-3335/59/1/014046>.
- PAUTASSO, G., DIBON, M., DUNNE, M., DUX, R., FABLE, E., LANG, P., LINDER, O., MLYNEK, A., PAPP, G., BERNERT, M., *et al.* 2020 Generation and dissipation of runaway electrons in ASDEX Upgrade experiments. *Nucl. Fusion* **60**, 086011. <https://doi.org/10.1088/1741-4326/ab9563>.
- PAZ-SOLDAN, C., ALEYNIKOV, P., HOLLMANN, E. M., LVOVSKIY, A., BYKOV, I., DU, X., EIDIETIS, N. W. & SHIRAKI, D. 2020 Runaway electron seed formation at reactor-relevant temperature. *Nucl. Fusion* **60**, 056020. <https://doi.org/10.1088/1741-4326/ab7fe1>.
- PEETERS, A. G. 2000 Reduced charge state equations that describe Pfirsch Schlüter impurity transport in tokamak plasma. *Phys. Plasmas* **7**, 268. <https://doi.org/10.1063/1.873812>.
- PETROV, Y. V., PARKS, P. B. & HARVEY, R. W. 2021 Numerical simulation of the hot-tail runaway electron production mechanism using CQL3D and comparison with Smith-Verwichte analytical model. *Plasma Phys. Control. Fusion* **63**, 035026. <https://doi.org/10.1088/1361-6587/abdacc>.
- REUX, C., PAZ-SOLDAN, C., ALEYNIKOV, P., BANDARU, V., FICKER, O., SILBURN, S., HOELZL, M., EIDIETIS, N., LEHNEN, M., SRIDHAR, S., *et al.* 2021 Demonstration of safe termination of megaampere relativistic electron beams in tokamaks. *Phys. Rev. Lett.* (accepted for publication).
- SÄRKIMÄKI, K., EMBREUS, O., NARDON, E. & FÜLÖP, T. & JET CONTRIBUTORS 2020 Assessing energy dependence of the transport of relativistic electrons in perturbed magnetic fields with orbit-following simulations. *Nucl. Fusion* **60**, 126050. <https://doi.org/10.1088/1741-4326/abb9e9>.
- SCHNEIDER, P. A. 2012 Characterization and scaling of the tokamak edge transport barrier. PhD thesis, Ludwig-Maximilians-Universität. <https://doi.org/10.5282/edoc.14723>.
- SMITH, H. M. & VERWICHTE, E. 2008 Hot tail runaway electron generation in tokamak disruptions. *Phys. Plasmas* **15**, 072502. <https://doi.org/10.1063/1.2949692>.
- STAHL, A., EMBREUS, O., PAPP, G., LANDREMAN, M. & FÜLÖP, T. 2016 Kinetic modelling of runaway electrons in dynamic scenarios. *Nucl. Fusion* **56**, 112009. <https://doi.org/10.1088/0029-5515/56/11/112009>.
- SUMMERS, H. P. 2004 The ADAS User Manual, version 2.6. Available at: <https://www.adas.ac.uk>.
- SVENNINGSSON, I. 2020 Hot-tail runaway electron generation in cooling fusion plasmas. Master's thesis, Chalmers University of Technology. Available at: <https://hdl.handle.net/20.500.12380/300899>.

- SVENSSON, P., EMBREUS, O., NEWTON, S. L., SÄRKIMÄKI, K., VALLHAGEN, O. & FÜLÖP, T. 2021 Effects of magnetic perturbations and radiation on the runaway avalanche. *J. Plasma Phys.* **87**, 905870207. <https://doi.org/10.1017/S0022377820001592>.
- TINGUELY, R. A., GRANETZ, R. S., HOPPE, M. & EMBRÉUS, O. 2018 Measurements of runaway electron synchrotron spectra at high magnetic fields in Alcator C-Mod. *Nucl. Fusion* **58**, 076019. <https://doi.org/10.1088/1741-4326/aac444>.
- VALLHAGEN, O., EMBREUS, O., PUSZTAI, I., HESSLOW, L. & FÜLÖP, T. 2020 Runaway dynamics in the DT phase of ITER operations in the presence of massive material injection. *J. Plasma Phys.* **86**, 475860401. <https://doi.org/10.1017/S0022377820000859>.